MINERALOGY, GEOCHEMISTRY AND GENESIS OF THE HYDROTHERMAL REE-FLUORITE-AG-PB-CU ORE DEPOSITS OF THE GALLINAS MOUNTAINS, NEW MEXICO

by

Zachary Vance

Submitted in Partial Fulfillment
Of the Requirements for the

Masters of Science in Geology

New Mexico Institute of Mining and Technology
Department of Earth and Environmental Science

Socorro, New Mexico

May, 2013

ABSTRACT

During the past decade, worldwide demand for rare earth elements (REE) has surged; however, the genesis and geochemical characteristics of hydrothermal REE deposits associated with alkalic igneous systems remain poorly understood. This is significant given that much of the world's historical production of REE is associated with alkaline igneous activity, including carbonatites. This study addresses the genesis of bastnaesite-fluorite breccia deposits and their association with Ag-Pb-Zn sulfide mineralization in the Gallinas Mountains intrusive alkalic suite. The spatial and chemical association between these two types of deposits and the amenability of many ore and gangue minerals to stable isotopic study provides a unique opportunity to examine the history of hydrothermal fluids responsible for mineralization.

Mineral associations, especially products of sulfide weathering i.e. agardite, indicate a genetic link between REE and sulfide mineralization in some deposits. $\delta^{34}S$ isotopic ratios of sulfide and sulfate species vary from -21.1 to 1.5‰ and 9.6 to 13.3‰ vs. CDT, respectively. Isotopic ratios of carbonate species ($\delta^{13}C$ and $\delta^{18}O$) vary from -11.1 to -3.4‰ vs. PDB and 15.0 to 23.8‰ vs. VSMOW, respectively. $\delta^{34}S$ and $\delta^{18}O_{SO4}$ data, barite and galena trace-element chemistry, and the overall mineralogy of the district suggest the presence of an oxidized hydrothermal fluid and that cooling was responsible for large spatial and temporal isotopic changes. Mixing of a primary magmatic fluid with regional groundwater in isotopic equilibrium with the overlying Yeso Formation, known to contain abundant gypsum, appears responsible for mineralization. Stable isotope geothermometry (bar-gn) yields a temperature of formation of ~310°C in the deeper parts of the system and fluid inclusion temperatures from previous studies indicate a temperature of ~200°C for late sulfide formation in the upper reaches of the system. $\delta^{13}C$ data from the M and E No. 13 prospect fall within the range of primary carbonatites although $\delta^{18}O$ data are somewhat positive. These data suggest that calcite mineralization, particularly in the vicinity of the M & E No. 13 prospect, was late-stage fracture filling and that calcite precipitated at low temperatures from a cooled magmatic fluid. Whole rock and mineral trace-element abundances and ratios indicate that the M and E No. 13 underwent different formation processes than other deposits and that ore mineralization was likely derived from a carbonatite source.

A model developed from this data suggests that REE were derived from a highly differentiated alkalic parent source rock along with base and precious metals. Deposition of bastnaesite, base, and precious metals occurred due to fluid mixing and cooling. Base and precious metal mineralization continued into the upper reaches of the system until solutions finally became relatively cool near the Yeso contact. This study suggests that the association between bastnaesite (REE) and sulfide mineralization is complex, but likely to occur in alkalic igneous districts that have seen drastic changes in fluid physiochemistry during the lifetime of the hydrothermal system. The presence of a carbonatite source at depth is indicated by the petrologic association with alkalic rocks, metal ratios, REE spider diagrams, alkali metasomatism, high levels of REE, F, Ba, Sr, and stable isotopic ratios associated with carbonitization. The model suggests that this type of hydrothermal REE-fluorite-sulfide mineralization may be intimately associated with a carbonatite at depth.

Keywords: Rare Earth Elements; Gallinas Mountains, Stable Isotopes

ACKNOWLEDGEMENTS

The funding for this study was provided by the New Mexico Geological Society, Society of Economic Geologists and the Colorado Scientific Society. I would also like to thank the New Mexico Tech department of Earth and Environmental Science and the New Mexico Bureau of Mines and Mineral Resources for their ongoing support.

I would like to thank Strategic Resources Inc. for their samples of core and guidance around the district. I would also like to thank Rare Element Resources Inc. (Dr. Jim Clark) for employment and guidance during the summer of 2012.

I would particularly like to thank Dr. Virgil Lueth and Dr. Andrew Campbell for their many thoughtful discussions and helpful comments. Without their guidance this project would have neither started nor finished. I would also like to thank them for their guidance in the field and lab for they have taught me most of what I know about mineral relationships and made me believe in the power of geochemistry. I would also like to thank Dr. Peter Mozley for serving on my thesis committee.

I would like to thank Dr. William Chavéz, Dr. Nelia Dunbar, Dr. Shari Kelly, Bonnie Frey, and Lynn Heizler for helping me in their respective labs as well as being great teachers. I would also like to thank Gus Tolley, Mark Green and Brad Sion for working through computer based software with me. This project would not have been possible without support from my friends made here in New Mexico. Hunter and James Knox provided ongoing support during my first year and Nels Iverson provided much support during my second year.

Lastly, I would like to dedicate this thesis to my wife, Erica. Without her kindness, support and encouragement this could not have been a success.

TABLE OF CONTENTS

LIST OF FIGURES

LIST OF TABLES

This thesis is accepted on behalf of the
Faculty of the Institute by the following committee:

_____

Advisor

_____

_____

_____

_____

_____

Date

I release this document to the New Mexico Institute of Mining and Technology.

_____

Student's Signature Date

1. INTRODUCTION

Worldwide demand for Rare Earth Elements (REE) has surged in recent years. Their unique electromagnetic characteristics are useful in a wide variety of green technologies, batteries, magnets, and electronics. Since the 1980's demand for REE has been met by a large supply from a number of Chinese deposits, in particular the Bayan Obo deposit in northern China and ion-adsorption clays from southern China. Recent interest by the United States government has initiated much exploration activity in North America. Deposits of interest include Mountain Pass, CA; Bear Lodge, WY; Iron Hill, CO; and the Gallinas Mountains, NM (Long et al., 2010).

Rare Earth Elements are a group of elements ranging from Lanthanum to Lutetium (atomic numbers 57 to 71) on the periodic table. The elements Yttrium (39) and Scandium (21) are also often included in this grouping but are not strictly rare earth elements. REE are often subcategorized into two groups, light REE (LREE) and heavy REE (HREE). This distinction is based on a structural change in any particular REE phosphate. The elements La through Gd in phosphates are monoclinic while Tb through Lu phosphates are a tetragonal zircon structure (Ni et al. 1995). LREE comprise elements La-Gd and HREE comprise Tb-Lu.

REE occur in trace amounts in almost every common mineral but economically significant deposits occur in only a few varieties of host lithologies with specific mineralogies. Historically, the minerals monazite [$REE(PO_4)$] and bastnaesite [$REE(CO_3)F$] have been the two most common sources of REE. Monazite occurs as a trace mineral in many granitic rocks and often concentrates in pegmatite phases. It is a very dense mineral; thus it can also concentrate in heavy mineral sands. Bastnaesite is

commonly associated with carbonatites; a relatively rare rock type comprised of over 50 wt. % igneous carbonate minerals which often has anonymously high REE concentrations (Long et al, 2010). Carbonatites are often associated closely with continental rift settings; more specifically, alkaline igneous rocks (Long et al., 2010). Almost all bastnaesite mineralization is related to carbonatites, although in the case of the Gallinas Mountains, NM, bastnaesite mineralization is related to a hydrothermal system and the fluid source is unknown (Perhac, 1970; Mariano, 1989; and Schreiner, 1993).

A number of hydrothermal REE-fluorite-Ag-Pb-Cu deposits occur in the Gallinas Mountains, NM with a spectrum of features. Deposits range in style from sulfide veins within fluorite cemented breccias to fault breccias to isolated breccia pipes. In all cases, bastnaesite occurs within a fluorite cemented breccia (Perhac and Heinrich, 1964; Perhac, 1970; and Schreiner, 1993). The overwhelming presence of fluorite, REE bearing minerals, the alkaline nature of the igneous phases, carbonate flooding, sodic and potassic alteration in the district has led some authors to call upon a hidden carbonatite as the REE metal source and hydrothermal heat source (Schreiner, 1993 and McLemore, 2010).

To date, the relationship between REE mineralization and associated sulfide mineralization in the Gallinas Mountains was largely overlooked. Although the presence of sulfides in primary carbonatite systems is well known, hydrothermal deposits containing both REE and sulfide mineralization are rare (Mitchell and Krauss, 1975 and Deines, 1989). This study will address the relationship between REE and sulfide mineralization as well as evaluate the role (if any) of a carbonatite with respect to hydrothermal fluid generation and REE-fluorite-sulfide mineralization.

Previous authors used fluid inclusion data from the Gallinas Mountains to discuss REE transport in hydrothermal systems (Williams-Jones et al., 2000). They also used this data to suggest a depositional mechanism for REE-fluorite breccias (Williams-Jones et al., 2000). This study uses $\delta^{13}C$, $\delta^{18}O$, $\delta^{34}S$ and $\delta^{18}O_{SO4}$ data coupled with detailed mineralogy to independently test the model proposed by Williams-Jones et al. (2000) for the formation of REE deposits in the Gallinas Mountains.

1.1 Previous Work

Geologic descriptions on the regional, district, and deposit scale made by previous authors provides the necessary framework in which geochemical analyses of the present study are interpreted. A compilation of these works and their findings is presented below.

Lindgren et al. (1910) was the first to mention the iron deposits of the Gallinas Mountains, NM also noting that there were significant potential sources of base and precious metals in the area. Fluorspar deposits were first described by the United States Geological Survey who was also the first to map the district both topographically and geologically (Kelly, 1946). The U.S. Bureau of Mines published a report in 1946 describing the general geology, ore deposits and accessibility of the area (Soulé, 1946). Mining information was compiled and the geology of the district was again described by the New Mexico Bureau of Mines and Mineral Resources (Griswold, 1959). The first study on mineral paragenesis and fluid inclusion microthermometry was published in by Perhac and Heinrich (1964) and was followed closely by a mapping, rock and ore deposit descriptions, and alteration descriptions (Perhac, 1970). A short publication on the possibilities of gold mineralization was published by the New Mexico Bureau of Geology

noting the common connection between alkaline igneous rocks and large gold deposits (Woodward and Fulp, 1991).

The United States Bureau of Mines conducted a vigorous study in 1993 which included: mapping, cathodoluminescence, Scanning Electron Microscopy – Energy-dispersive X-ray spectroscopy, whole rock geochemistry, rock type and ore deposit descriptions (Schreiner, 1993). This study was the first to highlight Na and K metasomatism of country rocks. This observation led the author to suggest the presence of a carbonatite noting that Na and K metasomatism is ubiquitous wherever carbonatites occur. The cathodoluminescence of certain minerals also provided evidence suggesting the presence of a carbonatite (Schreiner, 1993). However, it is necessary to have direct evidence of a carbonatite in order to refer to this type of alteration as fenitization. Because direct evidence has never been established, what previous authors have deemed "fenitization" will be referred to as Na and K metasomatism.

In 2000, a study was published on the topic of REE mobility in hydrothermal systems (Williams-Jones et al. 2000). The authors used fluid inclusions from fluorite, bastnaesite, and quartz from two representative deposits to suggest a model for mineralization. From fluid inclusion homogenization temperatures and compositions as well as deposit mineralogies, they concluded that deposits were formed by the mixing of a REE-bearing orthomagmatic fluid and a Ca-bearing formation water. Through fluid inclusion homogenization temperatures, the study concludes that quartz and bastnaesite were deposited at temperatures of ~300-400 °C while fluorite fluid inclusions homogenize from ~100-250°C. Bulk salinity of fluids responsible for quartz and bastnaesite deposition was ~15 wt. % NaCl equivalent.

Most recently a report with new bulk geochemical analyses was compiled at the New Mexico Bureau of mines and Mineral Resources with some financial support for analyses from Strategic Resources Inc. (McLemore, 2010).

A growing body of work suggests that hydrothermal processes play important role in many REE deposits (Mariano, 1989; Campbell et al. 1995; Sampson et al. 1995; Williams-Jones et al. 2000; Van Dongen et al. 2010). To date few studies have employed stable isotopic ratios to help discern major mechanisms and processes through which mineralization occurs, particularly in hydrothermal epithermal environments.

Isotopic studies focused on the petrogenesis of carbonatites are fairly abundant (Deines, 1989) while similar studies on related mineralization, especially sulfide, is rare. Carbonatites, by definition, are always C and O bearing and in some cases are rich in S as well. Variations in stable isotope ratios of carbonatites are attributed to (a) isotopic compositions of the source magma, (b) fractionation processes, and (c) alteration. It has been shown by many authors that $\delta^{13}C$ and $\delta^{18}O$ ratios of carbonatites can vary greatly (-12‰ to 2‰ and 4‰ to 25‰ respectively) due to changing combinations of the above factors but $\delta^{18}O$ values most commonly fall within 5 to 10‰ (Deines, 1989). $\delta^{34}S$ ratios of sulfur bearing minerals are normally much more narrowly constrained with 95% of values falling within -5‰ and 2% (Deines, 1989). In one instance, $\delta^{34}S$ values were abnormal and this was attributed to fO_2, pH, and temperature conditions which control the dominant sulfur bearing species (Mitchell and Krauss, 1975).

2. REGIONAL GEOLOGY

The Gallinas Mountains are located in Lincoln County approximately 40 miles north of Carrizozo and 10 miles west of Corona. They are elevated about 2,000 feet from the surrounding plains to a maximum height of 8,637 ft on Gallinas Peak. They occur at the northern end of the Lincoln County porphyry belt (Allen and Foord, 1991) on the eastern most margin of the Rio Grande Rift.

2.1 Geology

The Lincoln County porphyry belt is a group of Tertiary igneous rocks exposed in east-central New Mexico (Kelly and Thompson, 1964). Due to chemical and spatial relationships, these rocks are considered part of the Rocky Mountain alkalic province which extends from Canada along the eastern front of the Rocky Mountains into Mexico (Carmichael et al., 1974). A single K-Ar date on orthoclase was reported by Perhac (1970) of 29.9 Ma for the Gallinas Mountains; however, due to lack of cross cutting relationships and modern dating techniques, a low level of confidence is placed on this age.

The LCPB includes the Capitan pluton, an east-west trending alkalic intrusion ~40 miles southeast of the Gallinas. The Capitan Mountains are host to Fe-skarns as well as the REE silicate (allanite) in quartz veins (Campbell et al., 1995).

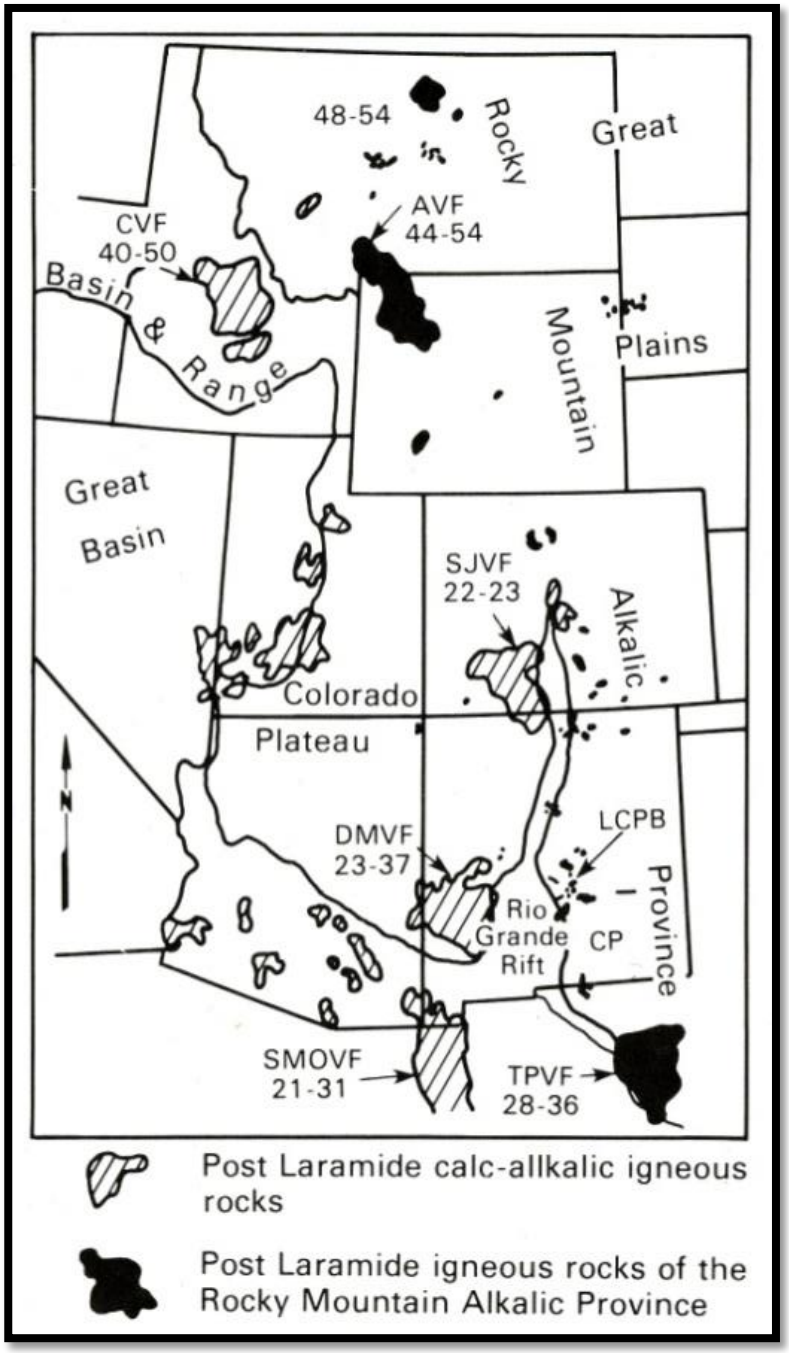

Figure 1. The Rocky Mountain Alkalic Belt. Numbers given denote ages in Ma. LCPB is an abbreviation for Lincoln County Porphyry Belt, a group of alkalic igneous rocks within east central New Mexico of similar ages. The north-south trending Rocky Mountain Alkalic Province is host to a number of REE deposits including the Bear Lodge, WY, Iron Hill, CO, the Gallinas Mountains, NM, and the Capitan Mountains, NM. Figure modified from Allen and McLemore (1991). The Rio Grande Rift was initiated ~35 Ma and extends from central Colorado into northern Mexico bisecting New Mexico. Rifting has introduced regional uplift and is responsible, along with the subduction of the Laramide plate, for much of the Tertiary volcanism.

2.2 District Geology

The description of the local geology is largely taken from Perhac (1970), Schreiner (1993), McLemore (2010) and modified by recent field and petrographic observations. Absolute abundances of phases, mineralogy, and petrography of the rock units in the area are explained in detail by cited reports.

The district is underlain by Precambrian granite which exposed in three outcrops in Red Cloud Canyon. The granite is coarse grained, equigranular, light gray to pink-gray in color. This rock type is primarily comprised of quartz, microcline, albite with accessory biotite, zircon, magnetite, sphene, and apatite. Mild alteration and weathering of mafic minerals to clay and Fe-oxides is common.

The Permian Abo Formation is a basal conglomeratatic arkose and interbedded shale, siltstone, sandstone, and conglomerate, which overlays the Precambrian basement (Schreiner, 1993). The Abo is exposed in a few places of uplifted fault blocks in Red Cloud Canyon. It can be as thick as 150 ft and forms a gradational contact with the overlying Yeso that is defined by the disappearance of conglomeratic material. (Perhac, 1970).

The Permian age Yeso Formation consists of interbedded limestone, feldspathic sandstone, siltstone, and shale. It is approximately 1,500 ft thick and forms a gradational contact with Glorieta sandstone (Perhac, 1970). The Yeso caps many of the ridges of the Gallinas Mountains and is unusually sparse with respect to gypsum content.

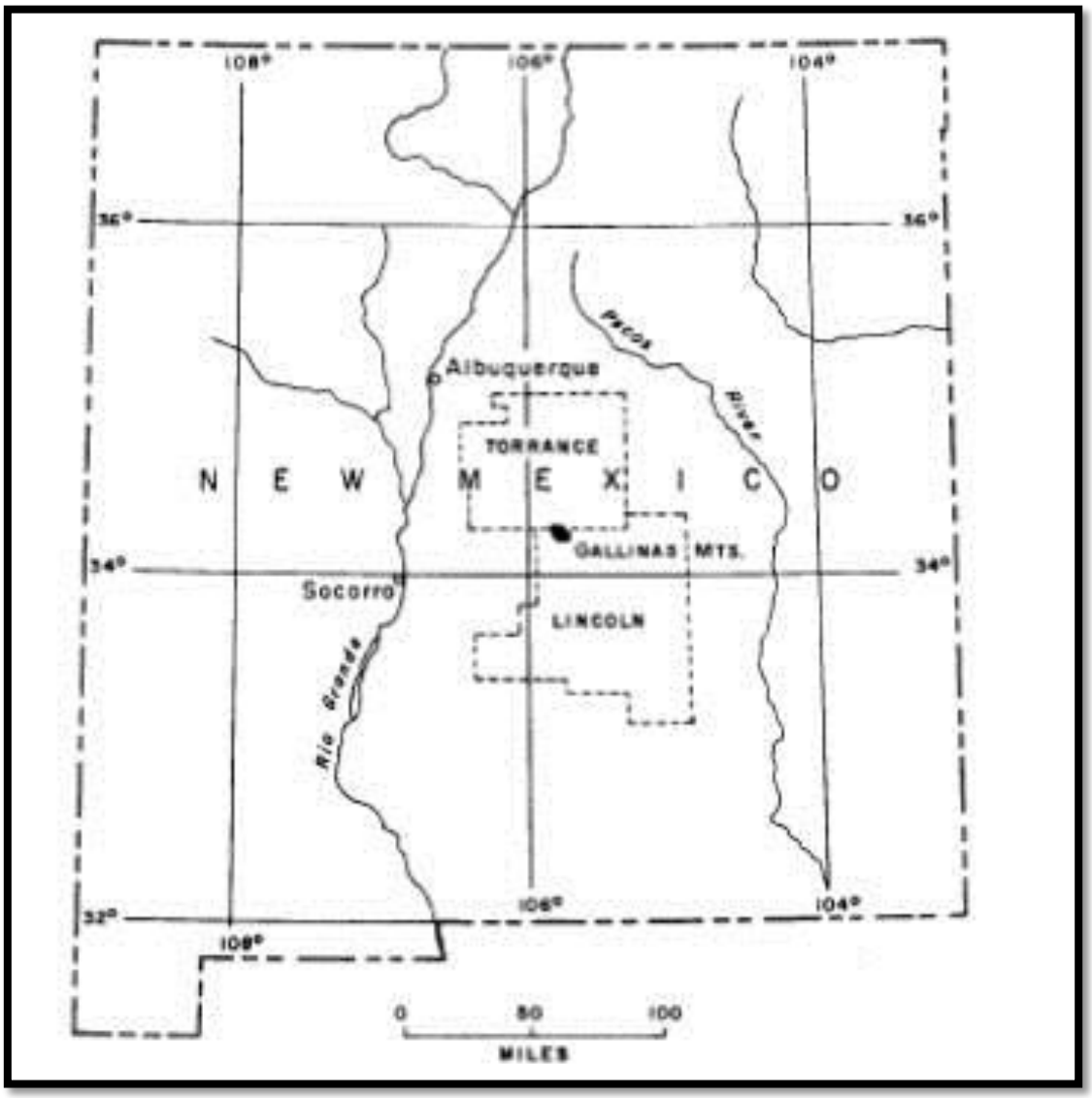

Figure 2. New Mexico Map. Shows the location of the Gallinas Mountains within the State of New Mexico. Modified from (Perhac, 1970).

The Permian Glorieta sandstone outcrops along with Yeso on many ridges in the district. It is a coarse grained, white to light gray orthoquartzite (Schreiner, 1993). The maximum thickness of Glorieta in the area is about 250 ft. This outcrop lies on the South Mesa and is partially eroded (Perhac, 1970).

A single, isolated stock of porphyritic latite exists in the northeast corner of the Gallinas Mountains. It covers a total of about 1.5 square miles and was intruded into the overlying Permian sedimentary rocks. The contact between latite and sedimentary rock units is completely covered by alluvium. Perhac (1970) notes that surrounding sedimentary beds are essentially horizontal concluding that there is little evidence of structural deformation around the intrusion. The porphyritic latite is comprised of about 50% orthoclase and hornblende phenocrysts ~5 mm in length within an aphanitic groundmass. The groundmass consists of orthoclase and less abundant plagioclase grains ~0.2 mm in length. Accessory minerals include quartz, sphene, magnetite, apatite, and zircon (Perhac, 1970).

A porphyritic rhyolite occurs on the northern end of the range and forms the cap rock of Gallinas Peak, the area of a probable laccolithic center (Schreiner, 1993). It is a white to tan colored rock with albite phenocrysts (0.5 – 1 mm in length) in an aphanitic groundmass. The groundmass grain size is generally ~0.2 mm in length and consists of orthoclase, quartz, and minor albite. Accessory minerals include aegirine-augite, biotite, apatite, sphene, magnetite, ilmenite, zircon, and muscovite (Perhac, 1970).

Porphyritic trachyte occurs in the southern portion of the district is the main igneous unit in the area of investigation. The suspected laccolithic center and thickest portion of trachyte occurs just north of Rattlesnake Ridge (Perhac, 1970; Schreiner,

1993). It is white to gray with apparent phenocrysts of both mafic minerals and potassium feldspar within an aphanitic groundmass. The groundmass consists of albite and potassium feldspar ~0.2 mm in length. Originally, mafic mineral abundance ranged from 2% – 10% but now commonly occur as Fe-oxides. The trachyte contains accessory apatite, quartz, and zircon. Whole rock analyses by Schreiner (1993) indicate that unaltered trachyte is silica undersaturated with SiO_2 ranging from 60.25 – 68.34 wt. % and alkalic $K_2O + N_2O$ ~10.5 wt. % (See Appendix C in Schreiner, 1993). Many breccia zones, prospect pits, and mines occur at or near the upper contact between trachyte and Yeso.

A single andesite dike, approximately 30 ft in width, is exposed along road cut heading north from Red Cloud Canyon. It intrudes and alters sandstone near the Sky High Prospect. It is porphyritic with grains of hornblende, pyroxene, and plagioclase in a fine grained groundmass of potassium feldspar and plagioclase. Accessory apatite, biotite, magnetite, and quartz are present.

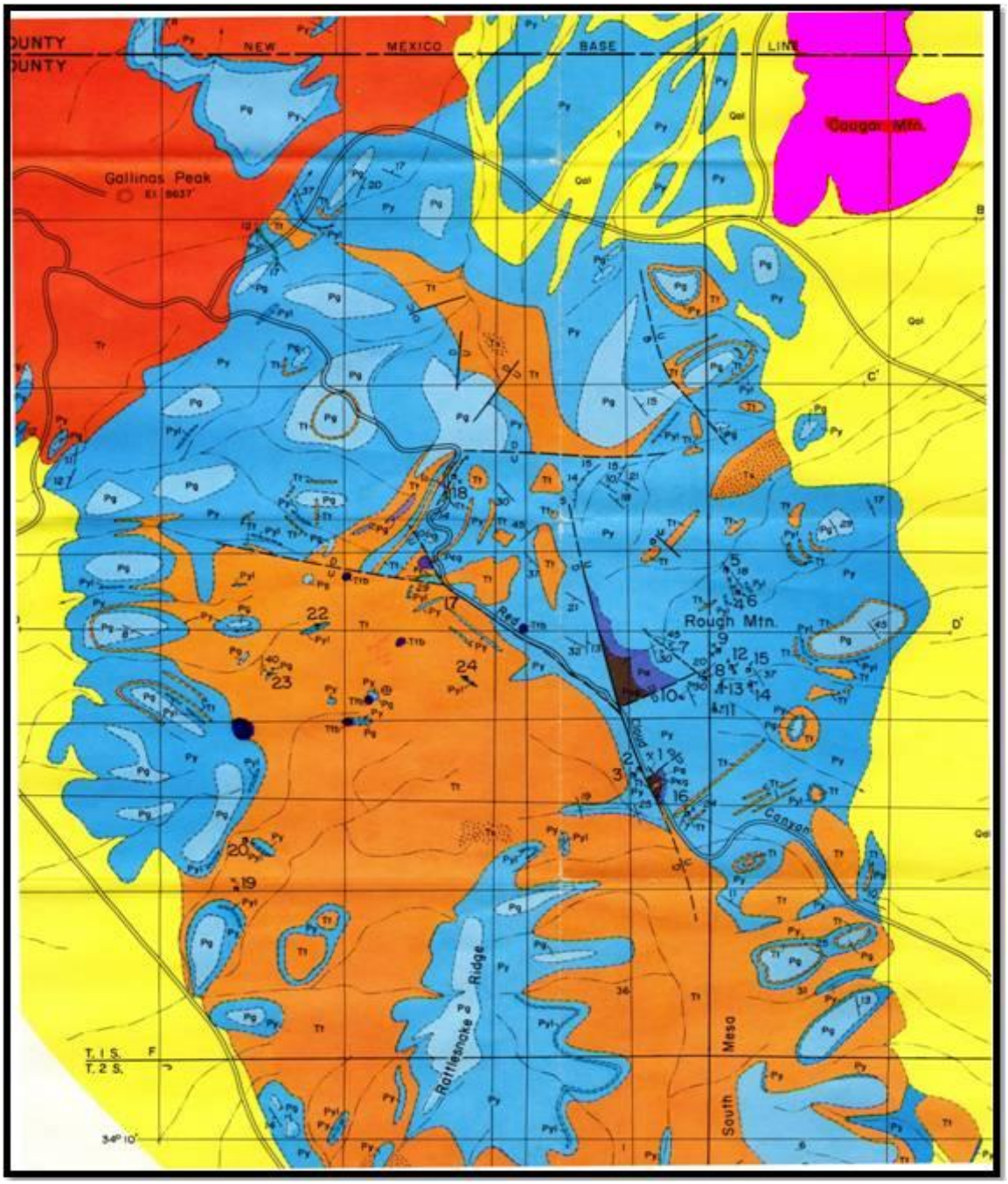
NEW MEXICO BASE LINE
Gallinas Peak
El. 9037'
Cougar Mtn.
Rough Mtn.
Rattlesnake Ridge
South Mesa
Canyon
T. 1 S.
T. 2 S.
34° 10'

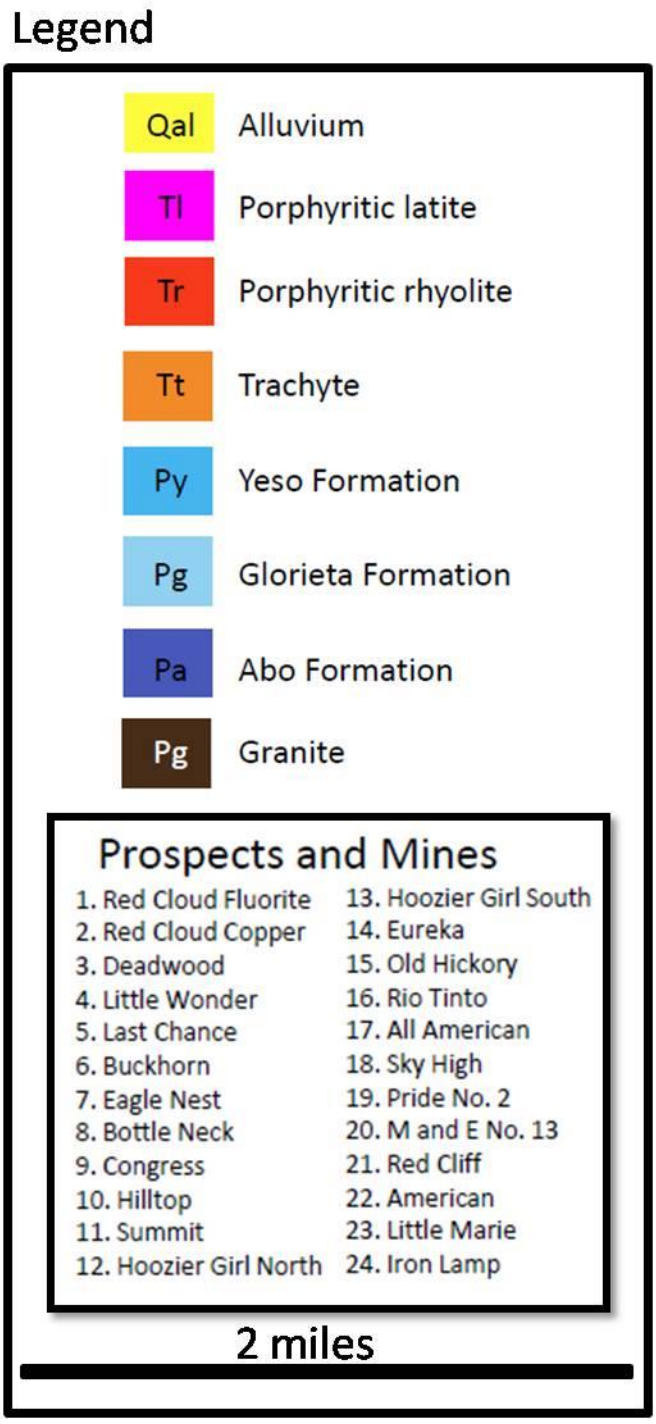

Figure 3. Geologic map of the Gallinas Mountains, New Mexico. Rough Mountain lies in the eastern portion of the range while the M and E No. 13 prospect is isolated in the west. Three distinct igneous rocks exist within the district but relative timing of intrusion remains unknown due to a lack of cross cutting relationships. Deposits in the eastern portion of the range in the vicinity of Rough Mountain share similar geological characteristics occur near the Trachyte-Yeso contact, and all contain or once contained some amount of sulfide. This map is modified after Perhac (1970).

2.3 Deposit Geology

A total of 29 mines or prospects exist in the Gallinas Mountains district. Four copper, five iron, and twenty fluorite areas were either mined or prospected (Perhac, 1970). Fe-skarn type deposits also occur throughout the district and were studied by Soulé (1946), Rothrock et al. (1946) and Kelly (1949). The remaining deposits were studied in detail by Perhac (1970) and Schreiner (1993). This study focuses on six historically productive fluorite/copper/bastnaesite deposits: Red Cloud fluorite, Red Cloud copper, Old Hickory, Buckhorn, Rio Tinto, and M & E No. 13. These deposits were chosen for study for a number of reasons. They are relatively enriched in sulfide-sulfate, bastnaesite, fluorite and/or calcite mineralization. Geologic materials used for study were obtained from waste rock piles and/or open adits that were accessible. Lastly, these deposits all occur in distinctly different locations and each has a distinctly different geology. For a complete description of the geometry of mine workings, analytical data, grade estimates, mineralogy and mineral abundances please refer to: Soule (1946), Perhac (1970), and Schreiner (1993).

2.3.1 Fe-Skarn Deposits

Five Fe-skarn deposits occur in the Gallinas Mountains district. They were first mapped and studied in detail by Kelly (1949) and again by Schreiner (1993). All Fe-skarn deposits occur at the contact between Trachyte (Tt)-Yeso (Py). Iron deposits were small and reserves were mostly exhausted by the mid 1940's (Kelly, 1949). Their mineralogy is relatively simple consisting of magnetite, hematite, diopside, tremolite, epidote, allanite, and feldspar (Kelly, 1949 and Schreiner, 1993).

Fe-skarn deposits are important for three reasons: 1) a clast of Fe-skarn was found as large breccia clasts near the M & E No. 13 deposit, 2) a small amount of fine grained purple fluorite and galena occurs at the Rare Metals iron deposit (Kelly, 1949), and 3) similar Fe-skarn mineralization, although more widespread, exists in the neighboring Capitan Mountains. The clast of Fe-skarn mineralization is evidence that skarns existed before trachyte brecciation. The presence of galena and purple fluorite suggests that both reduced sulfur and fluorine were present early in the hydrothermal system history. Lastly, the occurrence of Fe-skarn mineralization along with later REE mineralization in the Capitan Mountains, a large alkalic intrusion ~40 miles south of the Gallinas Mountains, provides an excellent opportunity to compare and contrast two similar styles of deposits.

2.3.2 Red Cloud Copper

The Red Cloud REE- -copper (Corona Queen, Deadwood) deposit occurs at the intersection of two major faults and one minor fault within Yeso sandstone. The deposit is centrally located in Red Cloud Canyon adjacent to the road. It was mined between 1943 and 1955 for fluorite, copper, lead, silver and was the largest producer of base and precious metals in the district. Ore occurs within breccia zones consisting of angular sandstone clasts and a fine grained purple fluorite matrix. Agardite [$(REE,Ca)Cu_6(AsO_4)(OH_6)\cdot H_2O$], a secondary REE-arsenate, was also identified from the deposit (DeMark, 1980).

2.3.3 Red Cloud Fluorite

The deposit is classified as a matrix supported fault breccia. Clasts are primarily angular sandstone and range in size from a few millimeters to several centimeters. The matrix consists almost entirely of fine grained (~2 mm in diameter) dark purple fluorite, clear quartz, and yellow bastnaesite. Two types of fluorite were recognized in the breccia matrix (Williams-Jones et al., 2001). The first (R1) is "purple, fine grained, and occurs as irregular diffuse patches in the breccia matrix, and as large angular to subrounded masses or as rims on sandstone fragments." The rims were interpreted as replacement textures of sandstone by fluorite. The second (R2) is colorless, massive, and forms the matrix to patches of R1 fluorite. R2 fluorite commonly contains randomly oriented barite laths (Williams-Jones et al., 2000).

Bastnaesite occurs as yellow or pink euhedral grains up to a few millimeters in diameter and fine grained aggregates within the breccia matrix. It can form large (0.5 cm long) broken prismatic crystals but these are rare. Some bastnaesite has undergone replacement by Ca bastnaesite, which occurs as bladed rosettes (Williams-Jones et al. 2001).

Accessible sulfide mineralization within the deposit is rare as the workings have been reclaimed. However, samples of galena with small pyrite inclusions and samples of galena occurring within large barite veins were obtained through the New Mexico Mineralogical Museum. Galena also rarely occurs as small (<0.5 cm) euhedral crystals within the fluorite matrix. Barite commonly occurs as small bladed aggregates (<1 cm) or as intergrowths within the fluorite matrix. Grains of barite are often white and opaque. Bournite and chalcocite are also reported as present in the deposit but were not sampled

due to lack of material found in the mine dump. Other mineralization includes malachite, azurite, chrysocolla, wulfenite, mimetite, anglesite, and cerussite.

2.3.4 M & E No. 13

The M & E No. 13 is classified by Schreiner (1993) as an intrusive breccia deposit, roughly circular in plan view. It occurs entirely within porphyritic trachyte and shows no spatial relationship to any of the main faults in the area. It consists of a caved main shaft, an 18-ft-deep shaft, 3 pits, and a 70- by 50-ft bulldozed area (Schreiner, 1993). Mapping of the breccia pipe revealed widths ranging from 150 to 350 ft.

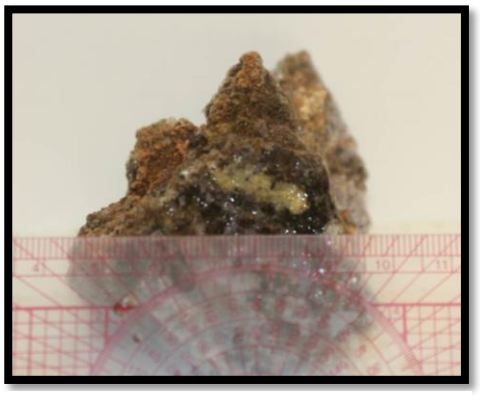

Figure 4. Yellow bastnaesite crystal within a fluorite matrix. The crystal is large measuring ~2 cm. Sampled from the M & E No. 13 prospect.

The breccia is clast supported. Clasts are mostly angular trachyte, sandstone, and limestone (Yeso) 2-4 inches in diameter. Schreiner (1993) notes that a single clast of granite was found. The breccia matrix assemblage is dominated by fluorite with minor quartz, barite, and bastnaesite. Accessory phases include parisite, pyrite, and trace xenotime and celestite (Williams-Jones et al., 2001). Minor chrysocolla and malachite occur coating vugs. Alkali alteration of clasts and carbonatization within the deposit was reported by Schreiner (1993).

Bastnaesite occurs as yellow euhedral to anhedral hexagonal crystals up to 2.5 cm in length (Figure 4). In every case crystals were fractured and broken. An unidentified REE-bearing mineral occurring as acicular bundles in vugs and cracks was reported by

Schreiner (1993) and Williams-Jones et al. (2000). Both authors determined that this mineral was parisite by scanning electron microscopy (SEM).

Xenotime was observed by both Schreiner (1993) and Williams-Jones (2000) during SEM analysis. It was tentatively observed during this study by traditional petrography. It occurs as 10- to 50 micron, subhedral to euhedral crystals within the fluorite breccia matrix. Barite occurs as fine- to coarse-grained, white, anhedral to euhedral, crystals throughout the breccia matrix. It is as long as 2.5 cm but is mostly less than 2 mm in length. Quartz is regularly dispersed throughout the breccias commonly occurring as 2 mm euhedral prisms. Limonite-goethite pseudomorphs after pyrite are common throughout the deposit. The minerals commonly occur as pyritohedrons or cubes ~2 mm in diameter. Unaltered pyrite is extremely rare.

Calcite is very common and occurs in veinlets up to 2 mm in diameter, disseminated masses within the breccias matrix, and as euhedral crystals up to 0.5 cm in diameter in fractures and cavities. Calcite is often found surrounding quartz and fluorite crystals and rimming rock clasts. It is found in amounts ranging from a few percent to 44% at various sites within the deposit (Schreiner, 1993).

The breccia deposit as well as surrounding country rock was altered by two episodes of "fenitization" (Schreiner, 1993). An episode of sodic metasomatism was followed later by an episode of potassic metasomatism. The areal extent of alteration was not determined, but is present to at least 100 ft from the edge of the breccia pipe (Schreiner, 1993).

2.3.5 Old Hickory

The Old Hickory mine occurs on the eastern side of Rough Mountain near the Yeso (Py)-trachyte (Tt) contact. It is situated on a mineralized breccia zone that trends approximately northeast along Rough Mountain. The deposit was mined primarily for copper, lead, and silver but abundant fluorite and minor bastnaesite are also present.

The breccia is matrix supported with clasts of sandstone and trachyte. The matrix consists of fine grained purple fluorite with intergrown quartz and minor bastnaesite and is similar to that seen in the Red Cloud Copper deposit.

Sulfide mineralization is common as disseminated crystals within the fluorite matrix and as veins ~3 cm in diameter (Perhac, 1970). Sulfides present at the Old Hickory mine include galena, chalcocite, pyrite, chalcopyrite, tennantite, digenite and sphalerite. Sulfates present within the deposit include celestite [$SrSO_4$] and barite. Celestine occurs as brown-orange-white blades within vugs. Barite is usually massive only rarely occuring as small blades.

2.3.6 Buckhorn

The Buckhorn mine (Little Wonder) appears to lie on the same northeast trending fault breccia zone as the Old Hickory mine and is located about 0.5 miles to the north. Brecciation ranges from 5 to 15 ft wide and is near vertical. Mineralization is located along fracture zones and within the matrix of the breccia. The mineralized zone consists of fluorite and lead and copper sulfides. Abundant secondary copper and lead oxides are also present apparently formed from the oxidation of sulfide ores.

Minerals identified from the mine include galena, tennantite, freibergite, proustite, xenotime, zircon, fluorite, quartz, minor calcite, and hematite-limonite pseudomorphs

after pyrite (Schreiner, 1993). The breccia is very similar to Old Hickory. Clasts are comprised of angular sandstone and trachyte. The matrix consists of fine grained purple fluorite, quartz, and minor bastnaesite.

2.3.7 Rio Tinto

The Rio Tinto mine lies a few hundred meters to the southeast of the Red Cloud Copper-fluorite-REE deposits. It contains abundant fluorite, barite, bastnaesite, hematite-limonite pseudomorphs after pyrite, malachite, chrysocolla, manganese oxide, jarosite, and calcite. The mineralogy of the Rio Tinto mine is very similar to that of the Red Cloud copper deposit including many secondary copper oxide minerals.

3. STUDY OBJECTIVES

This study examines the hydrothermal fluid geochemistry associated with sulfide, sulfate, bastnaesite, and fluorite mineralization of five historic mines in the Gallinas Mountains district. It also aims to provide new insight into the processes and requirements for deposit formation by describing the relationships between diverse deposit types. Hydrothermal REE mineralization occurring with sulfide mineralization is rare and this study area provides a unique opportunity to study this relationship. By carefully examining the stable isotope compositions of ore and gangue mineralization, it may be possible to shed light on the composition of the source rock, fractionation processes, and alterations that are present in the Gallinas Mountains, NM.

This work builds upon the work of previous workers that suggest that the hydrothermal fluids responsible for mineralization in the Gallinas Mountains were derived from a Ca-poor, REE-F-bearing orthomagmatic fluids and later mixed with Ca carbonate-bearing formation waters resulting in the deposition of bastnaesite and fluorite (Williams-Jones et al., 2000). Previous geochemical studies in the area were based in large part on fluid inclusion compositions, salinities, decrepitate analyses, homogenization temperatures, and mineral composition relationships of two deposits in the district. The purpose of this study is three-fold:

1) To determine the relationship between and causes of fluorite-bastnaesite-sulfide base-metal mineralization.
2) To establish a mechanism of mineral deposition with respect to deposit.
3) To provide further insight into the source rock type present in the district.

4. METHODS

4.1 Petrography

Hand samples were selected, cut and sent for the fabrication of thin sections for petrographic analysis. Petrographic descriptions of 10 thin sections representing various lithologies present in the district were done using a Nikon OPTIPHOT-POT petrographic microscope under both plane and cross polarized light. Thin sections were analyzed using standard petrographic analysis techniques (mineral identification, abundances, percentages, alteration, textures and photomicrography).

4.2 Fluid Inclusion Microscopy

Several ore samples from the M & E No. 13 and Red Cloud Fluorite mines were cut and doubly-polished to fabricate standard fluid inclusion thick sections. A bastnaesite mineral concentrate consisting of several grams of sand sized bastnaesite chips from the Red Cloud Fluorite mine as well as fluorite cleavage chips from both mines were examined using a Nikon OPTIPHOT-POT petrographic microscope. Fluid inclusions were described by the standard method (size, phase relations, origin, photomicrography, and solid inclusion identification). There were no temperature measurements made on any of the fluid inclusions.

4.3 X-ray Diffraction

X-ray diffraction (XRD) analysis was performed on either whole rock or mineral separates on over 50 samples. All XRD analyses were performed on a PANalytical X-

Pert PRO® diffractometer at the New Mexico Bureau of Mines and Mineral Resources Mineral Museum X-ray Diffraction Laboratory. All analyses were conducted using 45 kV X-ray beam tension and 40 mA X-ray beam current. All samples were crushed to a fine powder, placed on single silicon crystal sample holders, leveled and analyzed from 6° to 70° 2θ. X-ray intensities were measured using an X'Celerator® detector which measures and integrates X-ray intensity over 5° 2θ simultaneously. All XRD scans were identified using X'Pert HighScore Plus® which identifies intensity peaks and matches patterns to a Powder Diffraction File database.

4.4 Stable Isotope Geochemistry

Stable isotope ratios of carbon, sulfur, carbonate oxygen, and sulfate oxygen were measured on a variety of minerals from throughout the district. The following list describes the types of measurements made: carbon and carbonate oxygen ratios of calcite and bastnaesite, sulfur ratios of galena, pyrite, jarosite, and barite, and sulfate oxygen ratios of barite and jarosite. All isotope measurements were made on a Thermo Finnigan Delta Plus XP in the New Mexico Institute of Mining and Technology Stable Isotope Laboratory.

4.4.1 Sulfur Measurements

Sulfur bearing phases analyzed were galena, pyrite, barite, and jarosite. Barite represents the most abundant sulfur bearing mineral in the deposit while sulfides are considerably scarcer. Mineralogy was confirmed by XRD prior to isotope analysis.

Samples were either chips from hand samples or drill residue in the cases where grains were small (< 0.5 cm).

Due to fluorite contamination in galena samples, heavy liquid separates were made. Heavy liquid separation was achieved by floating fluorite in methylene iodide (density 3.32 g/cm^3) and allowing galena to sink and flow into a beaker. The heavy concentrate was filtered through a standard coffee filter and the remaining solid phase was separated.

Samples were weighed and sealed in tin capsules, placed into a rotating turret, and combusted with high purity (99.99%) O_2 gas at 1020°C forming SO_2. Vanadium pentaoxide (~3 mg) is added to sulfate samples to aid combustion. The gas was then moved via He carrier gas into through a Finnigan gas bench and the $\delta^{34}S$ ratios were measured relative to a SO_2 reference gas. Sample measurements were corrected to $\delta^{34}S$ ratios of a National Bureau of Standards barite (NBS 127), argentite (NZ1), and sphalerite (NBS 123). Duplicates of both samples and standards were measured to ensure precision and repeatability of analyses. Barite (NBS 127) analyses were ±0.2‰, argentite (NZ1) analyses were ±0.1‰, and sphalerite (NBS 123) analyses were ±0.3‰ of the mean. Standard duplicates indicate that all sulfur measurements were repeatable to within ±0.2‰.

4.4.2 Sulfate Oxygen Measurements

$\delta^{18}O$ measurements on sulfate oxygen were made on barite and jarosite. Barite samples were weighed and sealed in silver capsules and heated to 1450°C in a Finnigan™ TC/EA (Thermocatalytic/Elemental Analyzer). Sulfates were converted to

CO by high temperature pyrolysis in a carbon tube. The gas was delivered to the mass spectrometer via continuous flow. All samples were measured and corrected relative to a National Bureau of Standards barite (NBS 127) and a HEKAtech benzoic acid ($C_7H_6O_7$).

Because jarosite ($KFe_3(SO_4)_2(OH)_6$) contains oxygen in the hydroxyl site, sulfate oxygen cannot be measured directly. Wasserman et al, (1998) developed a method to dissolve alunite ($KAl_3(SO_4)_2(OH)_6$) and precipitate the sulfate in barite. This method was used on jarosite, a member of the alunite mineral family, with the same result.

120 ml of 0.5 N NaOH was added to a 200 mL beaker. Approximately 60 mg of jarosite was added to the heated (~80°C) solution and placed on a stir plate for 3 hours. The solution was periodically checked for jarosite dissolution and hematite precipitation. The sample was allowed to cool and filtered through a 0.8 µm cellulose nitrate membrane using a Millipore vacuum filter device. The filtrate was discarded. The remaining solution was heated to 80°C and titrated to a pH of ~1.9 using 10 N HCl. 2 mL of 0.5 N $BaCl_2$ was added and the solution, it was heated and stirred for an additional 3 hours. The solution was set aside and allowed to cool overnight. The solution was filtered through a 0.45 µm cellulose nitrate membrane and dried in an oven. The newly formed barite was then weighed and the $\delta^{18}O$ was measured according to the method previously described.

Data were corrected by performing two calculations. Differences in reference and sample peak intensity can affect the accuracy of measurements; therefore a normalization calculation was performed for all standards. This calculation was also applied to samples. The measured values of standard barite (NBS 127) and HEKAtech benzoic acid ($C_7H_6O_7$) were then plotted against the accepted known values and a line was fitted to the resulting points. The equation of the resulting line was then used to correct sample measurements

ensuring accuracy. Duplicates of standards were measured to determine precision or measurements. Barite (NBS 123) standards were run seven times with all values falling within ±0.5‰ of the mean and HEKAtech benzoic acid ($C_7H_6O_7$) standards were run five times with all values falling within ±0.3‰ of the mean. Duplicates indicate that all measurements were precise to within ±0.4‰.

4.4.3 Carbon and Oxygen Measurements

Isotopic ratios of $\delta^{13}C$ and $\delta^{18}O$ on a total of 17 calcite and 5 bastnaesite samples were measured in the New Mexico Tech Stable Isotope Laboratory using a continuous flow method. Samples of calcite and bastnaesite were taken from various localities and deposits within the Gallinas District. Separates were made by either chipping the desired mineral from a vein or surface coating or through the use of a drill press. Samples were powered, weighed, and placed in glass vials and sealed with penetrable caps. Samples were then flushed for 2 minutes with He gas to remove all atmosphere within the capsule. Next, ten drops of 100% phosphoric acid were delivered to the sample with a small gauge insulin syringe. Samples were placed in a heating block at 45° allowing a reaction forming CO_2 gas at a constant temperature. Acid fractionation for bastnaesite was assumed to be the same as that of calcite.

An auto sampler was used to deliver the CO_2 gas into the gas bench and into the mass spectrometer. Duplicates of standards (NBS 18 Carbonatite, NBS 19 Solnhofen Limestone, and IAEA-CO-8 calcite) were used to ensure accuracy in all analyses. Duplicates of standards and samples were analyzed to ensure precision. IAEA-CO-8 was measured three times and $\delta^{13}C$ and $\delta^{18}O$ measurements were precise to within ±0.1 and

±0.4‰, respectively. NBS 19 was measured four times and $\delta^{13}C$ and $\delta^{18}O$ measurements were precise to within ±0.3 and ±0.5‰, respectively. NBS 18 was measured three times and $\delta^{13}C$ and $\delta^{18}O$ measurements were precise to within ±0.1 and ±0.1‰, respectively. These measurements yield an average precision for $\delta^{13}C$ and $\delta^{18}O$ of ±0.1 and ±0.3‰, respectively. Blanks of a reference CO_2 gas were analyzed after every fifth sample to clear the sampling device of any accumulated water or acid.

All data obtained during these analyses was corrected according to the method described in the previous section.

4.5 Electron Probe Microanalysis

Backscatter imaging and qualitative wavelength dispersive analyses were conducted on four samples using a Cameca SX-100 electron microprobe. All analyses were conducted with a spot size of 1µm, a 20 kV accelerating voltage and a 10 nA probe current. Samples include: M and E No. 13 Bastnaesite Bx, Red Cloud Bastnaesite Concentrate grain mount, Old Hickory Spotty Sulfide, and Red Cloud Barite-Galena. All images, qualitative spectra and qualitative data are included in Appendix 5.

4.6 Laser Ablation Inductively Coupled Plasma Mass Spectrometry

Laser Ablation Inductively Coupled Plasma Mass Spectrometry analyses were performed using a New Wave Research model LUV213 Nd/YAG laser and an Aligent 7500 Series inductively coupled plasma quadrapole mass spectrometer. Research grade Ar gas used as a carrier gas. Standardization was performed before each of the two samples was analyzed on internal standards of concentration 0, 5, 20, 35, 75, and 150

ppm. To maximize intensity delivered to the sample, the laser was set to 100% power at a 100 μm beam diameter. The sample M and E No. 13 was a standard petrographic fluid inclusion thick section. All analyses performed on this sample were line scans of bastnaesite that totaled five distinct counting periods. The sample RCBST was composed of polished bastnaesite grains mounted in epoxy. All measurements on this sample were made by selecting a spot and analyzing for REE for 6 seconds with a beam strength of 100% a laser beam diameter of 50 μm. Values were corrected to a series of standards with REE concentrations of 0, 5, 10, 20, 35, 75, and 150 ppm. These standards were analyzed until duplicate analyses produced results to within ± 5%. Because bastnaesite is extremely enriched compared to these standards, data is used as qualitative only.

5. RESULTS

5.1 X-ray Diffraction

The results of the X-ray diffraction (XRF) analyses are summarized in Table 1 and all patterns are available in Appendix 3. The occurrence of rostite was confirmed by XRD at the Rio Tinto copper mine. The occurrence of agardite at the Red Cloud copper mine was also confirmed.

Rostite is a mineral that forms from the breakdown of aluminosilicate minerals in environments containing sulfuric and hydrofluoric acids (Anthony et al., 2003). This is the first reported occurrence of rostite in New Mexico. Its presence indicates the presence of these acids during deposit genesis. Agardite was first reported in the Gallinas Mountains by DeMark (1980). This mineral is very rare and forms as an alteration product of sulfides with a high REE content (Anthony et al, 2003).

In addition to identifying unknown minerals, XRD was performed to ensure sulfide sample identification and purity for stable isotope analyses.

Table 1. Minerals identified via XRD by deposit.

Deposit	Mineral Identified by XRD	Deposit	Mineral Identified by XRD
Red Cloud Copper and Fluorite	Bastnaesite-(Ce)	**Rio Tinto**	Fluorite
	Fluorite		Barite
	Barite		Kaolinite
	Mimetite		Cerussite
	Agardite-(Ce)		Mimetite
	Quartz		Jarosite
	Kaolinite		Calcite
	Ashoverite		
	Anglesite	**Buckhorn**	Anglesite
	Cerussite		Galena
	Wulfenite		Covellite
	Stolzite		Tennantite
			Coronadite
M and E No. 13	Bastnaesite		
		Old	
	Calcite	**Hickory**	Fluorite
	Fluorite		Celestine
			Sylvine
All-American Iron Prospect, Alkali Metasomatism	Orthoclase		Beauantite
			Sphalerite
Honeywell	Barite		Azurite
	Hematite		Digenite
	Goethite		Clinomimetite
	Lepidocrocite		Cerianite

5.2 Stable Isotopes

$\delta^{34}S$ measurements (including duplicates) were made on a total of 43 samples (Table 2, Appendix 4). $\delta^{18}O_{SO4}$ measurements (including duplicates) were made on a total of 12 samples. $\delta^{13}C$ and $\delta^{18}O$ measurements (including duplicates) were made on a total of 27 samples (Table 2). All isotope δ values and calibration curves are available in Appendix 4.

Table 2. Results of stable isotope analyses.

Sample Name	Sample Location	Ore Type	Mineral	$\delta^{34}S$ vs. CDT	$\delta^{18}O_{SO4}$ vs. VSMOW	$\delta^{13}C$ vs. PDB	$\delta^{18}O$ vs. VSMOW
RC GL 1	Red Cloud	Fl Bx	Galena	**1.5**			
RC GL 2	Red Cloud	Fl Bx	Galena	**0.4**			
RC GL 3	Red Cloud	Fl Bx	Galena	**0.3**			
RC GL 4	Red Cloud	Fl Bx	Galena	**-0.8**			
RC GL 5	Red Cloud	Fl Bx	Galena	**0.4**			
RC GL 6	Red Cloud	Fl Bx	Galena	**0.7**			
RC GL 7	Red Cloud	Fl Bx	Galena	**1.1**			
RC GL 8	Red Cloud	Fl Bx	Galena	**0**			
RC GL 13	Red Cloud	Fl Bx	Galena	**1.8**			
OH Gl eq (Py)	Old Hickory	Fl Bx	Galena	**-18.6**			
RC Gl eq (Py)	Red Cloud	Fl Bx	Galena	**-0.6**			
BKN Galena 1	Buckhorn	Fl Bx	Galena	**-21.1**			
BKN Galena 2	Buckhorn	Fl Bx	Galena	**-19.8**			
BKN Galena 3	Buckhorn	Fl Bx	Galena	**-18.6**			
BKN Galena 4	Buckhorn	Fl Bx	Galena	**-19.6**			
BKN Galena 5	Buckhorn	Fl Bx	Galena	**-20.8**			
OH Galena 1	Old Hickory	Fl Bx	Galena	**-10.4**			
OH Galena 3	Old Hickory	Fl Bx	Galena	**-17.4**			
RC GL 10C	Red Cloud Cu	Within Barite Vein	Galena	**-7.2**			
RC GL 10B	Red Cloud Cu	Within Barite Vein	Galena	**-7.6**			
RC GL 10A	Red Cloud Cu	Within Barite Vein	Galena	**-9**			
RC Barite 1	Red Cloud	Fl Bx	Barite	**13.3**	**3.6**		
RC Barite 2	Red Cloud	Fl Bx	Barite	**11.1**	**5.2**		
HW Barite 1	Honeywell	Fl Bx	Barite	**9.6**	**5.1**		
RC Barite 11A	Red Cloud Cu	Within Barite Vein	Barite	**13.2**	**0.5**		
RC Barite 11B	Red Cloud Cu	Within Barite Vein	Barite	**11.1**			
RC Barite 11C	Red Cloud Cu	Within Barite Vein	Barite	**11**	**4.2**		

RM Barite	Rough Mtn	Fl Bx	Barite	**9.6**	**7.2**		
OH Brown Celestine	Old Hickory	Fl Bx	Celestine	**1.4**			
OH White Celestine	Old Hickory	Fl Bx	Celestite	**5.2**			
RT Jarosite	Rio Tinto	On Fl Bx	Jarosite	**-18.3**	**9.0**		
RC Py eq (Gl)	Red Cloud	Fl Bx	Pyrite	**-9.4**			
OH Py 1 eq (Gl)	Old Hickory	Fl Bx	Pyrite	**-11.3**			
OH Py 2 eq (Gl)	Old Hickory	Fl Bx	Pyrite	**-9.5**			
RC Pink Bast	Red Cloud	Fl Bx	Bastnaesite			**-11.1**	**15**
Red Cloud Y. Bast	Red Cloud	Fl Bx	Bastnaesite			**-7.6**	**20.7**
ME 13 Y Bast 1	M + E No. 13	Fl Bx	Bastnaesite			**-7.9**	**21.1**
ME 13 Y Bast 2	M + E No. 13	Fl Bx	Bastnaesite			**-7.4**	**22.5**
ME 13 Y Bast 3	M + E No. 13	Fl Bx	Bastnaesite			**-8**	**21.7**
ME 13 Calcite Flooding	M & E 13	Fl Bx	Calcite			**-6.8**	**21.9**
ME 13 Calciteite vein 7b	M & E 13	Fl Bx	Calcite			**-6.7**	**22.6**
Rough Mtn YESO	Rough Mtn	Yeso Fm.	Calcite			**-0.5**	**18.7**
RT Calcite coating 2	Rio Tinto	On Fl Bx	Calcite			**-7.4**	**20.8**
ME 13 Calcite vug 12	M & E 13	Fl Bx	Calcite			**-5.6**	**21.6**
ME 13 Calcite veining 1	M & E 13	Fl Bx	Calcite			**-6.9**	**22.4**
Conq. Calcite Coating 1	M & E 13	Fl Bx	Calcite			**-7.4**	**21**
ME 13 Calciteite vein 7a	M & E 13	Fl Bx	Calcite			**-6.9**	**23.8**
ME 13 Calcite vug 11	M & E 13	Fl Bx	Calcite			**-5.7**	**22.2**
Honeywell Calcite 1	Rough Mtn	On Fl Bx	Calcite			**-9**	**20.3**
Gallinas H1 98.5'	Honeywell	Trachyte Vein	Calcite			**-3.4**	**22.4**
Rio Tinto Calcite 2	Rio Tinto	Calcite Vein	Calcite			**-7.3**	**22.1**
Rough Mtn Calcite 2	Rough Mtn	Veining Fl Bx	Calcite			**-5**	**22.8**
Honeywell Calcite 4	Honeywell	On Fl Bx	Calcite			**-8.1**	**21.9**
Sky High Calcite 2	Sky High	Vein in Fl Bx	Calcite			**-5.8**	**22.7**
Honeywell Calcite 2	Honeywell	On Fl Bx	Calcite			**-7.7**	**21.8**
Sky High Calcite 1	Sky High	Vein in Fl Bx	Calcite			**-6.4**	**22**

All values given in ‰. RC = Red Cloud Fluorite. OH = Old Hickory. BKN = Buckhorn. HW= Honeywell. RM = Rough Mountain (Sample taken from a prospect pit at the peak of Rough Mountain). RT = Rio Tinto (Conqueror No. 4). ME 13 = M and E No. 13 prospect. Gallinas H1 98.5’ = Gallinas drill hole #1, sample taken at 98.5’. Fl = Fluorite. Bx = Breccia. Fm. = Formation. Y = yellow.

5.2.1 Sulfur Isotopes

Minerals analyzed for $\delta^{34}S$ values include: galena (21), barite (7), celestine (2), jarosite (1), and pyrite (3). Several mineral pairs were sampled including barite-galena and pyrite-galena, some representing equilibrium assemblages. Galena $\delta^{34}S$ ranges from -21.1 to 1.8‰, barite ranges from 9.5 to 13.2‰ and pyrite from -11.3 to -9.4‰. Two samples of celestine and one sample of jarosite were analyzed and have values of 1.4, 5.2‰, and -18.28‰, respectively. Galena $\delta^{34}S$ values display a wide range but occur in three populations centered at 0, -8 and -20‰. Barite $\delta^{34}S$ values occur in one population centered near 11‰.

5.2.2 Sulfate Oxygen Isotopes

$\delta^{18}O$ measurements were made on a total of 8 samples. Seven barite samples were analyzed and $\delta^{18}O_{SO4}$ measurements ranged from 0.5 to 7.2‰ vs. VSMOW. The $\delta^{18}O_{SO4}$ values of barite are evenly distributed across this range with an average value of 4.2‰. One jarosite sample was measured for total $\delta^{18}O$ and sulfate $\delta^{18}O$ yielding values of 0.3 and 9.0‰, respectively.

5.2.3 Carbon and Oxygen Isotopes

$\delta^{13}C$ and $\delta^{18}O$ values of twenty-two samples of carbonate bearing minerals were determined. Three samples of bastnaesite and ten samples of calcite from various deposits were analyzed.

The range of $\delta^{13}C$ and $\delta^{18}O$ values are summarized in Table 1 (Appendix 4). Calcite $\delta^{13}C$ and $\delta^{18}O$ values range from -9.4 to -0.4‰ and 18.7 to 23.7‰, vs. PDB and

VSMOW, respectively. Bastnaesite $\delta^{13}C$ and $\delta^{18}O$ values range from -11.1 to -7.5‰ and 15.0 to 21.1‰, vs. PDB and VSMOW, respectively. $\delta^{18}O$ values show little variation while $\delta^{13}C$ values differ by almost 10‰. The ranges in $\delta^{13}C$ and $\delta^{18}O$ values are further constrained when individual minerals are considered. Bastnaesite $\delta^{13}C$ values center around -7.5‰ vs. PDB and $\delta^{18}O$ values center around 21‰ vs. VSMOW. Calcite $\delta^{13}C$ values show wider variation but $\delta^{18}O$ values are generally within ±3‰ of 21‰ vs. VSMOW.

5.3 Fluid Inclusions

Detailed fluorite relationships and fluid inclusion data were based largely on work of previous authors (Williams-Jones et al., 2000). Mineralogy and fluid inclusion morphology of the M and E No. 13 deposit and the Red Cloud fluorite deposit differ slightly. The presence of an early blue/green fluorite (ME13 fluorite 1; Figure 5B) is unique at the M and E No. 13 deposit and was followed by a fluid inclusion-rich, clear to purple fluorite (ME13 fluorite 2; Figure 5A), which was followed by a fine grained purple fluorite (ME13 fluorite 3: Figure 5 (1)) (Williams-Jones et al., 2000). Two types of fluorite were recognized at the Red Cloud deposit. The first type (RC fluorite 1) is purple and occurs as fine grained patches and as replacements of sandstone breccia fragments. The second type (RC fluorite 2) occurs as inter-grain fillings between RC fluorite 1 and replaces RC fluorite 1 (Williams-Jones et al. 2000).

Because fluid inclusion microthermometry and salinity determinations were made in a previous study, this thesis focused only on comparing fluid inclusion morphology to Williams-Jones et al., (2000). Three types of fluid inclusions from the M and E No. 13

prospect were identified: liquid rich, liquid-vapor (L-V), liquid rich, liquid-vapor-solid (L-V-S), and aqueous-carbonic (A-C). Two types of fluid inclusions were identified from the Red Cloud Fluorite deposit: liquid rich, liquid-vapor (L-V), and liquid-vapor-solid (L-V-S) (Figure 5). No aqueous-carbonic inclusions were recognized from this deposit. In general, liquid rich, liquid-vapor inclusions were common in quartz, bastnaesite, and second generation (fluorite).

Although compositions, homogenization temperatures, and salinities were not measured during this study, the morphology of fluid inclusions from the M and E No. 13 and Red Cloud Fluorite deposits agree with those previously published (Figure 5) (Williams-Jones et al., 2000).

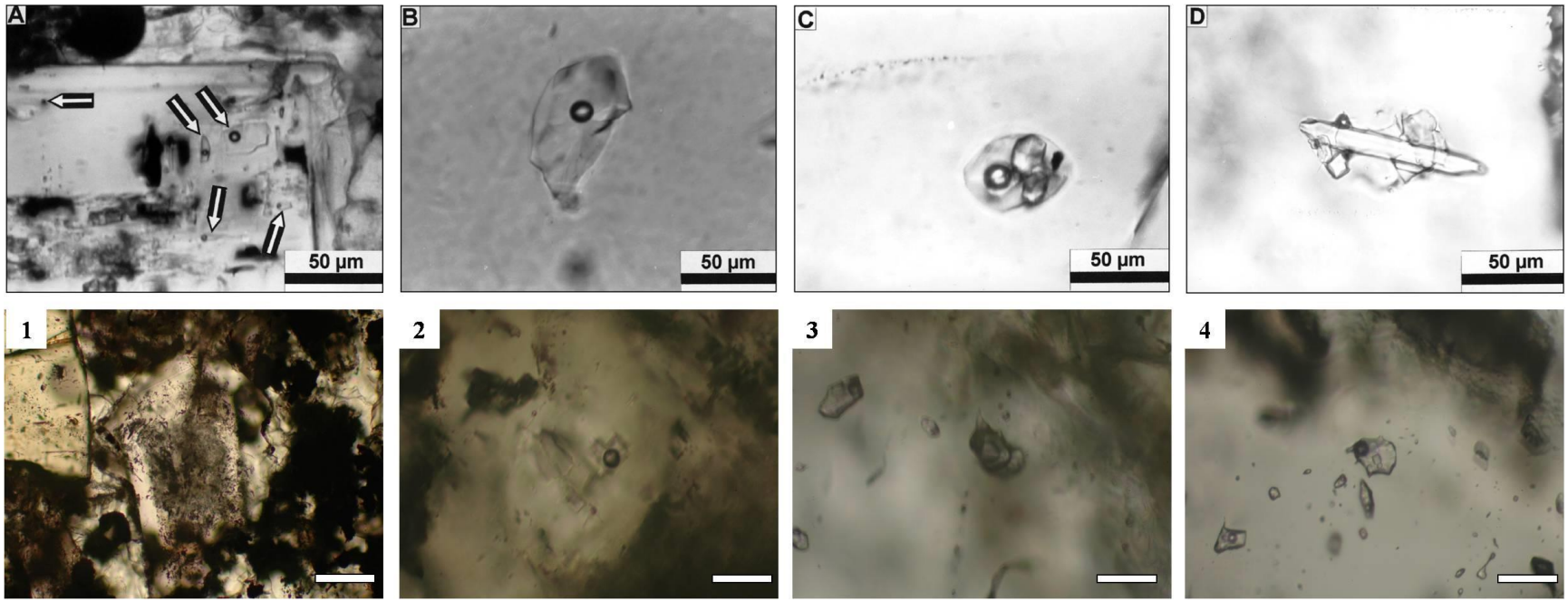

Figure 5. Fluid inclusions. Images A-D were modified from: Williams-Jones et al. (2000). A) "Primary L-V inclusions (arrows) near edge of a P2 fluorite crystal." B) "Primary L-V inclusion in P1 fluorite." C) Primary L-V-S inclusion in P1 fluorite; three crystals are visible in this inclusion, the two translucent ones being gypsum." D) "Complex L-V-S_G inclusion in P1 fluorite; the acicular crystal in the center of the inclusion in gypsum." Images 1-4 were taken during this study. Scale bars represent 50 µm. 1) L-V inclusions at the edge of a ME13 fluorite 2. 2) Primary L-V inclusion in ME13 fluorite 1. 3) Rare, large A-C inclusion in the middle of the image. Complex L-V-S inclusion in the upper left hand side of the image in ME13 quartz. 4) Complex grouping of L-V-S inclusions in ME13 quartz.

5.4 Electron Probe Microanalysis

Quantitative electron probe microanalysis results are summarized in Table 2 and presented in Appendix 5. Quantitative analyses were performed on barite and galena pairs attempting to analyze for Ba substitution in galena and Pb substitution in barite in order to evaluate oxygen fugacity during ore formation using the methods published by Kajiwara and Honma (1972).

Ba substitution in galena from the Red Cloud copper mine ranges from 0.00 to 0.25 normalized wt. % with most values near 0.00 wt. %. Pb substitution in barite from the same sample from the Red Cloud copper mine ranges from 0 to 0.19 wt. % with most values near 0.00 wt. %. Pb substitution in barite from the Honeywell prospect ranges from 0 to 0.16 normalized wt. % with most values near 0.00 wt. %. Galena was not observed in hand sample from the Honeywell prospect nor was it seen with SEM imaging.

Qualitative analyses were performed to assess the presence of REE in fluorite and to recognize mineral phases to determine paragenetic relationships. Qualitative analyses of REE in fluorite did not indicate that there was any REE substitution into the fluorite structure (Appendix 5). Mineralogy and paragenetic relationships are discussed at length in the Discussion section.

Table 3. Electron probe microanalysis data of barite and galena from the Red Cloud Copper mine and Barite from the Honeywell prospect.

	Galena	Elemental				Normalization						
Point	Sample	S	Ba	Pb	Total	S	Ba	Pb	Total	Pb ppm	Ba ppm	Log_{10} BaS activity
Standard	galena-01	13.40	0.15	85.19	98.73	13.57	0.15	86.28	100.00	8.40E+05	1.31E+03	
Standard	galena-02	13.36	0.02	86.02	99.40	13.44	0.02	86.54	100.00	8.42E+05	1.44E+02	
Standard	galena-03	13.45	0.11	85.74	99.30	13.54	0.11	86.34	100.00	8.40E+05	1.02E+03	
Standard	galena-04	13.54	0.00	85.46	99.00	13.68	0.00	86.32	100.00	8.40E+05	0.00E+00	
1	RCBA-GL-021	12.63	0.00	82.81	95.45	13.23	0.00	86.77	100.00	**8.44E+05**	**0.00E+00**	
2	RCBA-GL-022	12.72	0.00	82.79	95.51	13.32	0.00	86.68	100.00	**8.43E+05**	**0.00E+00**	
3	RCBA-GL-023	12.65	0.08	82.68	95.41	13.26	0.08	86.65	100.00	**8.43E+05**	**7.60E+02**	-3.05
4	RCBA-GL-024	12.76	0.08	82.55	95.39	13.38	0.08	86.54	100.00	**8.42E+05**	**7.60E+02**	-3.04
5	RCBA-GL-025	12.97	0.00	82.81	95.78	13.54	0.00	86.46	100.00	**8.41E+05**	**0.00E+00**	
6	RCBA-GL-026	12.72	0.11	82.61	95.45	13.33	0.12	86.55	100.00	**8.42E+05**	**1.06E+03**	-2.90
7	RCBA-GL-027	12.84	0.00	82.40	95.24	13.48	0.00	86.52	100.00	**8.42E+05**	**0.00E+00**	
8	RCBA-GL-028	12.88	0.00	82.46	95.34	13.51	0.00	86.49	100.00	**8.42E+05**	**0.00E+00**	
9	RCBA-GL-029	12.81	0.00	83.35	96.15	13.32	0.00	86.68	100.00	**8.43E+05**	**0.00E+00**	
10	RCBA-GL-030	12.76	0.24	83.33	96.34	13.25	0.25	86.50	100.00	**8.42E+05**	**2.25E+03**	-2.57

	galena-05	13.42	0.00	86.19		99.61	13.47	0.00	86.53		100.00	8.42E+05	0.00E+00			
	galena-06	13.49	0.11	85.75		99.35	13.58	0.11	86.31		100.00	8.40E+05	1.02E+03			

	Barite			**Elemental**						**Normalization**						**Log_{10} $PbSO_4$**
Point	**Comment**	**S**	**Ba**	**Pb**	**Sr**	**O**	**Total**	**S**	**Ba**	**Pb**	**Sr**	**O**	**Total**	**Pb ppm**	**Ba ppm**	**activity**
Standard	barite-01	14.07	53.12	0.02	2.60	20.71	90.52	15.54	58.68	0.02	2.87	22.88	100.00	1.72E+02	5.25E+05	
Standard	barite-02	14.01	53.08	0.09	2.32	20.60	90.11	15.55	58.91	0.10	2.57	22.86	100.00	1.02E+03	5.27E+05	
Standard	barite-03	13.80	53.44	0.02	2.38	20.44	90.08	15.32	59.32	0.03	2.64	22.69	100.00	2.59E+02	5.31E+05	
Standard	barite-04	14.16	53.38	0.02	2.40	20.79	90.75	15.60	58.82	0.02	2.64	22.91	100.00	2.14E+02	5.27E+05	
1	HWBA-01	13.75	54.82	0.00	1.04	20.30	89.91	15.29	60.98	0.00	1.16	22.57	100.00	**0.00E+00**	**5.46E+05**	-2.92
2	HWBA-02	13.72	54.96	0.06	0.96	20.28	89.98	15.25	61.08	0.07	1.06	22.54	100.00	**6.60E+02**	**5.47E+05**	-3.03
3	HWBA-03	13.71	55.23	0.05	0.74	20.25	89.98	15.23	61.39	0.05	0.82	22.51	100.00	**5.19E+02**	**5.50E+05**	-3.80
4	HWBA-04	13.57	54.64	0.01	1.04	20.10	89.36	15.18	61.15	0.01	1.17	22.49	100.00	**8.71E+01**	**5.47E+05**	-3.01
5	HWBA-05	13.86	55.05	0.05	0.67	20.38	90.00	15.40	61.16	0.05	0.74	22.64	100.00	**5.30E+02**	**5.48E+05**	-3.01
6	HWBA-06	13.81	54.22	0.05	1.30	20.35	89.73	15.39	60.43	0.05	1.45	22.67	100.00	**5.31E+02**	**5.41E+05**	-2.79
7	HWBA-07	13.93	53.83	0.08	1.63	20.48	89.94	15.49	59.85	0.09	1.81	22.77	100.00	**8.76E+02**	**5.36E+05**	-2.87
8	HWBA-08	13.61	55.39	0.07	0.77	20.18	90.02	15.12	61.53	0.08	0.86	22.42	100.00	**7.46E+02**	**5.51E+05**	
9	HWBA-09	14.00	54.20	0.00	1.25	20.51	89.95	15.56	60.25	0.00	1.39	22.80	100.00	**0.00E+00**	**5.39E+05**	-3.33

10	HWBA-010	14.05	55.28	0.02	0.34	20.53	90.22	15.57	61.27	0.03	0.38	22.75	100.00	**2.59E+02**	**5.49E+05**	-2.58
11	HWBA-011	13.81	54.62	0.13	1.11	20.36	90.03	15.34	60.67	0.15	1.23	22.61	100.00	**1.45E+03**	**5.43E+05**	-2.54
12	HWBA-012	13.98	54.43	0.15	1.27	20.54	90.38	15.47	60.23	0.16	1.41	22.73	100.00	**1.57E+03**	**5.39E+05**	-3.43
13	HWBA-013	13.94	55.56	0.02	0.27	20.44	90.22	15.45	61.58	0.02	0.29	22.65	100.00	**2.05E+02**	**5.51E+05**	-3.15
14	HWBA-014	13.18	55.44	0.04	0.31	19.68	88.65	14.87	62.54	0.04	0.35	22.20	100.00	**3.95E+02**	**5.60E+05**	
15	HWBA-015	13.47	54.97	0.00	0.39	19.92	88.76	15.18	61.94	0.00	0.44	22.44	100.00	**0.00E+00**	**5.55E+05**	
16	HWBA-016	13.62	55.29	0.00	0.53	20.13	89.57	15.21	61.72	0.00	0.59	22.48	100.00	**0.00E+00**	**5.53E+05**	-2.76
17	HWBA-017	13.84	55.11	0.09	0.69	20.37	90.09	15.36	61.17	0.10	0.76	22.61	100.00	**9.61E+02**	**5.48E+05**	-2.58
18	HWBA-018	13.65	54.72	0.13	0.35	20.07	88.92	15.35	61.53	0.15	0.39	22.57	100.00	**1.46E+03**	**5.51E+05**	-3.10
19	HWBA-019	13.97	54.70	0.04	0.57	20.42	89.70	15.57	60.97	0.04	0.64	22.77	100.00	**4.34E+02**	**5.46E+05**	
20	HWBA-020	13.80	52.99	0.00	2.20	20.34	89.33	15.45	59.32	0.00	2.46	22.77	100.00	**0.00E+00**	**5.31E+05**	-2.56
21	HWBA-021	14.01	54.05	0.14	1.64	20.59	90.43	15.49	59.77	0.15	1.81	22.77	100.00	**1.49E+03**	**5.35E+05**	-2.68
22	HWBA-022	13.96	55.01	0.11	0.58	20.46	90.12	15.49	61.04	0.12	0.64	22.70	100.00	**1.13E+03**	**5.47E+05**	
23	HWBA-023	13.69	55.39	0.00	0.52	20.21	89.82	15.25	61.67	0.00	0.58	22.50	100.00	**0.00E+00**	**5.52E+05**	-3.41
24	HWBA-024	13.87	55.75	0.02	0.48	20.43	90.54	15.32	61.57	0.02	0.52	22.56	100.00	**2.15E+02**	**5.51E+05**	
25	HWBA-025	14.11	54.10	0.00	0.96	20.56	89.73	15.73	60.29	0.00	1.07	22.91	100.00	**0.00E+00**	**5.40E+05**	
26	HWBA-026	13.71	55.21	0.00	0.44	20.19	89.55	15.31	61.66	0.00	0.49	22.54	100.00	**0.00E+00**	**5.52E+05**	
27	HWBA-027	13.99	56.30	0.00	0.13	20.54	90.96	15.38	61.89	0.00	0.14	22.59	100.00	**0.00E+00**	**5.54E+05**	
28	HWBA-028	14.01	54.84	0.00	0.23	20.40	89.47	15.65	61.29	0.00	0.26	22.80	100.00	**0.00E+00**	**5.49E+05**	-2.72
29	HWBA-029	13.96	55.10	0.10	0.26	20.41	89.83	15.54	61.34	0.11	0.29	22.72	100.00	**1.05E+03**	**5.49E+05**	-3.27

30	HWBA-030	13.74	56.21	0.03	0.12	20.29	90.39	15.20	62.19	0.03	0.13	22.45	100.00	**3.01E+02**	**5.57E+05**	-3.21
31	HWBA-031	13.82	54.96	0.03	0.97	20.38	90.15	15.33	60.96	0.03	1.07	22.60	100.00	**3.35E+02**	**5.46E+05**	
32	HWBA-032	13.99	54.08	0.00	1.74	20.58	90.39	15.47	59.83	0.00	1.93	22.76	100.00	**0.00E+00**	**5.36E+05**	
																-2.79
1	RCBA-GL-01	13.43	51.44	0.08	1.73	19.72	86.40	15.54	59.54	0.09	2.00	22.82	100.00	**8.67E+02**	**5.33E+05**	-2.45
2	RCBA-GL-02	13.37	50.89	0.17	2.06	19.67	86.16	15.52	59.07	0.19	2.39	22.83	100.00	**1.89E+03**	**5.29E+05**	-2.51
3	RCBA-GL-03	13.27	54.16	0.15	0.25	19.61	87.44	15.17	61.94	0.17	0.28	22.43	100.00	**1.70E+03**	**5.55E+05**	-3.07
4	RCBA-GL-04	13.28	52.71	0.04	1.84	19.73	87.60	15.16	60.18	0.05	2.10	22.52	100.00	**4.55E+02**	**5.39E+05**	
5	RCBA-GL-05	13.37	51.80	0.00	1.97	19.74	86.89	15.39	59.62	0.00	2.27	22.72	100.00	**0.00E+00**	**5.34E+05**	-3.47
6	RCBA-GL-06	13.49	51.23	0.02	2.04	19.81	86.59	15.58	59.17	0.02	2.36	22.88	100.00	**1.80E+02**	**5.30E+05**	
7	RCBA-GL-07	13.46	50.61	0.00	2.41	19.76	86.24	15.60	58.69	0.00	2.79	22.92	100.00	**0.00E+00**	**5.25E+05**	-3.15
8	RCBA-GL-08	13.52	50.95	0.03	1.88	19.78	86.16	15.70	59.13	0.04	2.18	22.96	100.00	**3.73E+02**	**5.29E+05**	
9	RCBA-GL-09	13.29	52.08	0.00	1.48	19.60	86.45	15.37	60.24	0.00	1.71	22.67	100.00	**0.00E+00**	**5.39E+05**	
10	RCBA-GL-010	13.50	51.25	0.00	1.72	19.75	86.22	15.66	59.44	0.00	1.99	22.91	100.00	**0.00E+00**	**5.32E+05**	
11	RCBA-GL-011	13.51	51.94	0.00	1.40	19.79	86.64	15.59	59.95	0.00	1.62	22.84	100.00	**0.00E+00**	**5.37E+05**	
12	RCBA-GL-012	13.67	51.83	0.00	1.82	20.01	87.33	15.65	59.35	0.00	2.09	22.91	100.00	**0.00E+00**	**5.31E+05**	-2.62
13	RCBA-GL-013	13.74	51.21	0.11	1.82	20.02	86.91	15.81	58.93	0.13	2.09	23.04	100.00	**1.28E+03**	**5.28E+05**	-3.60
14	RCBA-GL-014	13.50	51.73	0.01	1.74	19.82	86.79	15.55	59.60	0.01	2.00	22.83	100.00	**1.35E+02**	**5.34E+05**	-3.47
15	RCBA-GL-015	13.60	51.66	0.02	1.72	19.91	86.91	15.65	59.44	0.02	1.98	22.91	100.00	**1.79E+02**	**5.32E+05**	
16	RCBA-GL-016	13.32	51.48	0.00	1.69	19.60	86.09	15.47	59.80	0.00	1.96	22.77	100.00	**0.00E+00**	**5.35E+05**	-3.29

17	RCBA-GL-017	13.24	50.86	0.02	1.89	19.49	85.50	15.48	59.49	0.03	2.21	22.79	100.00	**2.73E+02**	**5.33E+05**	
18	RCBA-GL-018	13.37	51.84	0.00	1.67	19.69	86.57	15.44	59.89	0.00	1.93	22.74	100.00	**0.00E+00**	**5.36E+05**	
19	RCBA-GL-019	13.33	51.54	0.00	1.63	19.60	86.09	15.48	59.87	0.00	1.89	22.76	100.00	**0.00E+00**	**5.36E+05**	-3.06
20	RCBA-GL-020	13.31	50.91	0.04	1.94	19.57	85.76	15.52	59.36	0.05	2.26	22.82	100.00	**4.65E+02**	**5.31E+05**	
Standard	barite-05	14.12	52.91	0.03	2.53	20.72	90.31	15.63	58.58	0.04	2.80	22.94	100.00	3.56E+02	5.25E+05	
Standard	barite-06	13.98	52.64	0.08	2.38	20.53	89.60	15.60	58.74	0.09	2.65	22.91	100.00	8.91E+02	5.26E+05	

5.5 Laser Ablation Inductively Coupled Plasma Mass Spectrometry

REE concentrations were collected via laser-ablation inductively coupled plasma mass spectrometry from the Red Cloud fluorite mine and the M and E No. 13 prospect. The data shows great variation but generally show LREE enrichment (Table 4). Because Red Cloud bastnaesite samples were analyzed via spot analysis on a grain mount and M and E No. 13 samples were analyzed via a line scan on a standard thick section, total element values for the M and E No. 13 are lower than those from Red Cloud. All values presented are in parts per million.

Bastnaesite from both deposits show enrichment in LREE relative to HREE (Table 4). Although only ~75 wt. % REE is expected in bastnaesite, some analyses indicate that concentration is as high as ~120 wt. % (Anthony et al, 2003). Because this data is only used semi-quantitatively and is later discussed on a relative scale, all data was used. Standard deviations for samples from both locations are smaller when analyzing LREE (Table 4, Figure 6). This phenomenon is attributed to decreasing abundance with increasing atomic number.

Table 4. LA-ICP MS data collected on bastnaesite from the Red Cloud Fluorite mine and the M and E No. 13 prospect															
	La	**Ce**	**Pr**	**Nd**	**Sm**	**Eu**	**Gd**	**Tb**	**Dy**	**Ho**	**Er**	**Tm**	**Yb**	**Lu**	**Total**
RCBST1	384300	471500	46810	113600	14960	1283	3777	266	716	61	172	0	2	0	1037447
RCBST3	340600	415000	42190	108900	17820	1778	5729	478	1639	197	544	1	73	0	934949
RCBST4	307700	344300	32950	78510	9906	808	2528	162	451	30	97	0	0	0	777442
RCBST5	378000	324500	27870	62450	6834	562	1733	104	266	6	45	0	0	0	802370
RCBST6	384600	359500	31280	74470	7213	548	1721	106	249	6	46	0	0	0	859739
RCBST7	308700	285000	25920	58000	5920	392	1403	79	225	4	45	0	0	0	685687
RCBST8	190300	234500	25050	66550	12550	1225	3332	253	944	93	263	0	27	0	535086
RCBST9	326400	368400	35230	84000	10200	850	2676	188	534	43	140	0	0	0	828660
RCBST10	269100	328300	32120	77300	9966	786	2544	163	468	35	114	0	0	0	720895
RCBST11	255000	297700	28980	69980	8311	650	2127	124	363	20	79	0	0	0	663334
RCBST13	261100	328600	33500	84860	12840	1186	3544	245	707	59	159	0	0	0	726800
RCBST14	288300	344100	34140	83690	10780	944	2878	194	578	47	146	0	0	0	765796
RCBST15	243500	285100	28090	68830	8722	668	2242	131	384	20	70	0	0	0	637757
RCBST16	462700	549000	53590	130500	16550	1393	4078	293	720	62	173	0	0	0	1219059
RCBST17	328300	348600	33970	82540	10140	838	2542	176	499	36	115	0	0	0	807757
RCBST18	270700	307000	29030	69320	8508	667	2189	135	426	31	110	0	0	0	688116
RCBST19	287800	354000	38600	102500	16090	1448	4153	293	876	76	196	0	2	0	806034
RCBST20	286100	345800	35220	88910	14210	1316	4228	323	1040	104	287	0	18	0	777556
Average	**309622**	**349494**	**34141**	**83606**	**11196**	**963**	**2968**	**206**	**616**	**52**	**156**	**0**	**7**	**0**	**793027**
2σ Standard	**127870**	**143122**	**14704**	**38434**	**7098**	**759**	**2222**	**200**	**697**	**93**	**238**	**0**	**36**	**0**	**335472**
M+E 13 L.	13230	13070	1377	3810	361	68	224	22	114	14	54	0	31	0	32375
M+E 13 L.	10260	10730	937	2705	316	46	162	11	79	6	29	0	16	0	25298
M+E 13 L.	5291	6387	499	1554	144	27	82	4	51	1	19	0	10	0	14070
Average	**9594**	**10062**	**938**	**2690**	**274**	**47**	**156**	**13**	**81**	**7**	**34**	**0**	**19**	**0**	**23915**
2σ Standard	**8022**	**6782**	**878**	**2256**	**229**	**41**	**142**	**18**	**64**	**13**	**36**	**0**	**22**	**0**	**18503**

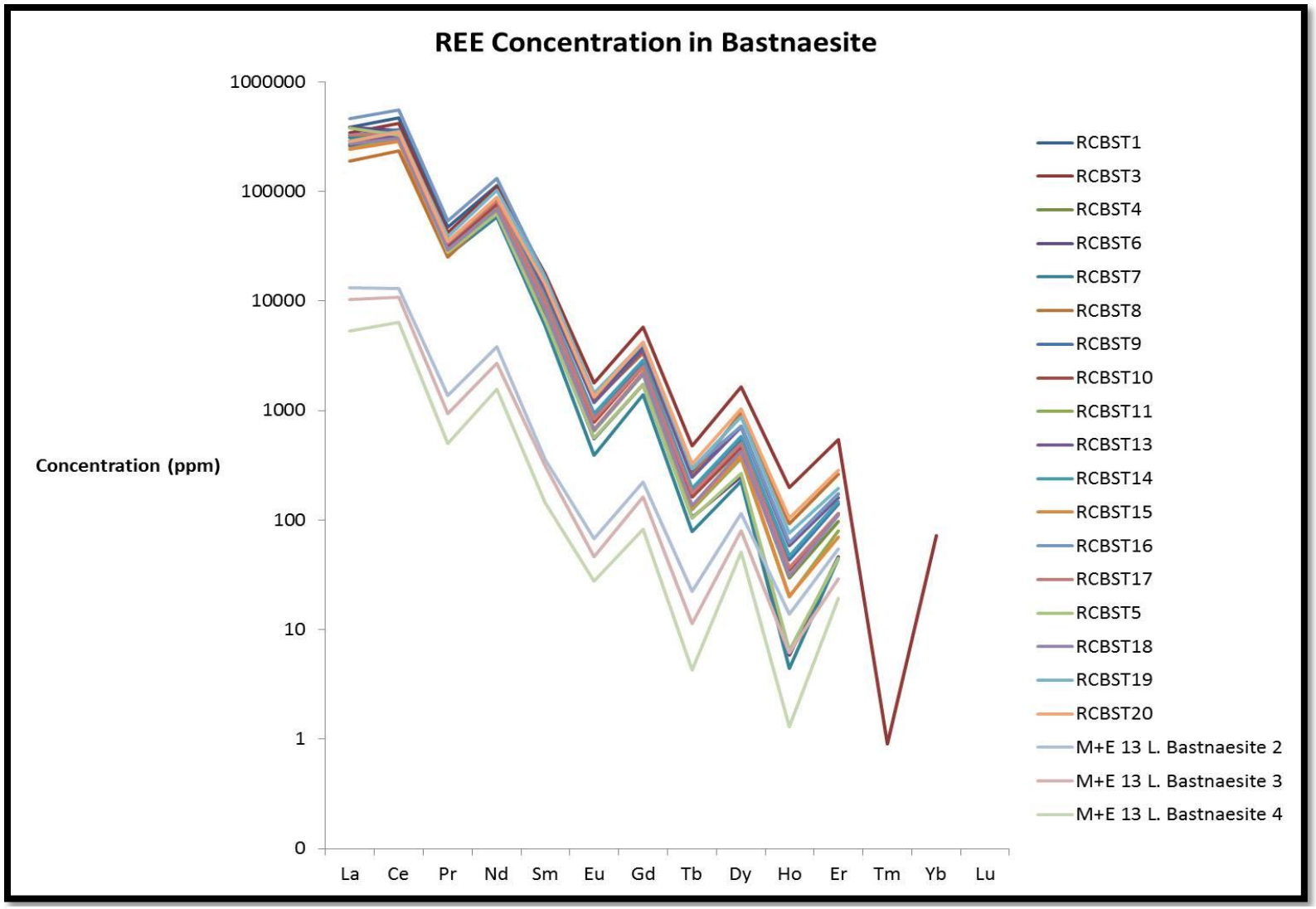

Figure 6. REE concentration in bastnaesite. Diagram shows results of LA ICP-MS analyses. RCBST denotes Red Cloud Bastnaesite. M+E 13 L. Bastnaesite samples are from the same large (2 cm) grain of bastnaesite from the M and E No. 13 prospect. Red Cloud bastnaesite was sampled differently than M and E No. 13 samples which led to the difference in measured REE abundance.

6. DISCUSSION

6.1 Mineralogy and Petrography

Mineralogical analysis of the rock units and mineral deposits confirms earlier observations of Perhac (1970) and Schreiner (1993). Detailed descriptions of deposit mineralogy are found in Table 5. In general, two types of deposits were identified and studied in detail. The first type of deposit is a fluorite breccia with significant sulfide, sulfate, and minor REE mineralization, which includes the Red Cloud Copper, Buckhorn, and Old Hickory mines. They generally occur in the eastern portion of the mountain range in the vicinity of Rough Mountain. This group of deposits will be referred to as the "Rough Mountain" deposits. The second type of deposit is a fluorite breccia with very minor sulfate and sulfide minerals but with significant REE and fluorite mineralization. The M and E No. 13 prospect and the Red Cloud fluorite mine are examples of this type of mineralization, although the Red Cloud fluorite mine assemblage contains significant barite.

Three separate mineral paragenetic relationships were determined (Figure 7). The mineral paragenesis for Red Cloud Fluorite mine and the M and E No. 13 prospect is very similar to previous reports (Williams-Jones et al., 2000). The M and E No. 13 prospect paragenesis differs from previous studies in that it includes the addition of late stage calcite veins (carbonitization) evidenced by cross cutting relationships (Schreiner, 1993). Additionally, this study did not recognize any significant amount of barite at the M and E No. 13 deposit reported by Perhac (1970).

The paragenesis diagram for the M and E No. 13 prospect was taken largely from previous authors (Williams-Jones et al., 2000). Three varieties of fluorite were recognized (ME13 fluorite 1, 2, and 3). ME13 fluorite 1 is green-blue and forms "subhedral to euhedral crystals up to ~1 cm in diameter" (Williams-Jones et al., 2000: fig. 3A, B). Clear-purple fluorite (ME13 fluorite 2) "occurs as euhedra but more commonly rims and replaces" ME13 fluorite 1 (Williams-Jones et al., 2000: fig. 3C). Fine grained purple fluorite (ME13 fluorite 3) constitutes the matrix of fluorite euhedra and formed last (Williams-Jones et al., 2000). Bastnaesite is often brecciated and forms subhedral to euhedral terminated prisms up to 2 cm in length. It can mantle fluorite euhedra (ME13 fluorite 1 and 2) or replace ME13 fluorite 1 or quartz (Williams-Jones et al., 2000). Quartz occurs as either euhedral grains or brecciated/fractured fragments and are sometimes replaced by ME13 fluorite 1 and bastnaesite (Williams-Jones et al., 2000: fig 4D). Barite was not recognized from the M and E No. 13 prospect but, according to previous workers, mantles and replaces ME13 fluorite 1 and bastnaesite (Williams-Jones et al., 2000). Pyrite (goethite/hematite pyritohedrons) occurs in ME13 fluorite 3 matrix and rarely as inclusions in ME13 fluorite 1 (Williams-Jones et al., 2000).

The Red Cloud fluorite mine paragenesis is largely taken from previous authors with a few exceptions (Perhac, 1970 and Williams-Jones et al., 2000). It differs from previous studies in that it includes presence of sulfides (galena and pyrite) occurring in the fluorite breccia matrix at the Red Cloud Fluorite mine (Perhac, 1970, Schreiner, 1993). This relationship suggests that galena and pyrite were forming earlier than previously reported.

Two types of fluorite were recognized from the Red Cloud fluorite deposit: RC fluorite 1 and RC fluorite 2. RC fluorite 1 is purple, occurs as masses in the breccia matrix or rim sandstone clasts (Williams-Jones et al., 2000: figs. 3B and 7A). RC fluorite 2 is colorless, massive, and forms the matrix to fragments of RC fluorite 1 (Williams-Jones et al., 2000: figs. 3B, 7A, and 7B). RC fluorite 2 also forms euhedral overgrowths on RC fluorite 1 cores. Bastnaesite occurs as euhedral prismatic crystals (~0.5 cm) is often fractured and usually within in masses of RC fluorite 1 (Williams-Jones et al., 2000). Bastnaesite was also found altering the growth of now oxidized pyrite grains indicating that pyrite and bastnaesite were forming at the same time and pyrite was later oxidized (Figure 7A). Quartz forms euhedral crystals which are often fractured. They also sometimes rim sandstone clasts indicating their early formation (Williams-Jones et al., 2000).

A simplified mineral paragenesis for Old Hickory, Buckhorn, and Honeywell suggests that, in general, quartz and bastnaesite were deposited early evidenced by euhedral crystals within the fluorite matrix. This was followed by two periods of fluorite mineralization, which was followed by barite and/or sulfide mineralization (Figure 7). Fluorite shows the same replacement textures in these deposits as it does in the Red Cloud fluorite mine as reported by previous authors (Williams-Jones et al., 2000). Sulfides and their oxidized equivalents exist as discrete grains within the fluorite matrix as well as in veins which cross cut fluorite breccia. The occurrence as grains within the matrix indicates that sulfides were forming during matrix formation. The cross cutting relationships indicate that sulfide mineralization continued later than breccia matrix formation.

An episode of hypogene oxidation took place which completely converted pyrite into hematite and goethite pseudomorphs, especially near the Honeywell prospect and Rio Tinto mine (Figure 8B). In the Red Cloud copper and Rio Tinto mines, it is likely that much of the original sulfide mineralization was oxidized during a period of supergene oxidation resulting in the formation of many copper, lead, iron oxide, and arsenate minerals (Perhac, 1970).

The rare mineral agardite [$(REE,Ca)Cu_6(AsO_4)_3(OH)_6 \cdot 3H_2O$] was reported from the Red Cloud Copper mine (DeMark, 1980). Its occurrence suggests that fluids responsible for sulfide mineralization may have also contained significant REE (Anthony et al., 2003). The later oxidation/weathering caused dissolution of REE and sulfide minerals and the later precipitation of agardite. Rostite [$Al(SO_4)(OH,F) \cdot 5H_2O$)] was identified and confirmed by X-ray diffraction at the Rio Tinto copper mine and is the first reported occurrence of this mineral in New Mexico. It typically forms from the destruction of Al bearing minerals by SO_2 and halogens (Anthony et al., 2003). The occurrence of this mineral indicates that abundant SO_2 and HF existed in the hydrothermal fluid during deposit formation.

The occurrence of abundant hydrothermal barite in Red Cloud fluorite mine and celestine [$SrSO_4$] in the Old Hickory mine is reported here. Celestine mineralization in this type of hydrothermal systems is unique given that it precipitates only at very low Ba/Sr (Hanor, 2000). It was therefore assumed that areas of celestine mineralization (i.e., at the Old Hickory deposit) represented areas relatively distal from the fluid source. This is reasonable given that copious amounts of barite exist at lower elevations on Rough

Mountain (i.e., the Honeywell prospect) which would have lowered the Ba concentration in the fluid.

6.2 Alteration

Petrographic and hand sample observations made on rock alteration types in the Gallinas Mountains, NM during this study supports those made by Perhac (1970) and Schreiner (1993). A simplified sequence of alteration events was determined (Figure 9).

In general, three igneous rock types intruded overlying sedimentary beds. Paleo landscape reconstructions of nearby areas during the Tertiary indicate a depth of implacement of ~1-3 km for the nearby Capitan Mountains and Jones Camp dike (Campbell et al, 1995 and Lueth, 2009). Fe-skarn formation was accompanied by minor fluorite and galena indicating that at least some S and F accompanied the main igneous bodies. Brecciation of the trachyte followed skarn formation, evidenced by the presence of Fe-skarn fragment found in unmineralized breccia. Alkali metasomatism occurred along with unmineralized brecciation (Schreiner, 1993). Sodic alteration was followed by potassic alteration (Perhac, 1970 and Schreiner, 1993). Mineralized (fluorite, REE, and sulfide) brecciation cross cuts unmineralized breccia zones and areas of alkali metasomatism (Perhac, 1970 and Schreiner, 1993).

Alkali metasomatism is present near intrusive breccia pipes, adjacent country rocks, in trachyte dikes, syenite, and the isolated outcrop of Precambrian granite (Schreiner, 1993). This alteration type was named fenitization by previous authors however; the name fenite implies the existence of a carbonatite, fenitization being the type of alteration inherently associated with carbonatites (Schreiner, 1993). Upon close

examination of the literature it was evident that previous authors had never identified a carbonatite (Perhac, 1970, Schreiner, 1993). Evidence of early sodic alteration is indicated by the replacement of original minerals by albite (Schreiner, 1993). Potassium feldspar replaces original minerals as well as the albite formed from sodic alteration indicating that the potassium bearing fluid was later than the sodium bearing fluid (Appendix 1, Fenite Zone 1; Schreiner, 1993). A detailed cathode luminescence study on alkali metasomatism in the Gallinas Mountains was carried out by previous workers (Schreiner, 1993).

An episode of hypogene oxidation occurred altering pyrite to goethite/hematite pseudomorphs in all deposits (Figure 8B). This was followed by an episode(s) of carbonitization evidenced by calcite veins in trachyte at Rough Mountain (drill core) and at the M and E No. 13 prospect (Schreiner, 1993). Lastly, an episode of supergene alteration occurred resulting in the formation of copper oxides, cerussite, anglesite and arsenates (Table 1, Figure 8D, Appendix 3).

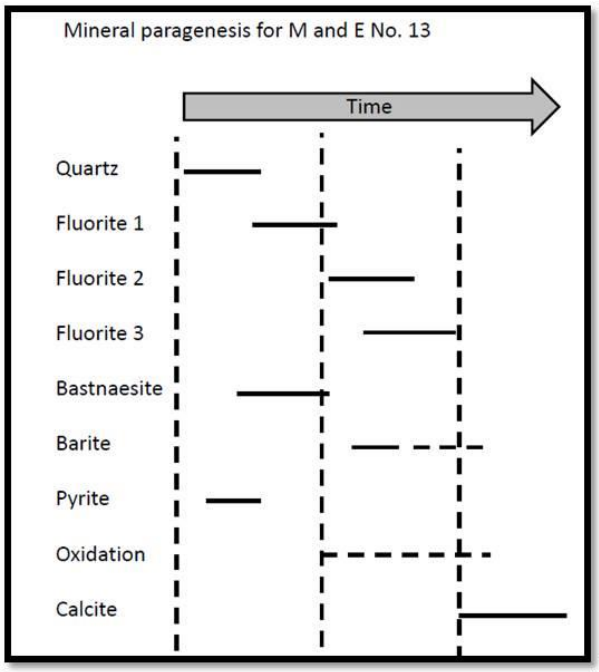

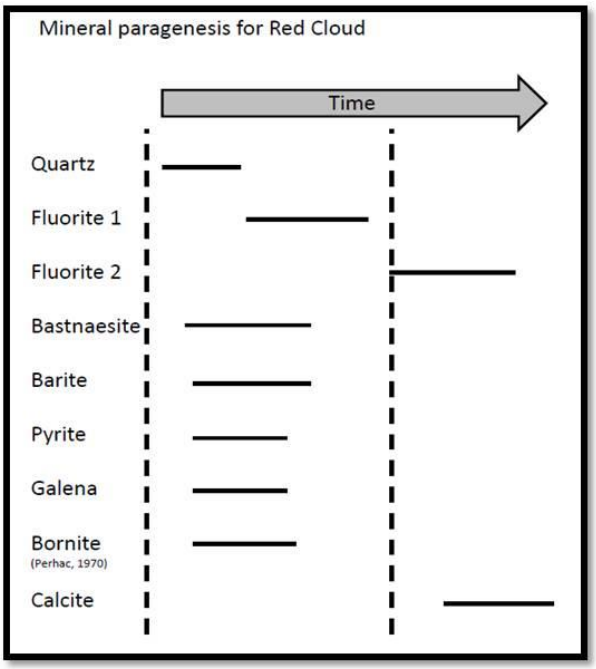

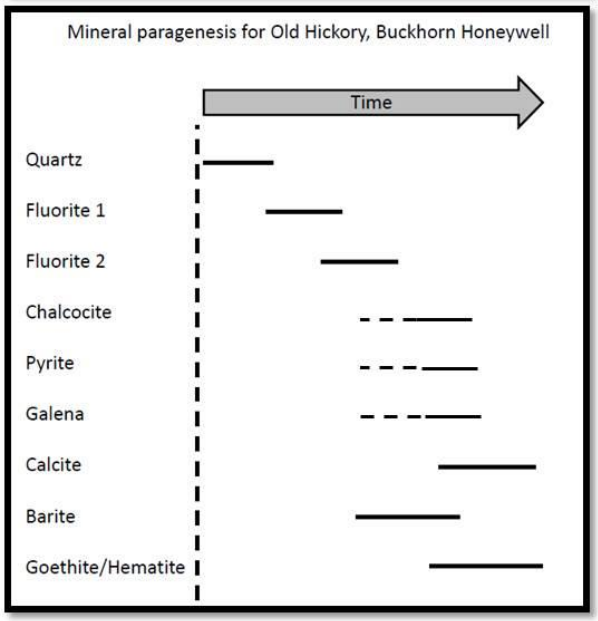

Figure 7. Paragenesis diagrams. Created by combining data from Perhac (1970), Schreiner (1993), Williams-Jones et al. (2000), and this study. Vertical dashed lines represent periods of brecciation and/or fracturing. Horizontal dashed lines represent likely periods of events. Numbers represent fluid inclusion T_h and stable isotope geothermometry temperatures in °C.

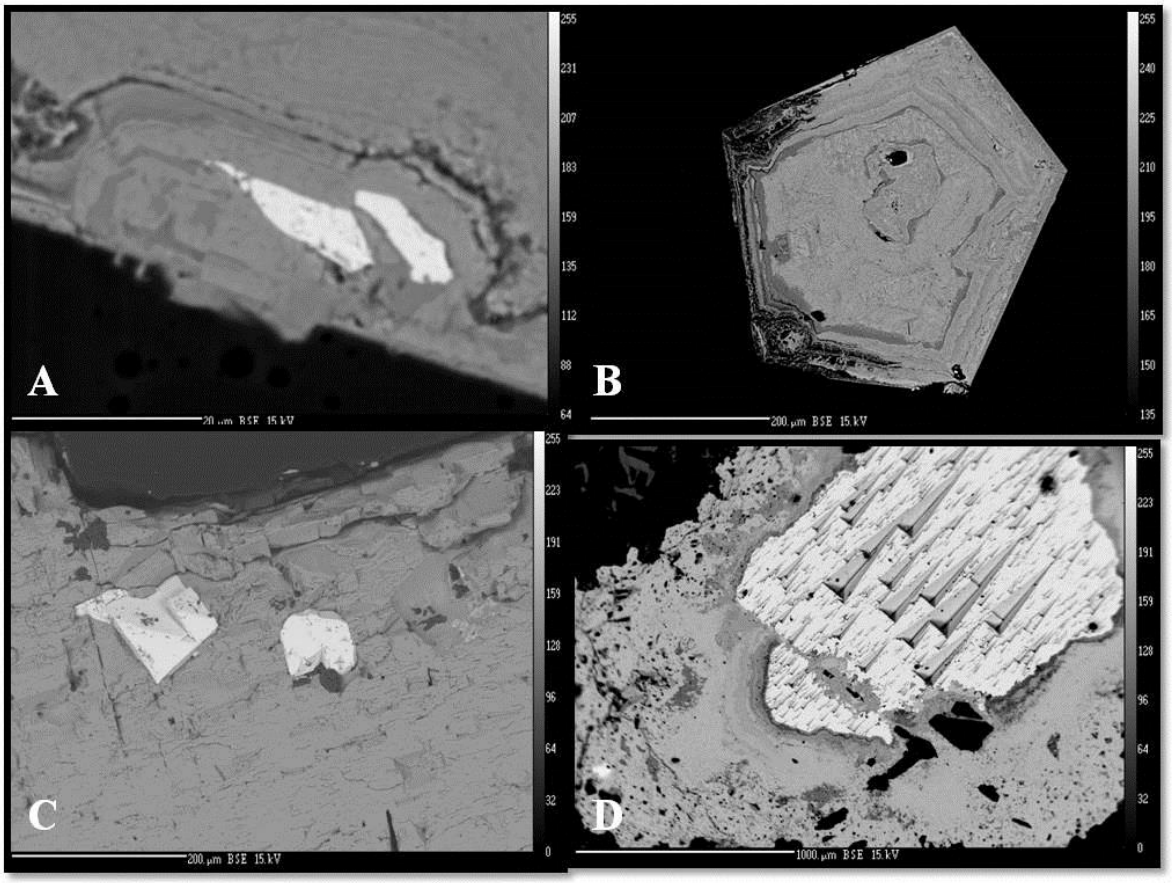

Figure 8. SEM backscatter images. A) Bastnaesite coprecipitating with pyrite grain. Pyrite is now altered to a goethite/hematite pseudormorph (Red Cloud Bastnaesite concentrate, Red Cloud Fluorite mine). B) Pyritohedron pseudomorph, now altered to goethite/hematite (Red Cloud Bastnaesite concentrate, Red Cloud Fluorite mine). C) Galena cubes (white) within barite (light gray). This sample was used for galena-barite stable isotope geocthermometry (Red Cloud Copper mine). D) Galena (white with triangle pits) rimmed by a number of silver, lead, and arsenic bearing alteration phases (Red Cloud Copper mine).

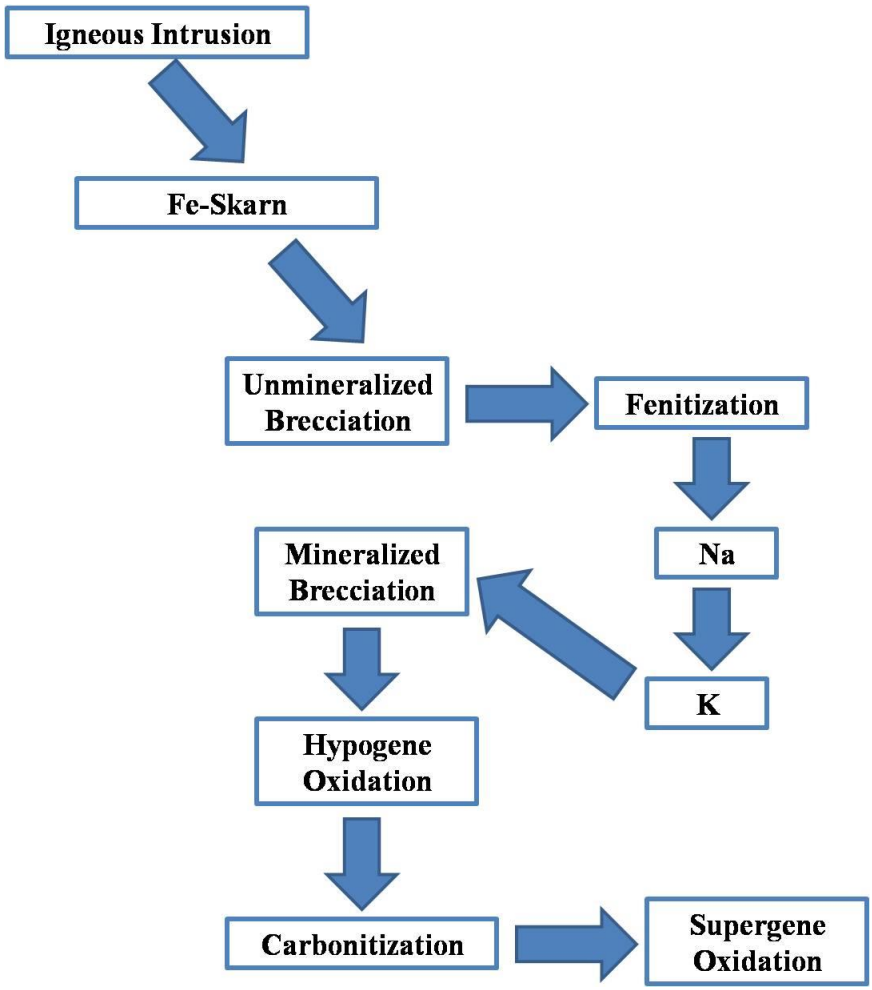

Figure 9. Sequence of alteration in the Gallinas Mountains. Fe-skarn formation was followed by unmineralized brecciation. This was followed by sodic-potassic metasomatism which is cross-cut by mineralized brecciaion. An episode of hypogene oxidation was followed by an carbonitization and supergene oxidation.

Table 5. Mineral abundances reported by deposit. Figure modified from: Perhac (1970).

	1	2,3	4	5	7	8	9	10	11	12	13	14	16	17	18	19	20
Fluorite	X	x	x	x	X	x	x	X	x	X	x	x	x	x	x	x	x
Quartz	M	t	m	m	m	m	t	m	M	m	m	t	m	m	x	m	m
Barite	x	x	t	m	M	M	M	M	m	M	m	m	m	m	m	M	m
Bastnaesite	m			t	t	t	m	t	t	t	t	t	t	t	t	t	t
Calcite	t	t	t	t						t	M	t	m		m	t	
Chalcedony													t		t		
Pyrite	t	t	t	m	t	t	m	t	t	t	t	t	t	t	t	t	t
Galena		m	t			t						t	m			m	
Bornite		t	t		t								t				
Chalcocite		m	M		t							t	t				
Limonite	t	t	t	t	t	t	t	t	t	t	t	t	t	t	t	t	t
Hematite	t	t	t	t	t	t	t	t	t	t	t	t	t	t	t	t	t
Pyromorphite		t	t								t		t		t		
Cerussite		?											m		t		
Anglesite			t										t			t	
Chrysocolla		m	m		t						t	t	t		t		
Malachite		t	t		t						t	t	t		t		
Azurite		t	t								t	t	t				

X > 50%
x — 25 — 50%
M = 10 — 25%
m = 5 — 10%
t — < 5%

1. Red Cloud Fluorite
2, 3. Red Cloud Copper and Deadwood
4. Little Wonder
5. Last Chance
7. Eagle Nest
8. Bottleneck
9. Congress
10. Conqueror No. 4 and Hilltop
11. Summit
12. Hoosier Girl North
13. Hoosier Girl South
14. Eureka
16. Rio Tinto
17. All American
18. Sky High
19. Pride No. 2
20. M and E No. 13

6.3 Fluid Inclusions

Based on published studies, the Red Cloud fluorite mine and M and E No. 13 prospect (Pinatosa), fluid homogenization temperatures indicate that mineral deposition began with quartz (~400°) followed by bastnaesite (~325°C) with a salinity of ~15-19 wt. % NaCl equivalent (Figures 10 and 11; Williams-Jones et al., 2000). Previous authors argued that although all fluids had similar salinities, fluid inclusion decrepitate data indicated that fluids responsible for lower temperature (T_h) fluorite (ME13 and RC fluorite 2) mineralization were dominated by Na and Cl. K and SO_4 dominated fluids responsible for quartz, bastnaesite, and higher temperature (T_h) fluorite (ME13 and RC fluorite 1) mineralization (Williams-Jones et al., 2000). Based on the similarities of fluid inclusion morphologies between those previously published and this work, previous temperature (T_h) and salinity ($T_{m\text{-}ice}$) measurements were used.

Aqueous-carbonic fluid inclusions in $quartz_{(RC+ME13)}$, $bastnaesite_{(RC+ME13)}$, and occasional blue $fluorite_{(ME13)}$ indicates the presence of a high ρCO_2 fluid during mineralization. Although interesting, the occurrence of aqueous-carbonic fluid inclusions is not a diagnostic feature of fluid source rock type nor is any specific fluid inclusion assemblage. Fluid inclusion studies of the Bayan Obo Fe-REE-Nb and Kalkfeld carbonatite complexes report aqueous-carbonic inclusions however; no aqueous-carbonic inclusions are reported from the Oka, Quebec carbonatite complex (Smith and Henderson, 2000, Bühn and Rankin, 1999, and Sampson et al., 1995).

In the Gallinas Mountains, Williams-Jones et al. (2000) suggests that mineralization occurred when a sulfate-bearing KCl-NaCl brine was mixed with a NaCl brine based on mineral paragenesis, distribution of fluid inclusion types, and decrepitate

data. Williams-Jones et al. (2000) also suggests that a CO_2-bearing fluid was also introduced at the time of mixing or possibly earlier.

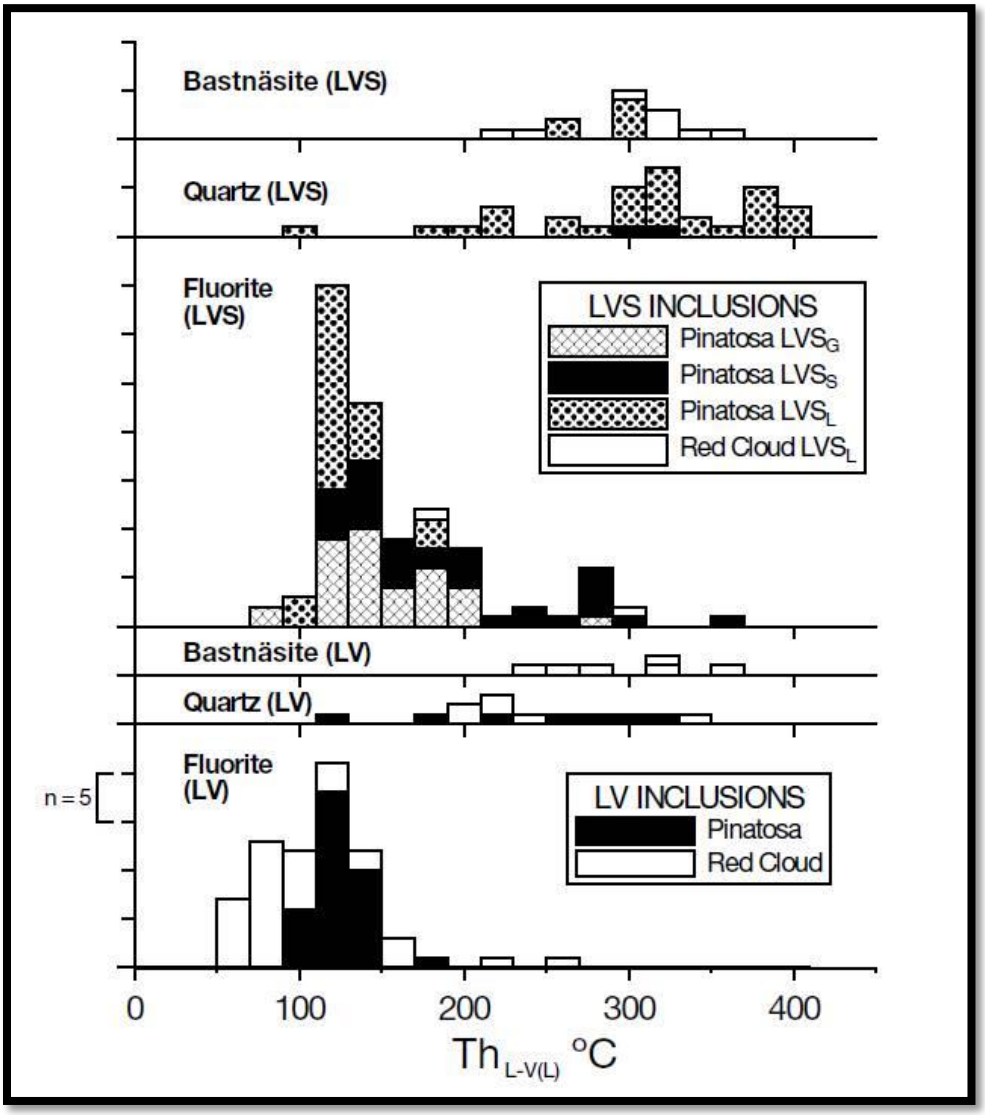

Figure 10. Homogenization temperatures (T_h) for quartz, bastnaesite, and fluorite from the Red Cloud Fluorite mine and the M and E No. 13 prospect (Pinatosa). In general, quartz and bastnaesite inclusions T_h was >250°C while fluorite T_h was <200°C. T_h temperatures between the two deposits show similar characteristics. LVS_G inclusions are gypsum-bearing, LVS_s inclusions are solid-rich and gypsum-free, and LVS_L inclusions are liquid-rich and gypsum-free. With the exception of the two high T_h from Red Cloud, fluorite (LV) T_h shown here are comprised of inclusions in ME13 and RC fluorite 2. Figure modified from: Williams-Jones et al. (2000).

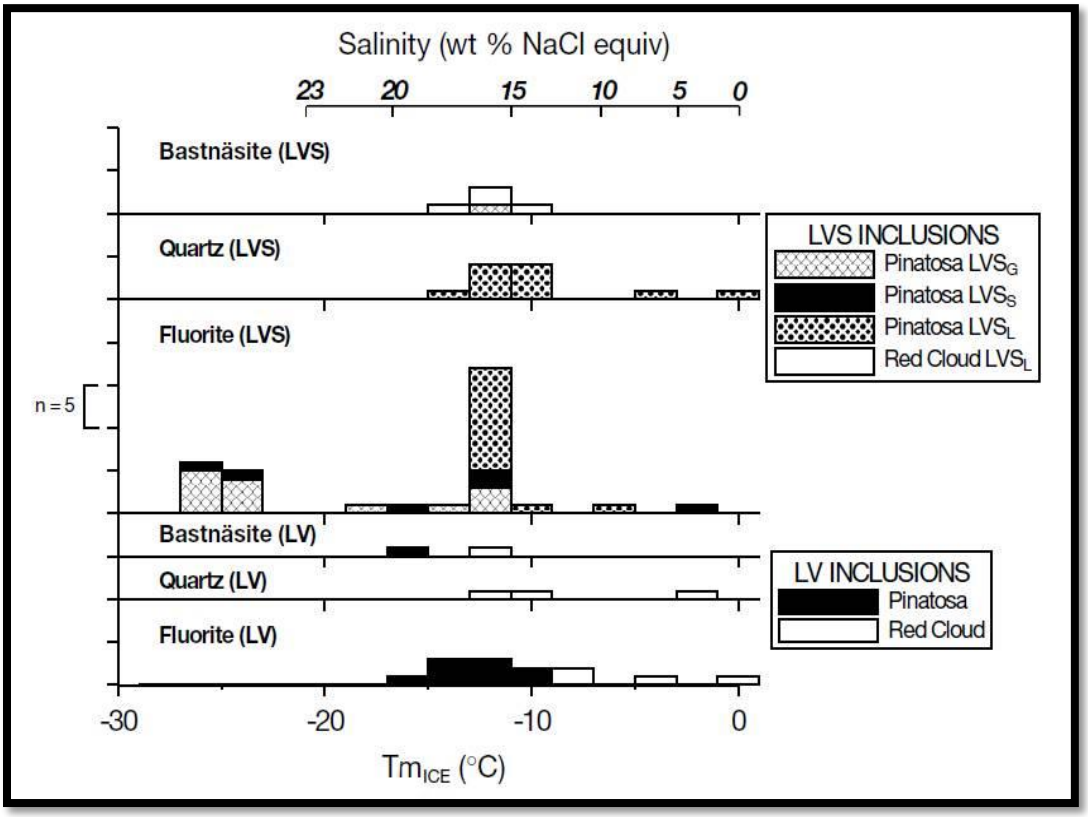

Figure 11. Freezing point measurements of fluid inclusions ($T_{m\text{-}ice}$) in Quartz, bastnaesite, and fluorite from the Red Cloud Fluorite mine and the M and E No. 13 (Pinatosa). Salinity measurements show a similar range of freezing point depression (12-18 wt. percent NaCl equivalent). Low fluorite (L-V-S) $T_{m\text{-}ice}$ measurements were seen only mainly in L-V-S_G inclusions and interpreted to represent metastability. The most common solid phases identified by Williams-Jones et al. (2000) were gypsum, barite, quartz, fluorite, and bastnaesite. Minor solids indentified include calcite, celestine, zircon, and other phases. Figure modified from: Williams-Jones et al. (2000).

6.4 Stable Isotope Geochemistry

6.4.1 Sulfur and Sulfate Oxygen Isotopes

The variation in sulfur values can be explained with reference to the mineralogical associations of these samples. $\delta^{34}S_{galena}$ values of ~0‰ occurred as discrete grains within the fluorite breccia matrix in the Red Cloud fluorite mine. They formed early in association with quartz and bastnaesite, but no barite. Because of their paragenetic relationship and the apparent absence of sulfate, this fluid would have been sulfide dominated and thus the calculated H_2S values would represent the bulk sulfur value of the fluid. The average calculated $\delta^{34}S$ of the fluid is 0.6‰ and is compatible with a magmatic source of sulfur (Ohmoto and Rye, 1979).

The galena $\delta^{34}S$ values near 8‰ are from the Red Cloud copper mine. These galena occurred within the same vein as barite with an average $\delta^{34}S$ value of 11.8 ‰ and were thought to represent mineralogical equilibrium (Figure 8C). This type of mineral relationship in a hydrothermal system implies that these two minerals may have attained isotopic equilibrium. Oxidation of the magmatic fluid described above would account for both the precipitation of sulfate minerals as well the isotopic isotopic fractionation to create lighter sulfide values. Because sulfates preferentially accept the ^{34}S isotope, any barite mineralization in this system is expected to be isotopically heavy relative to sulfide mineralization. If sulfate and reduced sulfur existed in equal proportions in the hydrothermal fluid then the formation of barite could cause the $\delta^{34}S$ of galena to change in equal proportions (Figure 13).

Given the assumption that these galena and barite were in isotopic equilibrium, temperature of formation was calculated. The temperature calculated from that pair is given by the following set of equations:

$$1000ln\alpha_{SO4-H2S} = A\frac{10^6}{T^2} + B\frac{10^3}{T} + C$$

where A = 3.00, B = 14.01, and C = -11.20. Because the SO_4 molecule bonds directly with the Ba molecule in solution without exchanging any additional S, it was used to represent barite.

$$1000ln\alpha_{H2S-Galena} = A\frac{10^6}{T^2} + B\frac{10^3}{T} + C$$

where A= 0.64, B=0, and C = 0. This simplifies to the following equation:

$$1000ln\alpha_{SO4-Galena} = A\frac{10^6}{T^2} + B\frac{10^3}{T} + C$$

A= 2.36, B=14.01, and C = 0 and T is in K (Ohmoto and Rye, 1979 and Li and Liu, 2006). When the equation is solved for T and the $\delta^{34}S$ value for galena (-7.9‰) are subtracted from the $\delta^{34}S$ value for barite (11.8‰) a difference of 19.7‰ is obtained at an equilibrium temperature of 310°C. According to paragenesis diagrams, this temperature is consistent with the fluid inclusion data of quartz and bastnaesite in the adjacent Red Cloud Fluorite deposit (Figure 7). However, given predictions of previous workers, at 310°C isotopic equilibrium between galena and barite may not have been obtained (Ohmoto and Lasaga, 1982).

Finally to explain the origin of the lightest galena values, two processes were considered, further oxidation and mixing. All galena values were compared to elevation (Figure 14). In this district elevation can be used as a proxy for distance from source because previously published cross sections suggest that there has been little regional

tilting (Perhac, 1970). In a sulfate dominated system (H_2S/SO_4 = 1:5) the decreasing trend in $\delta^{34}S$ of galena can be explained by temperature alone (Figure 15) (Rye, 1993). However, sulfate values become lighter rather than heavier with elevation as predicted (Figure 16) by Rye (1993).

This reverse trend is reconciled by mixing of hydrothermal magmatic waters with formation waters of the surrounding sedimentary units. The reverse in the barite $\delta^{34}S$ trend from theoretical predictions can also be a result of fluid mixing (Figure 16). As fluids mix barite continues to precipitate and become isotopically more similar to Yeso sulfate with elevation. Because the fluids are simultaneously cooling galena continues to become much lighter.

The mixing hypothesis is also supported by sulfate $\delta^{34}S$ and $\delta^{18}O$ isotope values. Sulfate $\delta^{34}S$ and $\delta^{18}O$ isotope values from barite display covariation, creating a trend that begins at magmatic values and moves towards known values of nearby Yeso (Py) sulfate (Figure 17). The mixing line is incomplete however, if the Ba/Sr ratio becomes significantly low, barite ceases to form and celestine [$SrSO_4$] forms instead (Hanor, 2000). The absence of barite in the Old Hickory and Buckhorn mines is indeed supplemented by the presence of celestine at higher elevations (i.e. Old Hickory). $\delta^{34}S$ values of celestine and barite indicate not only that mixing has occurred but also that the fluid was oxidizing (Figure 18).

$\delta^{34}S$ values of celestine (5.2 and 1.4‰) are lower than the Yeso (Py) $\delta^{34}S$ range (7-12‰) (Figure 18) (Seal et al., 2000). The white celestine $\delta^{34}S$ value of 5.2 ‰ is close to published Yeso (Py) values and can be result of mixing with Yeso formation waters. Mixing cannot be directly responsible for the lighter value of the brown celestine ($\delta^{34}S$ of

1.4‰). Because the oxidation of sulfide minerals involves no isotopic fractionation and the relatively light value, it is likely that this sulfate was a result of the oxidation of nearby sulfide (Field, 1966). Textural evidence (tabular clusters of crystals) suggests that these celestines were of hydrothermal origin and therefore the brown celestine ($\delta^{34}S$ of 1.4‰) was a result of the hypogene oxidation event.

Barite and galena (from the Red Cloud copper and fluorite mines) $\delta^{34}S$ values fall within the range expected from a carbonatite, however it is clear that they occur in a hydrothermal fluorite breccia rather than a primary carbonatite. More important in terms of deriving a fluid source rock is the $\Sigma^{34}S$ value of ~0-2‰ obtained if it is assumed that oxidized and reduced sulfur existed in equal proportions, this being near the accepted value of the mantle i.e. a carbonatite (Figure 19) (Deines, 1989). The hypothesized source of sulfur in the relatively deep part of the system is a carbonatite. Mixing of Yeso (Py) formation waters with this magmatic fluid resulted in cooling, addition of SO_4^{2-} (aq) and oxidation. These processes worked in coordination to cause the variations in $\delta^{34}S$ seen from the Rough Mountain deposits. This feature of mixing also agrees with the hypothesis of Williams-Jones et al. (2000) to explain fluid inclusion features.

6.4.2 Oxygen Fugacity

Another way to address the issues involving the oxidation state of the mineralizing fluid is to measure the barium content of galena and the lead content of barite (Kajiwara and Honma, 1972). At chemical equilibrium and physiochemical conditions, lead substitutes for barium in the barite structure ($PbSO_4$) and barium will substitute for lead (BaS) in the galena structure. Substitutions are dependent on

temperature, confining pressure, barium and lead concentrations, and oxygen fugacity. Because temperature constraints exist from this and previous studies and it is possible to measure barium and lead in galena and barite, respectively, it is possible to determine a range of oxygen fugacity in deposits in which barite and galena occur in chemical equilibrium.

When calculated activities are plotted two different oxygen fucacities were determined for a mineral pair of $\mathrm{Log}fO_2 = -30$ and $\mathrm{Log}fO_2 = -25$ at an isotopic equilibrium temperature of formation of ~310°C (Figure 20) (Kajiwara and Honma, 1972). Values should converge rather than plot as two separate points. Discrepancies are most likely attributed to chemical disequilibrium or deviations from theoretical predictions at higher temperatures. Mixing hydrothermal fluids may cause chemical disequilibrium and may have attributed to the wide range of Ba and Pb activities determined.

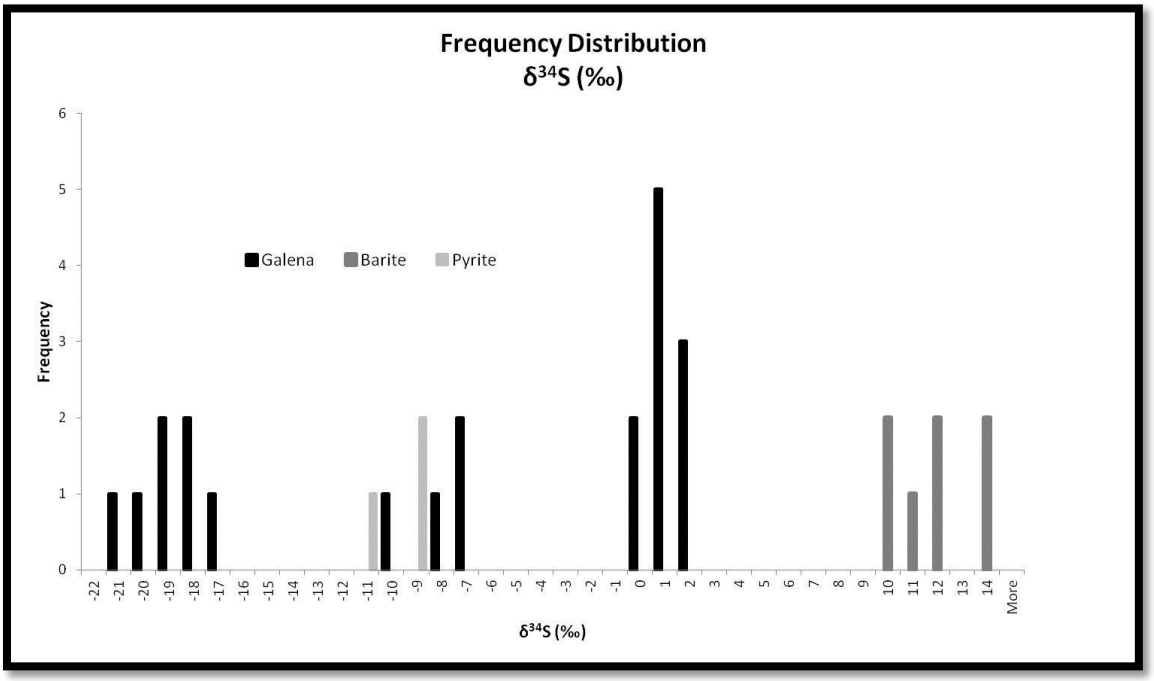

Figure 12. Histogram of all sulfur isotope data. Histogram shows distribution of $\delta^{34}S$ vs. CDT values for galena, barite, and pyrite. Galena samples show great variation from 2 to -21‰, pyrite shows little variation and is centered about -10‰, and barite shows slight variation from 10 to 14‰.

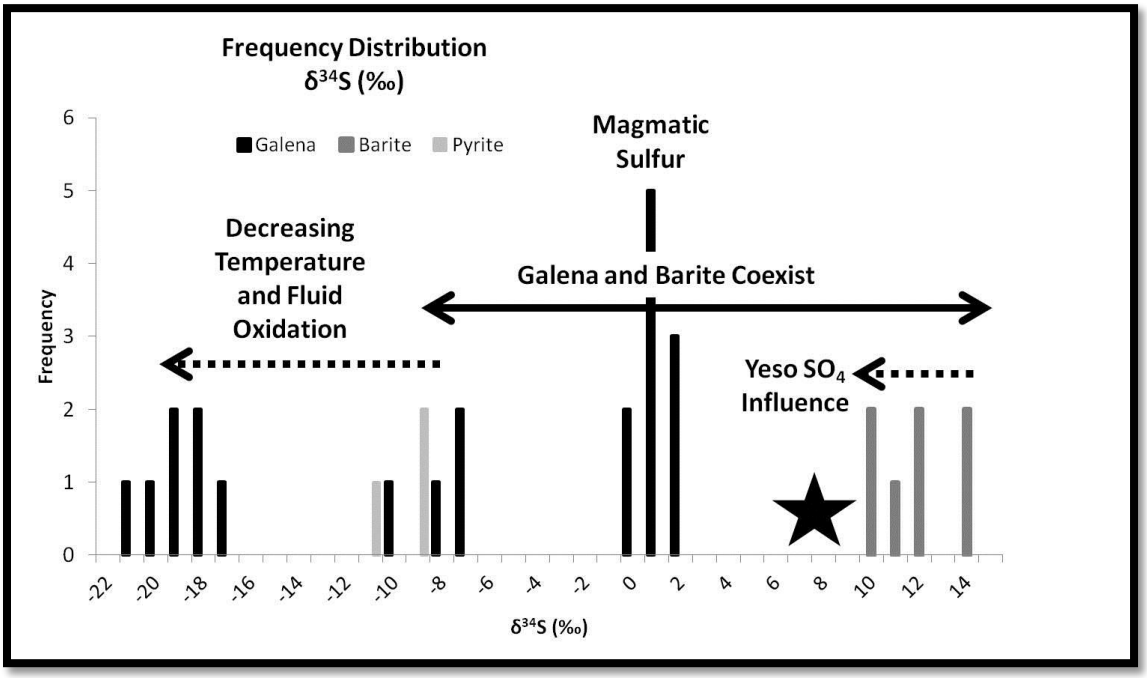

Figure 13. Histogram of all sulfur isotope data with interpretation. Histogram shows processes effecting sulfur isotope evolution. $\delta^{34}S$ values ~0‰ represent magmatic sulfur. As sulfate (barite) begins to form, galena values become lighter (-10‰) and barite forms at a $\delta^{34}S$ of ~13‰. As sulfate bearing Yeso formation water mixes with magmatic waters, temperature decreases and the fluid oxidizes. This causes galena $\delta^{34}S$ values to become more negative (-20‰) and barite $\delta^{34}S$ values to trend towards Yeso sulfate.

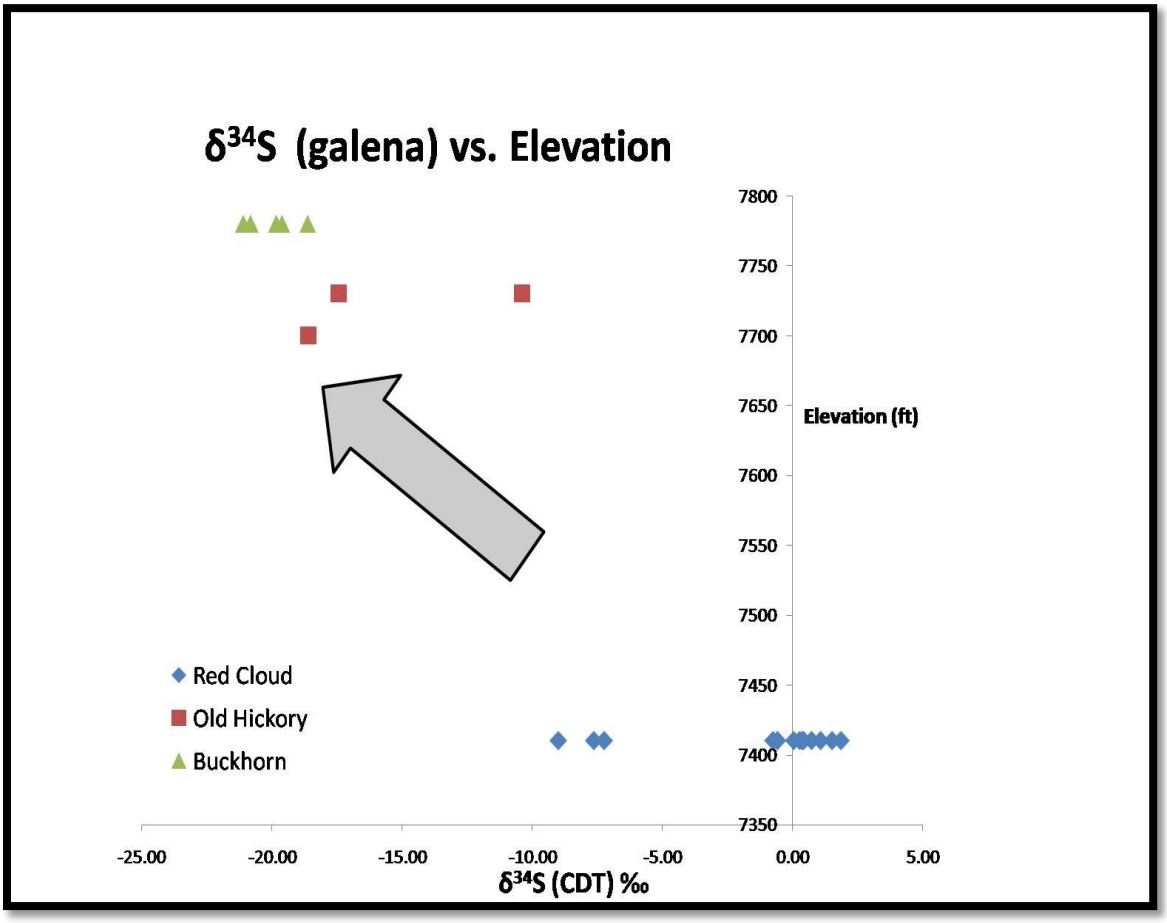

Figure 14. Galena $\delta^{34}S$ variation by elevation of deposit. Samples from Red Cloud are blue diamonds, samples from Old Hickory are red squares, and samples from Buckhorn are green triangles. The trend is decreasing $\delta^{34}S$ values with increasing elevation. $\delta^{34}S$ values from Red Cloud show two populations, one at ~-8‰ and one ~0‰. The former represents galena from the Red Cloud copper mine, the latter from the Red Cloud fluorite mine.

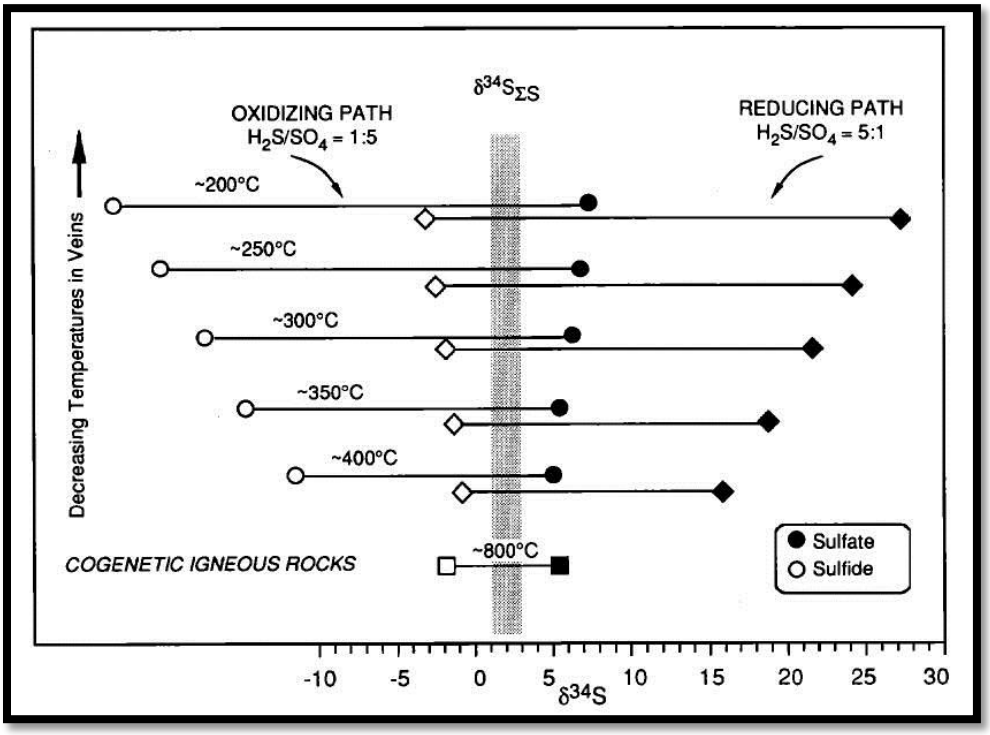

Figure 15. Sulfur isotope fractionation vs. fluid oxidation state. Diagram shows theoretical calculations of sulfur isotope fractionation between sulfate and sulfide species given a $\delta^{34}S_{\Sigma S}$, a reduced/oxidized sulfur ratio, and temperature. Predictions indicate that sulfate becomes slightly heavier while sulfide becomes much lighter with decreasing temperature. Figure modified from: Rye (1993).

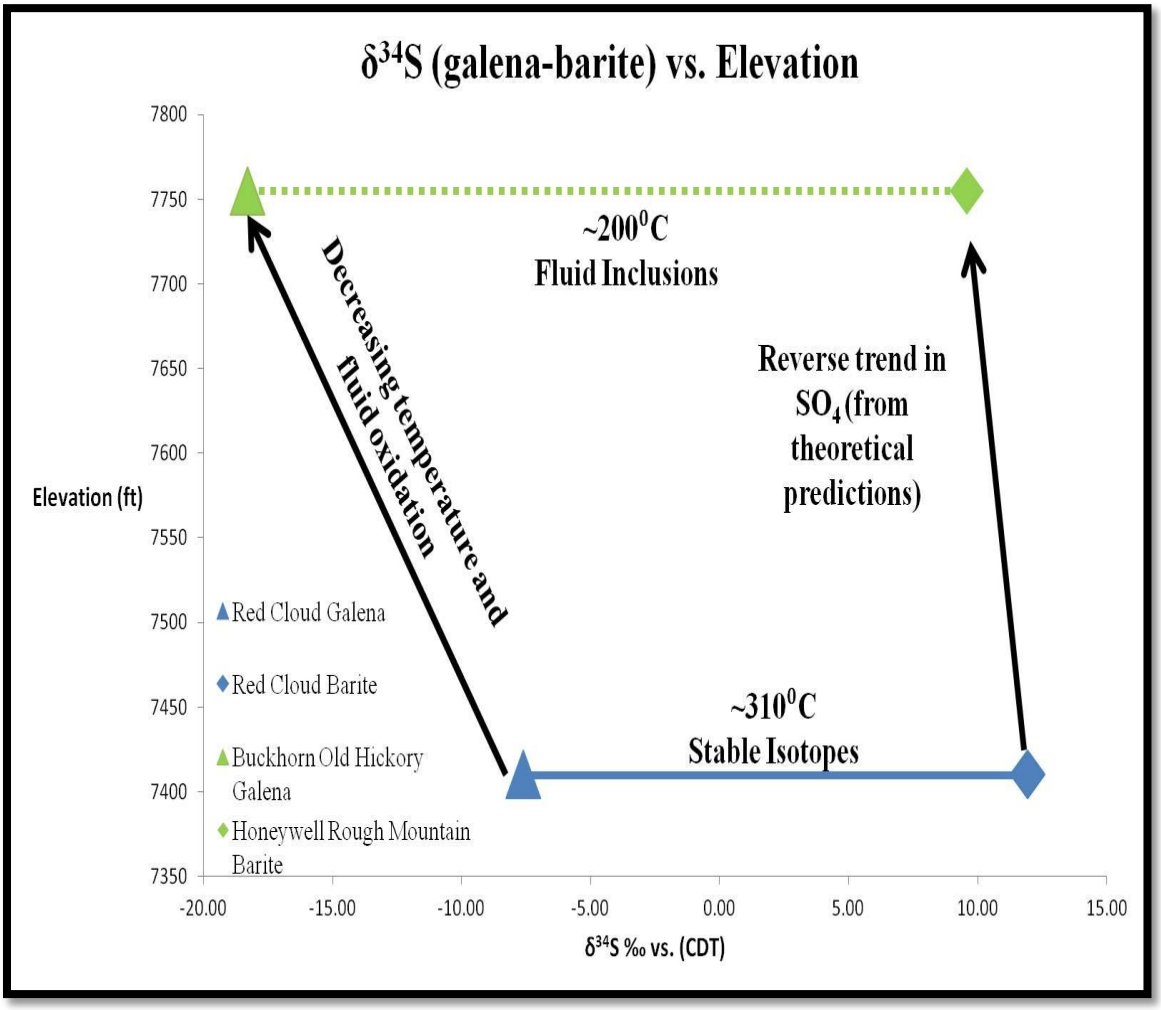

Figure 16. Galena and barite sulfur isotope data vs. elevation.Galena and barite (blue) pair in isotopic equilibrium yielding a temperature of 310°C low in the system. Cooling and fluid oxidation causes galena to become isotopically light. Theoretical predictions indicate that barite should become heavier however mixing with Yeso formation water (SO_4) has caused barite to become lighter with increasing elevation. Dashed line indicates that this galena and barite assemblage was not a pair but were both found at high elevations on Rough Mountain.

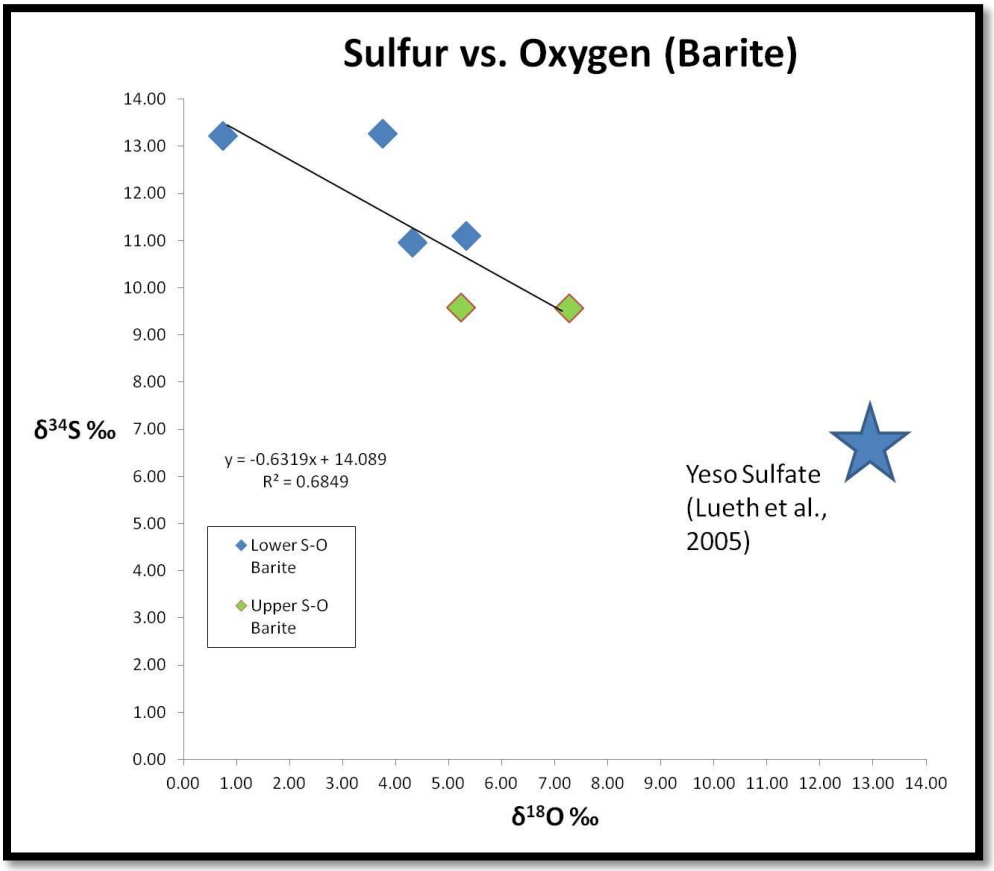

Figure 17. Sulfate sulfur vs. oxygen. Diagram showing sulfur and oxygen isotope ratios of barite from Red Cloud (dark diamonds) and the Honeywell prospect (light diamonds). A trend is seen of decreasing $\delta^{34}S$ values with increasing $\delta^{18}O$ values. There is also correlation shown by heavy sulfur and light oxygen (lower elevation) and lighter sulfur and heavier oxygen (higher elevation). This relationship is interpreted to occur because of mixing with formation waters from the overlying Yeso formation. The Yeso $\delta^{34}S$ and $\delta^{18}O$ values are represented by the dark star in the lower right portion of the figure.

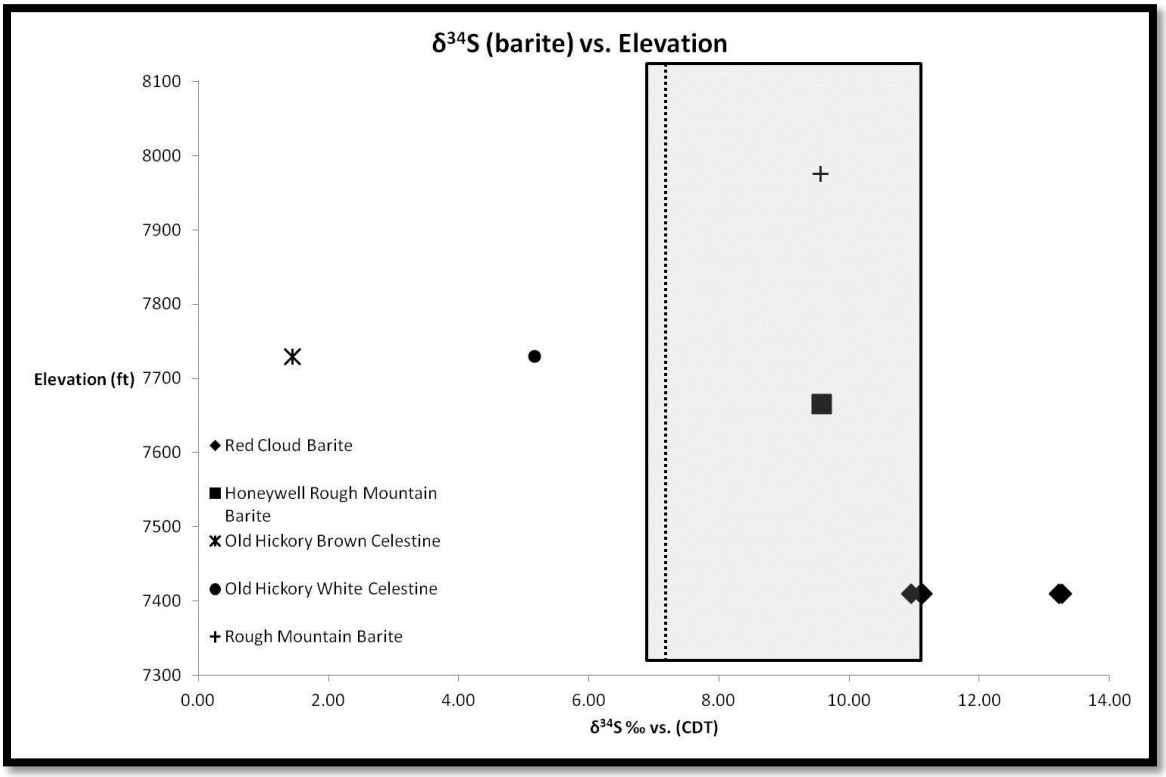

Figure 18. Barite sulfur values. The figure displays $\delta^{34}S$ values of barite and celestine from the upper (Old Hickory, Buckhorn, Honeywell) and lower (Red Cloud fluorite and copper) parts of the system. Yeso sulfate values are bounded by the gray rectangle (Seal et al., 2000). Dotted line represents nearby measured Yeso sulfate (Lueth et al, 2005). Most sulfate values fall within the given range of Yeso sulfate indicating some degree of mixing was occurring, especially in the upper parts of the system. Relatively light celestine values may due to the oxidation of light sulfide minerals and relatively heavy barite values are attributed to a magmatic origin and fractionation between sulfate and sulfide minerals.

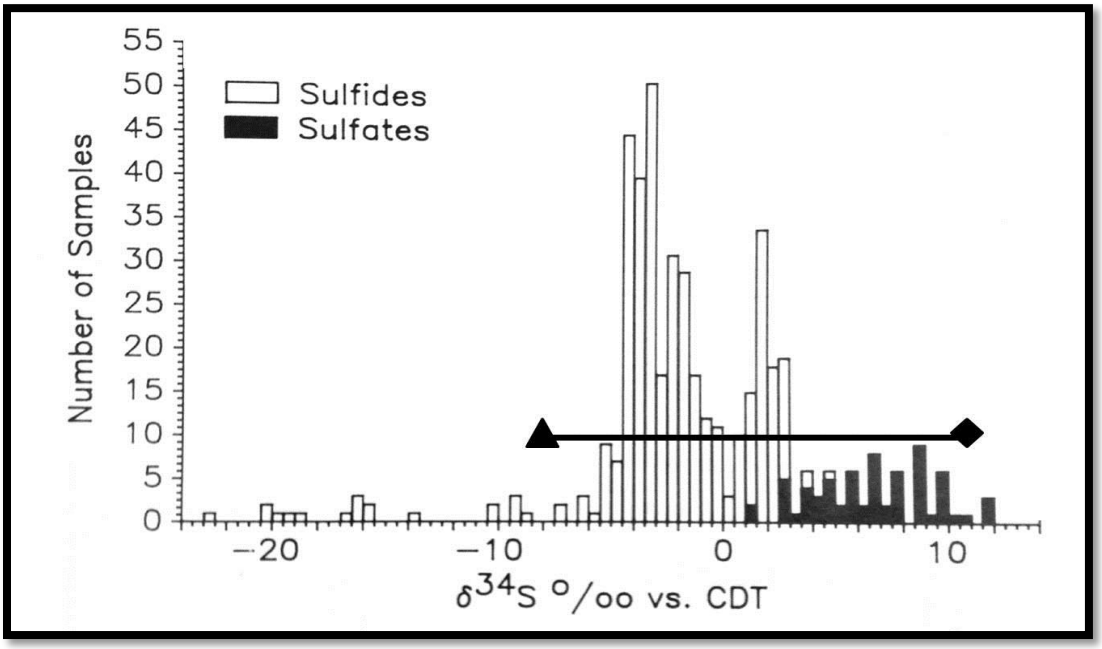

Figure 19. Compiled carbonatite sulfide and sulfate data. Diagram shows sulfur isotopic compositions of sulfides and sulfates from 14 carbonatites. The black triangle represents the average galena $\delta^{34}S$ value and the black diamond represents the average barite $\delta^{34}S$ value from the Red Cloud copper mine. Figure modified from: Deines (1989).

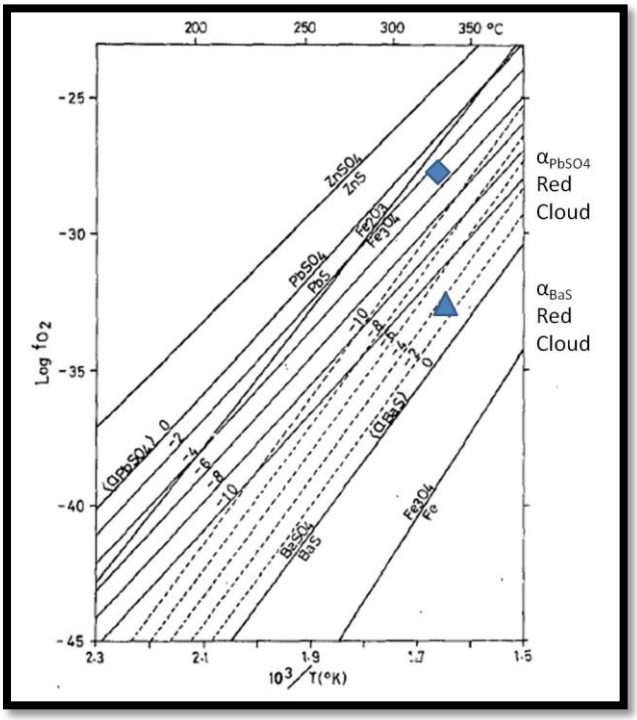

Figure 20. Oxygen fugacity. Diagram showsthe calculated oxygen fugacity at the Red Cloud copper mine. Temperature was calculated from barite-galena stable isotope equilibrium fractionation. The diamond represents lead substitution in barite and the triangle represents barium substitution in galena. Both data points are from the Red Cloud copper mine. Figure modified from Kajiwara and Honma (1972).

6.4.3 Carbon and Oxygen Isotopes

Carbon and oxygen isotopic ratios for bastnaesite and calcite were measured from Red Cloud fluorite, M & E No. 13, and Honeywell deposits (Figure 21). The isotopic composition of bastnaesite was measured in an attempt to distinguish isotopic differences between bastnaesite from the M and E No. 13 prospect and bastnaesite from the Red Cloud fluorite mine. Bastnaesite from the M and E No. 13 prospect and Red Cloud fluorite deposits show overlap in $\delta^{13}C$ and $\delta^{18}O$ values with the exception of an isolated occurrence of pink chalky bastnaesite from Red Cloud. Calcite isotopic compositions were measured to in an attempt to: 1) indicate a source of CO_2 in the mineralizing fluid, 2) detect changes acting upon that fluid, and 3) to compare results of bastnaesite isotopic measurements with those of calcite.

To address the first two questions, carbon and oxygen isotope values from carbonatites from various localities of the world were examined (Figure 22 a,b). Because carbonatites are a common host to REE mineralization and are often associated with copious amounts of fluorine, it should be examined as a possible source rock (Mariano, 1989). If the carbonate in the Gallinas Mountains was derived from a primary carbonatite fluid then $\delta^{13}C$ and $\delta^{18}O$ values could help establish this link. $\delta^{13}C$ values of bastnaesite and calcite generally fall within the limit of carbonatite values; however, $\delta^{18}O$ values are significantly heavier than average carbonatite (Figure 22 a,b) (Deines, 1989). This is not surprising given the fact that the "carbonatite box" represents primary igneous calcite and the calcite and bastnaesite sampled in this study is obviously of hydrothermal origin.

If primary magmatic carbonate and a magmatic fluid of $\delta^{18}O$ of 8‰ were in isotopic equilibrium at ~400°C and that fluid then cooled and precipitated calcite at temperatures of 100°C, $\delta^{18}O$ fractionation between calcite and water indicates calcite would be ~16‰ heavier than the water from which it precipitates (Figure 23) (Kim and O'Neil, 1997).

$$1000ln\alpha_{Calcite-H2O} = 18.03\frac{10^6}{T^2} \pm 32.42\frac{10^3}{T} + 0$$

This explanation is plausible given that calcite precipitation occurred at low temperatures ~100°C. Low temperature precipitation is assumed given the T_h of late stage fluorite at the M and E No. 13 of ~150°C and that calcite occurs as late stage fracture fillings (Williams-Jones et al., 2000). This interpretation also requires the existence of a high ρCO_2 fluid. This fluid is known to exist at the M and E No. 13 prospect in the form of aqueous-carbonic fluid inclusions (Williams-Jones et al., 2000).

It is clear from fluid inclusion temperatures (T_h ~300°C) that bastnaesite was precipitated at higher temperatures. Because $\delta^{18}O$ fractionation factors between water and the minerals dolomite, siderite, and calcite are all within about 1‰ at 300°C it was assumed that the fractionation factor for bastnaesite was also similar (Zheng et al., 1999). Evidence exists that indicates that the release of CO_2 (g) was occurring i.e. aqueous-carbonic fluid inclusions; however, this process would cause water in equilibrium with the escaping CO_2 (g) to become lighter (Truesdell, 1974). Equilibrium calculations between bastnaesite and water indicate that bastnaesite mineralized from a fluid with a $\delta^{18}O$ of ~18‰. This water $\delta^{18}O$ value is very heavy for a magmatic fluid and the isotopic composition of bastnaesite in the Gallinas Mountains remains unresolved.

A Yeso Formation calcite $\delta^{18}O$ value of ~19‰ and $\delta^{13}C$ value of ~0‰ indicates that the overlying sedimentary unit is isotopically heavy with respect to oxygen. It is possible that at least some of the overlying Yeso Formation was dissolved by low pH hydrothermal fluids. This idea is supported by the close spatial proximity of deposit occurrence to the Yeso-Trachyte contact. This may be used to explain some of the $\delta^{18}O$ enrichment but is however an unlikely source of carbon. Because carbon and oxygen are chemically linked by calcite dissolution reactions, it is unlikely that this the hydrothermal fluid responsible for mineralization at the M & E No. 13 prospect saw significant Yeso carbonate influence.

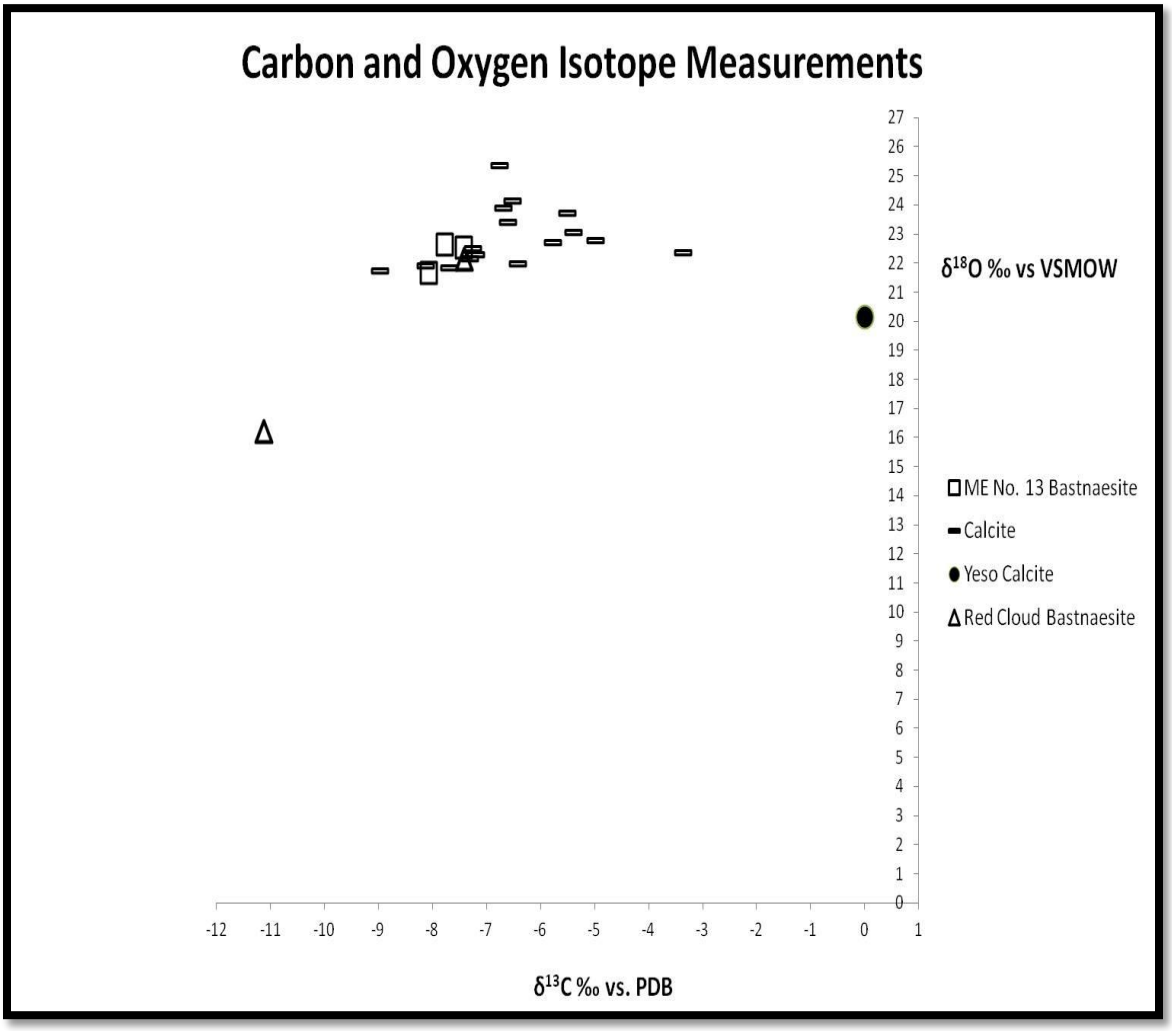

Figure 21. Carbon and oxygen isotope measurements. Measurements made on bastnaesite from the M and E No. 13 prospect and Red Cloud fluorite mine and calcite from the Yeso (Py) formation, M and E No. 13 prospect and trachyte calcite flooding. Almost all calcite values here represent calcite from the M and E No. 13 prospect.

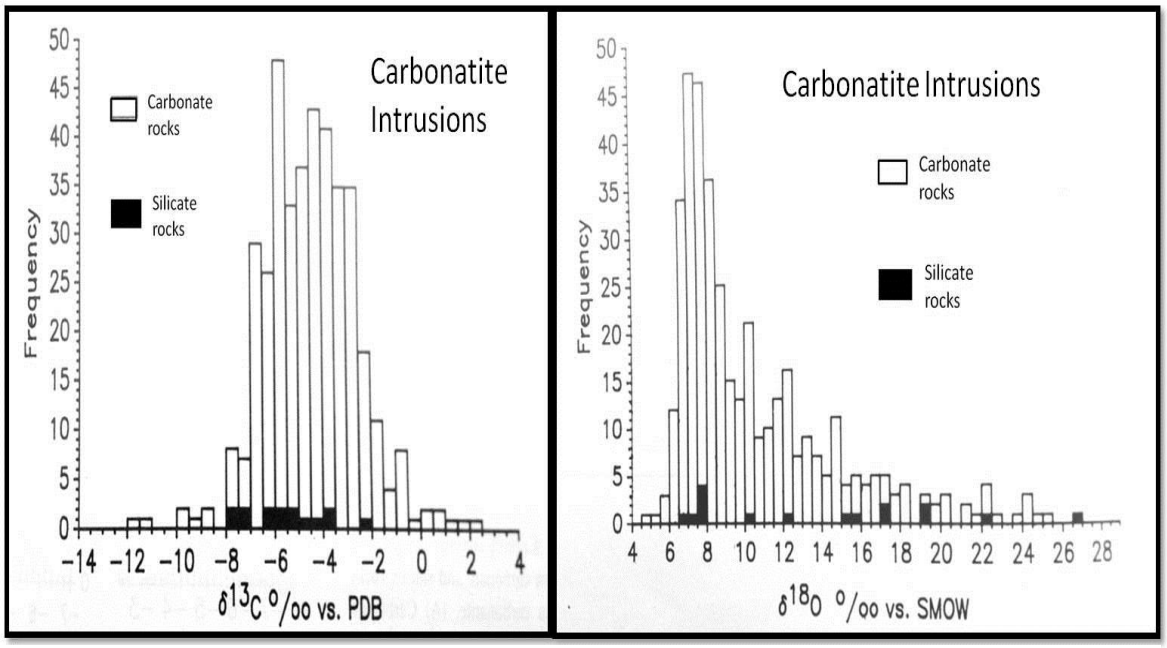

Figure 22. Compiled $\delta^{13}C$ (a) and $\delta^{18}O$ (b) data from worldwide carbonatites. A clear modal range is seen in $\delta^{13}C$ data of -8 to -2‰. $\delta^{18}O$ data show an average carbonate value of ~8‰ and rapidly decreasing abundances outside the range of ~6 – 10%. Figures modified from: Deines (1989).

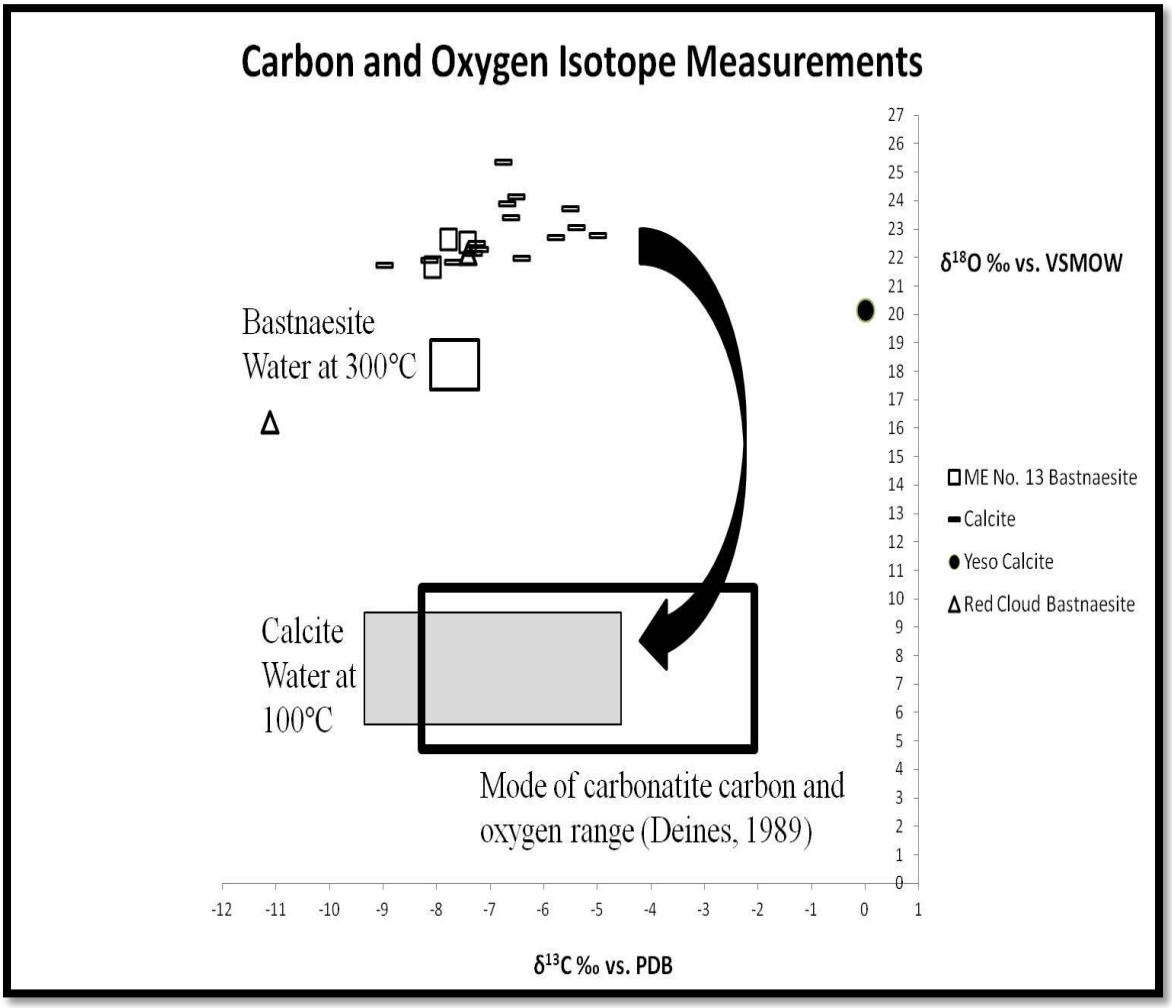

Figure 23. Carbon and oxygen isotope interpretation. Gray box constrains H_2O $\delta^{18}O$ values in equilibrium with late stage calcite at 100°C from the M and E No. 13 prospect. $\delta^{18}O$ values are typical of magmatic waters (vertical range of black box) and $\delta^{13}C$ values are typical of primary carbonatites (horizontal range of black box). Fluid inclusion data suggests that bastnaesite formed at much higher temperatures. H_2O in equilibrium with calcite (fractionation factor used as a proxy for bastnaesite) would plot within the small upper box. The mode of carbonatite carbon and oxygen ranges falls within the thick lined black box. Fluids derived from calcite at temperatures of 400°C (highest T_h of quartz and the lowest possible fluid temperature derived from a magma source during the onset of mineralization) would be ~2‰ lighter.

6.5 Whole Rock and Mineral Trace Element Geochemistry

Individual REE data on deposits is scarce in the literature often limited to assay data. REE distribution within the mineral bastnaesite is also scarce. Whole rock geochemical data from Schreiner (1993; Appendix 6) was combined with LA-ICP-MS data collected from bastnaesite in order to better speculate on the origin of ore fluids.

Igneous petrologists have long used chondrite normalized diagrams of REE abundances to provide insight into source rock and to indicate certain petrologic processes. REE chondrite normalized curves for trace element averages of various rock types as well as whole rock and mineral samples from the Gallinas Mountains (Figure 24). Data for curves labeled "M E 13 L. Bastnaesite Average and Average Red Cloud Bastnaesite" were collected during this study via LA-ICP-MS. The overall enrichment of REE values for these two samples are due to the fact that mineral rather than whole rock separates were analyzed. It is the overall similarity, characterized by steep slopes and slight negative Eu anomaly that the two mineral separate curves have to each other and to the carbonatite from Iron Hill, CO, that is important. Bastnaesite REE composition similarity suggests that the source of REE for both the Red Cloud and M & E No. 13 deposits was the same. The similarity of the curves to the carbonatite from Iron Hill, CO, suggests that the common source rock could be a carbonatite.

A trace element comparison of the igneous units of the Gallinas Mountains, the Capitan Pluton and the Cornudas Mountains with data from the Iron Hill carbonatite and the Gallinas Mountains bastnaesite was performed (Figure 24). This comparison provides compelling evidence that REE in bastnaesite was likely derived from a carbonatite source similar to the Iron Hill carbonatite. If REE in bastnaesite were derived from an alkalic

source (non carbonatite), the REE pattern of bastnaesite is expected to show slight LREE enrichment and minor (if any) HREE depletion similar to patterns of nearby alkaline igneous phases.

Previous work showed that trace element characteristics are diagnostic with respect to rock type, specifically petrologic processes involved in forming any given igneous phase (Loubet et al., 1972). Data of Schreiner (1993) which falls below ∑ REE (ppm) of 10,000 and below a La/Yb ratio of 1,000 plot mostly within the carbonatite region and show a positive trend (Figure 25). This trend is caused by an increase in both total REE content and the LREE/HREE ratio, a trend typical of carbonatite sources (Figure 25). The alkaline igneous rocks (i.e. trachyte) and sedimentary formations of the study area plot in their respective fields with some field overlap. This is probably due to metasomatic effects in the host rocks and/or ambiguities in sampling by Schreiner (1993).

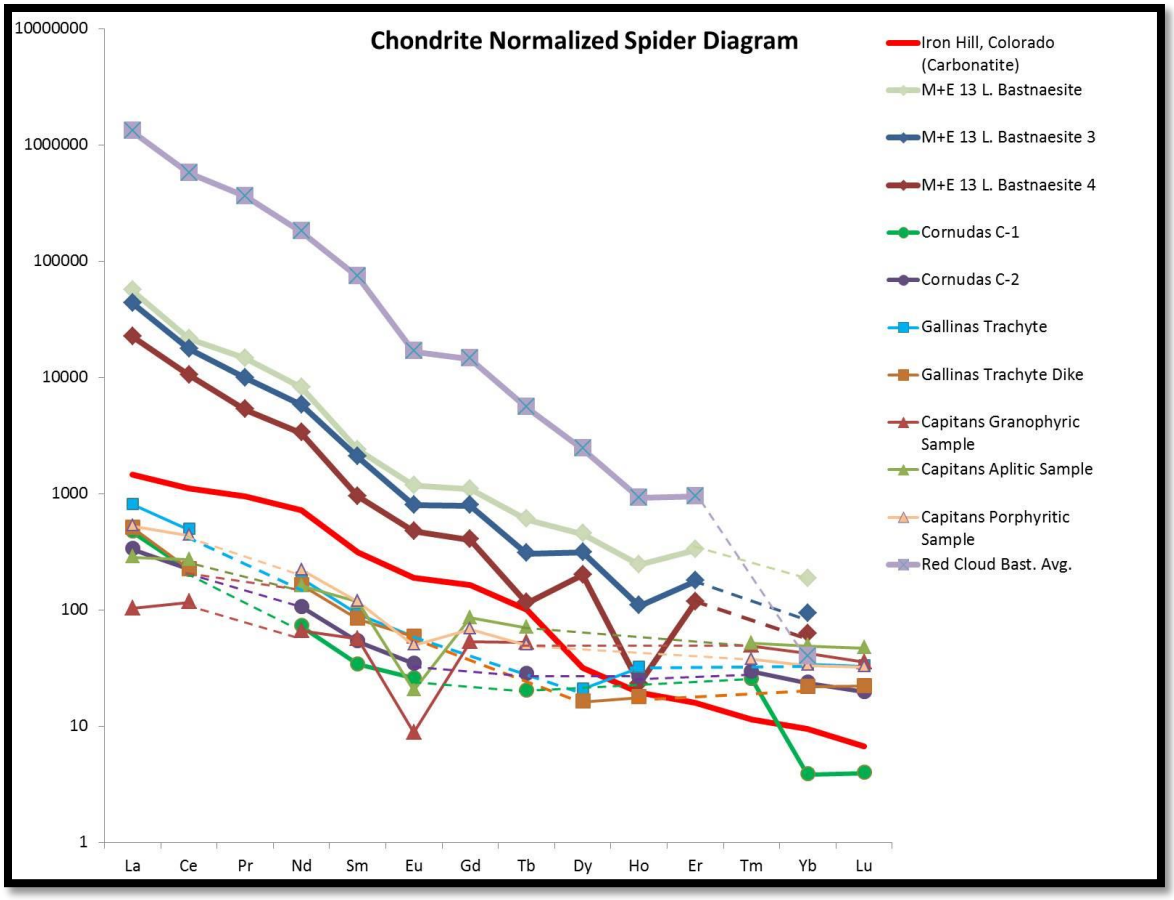

Figure 24. Chondrite normalized spider diagram of bastnaesite samples from the Gallinas Mountains, the Iron Hill Carbonatite, the Cornudas Mountains, and the Capitan pluton. Gallinas Mountains trachyte, Cornudas Mountains, and the Capitan pluton all show very similar trends in REE/Chondrite patterns in being slightly enriched in LREE and having flat HREE slopes. The Iron Hill carbonatite shows high levels of LREE enrichment and high HREE depletion compared to the LCPB alkalic suite. Bastnaesite from the Gallinas shows the same high LREE enrichment and HREE depletion as the Iron Hill carbonatite. Data taken from: Allen and McLemore (1991), Schreiner (1993), and Goodell, Lueth, and Willsie (2002).

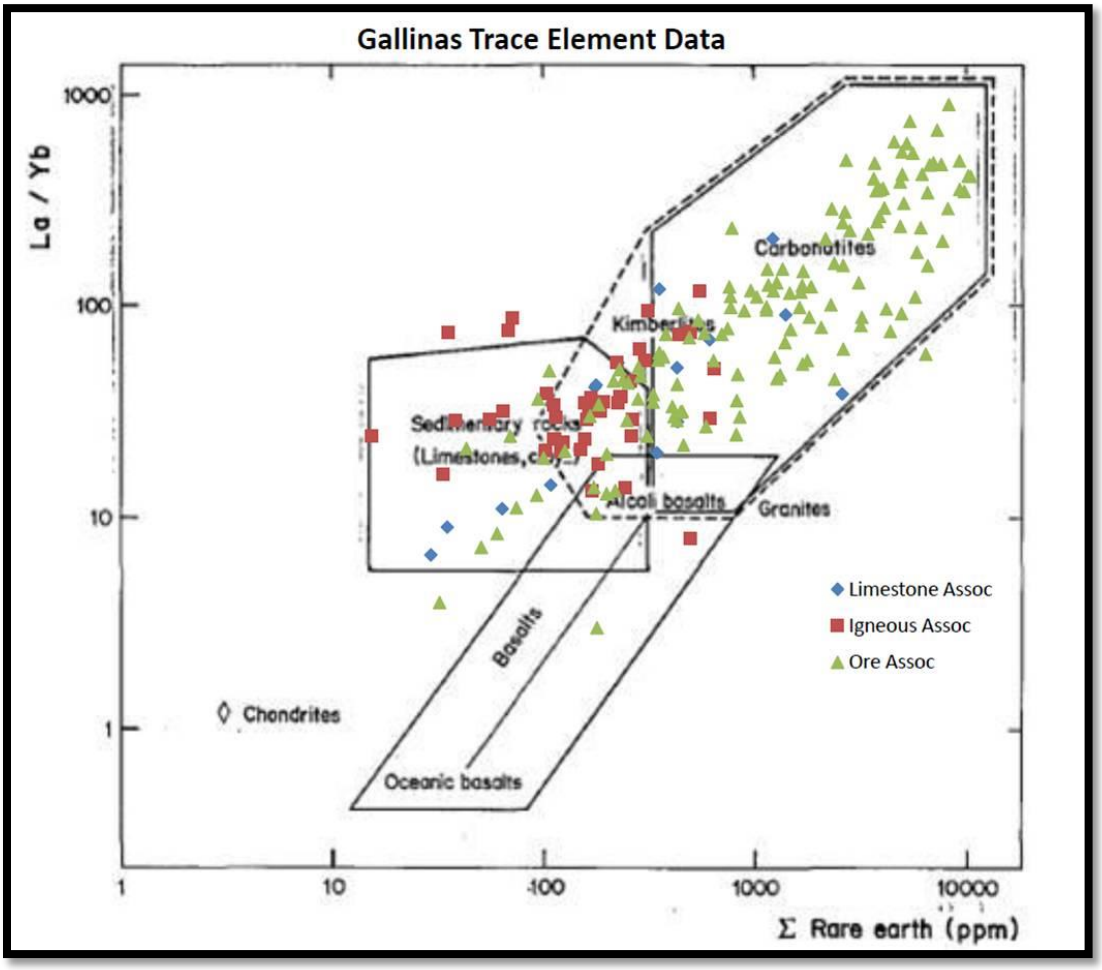

Figure 25. REE metal ratios plotted from whole rock data from the Gallinas Mountains (Schreiner, 1993). In general, rocks associated with mineralization fall within the carbonatite box while sedimentary rocks fall within the sedimentary zone. The positive relationship between total REE content and La/Yb is seen throughout the Gallinas Mountains. Red squares represent data from samples of igneous country rock. Blue diamonds represent data from samples of Yeso limestone and sandstones. Green triangles represent samples of fluorite breccias. Deviations in the data, such as blue diamonds plotting in the carbonatite field, are attributed to a relatively general description of hand samples by Schreiner (1993). Figure modified from: Loubet et al. (1972).

6.6 Metal Ratio Zoning

Zoning of metal ratios can provide insight into many geological and geochemical processes, especially in districts of polymetallic sulfide vein mineralization (Goodell and Petersen, 1974). If sulfide mineralization occurred due to a long lived hydrothermal system then distinct zoning patterns are likely to exist due to lithologic controls or changes in fluid physiochemistry (Goodell and Petersen, 1974). Assay data from grab samples of Schreiner (1993) were used to determine if metal zoning is present in the Gallinas Mountains, Samples from the from the following deposits: M and E No. 13, Old Hickory, Buckhorn, Honeywell, and Red Cloud were used.

Pb/Cu and Cu/Zn increase monotonically in the study area but vary across the spectrum of values within individual deposits (Figures 26 and 27) indicating their use as a zoning indicator is poor. It is important to note that the M and E No. 13 deposit is depleted in Pb, Cu, and Zn relative the "Rough Mountain" deposits by an order of magnitude, and in many cases, depletion is much greater. With respect to the Rough Mountain deposits, Pb/Cu and Cu/Zn ratios overlap indicating that there is no grade zoning within the district. Pb/Cu and Cu/Zn ratios also suggest that the M and E No. 13 is, with respect to sulfide mineralization, much different than other deposits within the district i.e. data fall within their own distinct zone. This depletion provides further evidence that suggests that the M and E No. 13 is genetically different than the "Rough Mountain" deposits.

The causes of the differences between the Rough Mountain and the M & E No. 13 prospect could be reconciled a number of ways: 1) if hydrothermal fluids were spatially isolated then it is likely that they did not interact with similar types of wall rock, 2) if the

M and E No. 13 was derived from a different source rock (primary carbonatite) then the mineralizing fluid contained little sulfur and was distinctly different, and 3) little mixing with Yeso sulfate-bearing groundwater occurred at the M & E No. 13 so few sulfur bearing species are likely to exist at that deposit. Deciphering between these hypotheses us unlikely given the current available data sets and would likely require additional study.

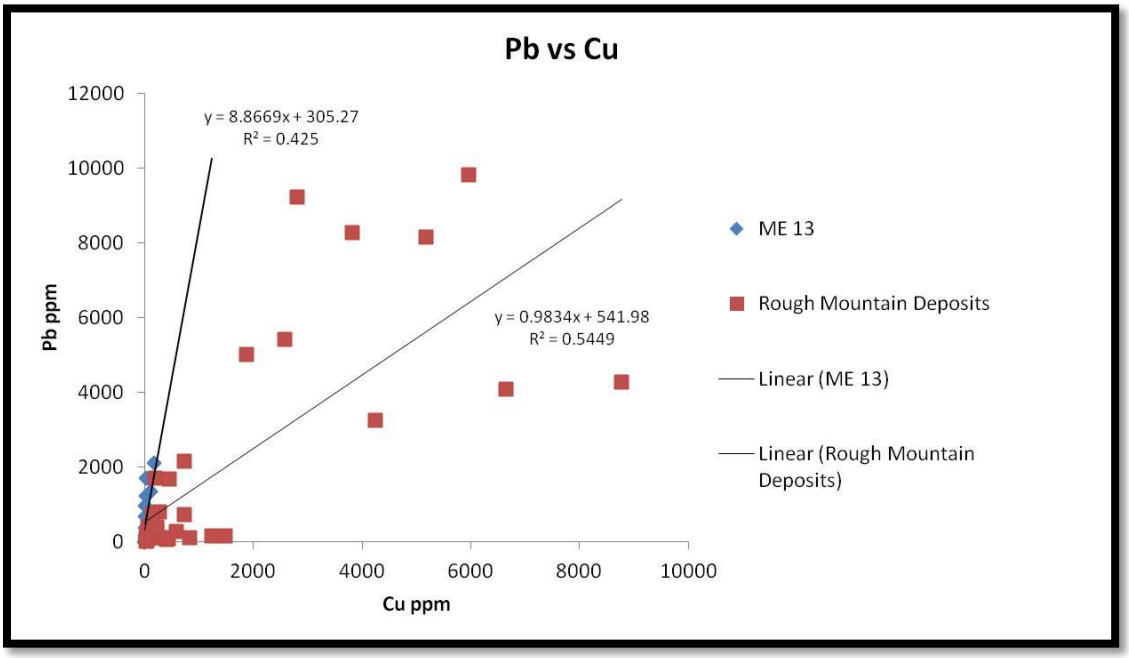

Figure 26. Pb vs. Cu from various deposits within the Gallinas Mountains. The M and E No. 13 prospect values show a different linear trend, and less spread than Rough Mountain deposits. Data from: Schreiner (1993).

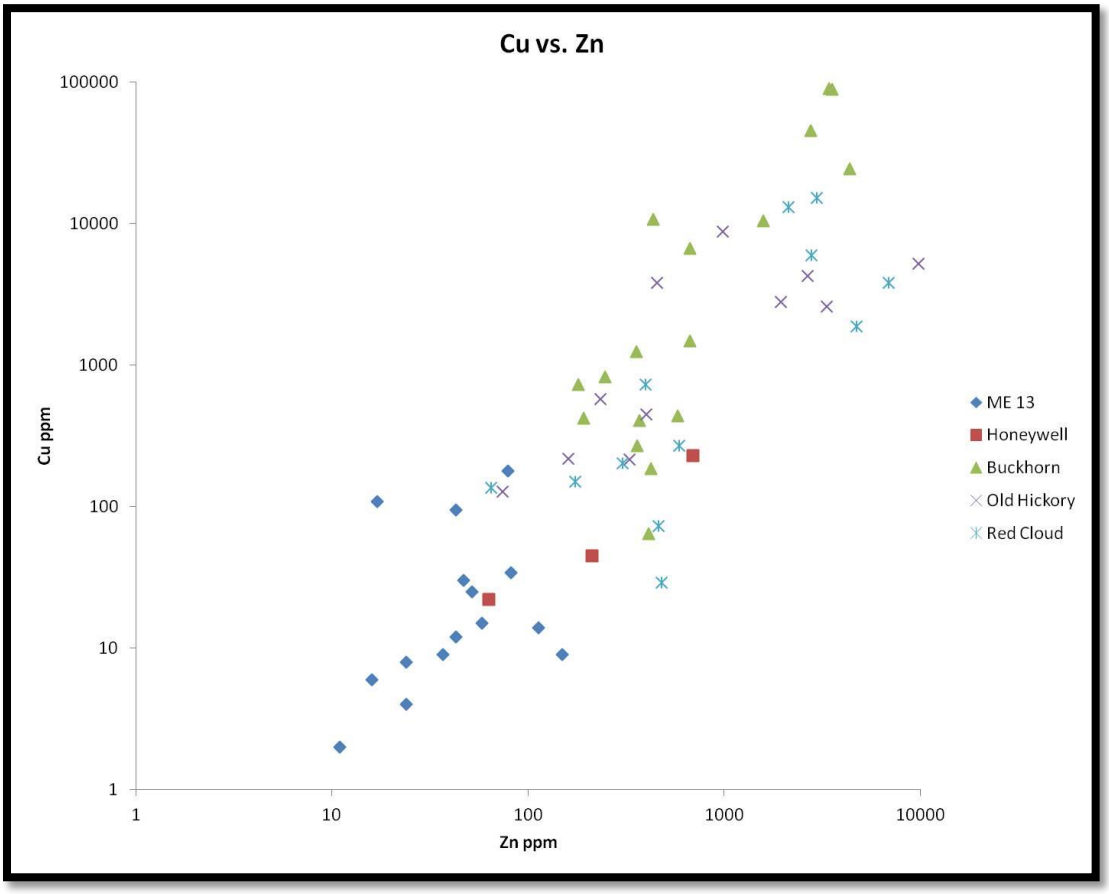

Figure 27. Log Cu vs. Zn from various deposits within the Gallinas Mountains. The M and E 13 prospect metal values are much smaller and cluster together. Rough Mountain deposit values are interspersed indicating a lack of metal zoning. Data from: Schreiner (1993).

6.7 Comparison with other REE Mineralized Systems

A number of other REE occurrences exist within the same trend of alkalic intrusions in eastern New Mexico. These igneous units were also intruded in the Mid-Tertiary (Barker et al., 1977 and Campbell et al., 1994). An examination of their REE mineralogies, intrusion style, and types was carried out during this study (Figure 28).

The lack of other REE bearing phases, specifically REE silicates and phosphates, in the Gallinas Mountains is significant. The main REE bearing mineral in the Gallinas Mountains (bastnaesite) is a carbonate. It is associated with alkaline igneous activity, carbonatites, pegmatites, and rarely detrital deposits however, other minerals which may be expected given the obvious REE enrichment in the district are absent.

In contrast, zirconium mineralogies dominated by the mineral eudialyte $[Na_{15}Ca_6(Fe,Mn)_3Zr_3(Si_{25}O_{73})(O,OH,H_2O)_3(OH,Cl)_2$ are the primary REE bearing phases associated with alkaline igneous complexes nearby in the nearby Wind Mountains (McLemore et al., 1996). The Wind Mountains occur on the southern border of eastern New Mexico along the same alkalic belt and were, like the Gallinas, intruded in the mid Tertiary (Barker et al., 1977).

Allanite $[(Ca,Ce)_2(Al,Fe^{2+},Fe^{3+})_3(SiO_4)_3(OH)]$ is the dominant REE mineral found nearby in the alkaline granite stock of the Capitan Mountains (Campbell et al., 1995) (Figure 28). The Capitan Mountains occur just to the southeast of the Gallinas Mountains and were also intruded during the Mid-Tertiary (Campbell et al., 1994).

A comparison of nearby REE occurrences of similar rock types and ages indicates that the occurrence of bastnaesite in the Gallinas Mountains is unique. This implies that REE mineralization was derived either through a different geochemical process and/or

from a different source than other nearby occurrences. It is likely, given the preponderance of evidence presented in this study, that the Gallinas Mountains contains a carbonatite at depth from which REE and S bearing fluids were derived.

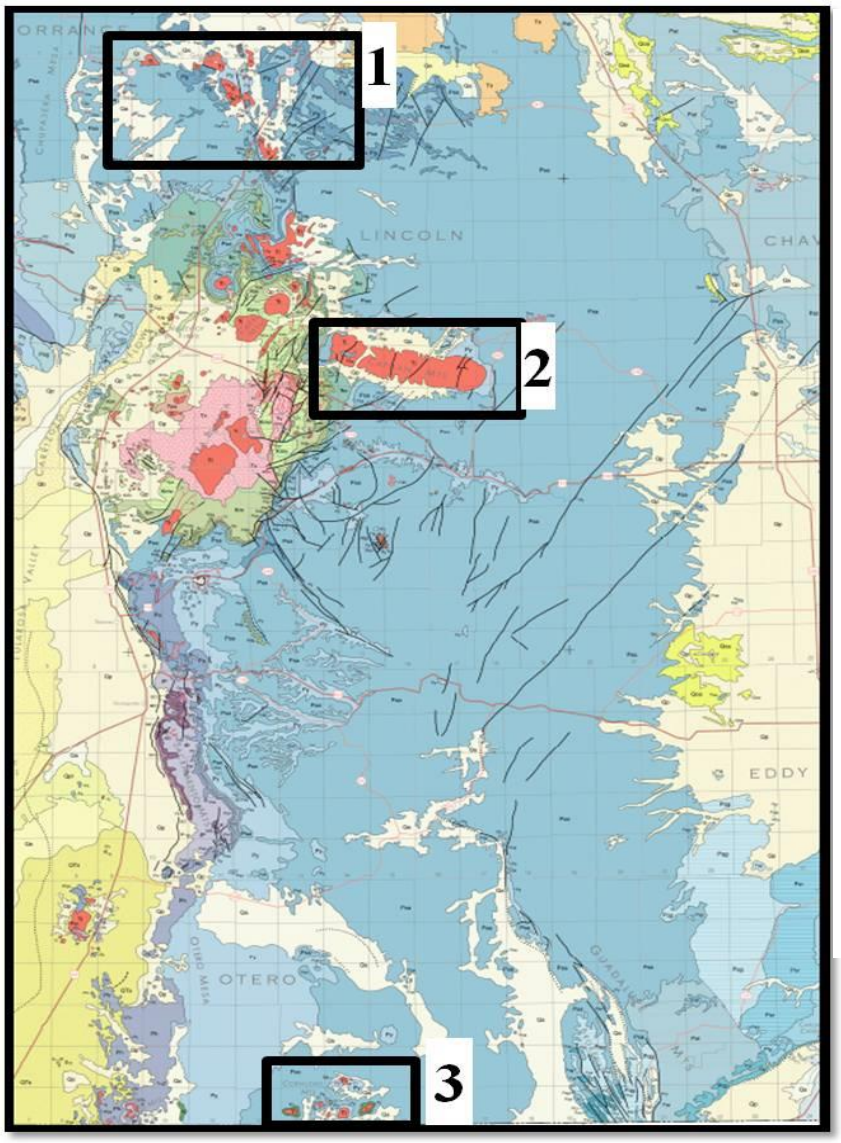

Figure 28. Comparison of REE occurrences.This map of southeastern New Mexico shows the Gallinas Mountains and nearby REE occurrences (outlined by black boxes). Table describes the dominant rock type in each mountain range, dominant REE mineralogies and the REE mineral occurrence. Map modified from: New Mexico Bureau of Geology and Mineral Resources (2003).

Deposit Number	District Name	Dominant Igneous Rock Types	REE Mineralogy	Occurrence
1	Gallinas Mountains	Tertiary trachyte, rhyolite	Bastnaesite	Fluorite Breccia (Laccolith)
2	Capitan Mountains	Tertiary alkaline granite	Allanite	Quartz Veins (Stock)
3	Wind Mountains	Tertiary syenite, nepheline syenite	Eudailyte	Dikes, sills, miarolitic cavaties (Laccolith)

6.8 Genetic Model

Igneous rock types represented in the Gallinas Mountains suggest the presence of a parent magma that differentiated over time (Perhac, 1970). The inferred sequence of events starts with the intrusion of the trachyte and/or the porphyrtitic latite followed by the emplacement of the Gallinas Peak rhyolite. Because of a lack of cross cutting relationships, the sequence presented here is mostly inferred from the differentiation process with the exception of the single andesite dike that may postdate laccolith emplacement and may represent one of the radial dikes of Chamberlin (2009).

Fe-skarn mineralization followed emplacement of the igneous units which was in turn followed by unmineralized brecciation. Fe-skarn mineralization occurred during the emplacement of the trachyte magma where trachyte is in contact with limestone beds of the Yeso (Py). The close association between many fluorite-copper sulfide vein deposits and the Yeso-trachyte (Py-Tt) interface is noteworthy with respect to deposit formation.

Fluorite breccia mineralization followed unmineralized brecciation of trachyte. Na and K metasomatism occurred during mineralized brecciation in isolated zones throughout the district. However, alkaline metasomatism surrounds the M and E No. 13 prospect suggesting that the two events occurred simultaneously. Carbonitization was observed from the M and E No. 13 prospect and Rough Mountain.

A model for the genesis of the Gallinas Mountains REE-Fluorite-Ag-Pb-Cu deposits is proposed (Figure 29). Mineralogical evidence suggests that in the vicinity of Rough Mountain, REE and sulfide ores are genetically related. The presence of agardite, a rare mineral that forms during the oxidation of sulfide minerals in REE rich environments, supports this conclusion.

Stable isotopic evidence from galena, barite, and celestine suggests that oxidation, mixing, and subsequent fluid cooling resulted in the deposition of many ore minerals in the vicinity of Rough Mountain. The role of a carbonatite in the district is much less certain, although stable isotopic evidence from the M and E No. 13 prospect, alteration, fluid inclusion types, trace element ratios and concentrations, and REE mineralogy favor the existence of a carbonatite at depth.

In general, the deposit formation model agrees with that of previous authors (Williams-Jones et al., 2000). It differs in that it offers different types geochemical evidence from other localities within the district which were independently evaluated with respect to deposit formation. Additionally, this study focused not only on the mechanism of deposition, but the relationship between sulfide and REE mineralization and provided evidence that some constituents of deposits were derived from a carbonatite. With respect to the presence of a carbonatite at depth, separately, each piece of evidence is not conclusive, however; the weight of the evidence suggests that a carbonatite is present at depth and is responsible for REE mineralization.

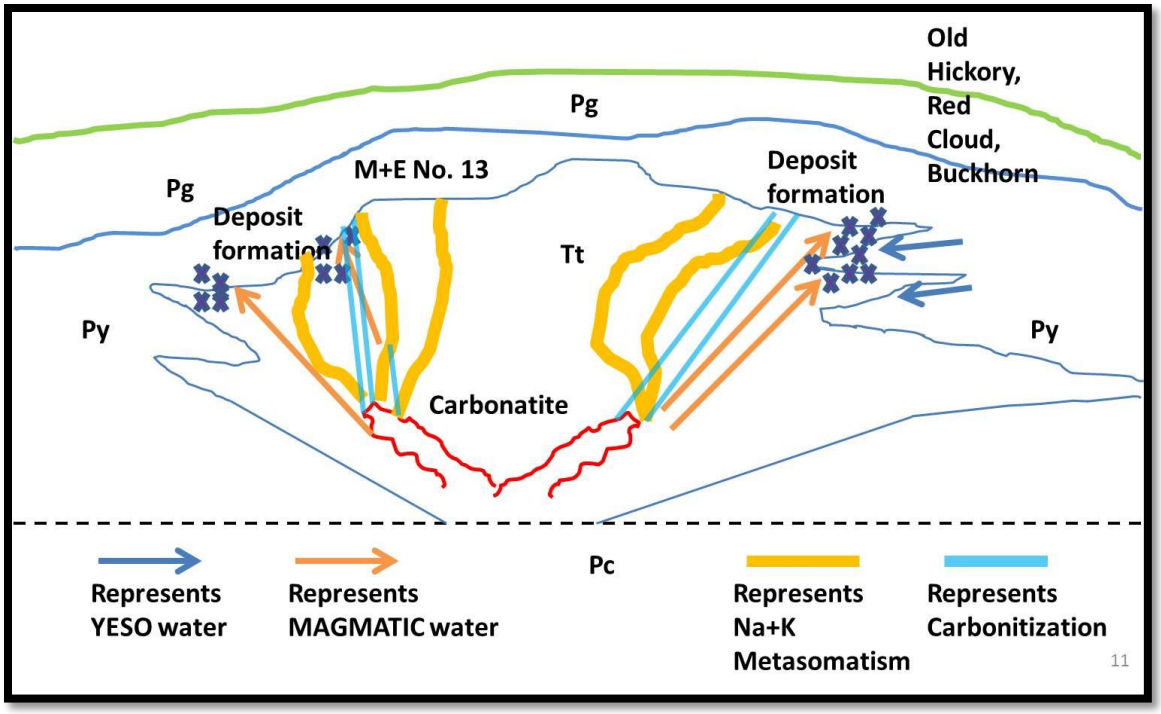

Figure 29. Proposed model of REE ore genesis in the Gallinas Mountains, NM. Trachyte was intruded into overlying, horizontal, sedimentary beds. This was followed by the formation of iron skarns in some areas near the Trachyte-Yeso (Tt-Py) contact. Brecciation of trachyte was closely followed by mineralized brecciation. It is thought that brecciation occurred due to fluid overpressure. The weight of the evidence suggests that a carbonatite exists at depth and was the source of REE. Reduced sulfur could have been derived from either the trachyte intrusion or a carbonatite. In the deeper parts of the system, the source of sulfate remains ambiguous. As hydrothermal fluids migrated upward, ore deposition began due to fluid cooling. Fluid cooling increased near the Trachyte-Yeso (Tt-Py) contact and, in the Rough Mountain deposits, mixing of magmatic and Yeso formation waters occurred.

7. CONCLUSIONS AND IMPLICATIONS

Given the mineralogy, fluid inclusions, REE trace element diagrams, trace element ratios, carbon and oxygen isotopic ratios, sodic and potassic metasomatism, abundance of REE and F, and a comparative study of nearby REE occurrences, the existence of a carbonatite fluid source is inferred. This statement is speculative however the preponderance of geological evidence suggests that a carbonatite source is the simplest and most reasonable conclusion. This study further suggests that a REE exploration program merits further deep drilling particularly in the vicinity of Red Cloud and the M and E No. 13 prospect to expose a primary REE source.

Hydrothermal REE-fluorite-sulfide deposits are unique occurrences. The model presented here speculates that the existence of this type of occurrence may be the upper reaches of a hydrothermal system established by a carbonatite at depth. The overall conclusions of this study are as follows:

1) REE mineralization is associated with sulfide mineralization in the Gallinas Mountains. This is evidenced by the occurrence of sulfide and REE within the same deposits. Evidence for the existence of a fluid that was both REE and sulfide bearing exists in the mineral agardite. Stable isotope evidence indicates a magmatic REE and sulfur source that is likely a carbonatite.
2) Microthermometry and stable isotope data indicate that magmatic fluid mixed with formation waters of the Yeso. Previous fluid inclusion studies call upon mixing to explain REE deposition and deposit formation. Stable isotope ratios (sulfide and sulfate) indicate that in the vicinity of Rough Mountain, fluid mixing has occurred.

3) The preponderance of chemical evidence suggests that mineralization may have been derived from a carbonatite. Mineralogy and trace element trends indicate that mineralization is associated with a carbonatite source. Carbon, sulfur, and oxygen stable isotope values also indicate that the source of REE bearing fluids was a carbonatite.

8. REFERENCES

Allen, M.S., and Foord, E.E., 1991, Geological geochemical and isotopic characteristics of the Lincoln County porphyry belt, N.M.: Implications for regional tectonics and mineral deposits: New Mexico Geological Society Fall Field Conference Guidebook, v. 42, p. 97-115.

Allen, M.S., and McLemore, V.T., 1991, The geology and petrogenesis of the Capitan pluton, New Mexico: New Mexico Geological Society Fall Field Conference Guidebook, v. 42, p. 115-127.

Anthony, J., Bideaux, R., Bladh K., and Nichols, M., 2003, *Handbook of Mineralogy*. 1st ed, v. 1, Tucson: Mineral Data Publishing, 597 p., Print.

Barker, D.S., Long, L.E., Hoops, C.K., Hodges, F.N., 1977, Petrology and Rb-Sr isotope geochemistry of intrusions in the Diablo Plateau, Northern Trans-Pecos magmatic province, Texas and New Mexico: Geological Society of America Bulletin, v. 88, p. 1437-1446.

Campbell, A.R. and Lueth, V.W., 2008, Isotopic and textural discrimination between hypogene, ancient supergene, and modern sulfates at the Questa mine, New Mexico: Applied Geochemistry, v. 23, p 308-319.

Campbell, A.R., Banks, D.A., Phillips, R.S., and Yardley, B.W.D., 1995, Geochemistry of Th-U-REE mineralizing magmatic fluids, Capitan Mountains, New Mexico, USA: Economic Geology, v. 90, p. 1271-1287.

Campbell, A.R., Heizler, M.T., and Dunbar, N.W., 1994, $^{40}Ar/^{39}Ar$ dating of fluid inclusions in quartz from the Capitan pluron, NM [abs]: Pan American Current Research on Fluid Inclusions V, Cuernavaca, Mexico, May 1994, Proceedings, p. 11.

Carmichael, I.S.E., Turner, F.J. and Verhoogen, J., 1974, *Igneous petrology*: New York, McGraw-Hill, 739 p., Print.

Deines, P., 1967, Stable carbon and oxygen isotopes of carbonatite carbonates and their interpretation, Ph. D. thesis, The Pennsylvania State University, University Park.

Deines, P., 1989, Stable isotope variations in carbonatites. *Carbonatites: Genesis and evolution*, 301-359.

DeMark, R.S., 1980, The Red Cloud Mines, Gallinas Mountains, New Mexico: Mineralogical Record, v. 11, p. 69-72.

Field, C.W., 1966, Sulfur isotopic method for discriminating between sulfates of hypogene and supergene origin, Economic Geology, v. 61, 1428-1435.

Griswold, G.B., 1964, Mineral resources of Lincoln County: New Mexico Geological Society Guidebook, Fifteenth Field Conference, Ruidoso County, p. 148-151.

Goodell, P.C. and Petersen, U., 1974, Julchani mining district, Peru: A study of metal ratios, Economic Geology, v. 69, p. 347-361.

Goodell, P.C., Lueth, V.W., and Willsie, T.C., The Chess Draw depression, Otero County, New Mexico: A hydrothermally-altered, sublaccolithic, alkalic system, New Mexico Geological Society Guidebook, v. 53, p. 357-361.

Hanor, J., 2000, Barite-Celestine geochemistry and environments of formation, in Reviews in Mineralogy & Geochemistry, v. 40, 193-275.

Kelly, V.C., 1946, Geologic and topographic map of the eastern Gallinas Mountains, Lincoln County, New Mexico: U.S. Geol. Survey, Strategic Minerals Inv. Prelim. Map 3-211.

Kelly, V.C., 1949, Geology and Economics of New Mexico iron-ore deposits: New Mexico University Publication, n. 2, 246 p.

Kelly, V.C., and Thompson, T.B., 1964, Tectonics and general geology of the Ruidoso-Carrizozo region, central New Mexico: New Mexico Geological Society Guidebook, v. 15, p. 110-121.

Kim, S.T., and O'Neil, J.R., 1997, Equilibrium and nonequilibrium oxygen isotope effects in synthetic carbonates: Geochimica et Cosmochimica Acta, v. 61, p. 3461-3475.

Lindgren, W., Graton, L.C., and Gordon, C.H., 1910, The ore deposits of New Mexico: U.S. Geological Survey, Professional Paper 68, 361 p.

Loubet, M., Bernat, M., Javoy, M., and Allegre, C.J., 1972, Rare earth contents in carbonatites: Earth and Planetary Science Letters, v. 14, p. 226-232.

Li, Y.B. and Liu, J.M., (2006), Calculation of sulfur isotope fractionation in sulfides: Geochimica et Cosmochimica Acta, v. 70, p. 1789-1795.

Long, K.R., Van Gosen, B.S., Foley, N.K., Cordier, D., 2010, The principal rare earth elements deposits of the United States–A summary of domestic deposits and a global perspective: United States Geological Survey Scientific Investigations Report 2010–5220, 104 p.

Lueth, V.W., Rye, B.O., Peters, L., 2005, "Sour Gas" Hydrothermal jarosite: Ancient to modern acid sulfate mineralization in the southern Rio Grande Rift: Chemical Geology, v. 215, p. 339-360.

Mariano, A.N., 1989, Nature of economic mineralization in carbonatites and related rocks. *Carbonatites: Genesis and evolution*, 149-172.

McLemore, V.T., 1991, Gallinas Mountains mining district, New Mexico: New Mexico Geological Society Guidebook: Forty-Second Field Conference, Sierra Blanca, Sacramento, Capitan Ranges, p. 63-64.

McLemore, V.T., 2010, Geology and mineral deposits of the Gallinas Mountains, Lincoln and Torrance counties, New Mexico; Preliminary Report: New Mexico Bureau of Geology and Mineral Resources Open-file Report OF-532, 92 p.

McLemore, V.T., Lueth, V.W., Pease, T.C., and Guilinger, J.R., 1996, Petrology and mineral resources of the Wind Mountain laccolith, Cornudas Mountains, New Mexico and Texas: The Canadian Mineralogist, v. 34, p. 335-347.

Mitchell, R. H., and Krouse, H.R., 1975, Sulphur isotope geochemistry of carbonatites: Geochimica et Cosmochimica Acta, v. 39, p. 1505-1513.

Mitzutani, Y. (1972). Isotopic composition and underground temperature of the Otake geothermal water, Kyushu, Japan: Geochemical Journal, 6, pp. 67-73.

Ni, Y., Hughes, J.M., Mariano, A.N., 1995, Crystal chemistry of the monazite and xenotime structures: American Mineralogist, v. 80, p. 21-26.

Ohmoto, H. and Rye, R.O., 1979, Isotope of sulfur and carbon, in Barnes, H. L. Ed., Geochemestry of Hydrothermal deposits, John Wiley & Sons, p. 509-567.

Ohmoto, H. and Lasaga, A.C., 1982, Kinetics of reactions between aqueous sulfates and sulfides in hydrothermal systems: Geochimica et Cosmochimica Acta, v. 46, p. 1727-1745.

Perhac, R.M., 1970, Geology and mineral deposits of the Gallinas Mountains, Lincoln and Torrance Counties, New Mexico: New Mexico Bureau of Mines and Mineral Resources Bulletin 95, 51 p.

Perhac, R.M., and Heinrich, E.W., 1964, Fluorite-bastnaesite deposits of the Gallinas Mountains, New Mexico, and bastnaesite paragenesis: Economic Geology, v. 59, p. 226-239.

Rothrock, H.E., Johnson, C.H., and Hahn, A.D., 1946, Fluorspar resources of New Mexico, N. Mex. School of Mines, State Bur. Mines and Mineral Res. Bull. 21.

Rye, R.O., 1993, The evolution of magmatic fluids in the epithermal environment: The stable isotope perspective: Economic Geology, v. 88, p. 733-753.

Sampson, I.M., Williams-Jones, A.E., Weining, L., 1995, The chemistry of hydrothermal fluids in carbonatites: Evodence from leachate and SEM-decrepitate analysis of fluid inclusions from OKA, Quebec, Canada: Geochimica et Cosmochimica Acta, v. 59, p. 1979-1989.

Scholle, P., 2003,Geologic Map of New Mexico, New Mexico Bureau of Mines and Mineral Resources.

Schreiner, R.A., 1993, Mineral investigation of the rare-earth-element bearing deposits, Red Cloud mining district, Gallinas Mountains, Lincoln County, New Mexico: U.S. Bureau of Mines, Open File Report 99-93, 189 p.

Seal , R.R. II, Alpers, C.N., Rye, R.O., 2000, Stable isotope systematic of sulfate minerals: Reviews in Mineralogy and Geochemistry, Mineralogical Society of America, v. 40, p. 541-593.

Sharp, Zachary, 2007. *Principles of Stable Isotope Geochemistry*. Pearson Prentice Hall.

Soulé, J.H., 1943, Gallinas fluorspar deposits, Lincoln County, New Mexico: U.S. Bureau of Mines War Minerals Report 125, 14 p. 22.

Soule, J.H., 1946, Exploration of the Gallinas Fluorspar deposits, Lincoln County, New Mexico: U.S. Bureau of Mines War Minerals Report of Investigation 3854, 25 p.

Truesdel, A.H., 1974, Oxygen isotope activities and concentrations in aqueous salt solutions at elevated temperature: consequences for isotope geochemistry: Earth and Planetary Science Letters, v. 23, p. 387-396.

Van Dongen, M., Weinberg, R.F., Tomkins, A.G., 2010, REE-Y, Ti, P Remobilization in magmatic rocks by hydrothermal alteration during Cu-Au deposit formation: Economic Geology, v. 105, p. 763-776.

Woodward, L.A., and Fulp, M.S., 1991, Gold mineralization associated with alkali trachyte breccia in the Gallinas Mountains mining district, Lincoln County, New Mexico: New Mexico Geological Society Guidebook: Forty-Second Field Conference, Sierra Blanca, Sacramento, Capitan Ranges, p. 323-325.

Zheng Y.-F. (1999). Oxygen isotope fractionation in carbonate and sulfate minerals: Geochemical Journal, 33, p. 109-126.

APPENDIX 1

Thin Section Petrography

Figure 1: FOV: 1.8mm xpl. Edge of myrolitic cavity filled with quartz. Notice termination of feldspar grains indicative open space filling. Scale bar is 1 mm.

Gallinas Peak Rhyolite, High

Mineralogy: Porphyritic quartz dominates the macroscopic mineral assemblage in this sample. Rare agerine-augite and riebekite is present (<1%). Muscovite is an accessory phase (<3%). Groundmass is extremely fine grained and composed of both quartz and orthoclase.

Alteration: Alteration is not as pronounced in this sample as it is in Gallinas Peak Mid and Gallinas Peak Low samples. Whole, unaltered phenocrysts of sanidine can be seen although many feldspar cores have been altered to clay.

Textural Relationships: The texture present in this sample is that of a typical porphyritic rhyolite. Flow texture is all but absent. This may be due to the fine grained nature of the groundmass or lack of abundance of phenocrysts. Myrolitic cavities, are filled mostly with quartz. Edges of myrolitic cavaties tend to show abundant euhedral feldspars.

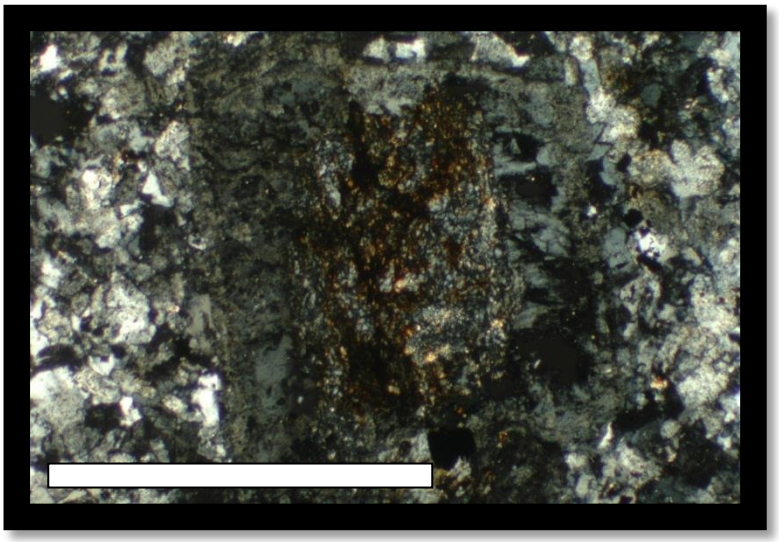

Figure 2: FOV: 1.8mm, xpl. Altered sanidine crystal. Carlsbad twinning is evident under xpl. Core of crystal was in the process of being altered to clay. Alteration of the core in this case is incomplete. Scale bar is 1 mm.

Gallinas Peak Rhyolite, Middle

Mineralogy: Quartz is very abundant (>70%). Riebeckite present. Groundmass is made up of grains that are .1-.3mm in size. Orthoclase (Carlsbad twinned) and quartz

predominate. Biotite is present in small amounts ~1% and is usually surrounded by hematite staining. Aegerine-Augite is present as an accessory phase.

Alteration: Sanidine phenocrysts are either wholly altered or partially altered (from core) to clay. One cluster of sanidine crystals contained a small crystal of aegerine-augite at its base.

Textural Relationships: Quartz phenocrysts and sanidine phenocrysts are present within a groundmass containing fine grained orthoclase and quartz crystals. Opaque fluorite is present (~1.5%) throughout the entire section. Minor biotite is also present in the groundmass located between grains. The groundmass grains are generally .1-.3mm in diameter while biotite (~1%) is slightly smaller.

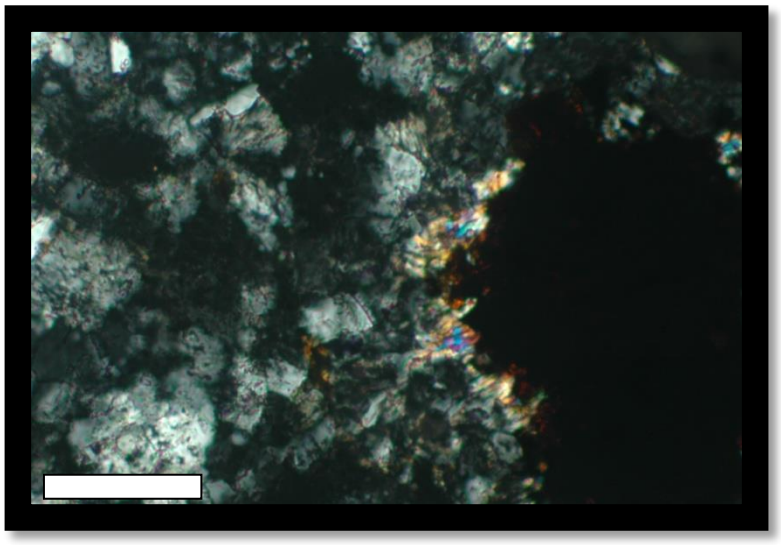

Figure 3: FOV: 0.89mm, xpl. Biotite grains surrounding an opaque mineral (magnetite). Scale bar is 0.25 mm.

Gallinas Peak Rhyolite, Low

Mineralogy: Microcline phenocrysts present with poor Tartan Plaid twinning ~1.8mm in long direction (~15%). Sanidine phenocrysts also abundant but less so than microcline. Fine grained quartz and sanidine crystals make up the groundmass. Fluorite is common in feldspar phenocrysts as ~0.1mm crystal aggregates. Microcline phenocrysts commonly contain fluid inclusions. Riebekite and agerine-augite are present as accessory phases. Biotite and magnetite grains are dispersed throughout the sample in small amounts.

Alteration: Microcline is relatively unaltered when compared to sanidine. The sanidine phenocrysts have been largely altered to clay. Biotite can often be found adjacent to magnetite grain boundaries and extends out ~<0.3mm.

Textural Relationships: Altered porphyritic sanidine clasts (~0.4mm) in an aphanitic groundmass. Amigduoidals are generally filled with microcline (~0.4mm) with abundant fluid inclusions and accessory fluorite. Groundmass is made up of small quartz and feldspar (probably sanidine) grains.
Picture Numbers: 10,11 xpl: FOV: 0.9mm, Biotite grains surrounding an opaque mineral (thought to be magnetite).

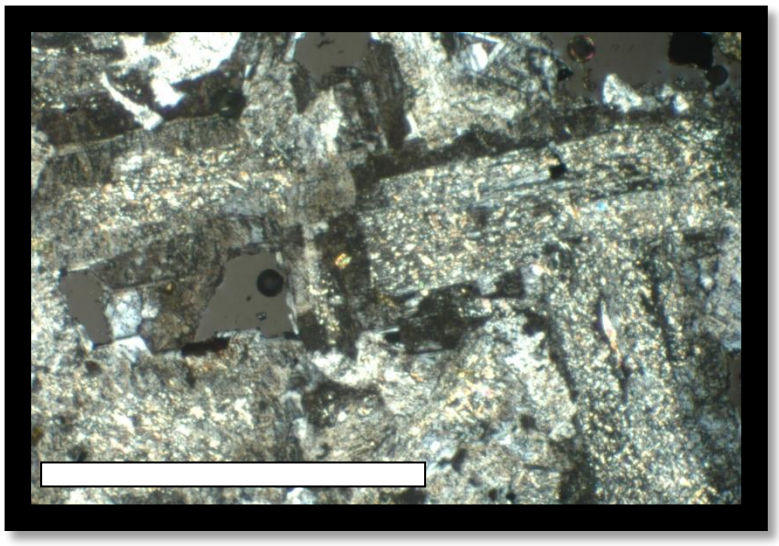

Figure 4: FOV: 1.8mm xpl. Orthoclase grains partially altered to clay. Scale bar is 1 mm.

Microsyenite-1, North of Yeso Hill

Mineralogy: Feldspars (albite and orthoclase) make up almost the entire sample (>90%). Quartz is not present. Aegerine-augite is present as an accessory phase. It is denoted by its blue color in ppl and second order birefringence interference colors in xpl. Accessory biotite with rutile inclusions present in small amounts (<2%). Magnetite forms euhedral grains is disupursed throughout sample and represents ~3% of entire section. It tends to cluster near biotite grains.

Alteration: Almost all of the orthoclase grains a moderate degree of seritization to clay in the core. The rims on orthoclase grains are often albitized. These rims have not been altered to clay.

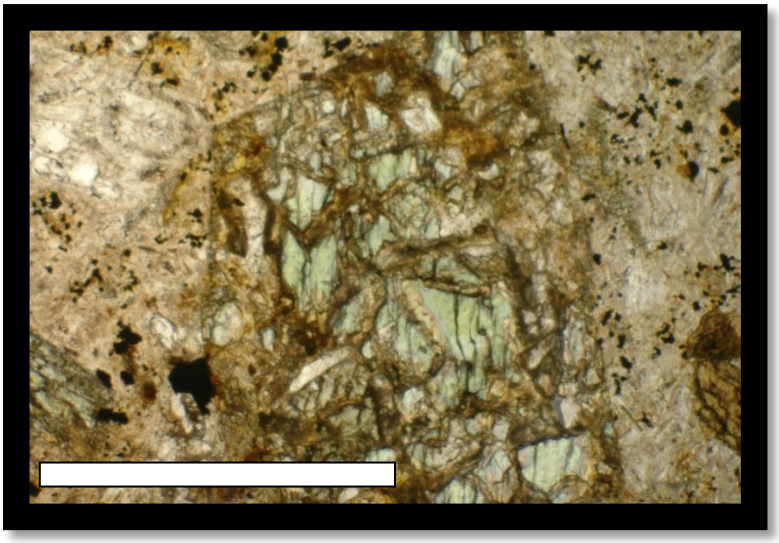

Figure 5a: FOV: 2mm ppl. Rare pyroxene grain. Scale bar is 1 mm.

Textural Relationships: Texture is described as holocrystalline and equigranular. Average grain size is ~0.7mm. Phenocrysts are generally ~<1.5mm.

Andesite Dike, Gallinas

Peak Road

Mineralogy: Euheadral hornblende is the main mafic phase that is macroscopically visible followed to a lesser extent

by plagioclase. Small euhedral grains Biotite, and magnetite are ubiquitous throughout the sample. Quartz is present in small amounts. Hydrothermal (Perhac). Minor apatite is present. Pyroxene (either augite or diopside) is present in small amounts ~<1% and is often altered to clay.

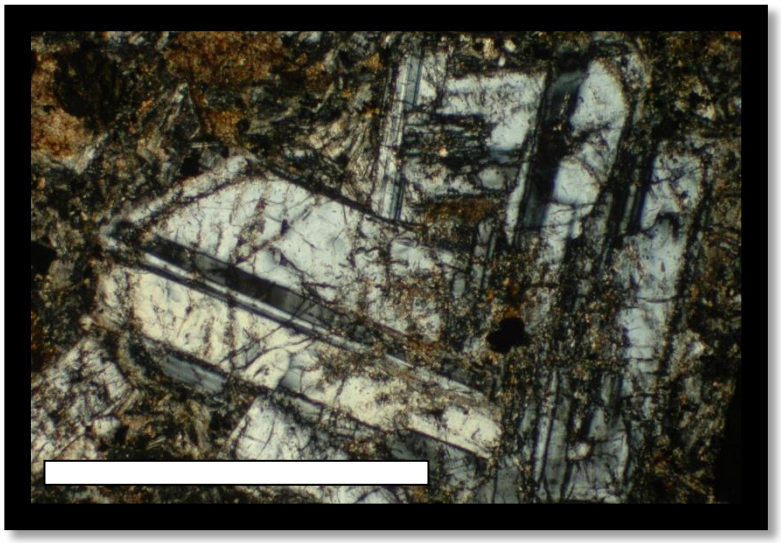

Figure 5b: FOV: 1.8mm xpl. Shows inter-grown plagioclase grains with clay alteration in the cores. Characteristic carlsbad twinning of albite. Scale bar is 1 mm.

Alteration: This sample is heavily altered. It was taken from the middle of the dike away from the edges. The edges are extremely friable and the rocks there have a very chalky feel to them indicating intense hydrothermal alteration. Hornblende crystals seem relatively fresh and unaltered when compared to the feldspars. The small grains that make up the groundmass are altered to some extent. Alteration in larger feldspar crystals is variable. Generally, the crystal center is altered to clay and the rims remain.

Textural Relationships: Trachytic texture is evident from alignment of feldspar and elongate hornblende phenocrysts.

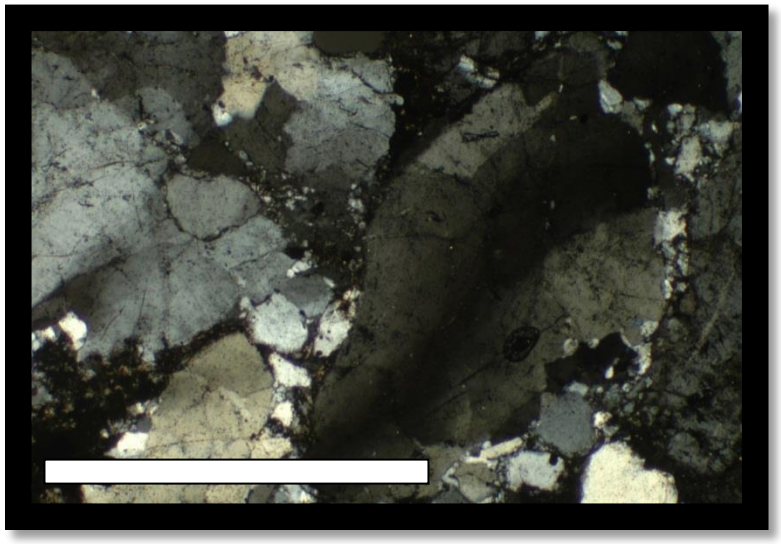

PC Deadwood, Precambrian Granite

Mineralogy: Quartz and Microcline predominate in this sample. The sample shows a very minor mafic constituent with trace amounts of magnetite. No biotite was seen in this sample. A ~0.6mm vein of muscovite bisects the section. Accessory rutile is

present along with zircon and apatite.

Figure 6: FOV: 1.8mm xpl. Example of undulatory extinction in a quartz grain. Note the lack of alteration, lack of crystal faces, and equigranular nature. Scale bar is 1 mm.

Alteration: This is a good example of very lightly altered granite. There is minor hematite/limonite staining but other than that the minerals are intact. Some quartz crystals show undulatory extinction indicating an exposure to some level of pressure and temperature at some point during its history.

Textural Relationships: This is an example of an alliotriomorphic coarse grained granite. There were no (none observed) crystal faces in thin section.

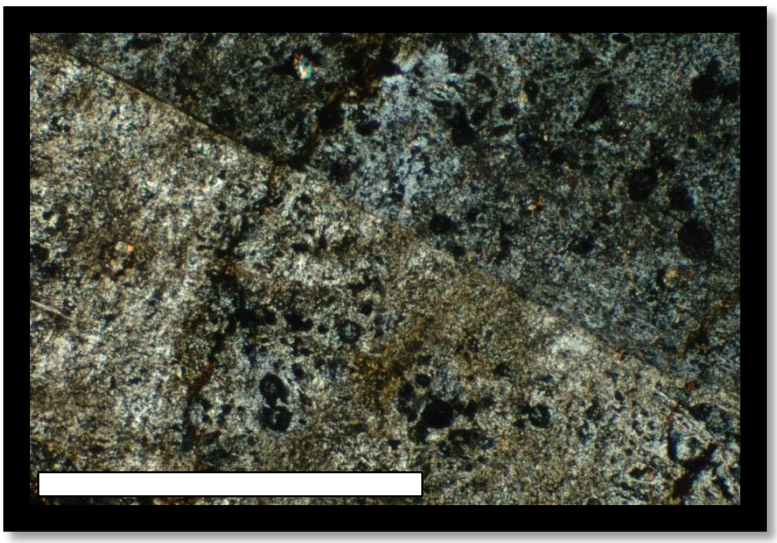

Figure 7: FOV 1.8mm. xpl. Altered sanidine phenocryst with remnant twinning. Scale bar is 1 mm.

GRT-3, Altered

Trachyte

Mineralogy: Sanidine and sericite (fanned needle aggregate) dominate the mineralogy of this sample of altered trachyte. The sample is highly altered (duteric) and mineralogy is difficult to discern. The thin section has a porphyritic texture to it and there is very minor <1% quartz.

Alteration: The most characteristic alteration feature of this section is the heavy alteration of feldspars to needle aggregates of sericite/clay. Quartz grains are unaltered. Sanidine phenocrysts (twinning noted) have been completely altered to clay with rare remnant twinning.

Textural Relationships: Original rock was porphyritic (probably trachyte). Alteration is so heavy that it is very hard to discern what original textures may have looked like. Texture now shows a sericite (needle) aggregate matrix hosting clay phenocrysts.

CM-3, Cougar Mountain

Mineralogy: Plagioclase dominates this sample and is extremely abundant as euhedral phenocrysts commonly up to ~0.75 cm along c-axis. Hornblende occurs as euhedral

grains commonly within plagioclase phenocrysts although not always. It is olive green-shady grass green in ppl and exhibits characteristic 60°-120° cleavage when viewed down the c-axis. Groundmass extremely fine grained and consists of orthoclase and quartz. Accessory phases include apatite, zircon and magnetite. Sphene was noted by Perhac (1970) but was not seen by the author.

Figure 8: FOV 1.8mm xpl. Example of poikiltic texture with hornblende crystal completely surrounded by plagioclase phenocryst. 23, FOV 1.8mm xpl. Alteration rims on plagioclase phenocrysts. Scale bar is 1 mm.

Alteration: Alteration is limited mostly to the plagioclase phenocrysts and occurs there to varying degrees. Some alteration to of plagioclase to white phyllosilicates has occurred on the rims of all phenocrysts in this thin section. Sometimes the entire phenocryst is altered to white phyllosilicate and sometimes only the very edge of the crystal is altered. Hornblende crystals are relatively unaltered.

Textural Relationships: Perhac (1970) describes hornblendes as poikilitic (numerous grains of various minerals in random orientation are completely enclosed within large, optically continuous crystals of different composition). This is true (see picture 22) but what does it mean? Nucleation of phenocrysts around already crystalized hornblende. Groundmass is cryptocrystalline. Quartz crystals are subhedral ~.25mm in diameter. Phenocrysts show no preferential crystallization patterns suggesting an intrusive nature. Its isolation to the NE of the main trachyte flows should provide some insight into magma evolution in this area.

Outlaw 3 Hole 2, 267.5'

Mineralogy: Anhedral to seldom subhedral orthoclase and albite phenocrysts max ~0.25 cm more commonly ~2 mm dominate this sample. Tartan plaid twinning is common in phenocrysts. Groundmass consists of albite and orthoclase. Quartz is rare. Accessories include magnetite/hematite, zircon. No hornblende or aegerine-augite was seen in this section.

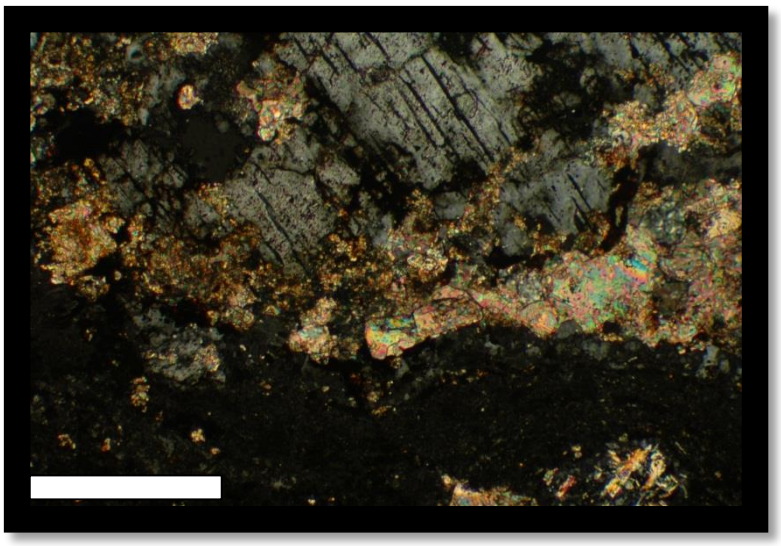

Figure 9: FOV: 0.89 mm, xpl. Alteration front. High birefringence minerals are feldspars altered to clay and white phyllosilicates. Scale bar is 0.25 mm.

Alteration: Hematite staining is abundant. Alteration front is apparent and abrupt one side of the section. Section undergoes a color change from light grey to light brown on one side. The light-grey (relatively unaltered) section contains sparse alteration of feldspars to white phyllosilicate. (See pic 24 of alteration front). Alteration zone has gone almost completely to clay and phyllosilicate. Quartz grains are unaltered and relatively easy to see under xpl in the alteration/oxidation zone.

Textural Relationships: Unaltered section of sample is holocrystalline with anhedral to subhedral phenocrysts. Groundmass consists of microcrystalline interlocking anhedral grains. Lack of crystal faces and textural relationship between phenocrysts and groundmass suggests incomplete crystallization.

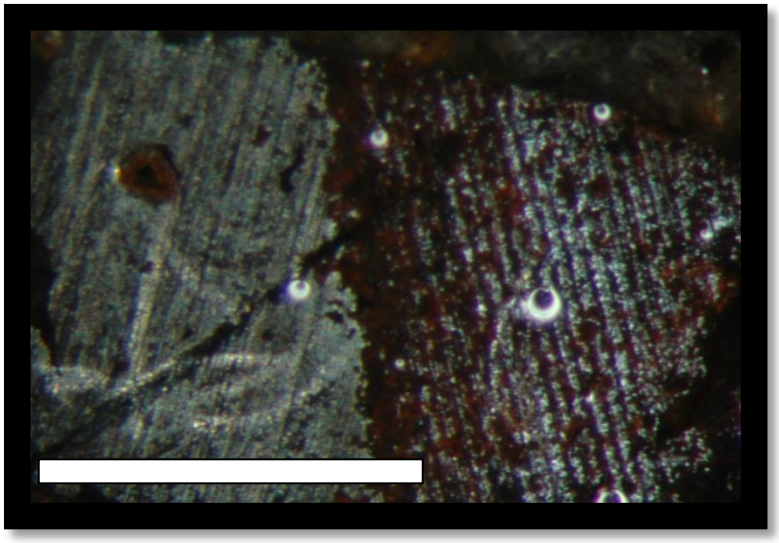

Figure 10: FOV, 1.8mm, xpl. Terminated orthoclase crystal, larger stained orthoclase crystal in a very fine grained groundmass. Scale bar is 1 mm.

Fenite Zone (1)

Mineralogy: Sample is dominated by orthoclase feldspar phenocrysts. The groundmass is extremely fine grained and crystals cannot be differentiated even under 40x. Orthoclase phenocrysts make up about 30% of the entire sample and generally around 2 mm in size.

Alteration: Heavy iron oxide staining can be seen under ppl. Orthoclase phenocrysts are often euhedral and lack any sort

of rim. Clay alteration of phenocrysts is minor. This sample was taken from a “fenite” zone and it is assumed that the entire sample was flooded with potassium at some point during its history.

Textural relationships: Textures are extremely hard to discern because of the heavy iron oxide staining.

APPENDIX 2

Fluid Inclusion Descriptions and Photomicrographs

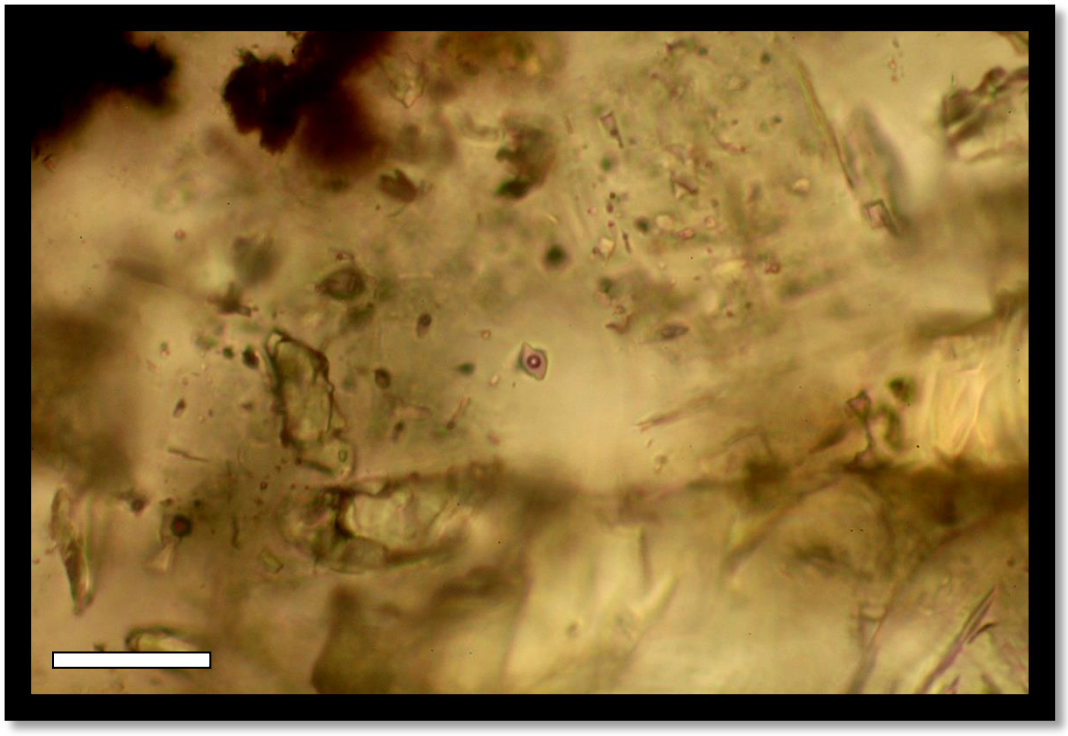

Sample: HTP-1
Deposit: Hill Top Prospect (Honeywell)
Mineral Type: Purple Fluorite (R2 - Same as fine grained purple fluorite at Red Cloud)
Fluid Inclusion Descriptions: L-V
Fluid Inclusion Type: Primary
Magnification: 40x. Scale bar is 12.5 µm.

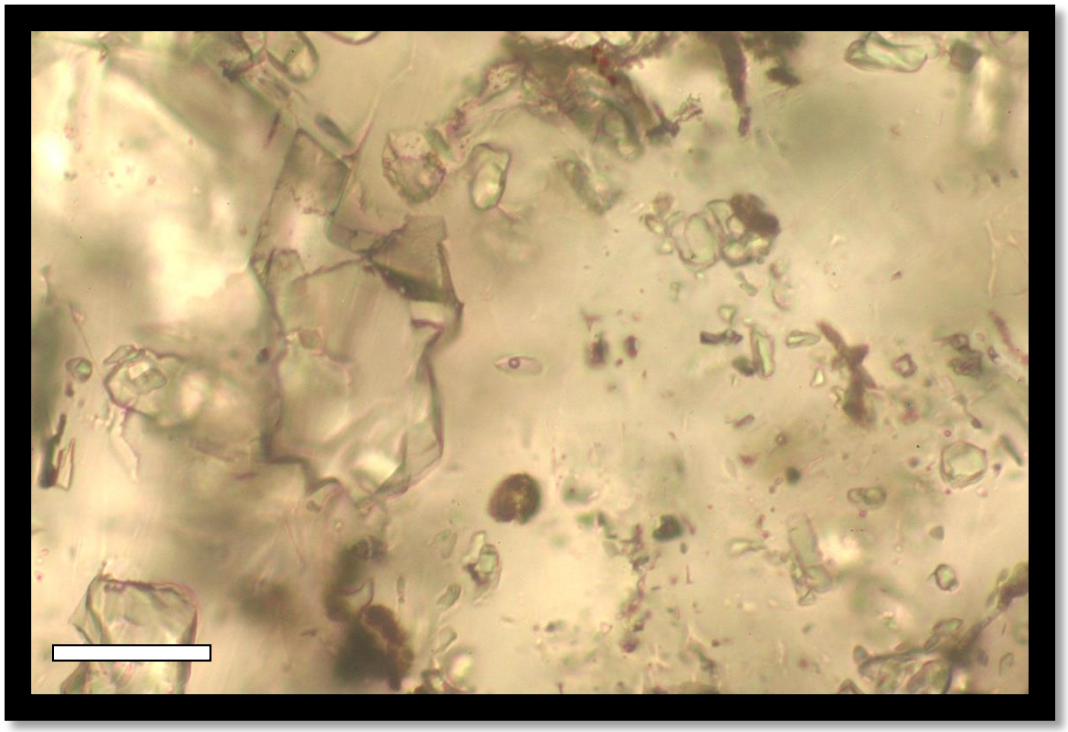

Sample: HTP-1
Deposit: Hill Top Prospect (Honeywell)
Mineral Type: Purple Fluorite (R2 - Same as fine grained purple fluorite at Red Cloud)
Fluid Inclusion Descriptions: L-V
Fluid Inclusion Type: Primary
Magnification: 40x. Scale bar is 12.5 µm.

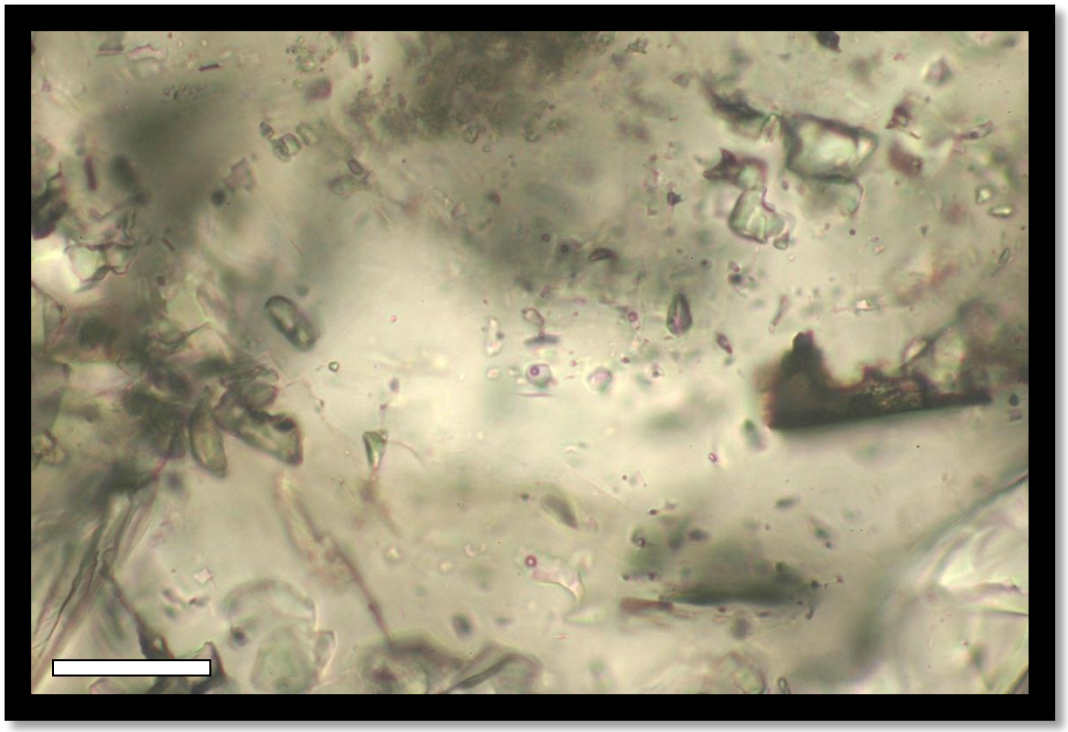

Sample: HTP-1
Deposit: Hill Top Prospect (Honeywell)
Mineral Type: Purple Fluorite (R2 - Same as fine grained purple fluorite at Red Cloud)
Fluid Inclusion Descriptions: L-V Small cluster on a growth plane.
Fluid Inclusion Type: Pseudosecondary
Magnification: 40x. Scale bar is 12.5 µm.

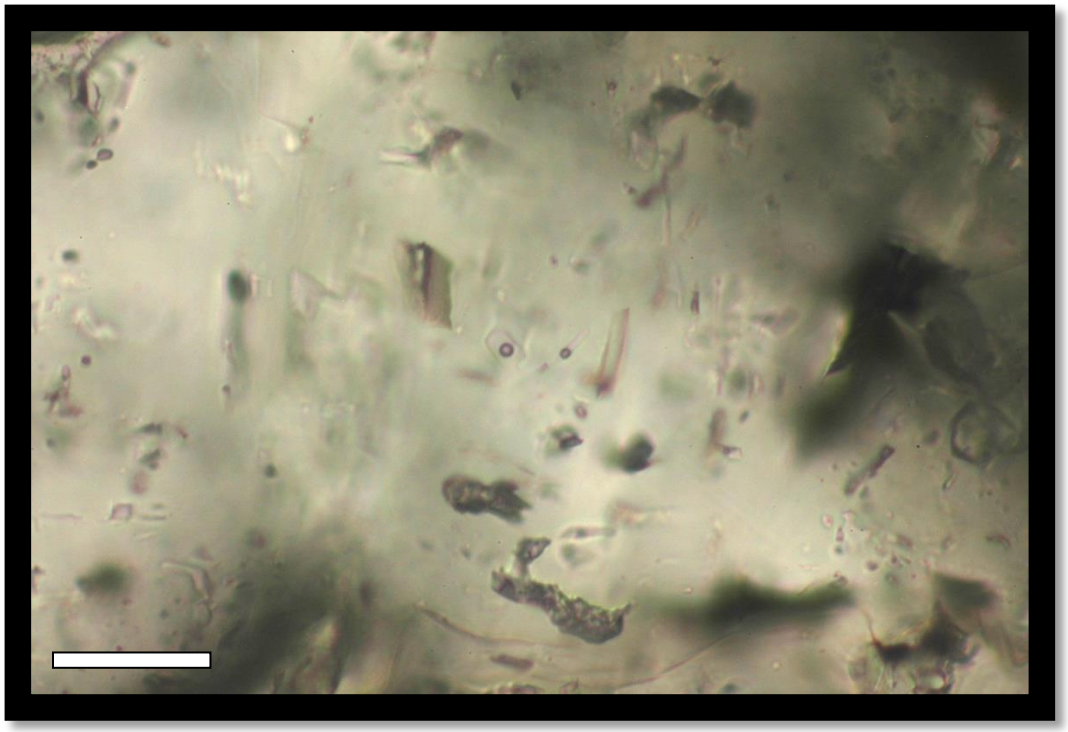

Sample: HTP-1
Deposit: Hill Top Prospect (Honeywell)
Mineral Type: Purple Fluorite (R2 - Same as fine grained purple fluorite at Red Cloud)
Fluid Inclusion Descriptions: L-V-S. Example of a fluid inclusion that is about to pinch two isolated vapor bubbles. Solid in the middle.
Fluid Inclusion Type: Pseudosecondary
Magnification: 40x. Scale bar is 12.5 µm.

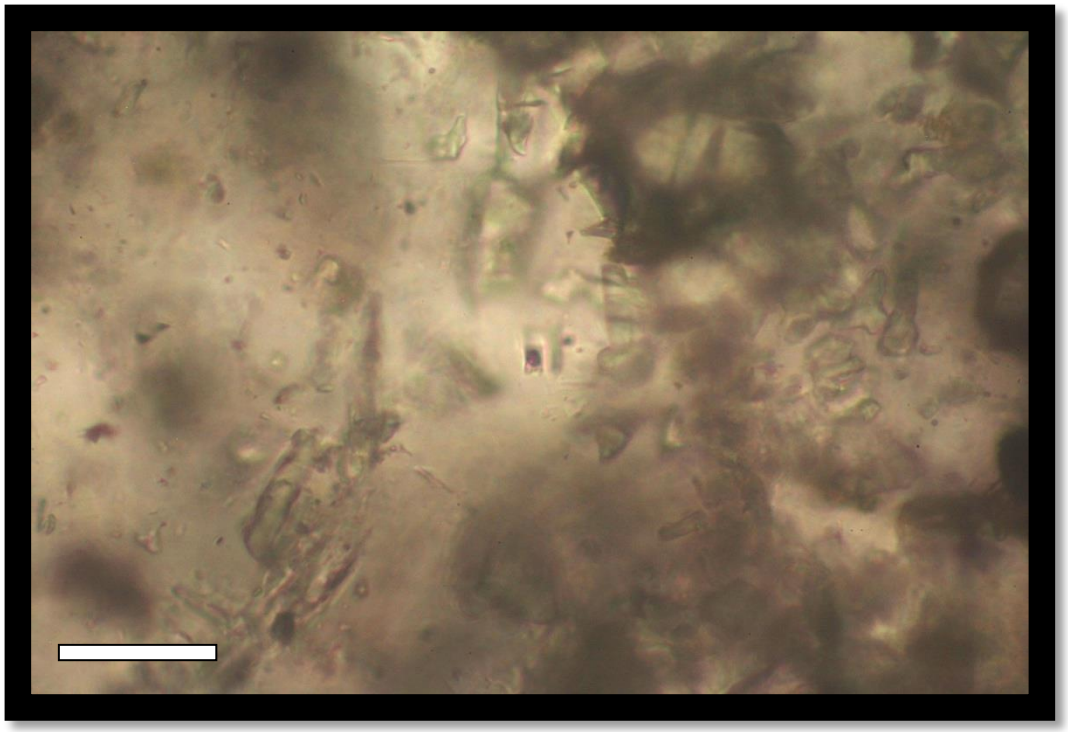

Sample: HTP-1
Deposit: Hill Top Prospect (Honeywell)
Mineral Type: Purple Fluorite (R2 - Same as fine grained purple fluorite at Red Cloud)
Fluid Inclusion Descriptions: L-V-S. 0.01 mm.
Fluid Inclusion Type: Pseudosecondary
Magnification: 40x. Scale bar is 12.5 µm.

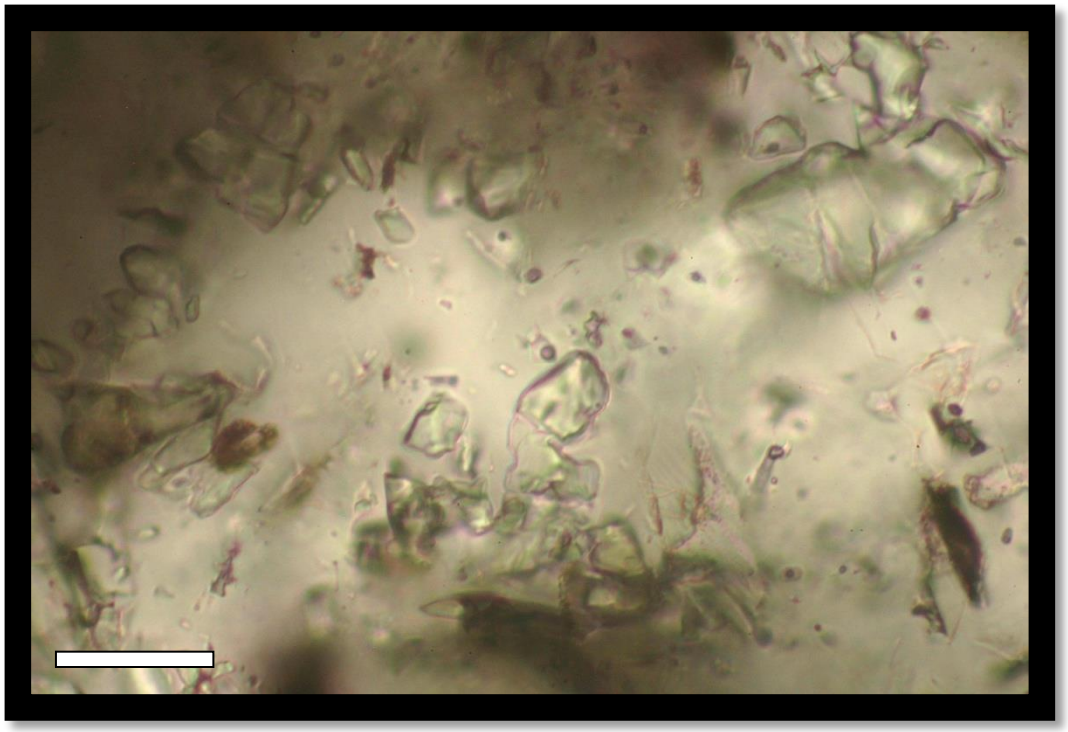

Sample: HTP-1
Deposit: Hill Top Prospect (Honeywell)
Mineral Type: Purple Fluorite (R2 - Same as fine grained purple fluorite at Red Cloud)
Fluid Inclusion Descriptions: L-V
Fluid Inclusion Type: Pseudosecondary
Magnification and F.I. Size: 40x. 0.01 mm. Scale bar is 12.5 µm.

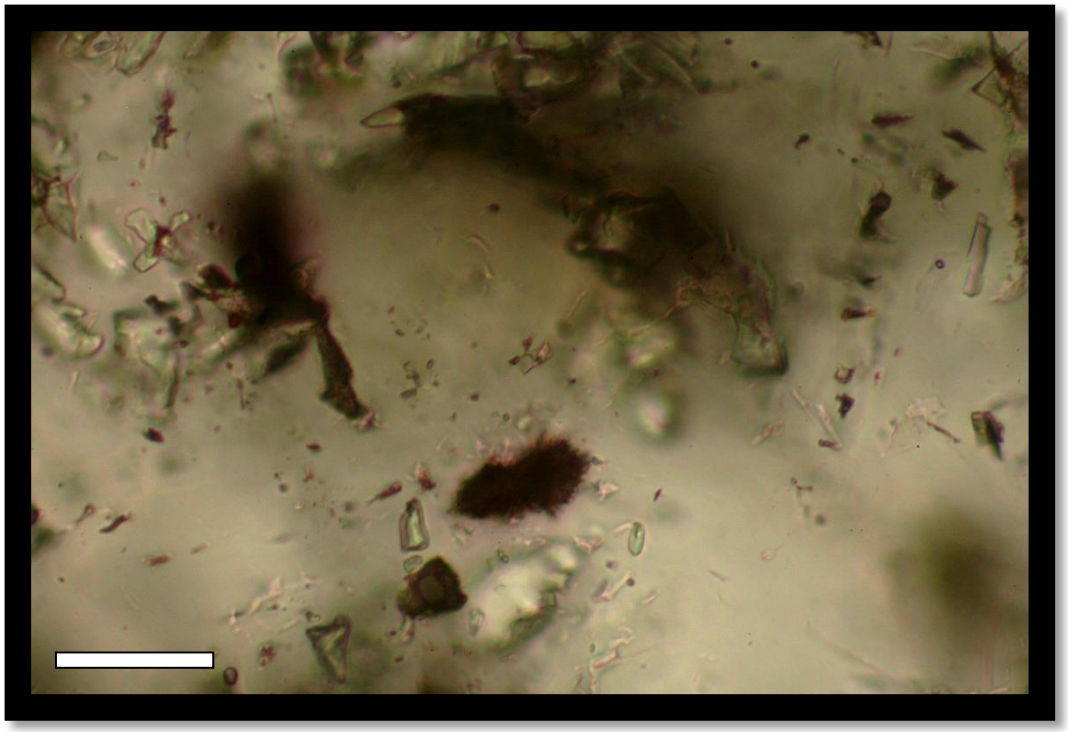

Sample: HTP-1
Deposit: Hill Top Prospect (Honeywell)
Mineral Type: Purple Fluorite (R2 - Same as fine grained purple fluorite at Red Cloud)
Fluid Inclusion Descriptions: L-V-S with multiple solid phases. Necking present.
Fluid Inclusion Type: Pseudosecondary
Magnification and F.I. Size: 40x. 0.0125 mm. Scale bar is 12.5 µm.

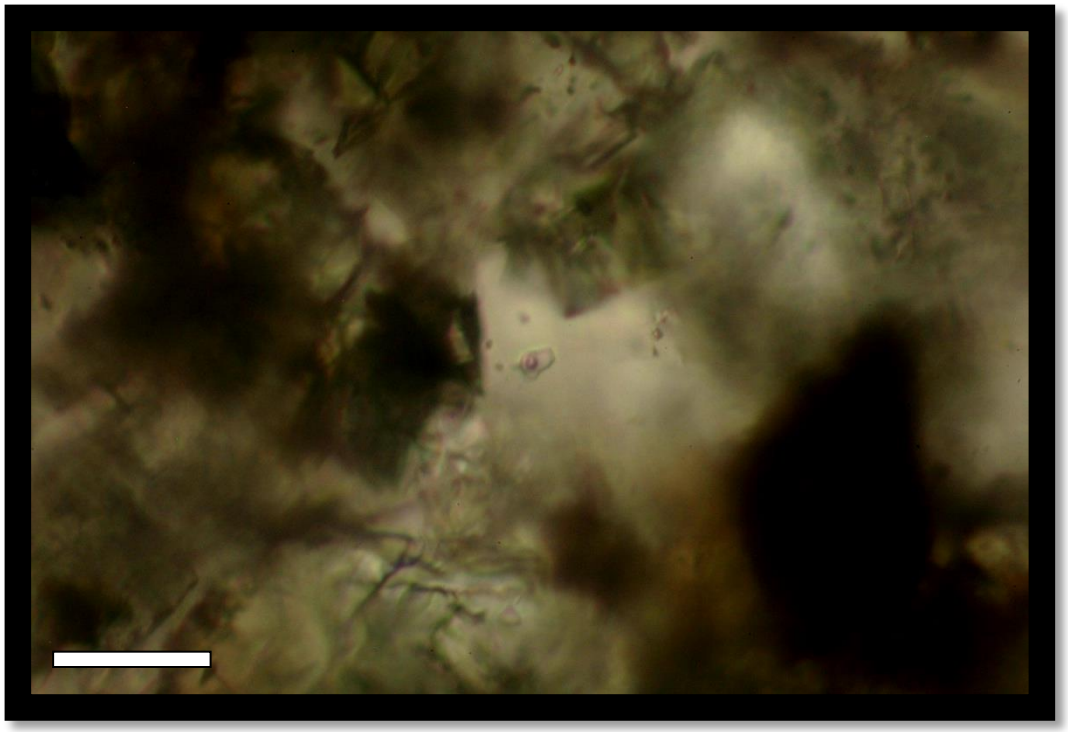

Sample: HTP-1
Deposit: Hill Top Prospect (Honeywell)
Mineral Type: Purple Fluorite (R2 - Same as fine grained purple fluorite at Red Cloud)
Fluid Inclusion Descriptions: L-V. Primary isolated fluid inclusion.
Fluid Inclusion Type: Pseudosecondary
Magnification and F.I. Size: 40x. 0.0075 mm. Scale bar is 12.5 µm.

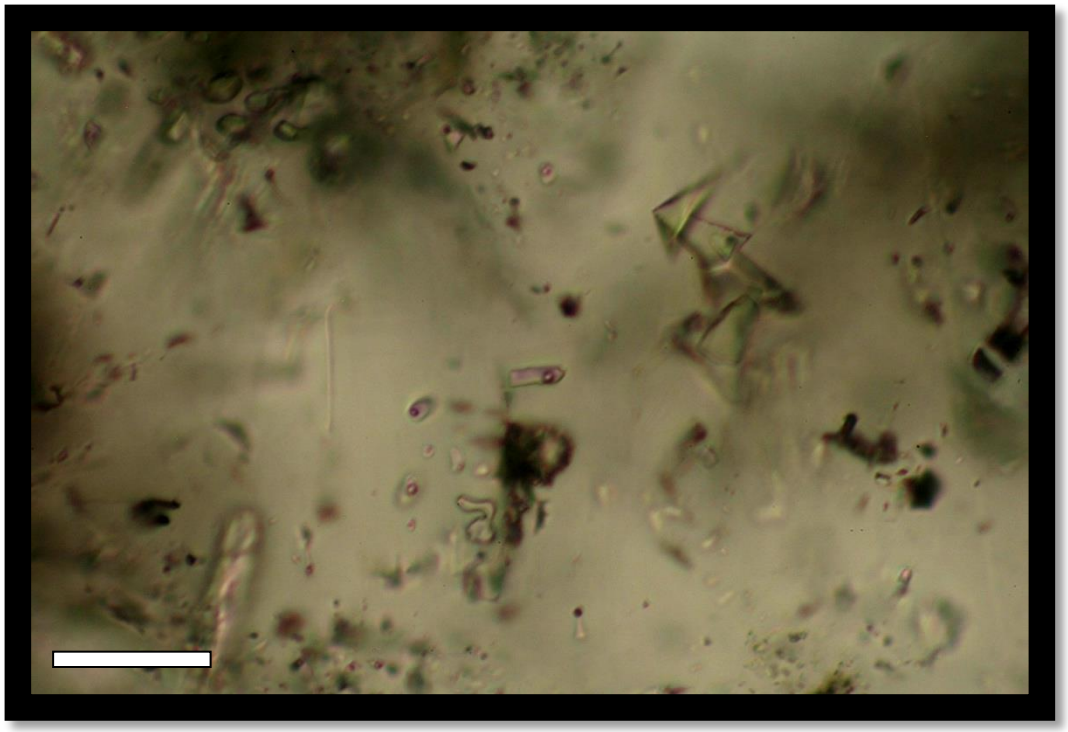

Sample: HTP-1
Deposit: Hill Top Prospect (Honeywell)
Mineral Type: Purple Fluorite (R2 - Same as fine grained purple fluorite at Red Cloud)
Fluid Inclusion Descriptions: L-V. Elongated
Fluid Inclusion Type: Primary
Magnification and F.I. Size: 40x. 0.0075 mm. Scale bar is 12.5 µm.

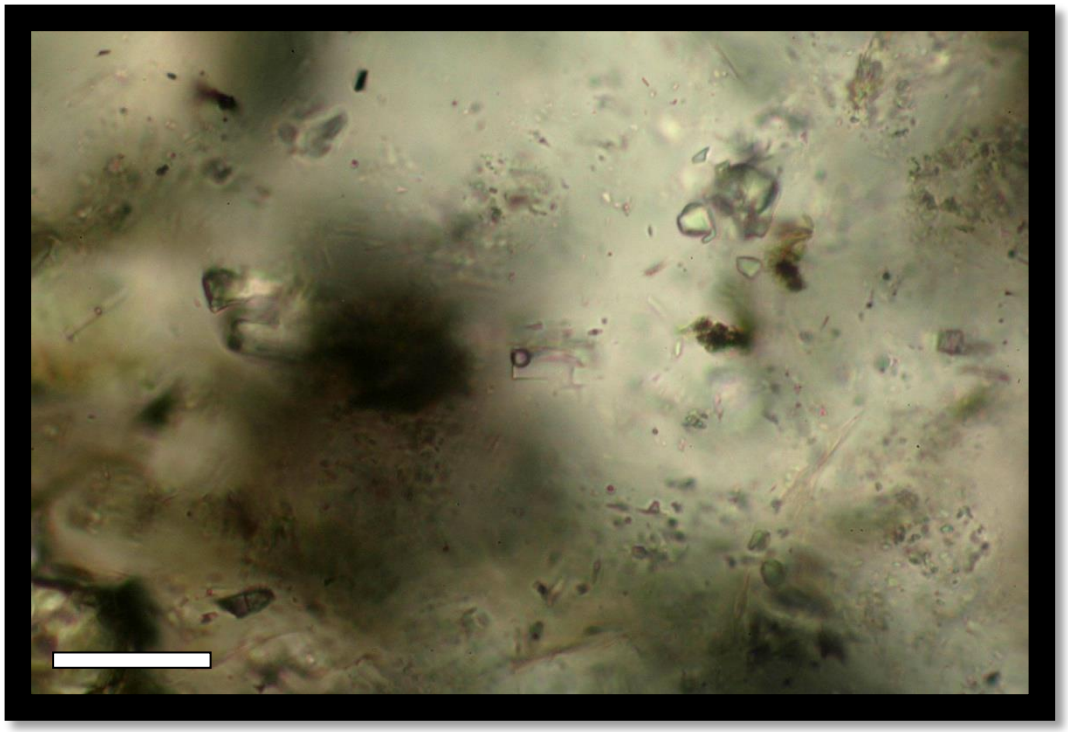

Sample: HTP-1
Deposit: Hill Top Prospect (Honeywell)
Mineral Type: Purple Fluorite (R2 - Same as fine grained purple fluorite at Red Cloud)
Fluid Inclusion Descriptions: L-V.
Fluid Inclusion Type: Primary
Magnification and F.I. Size: 40x. 0.025 mm. Scale bar is 12.5 µm.

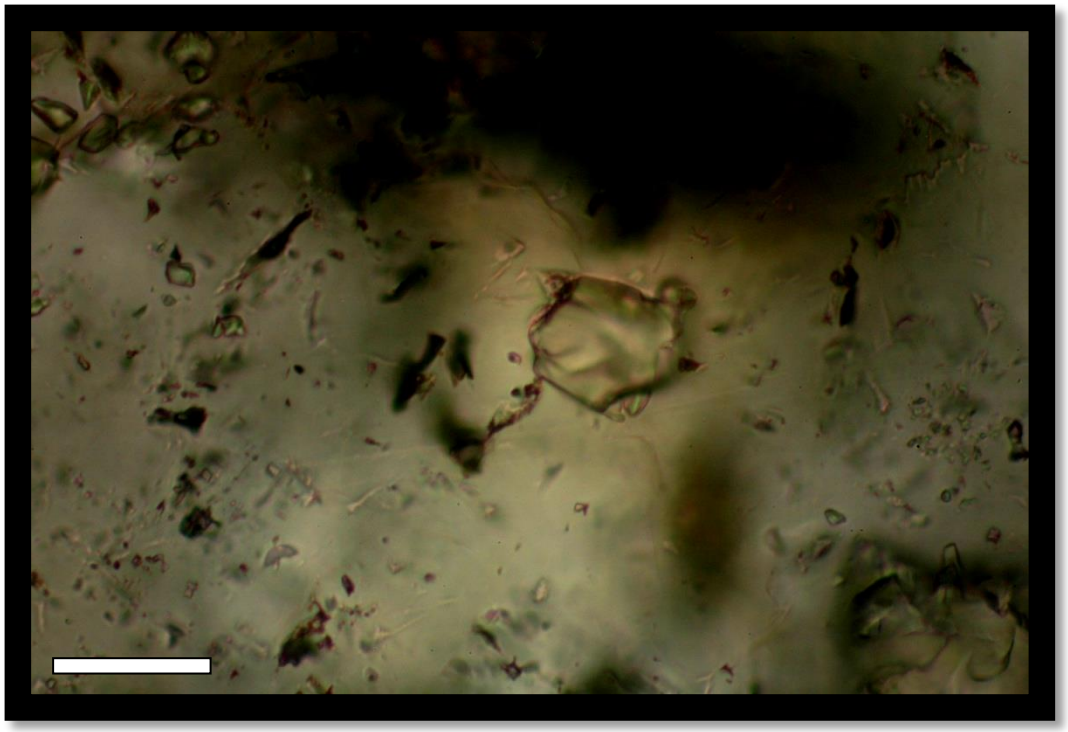

Sample: HTP-1
Deposit: Hill Top Prospect (Honeywell)
Mineral Type: Yellow Bastnaesite
Fluid Inclusion Descriptions: L-V. Very small ~ 1 µm.
Fluid Inclusion Type: Pseudosecondary
Magnification: 40x. Scale bar is 12.5 µm.

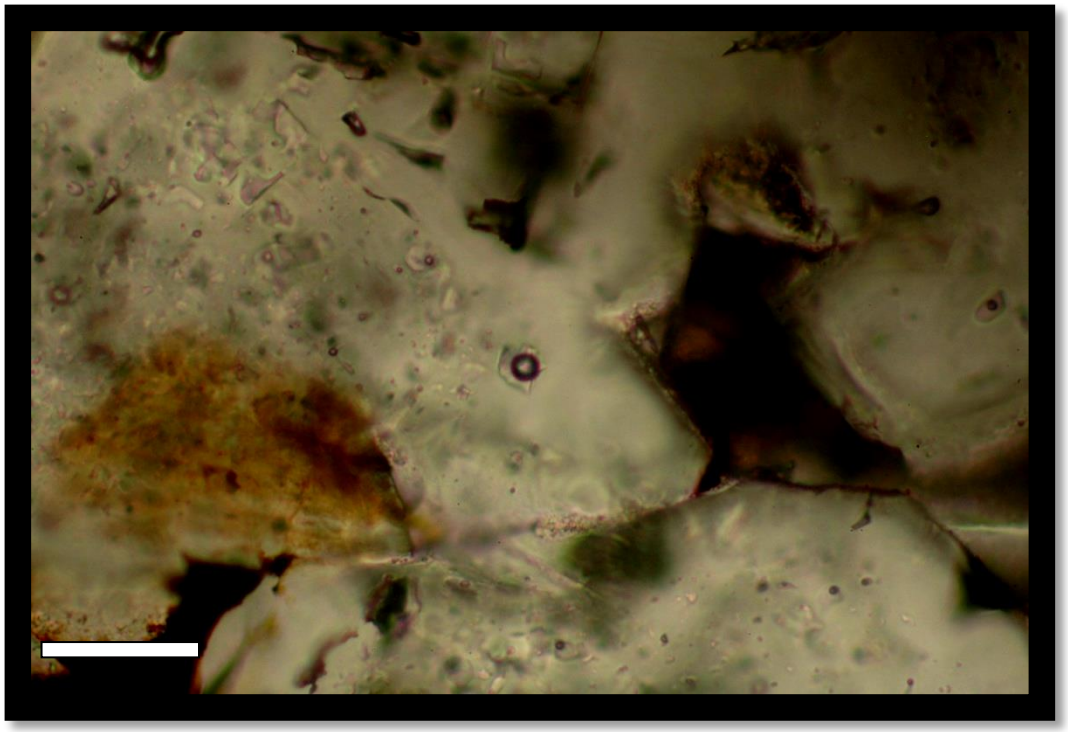

Sample: HTP-1
Deposit: Hill Top Prospect (Honeywell)
Mineral Type: Purple Fluorite (R2 - Same as fine grained purple fluorite at Red Cloud)
Fluid Inclusion Descriptions: L-V.
Fluid Inclusion Type: Pseudosecondary
Magnification and F.I. Size: 20x. 0.0125 mm. Scale bar is 0.1 mm. Scale bar is 25 µm.

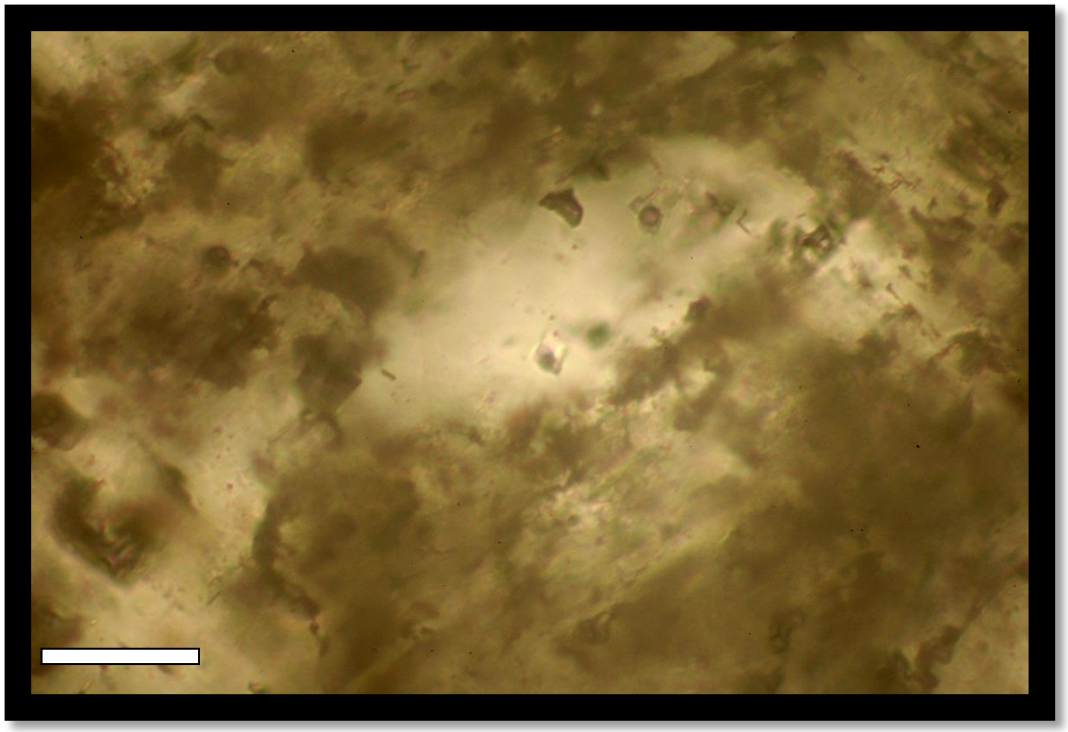

Sample: M+E 13 – 1
Deposit: M+E 13 (Pinatosa)
Mineral Type: Clear Fluorite (P2)
Fluid Inclusion Description: L-V-S
Fluid Inclusion Type: Pseudosecondary
Magnification and F.I. Size: 40x. 5 µm. Scale bar is 12.5 µm.

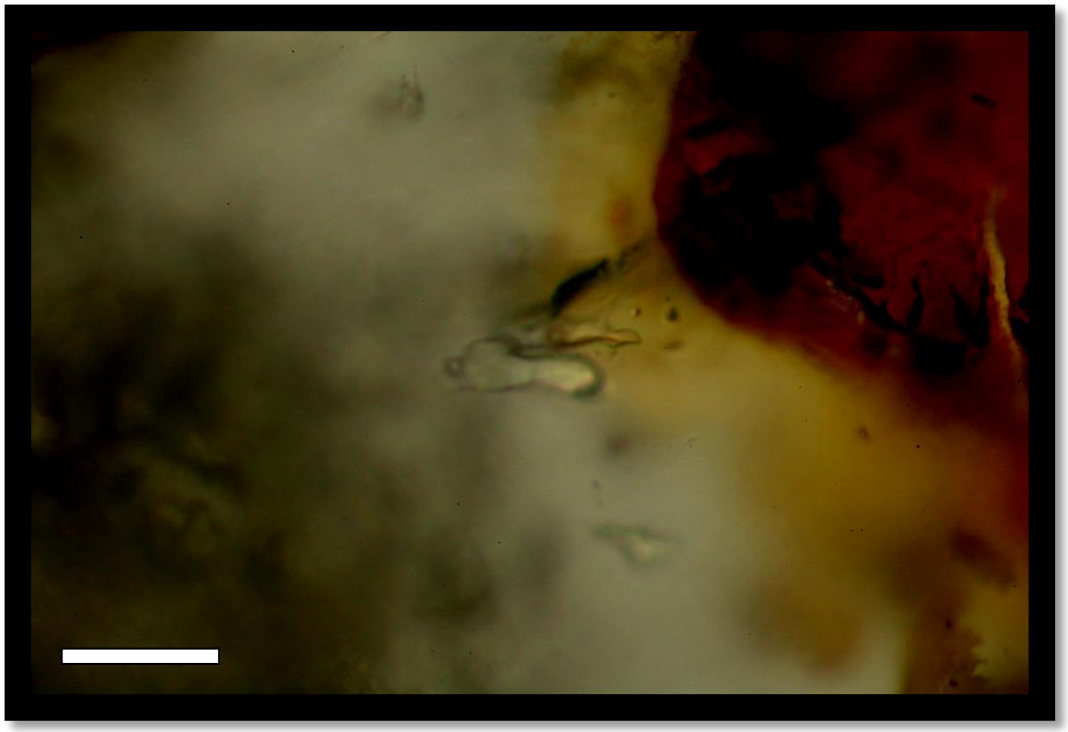

Sample: M+E 13 – 1
Deposit: M+E 13 (Pinatosa)
Mineral Type: Clear Fluorite (P2)
Fluid Inclusion Description: L-V
Fluid Inclusion Type: Primary
Magnification and F.I. Size: 40x. 50 µm. Scale bar is 12.5 µm.

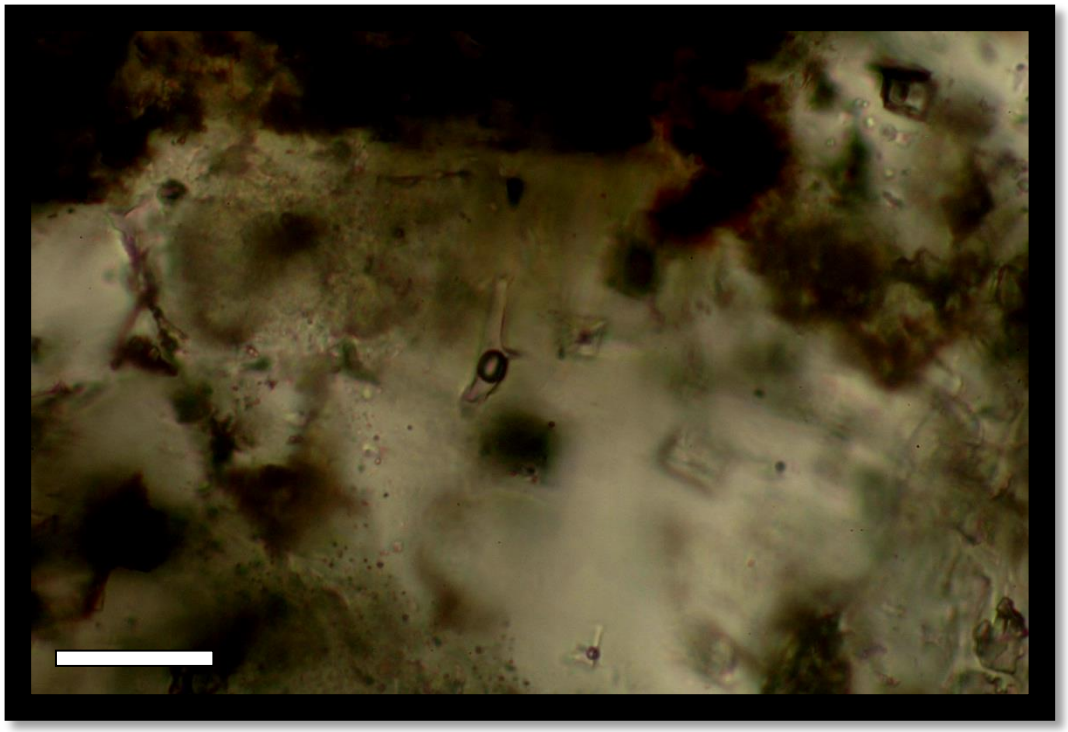

Sample: M+E 13 – 1
Deposit: M+E 13 (Pinatosa)
Mineral Type: Clear Fluorite (P2)
Fluid Inclusion Description: L-V. Example of necking between two Ps inclusions
Fluid Inclusion Type: Pseudosecondary
Magnification and F.I. Size: 40x. Longest inclusion is 35 µm. Scale bar is 12.5 µm.

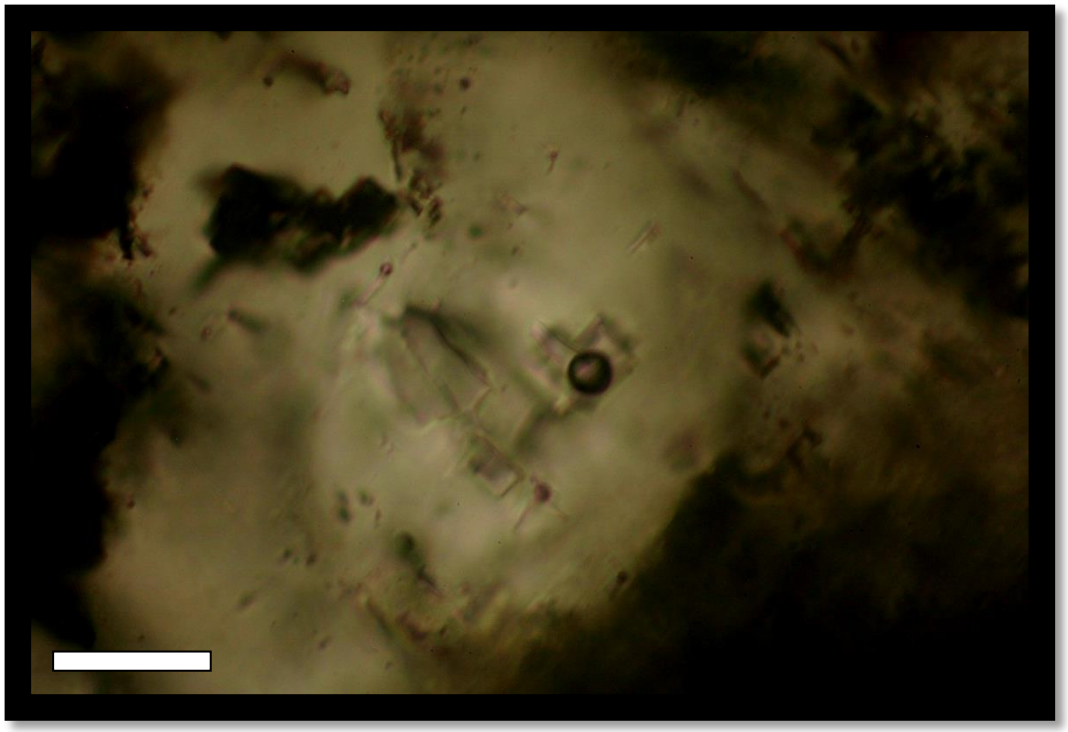

Sample: M+E 13 – 1
Deposit: M+E 13 (Pinatosa)
Mineral Type: Clear Fluorite (P1)
Fluid Inclusion Description: L-V
Fluid Inclusion Type: Pseudosecondary
Magnification and F.I. Size: 20x. 25 µm. Scale bar is 50 µm.

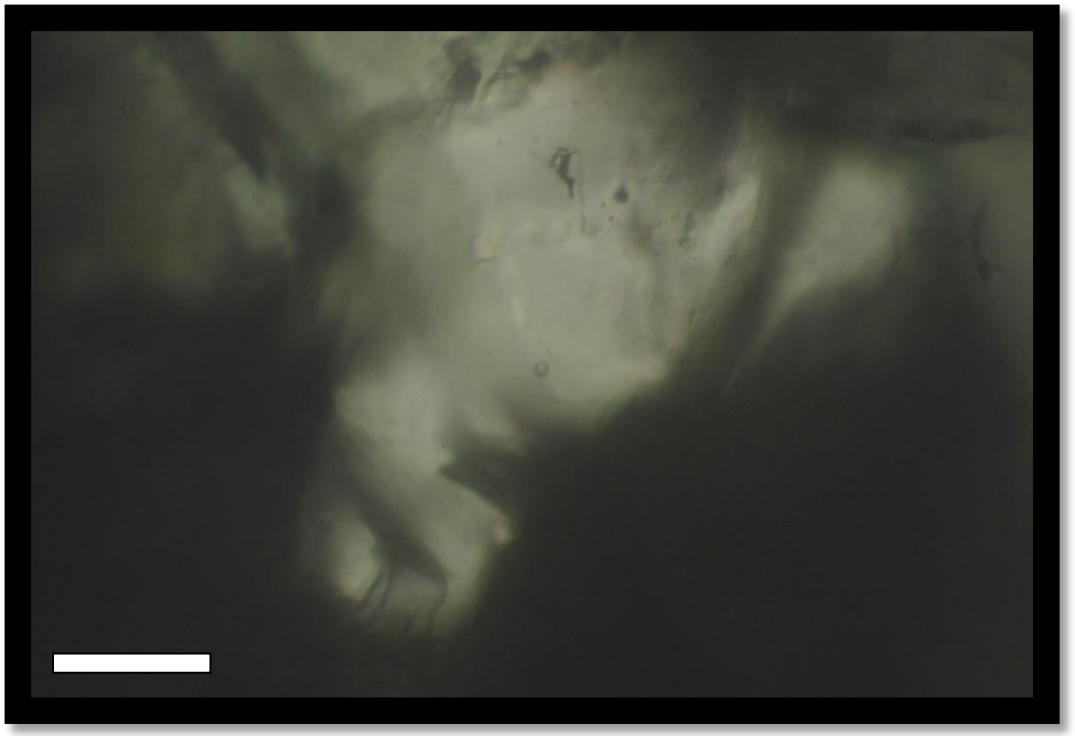

Sample: M+E 13 – 1
Deposit: M+E 13 (Pinatosa)
Mineral Type: Quartz
Fluid Inclusion Description: L-V
Fluid Inclusion Type: Pseudosecondary
Magnification and F.I. Size: 40x. 25 µm. Scale bar is 12.5 µm.

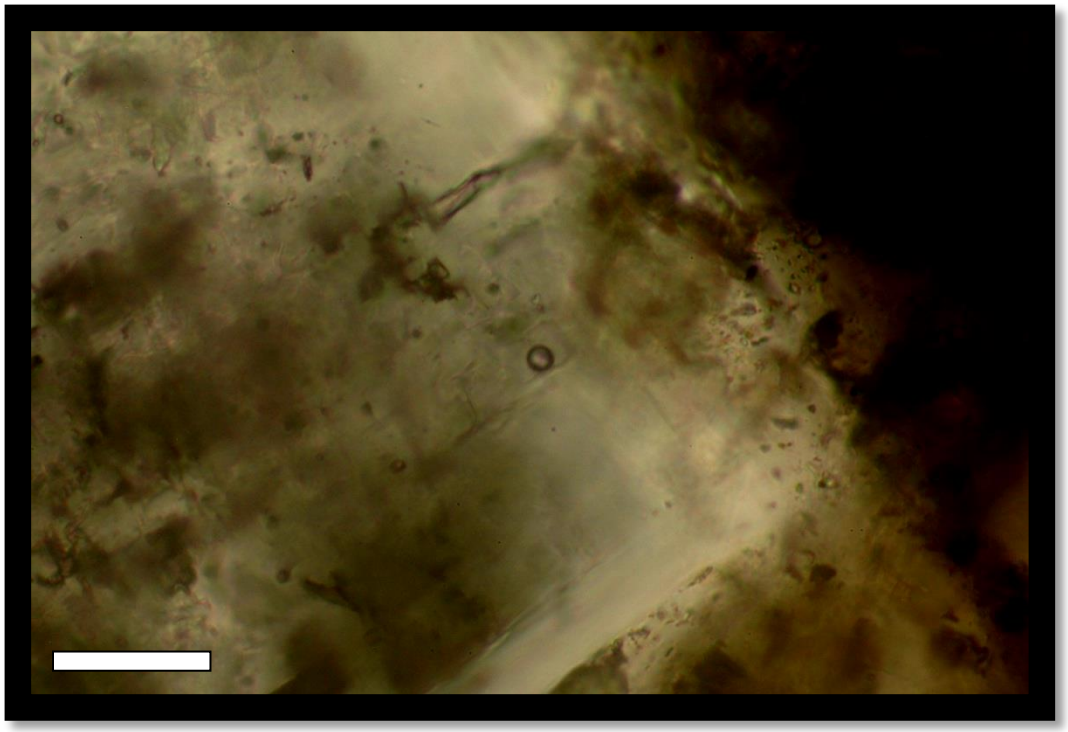

Sample: M+E 13 – 1
Deposit: M+E 13 (Pinatosa)
Mineral Type: Clear Fluorite (P2)
Fluid Inclusion Description: L-V. Within a growth plane and not near any other inclusions.
Fluid Inclusion Type: Primary
Magnification and F.I. Size: 40x. 12.5 µm. Scale bar is 12.5 µm.

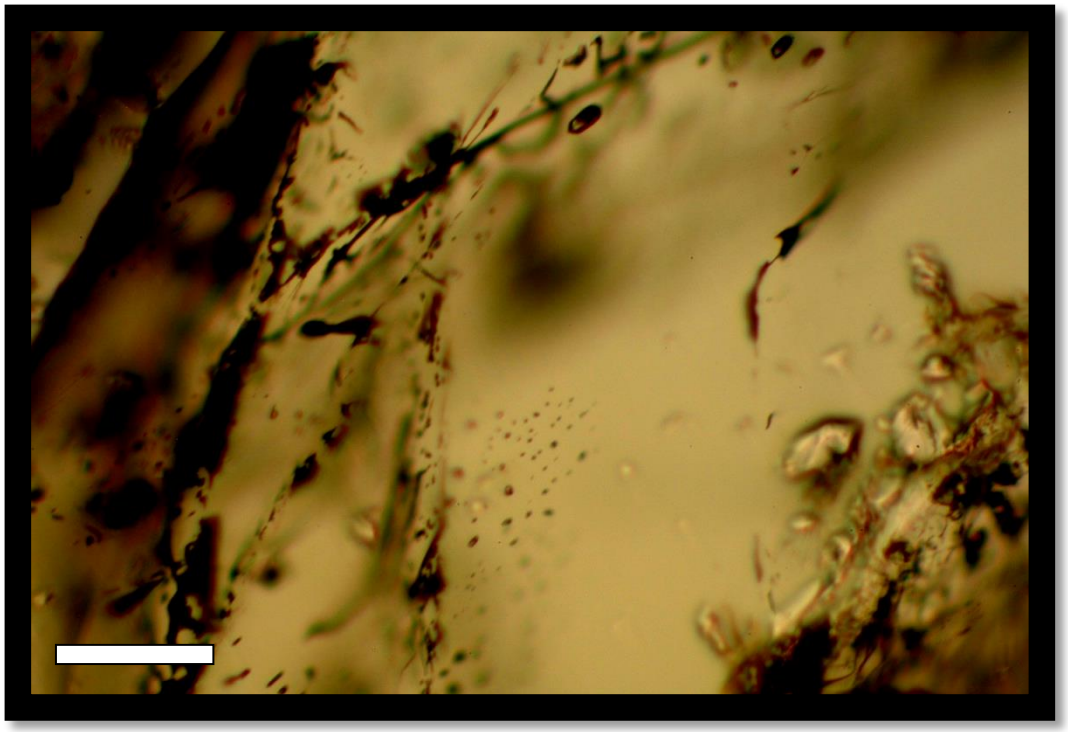

Sample: M+E 13 – 1
Deposit: M+E 13 (Pinatosa)
Mineral Type: Bastnaesite
Fluid Inclusion Description: Plane of Ps L-V inclusions. Isolated L-V-S primary inclusion (note hexagonal shape).
Fluid Inclusion Type: Primary and Pseudosecondary
Magnification and F.I. Size: Small inclusions in plane are ~3 µm. Large primary inclusion is ~ 25 µm. 20x ppl. Scale bar is 0.1 mm.

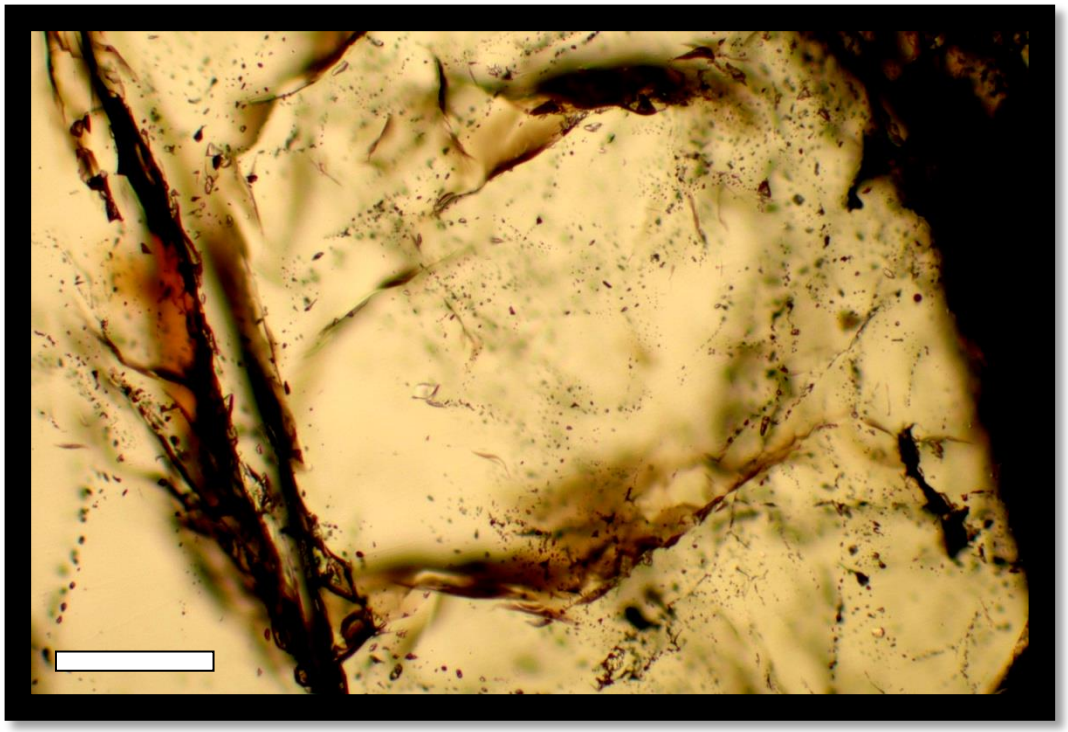

Sample: M+E 13 – 1
Deposit: M+E 13 (Pinatosa)
Mineral Type: Bastnaesite
Fluid Inclusion Description: L-V-S. 5 Solid phases plus vapor bubble
Magnification and F.I. Size: 10x ppl. Scale bar is 0.05 mm.
Bastnaesite texture. Note abundant pseudosecondary inclusions. Evidence for crystallization, fracturing, and healing stages of crystal growth. 10x ppl. Grain is ~1 mm in diameter.

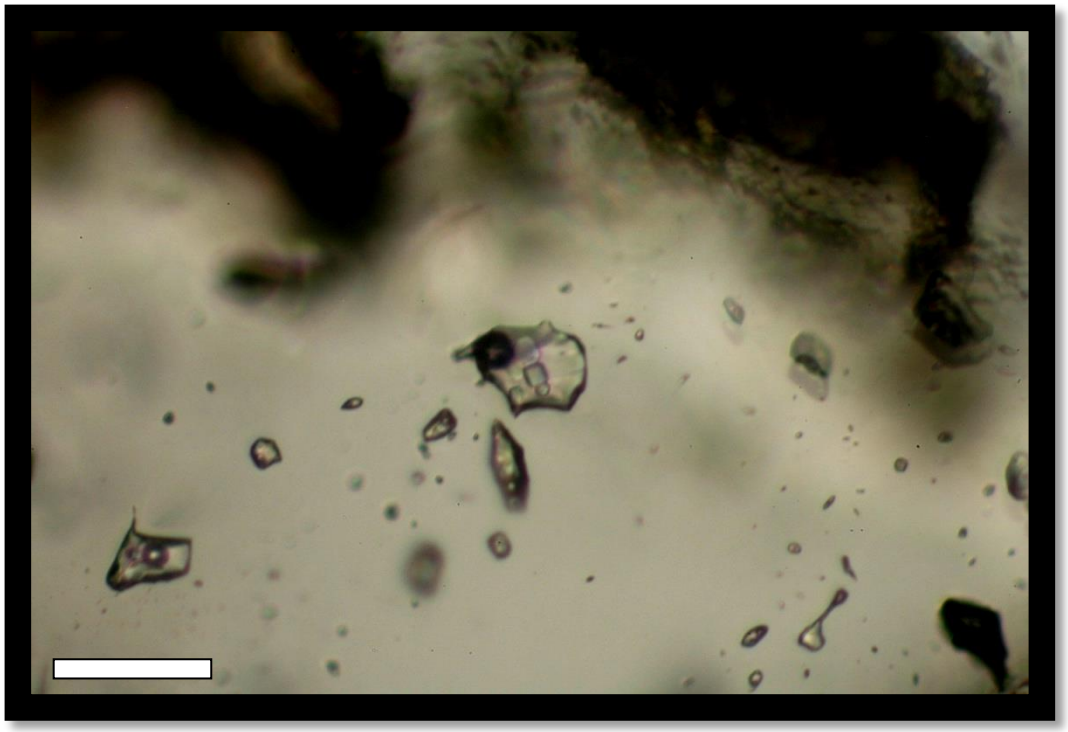

Sample: M+E 13 – 1
Deposit: M+E 13 (Pinatosa)
Mineral Type: Quartz
Fluid Inclusion Description: L-V-S. 5 Solid phases plus vapor bubble
Fluid Inclusion Type: Primary
Magnification and F.I. Size: 40x. 25 µm. Scale bar is 12.5 µm.

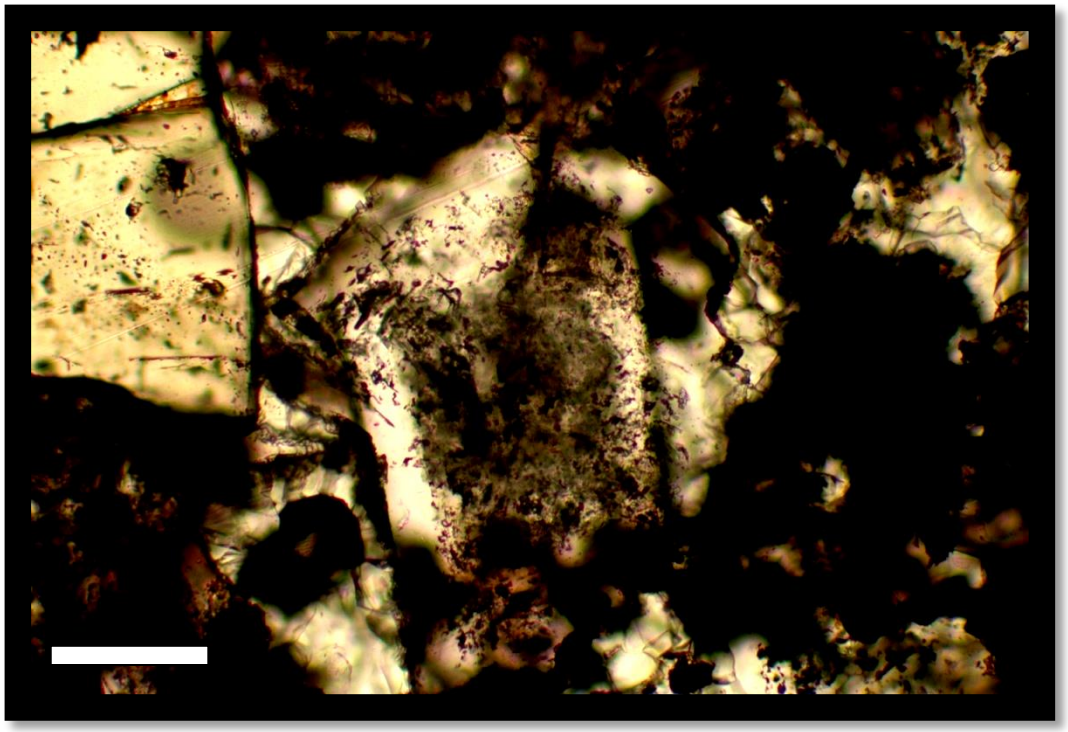

Sample: M+E 13 – 1
Deposit: M+E 13 (Pinatosa)
Mineral Type: Clear Fluorite (P2)
Typical clear fluorite texture. Relatively clean growth rims on the outside of the crystal. Center of crystal is cluttered with small inclusions resulting in a cloudy appearance under ppl. 10x ppl. Crystal is approximately 0.5mm in diameter. Scale bar is 0.05 mm.

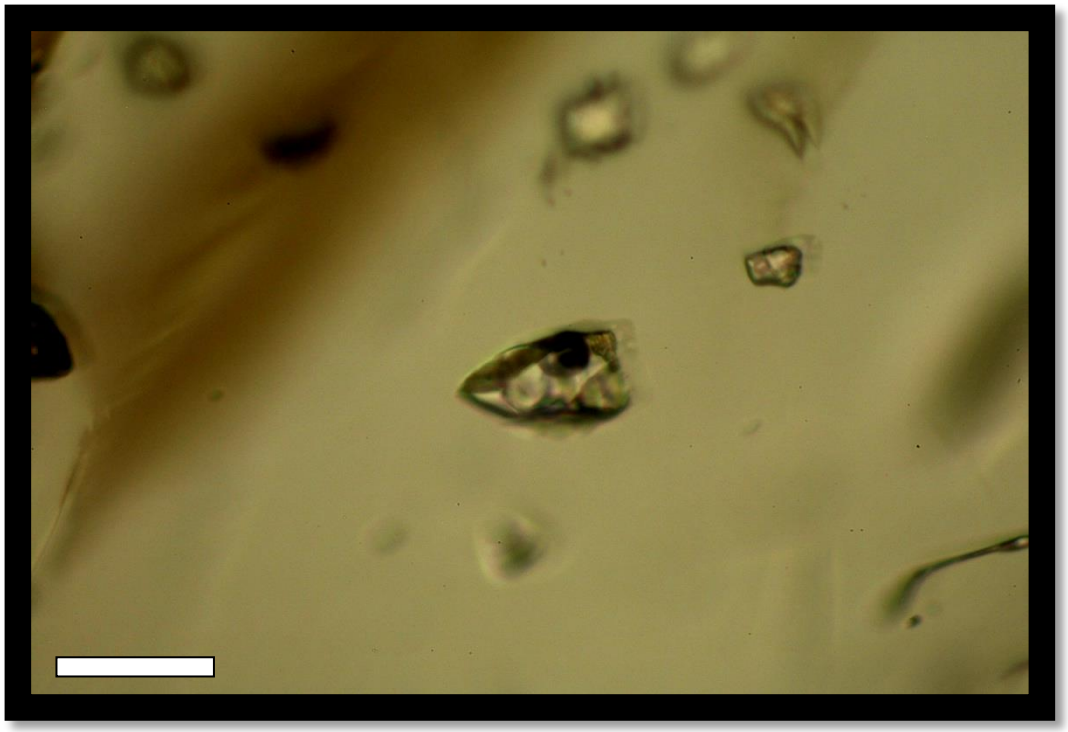

Sample: M+E 13 – 1
Deposit: M+E 13 (Pinatosa)
Mineral Type: Bastnaesite
Fluid Inclusion Description: L-V-S. ~5 solid phases.
Fluid Inclusion Type: Primary
Magnification and F.I. Size: 20x 50 µm. Scale bar is 0.1 mm.

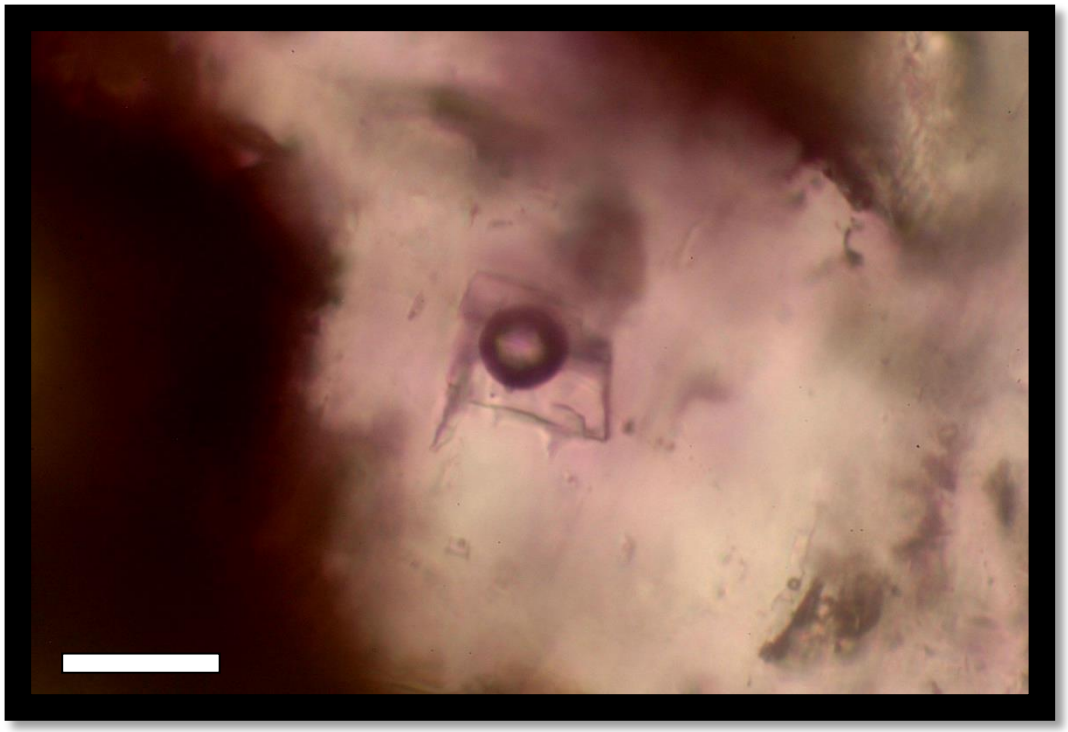

Sample: M+E 13 – 1
Deposit: M+E 13 (Pinatosa)
Mineral Type: Purple Fluorite
Fluid Inclusion Description: L-V
Fluid Inclusion Type: Primary
Magnification and F.I. Size: 20x. 45 µm. Scale bar is 0.1 mm.

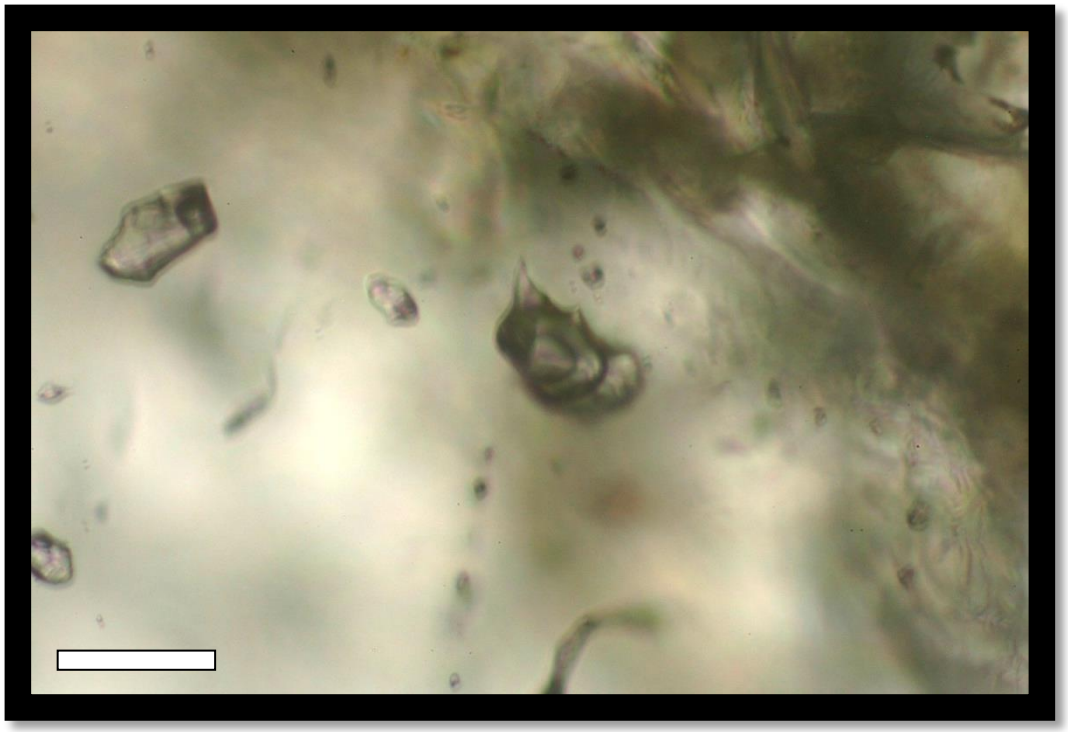

Sample: M+E 13 – 1
Deposit: M+E 13 (Pinatosa)
Mineral Type: Bastnaesite
Fluid Inclusion Description: A-C.
Fluid Inclusion Type: Primary
Magnification and F.I. Size: 20x. 25 µm. Scale bar is 0.05 mm.

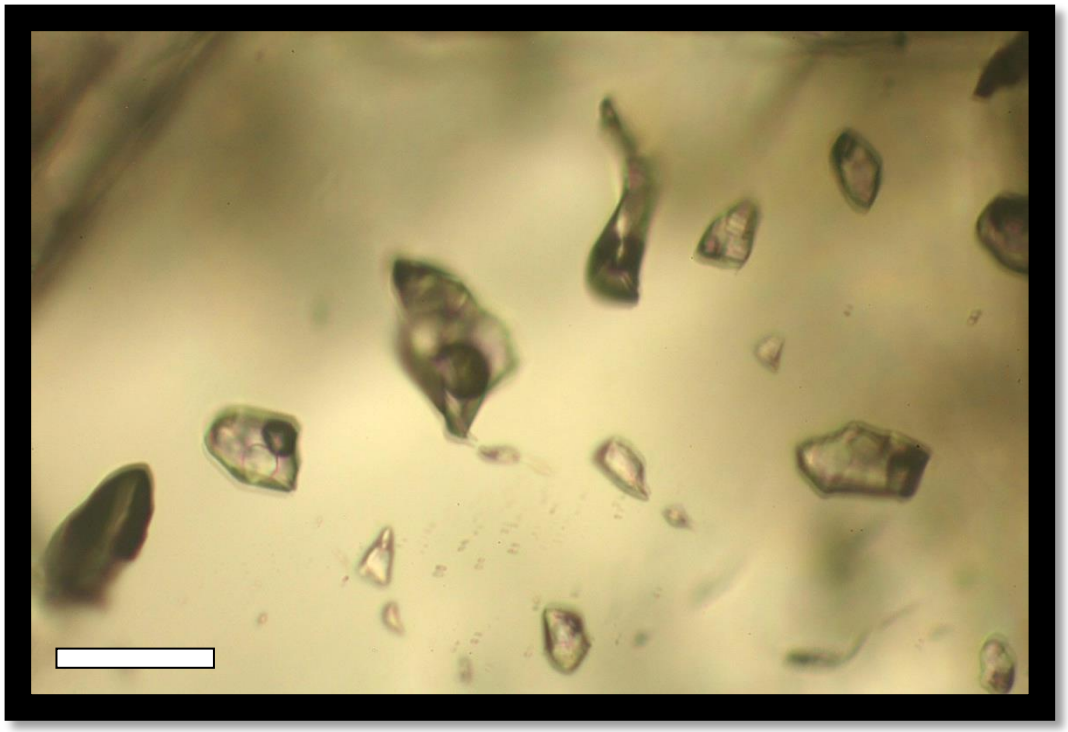

Sample: M+E 13 – 1
Deposit: M+E 13 (Pinatosa)
Mineral Type: Bastnaesite
Fluid Inclusion Description: Cluster of L-V-S inclusions.
Fluid Inclusion Type: Primary
Magnification and F.I. Size: 20x ~25 µm. Scale bar is 0.1 mm.

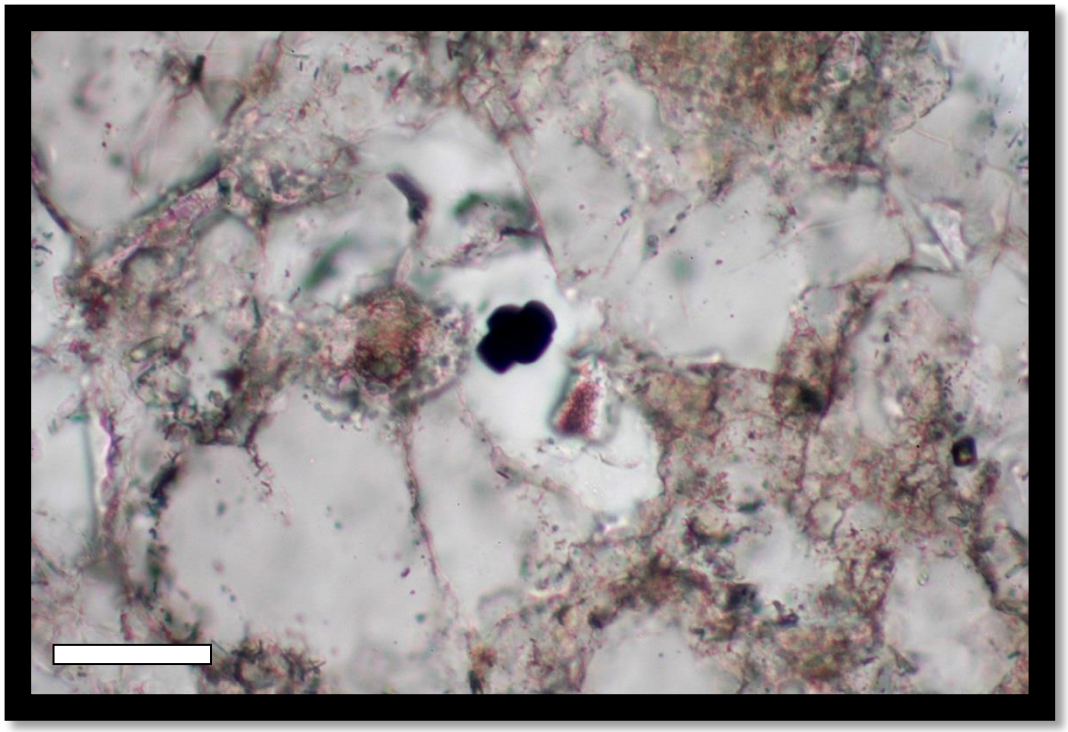

Sample: Sulfide Queen - 1
Deposit: Sulfide Queen (Red Cloud Copper)
Mineral Type: Quartz
Mineral: Possible Xenotime, monazite ECT.
Magnification and F.I. Size: 20x ~12 µm. Scale bar is 0.1 mm.

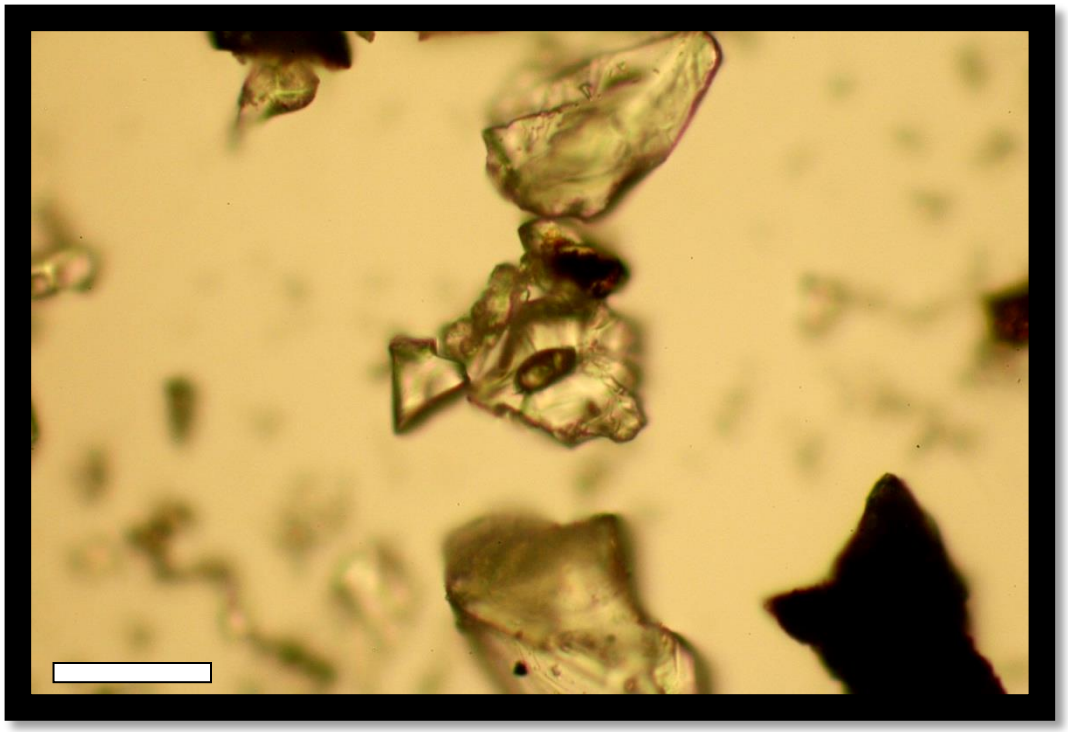

Sample: Old Hickory (spotty sulfide sample)
Deposit: Old Hickory
Mineral Type: Clear Fluorite
Fluid Inclusion Description: L-V
Fluid Inclusion Type: Primary
Picture Number and F.I. size: 40x. 5 µm. Scale bar is 12.5 µm.

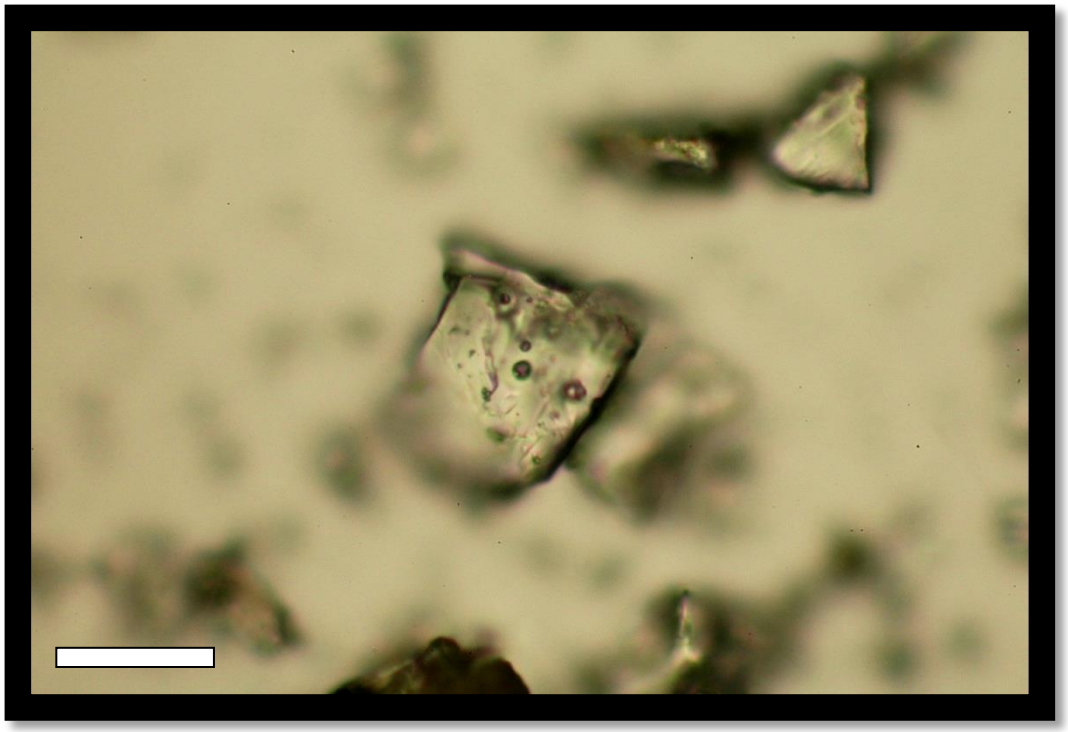

Sample: Old Hickory (spotty sulfide sample)
Deposit: Old Hickory
Mineral Type: Clear Fluorite
Fluid Inclusion Description: L-V. Abundant secondary inclusions.
Fluid Inclusion Type: Secondary
Picture Number and F.I. size: 40x. 5 µm. Scale bar is 12.5 µm.

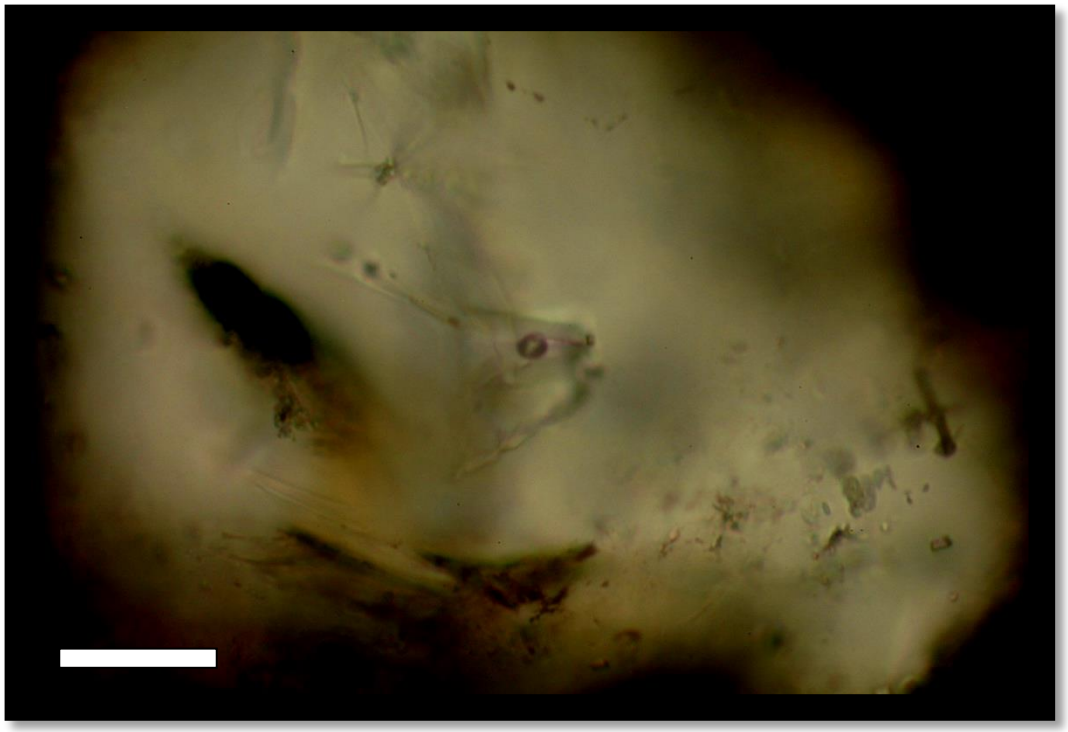

Sample: Perhac 16 (B)
Deposit: Rio Tinto/Conqueror
Mineral Type: Quartz
Fluid Inclusion Description: L-V
Fluid Inclusion Type: Primary
Picture Number and F.I. size: 40x. 15 µm. Scale bar is 12.5 µm.

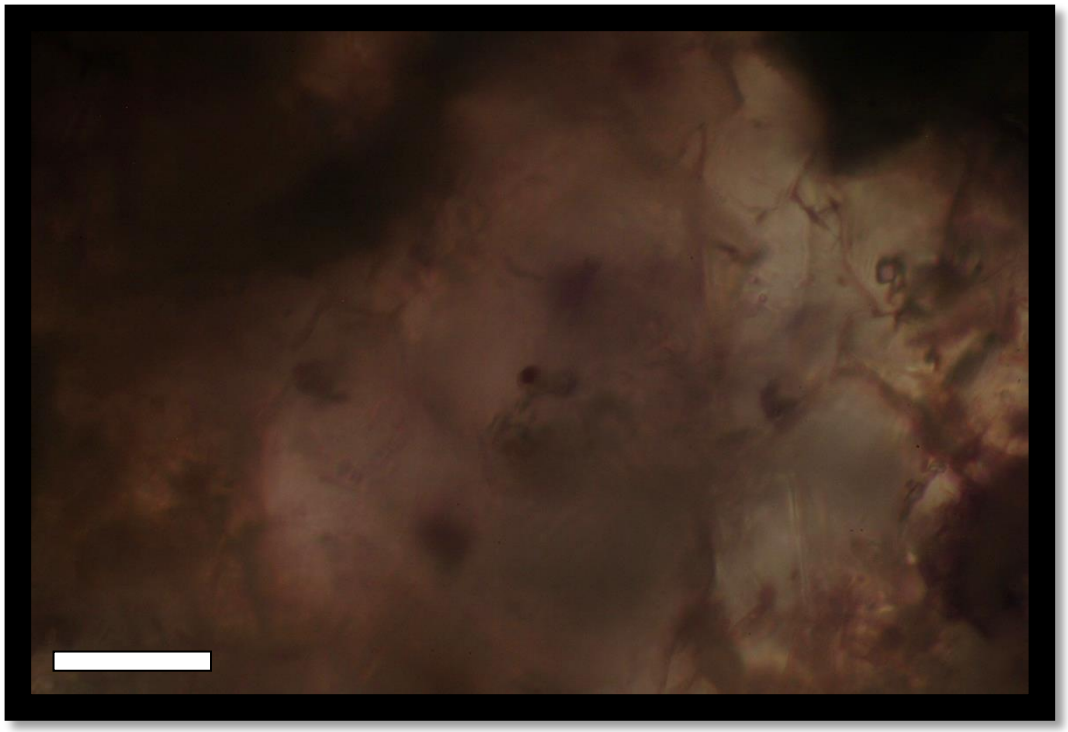

Sample: Perhac 16 (B)
Deposit: Rio Tinto/Conqueror
Mineral Type: Purple Fluorite
Fluid Inclusion Description: L-V-S. Halite
Fluid Inclusion Type: Primary
Picture Number and F.I. size: 10x. 25 μm. Scale bar is 0.05 mm.

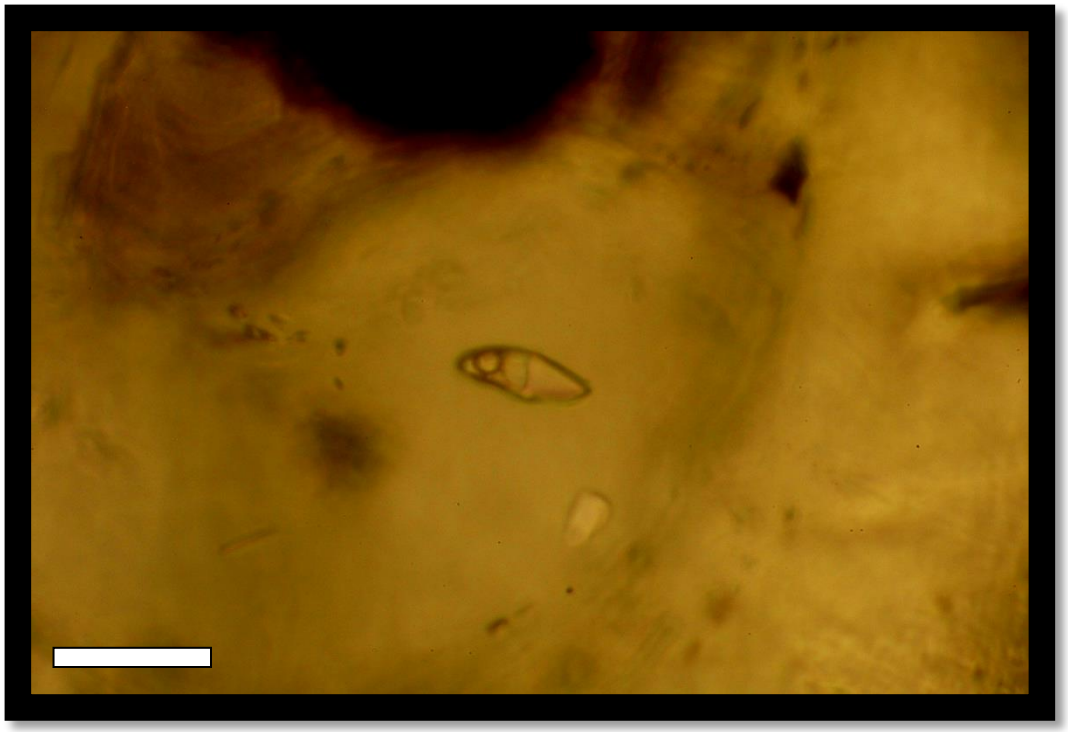

Sample: Red Cloud Bastnaesite Concentrate
Deposit: Red Cloud
Mineral: Bastnaesite
Fluid Inclusion Type: L-V-S
Fluid Inclusion Type: Primary
Picture number and F.I. Size: 10x. 30 µm. Scale bar is 0.05 mm.

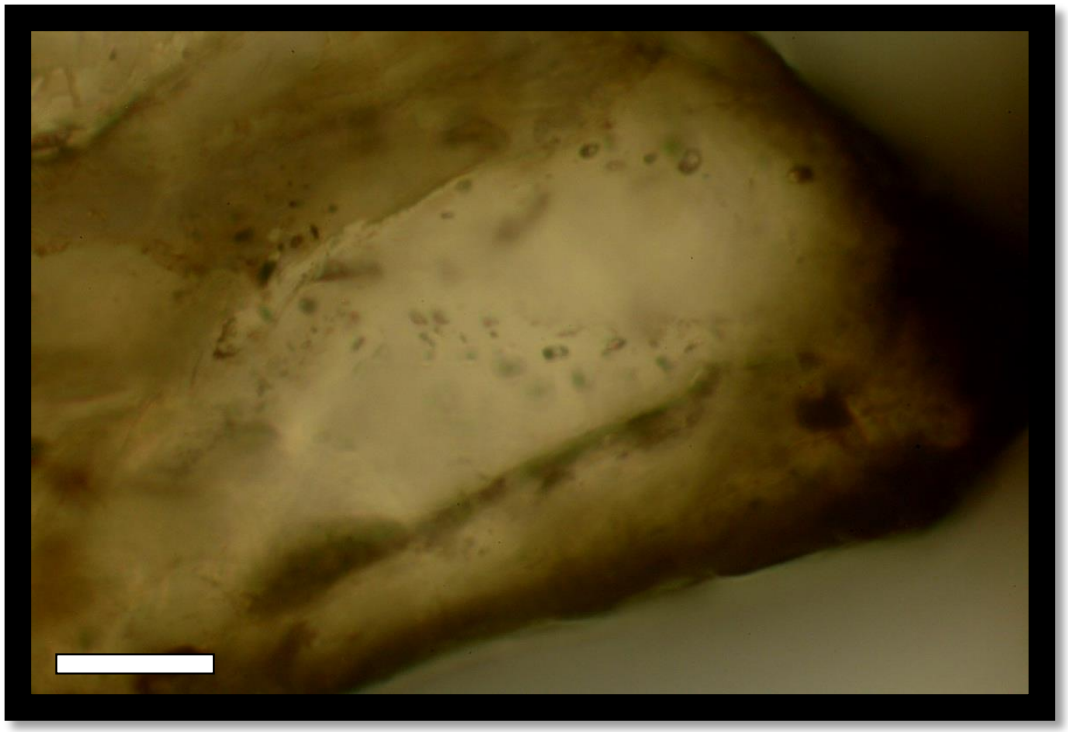

Sample: Red Cloud Bastnaesite Concentrate
Deposit: Red Cloud
Mineral: Bastnaesite
Fluid Inclusion Type: L-V-S. Plane of secondary inclusions.
Fluid Inclusion Type: Pseudosecondary
Picture number and F.I. Size: 20x. 5 µm. Scale bar is 25 µm.

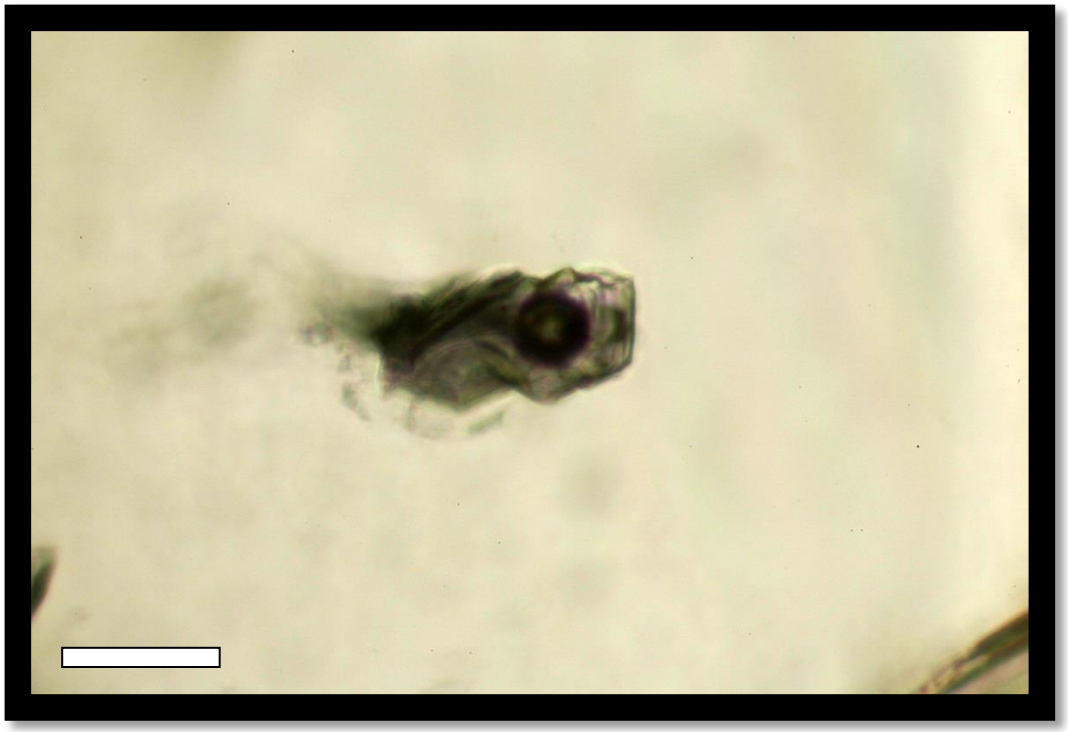

Sample: Red Cloud Bastnaesite Concentrate
Deposit: Red Cloud
Mineral: Bastnaesite
Fluid Inclusion Type: L-V
Fluid Inclusion Type: Primary
Picture number and F.I. size: 10x. 60 µm. Scale bar is 0.05 mm.

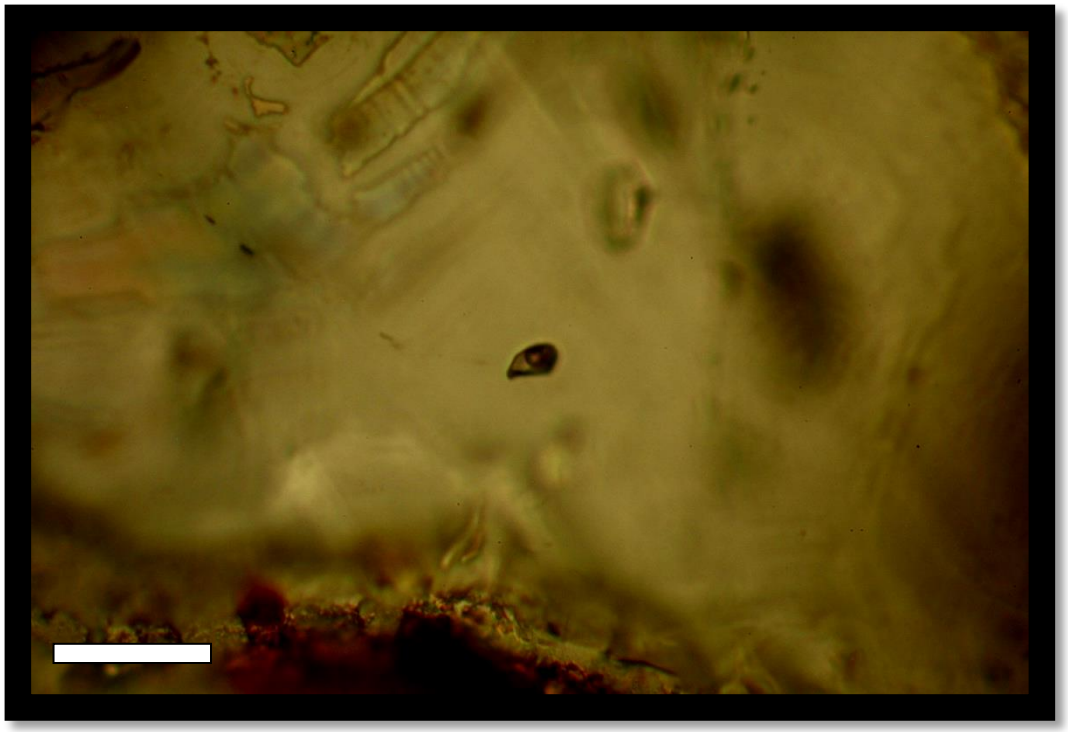

Sample: Red Cloud Bastnaesite Concentrate
Deposit: Red Cloud
Mineral: Bastnaesite
Fluid Inclusion Type: L-V. Elongate inclusion on a healed fracture plane.
Fluid Inclusion Type: Pseudosecondary
Picture number and F.I. size: 20x. 30 µm. Scale bar is 25 µm.

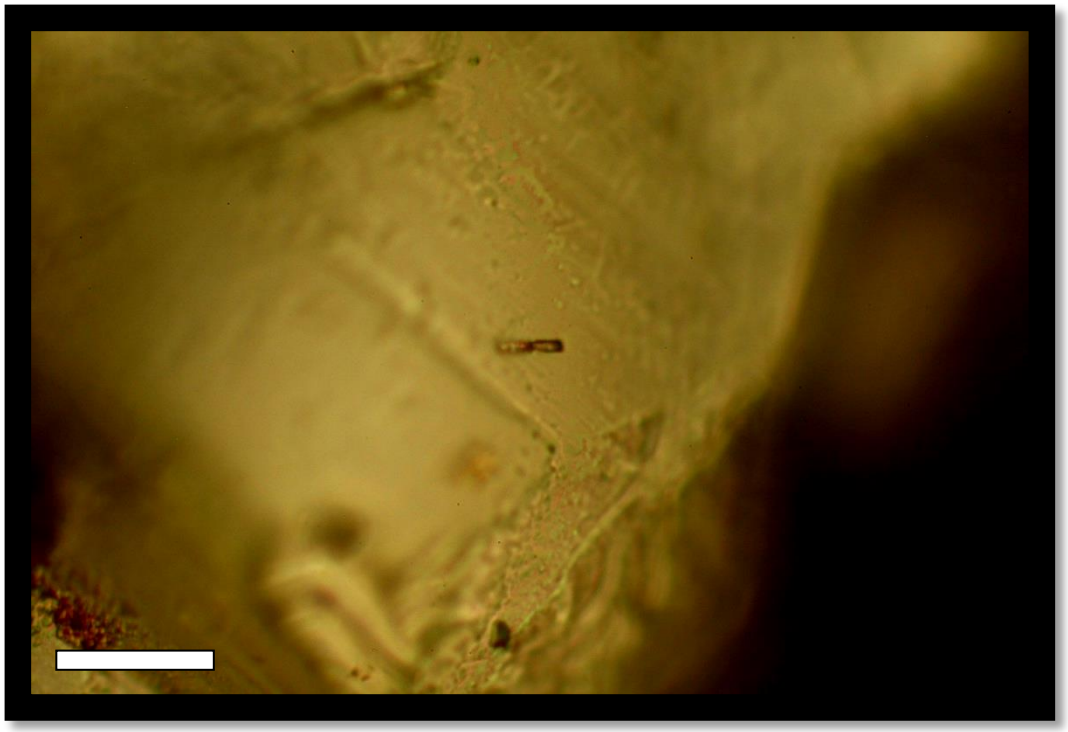

Sample: Red Cloud Bastnaesite Concentrate
Deposit: Red Cloud
Mineral: Bastnaesite
Fluid Inclusion Type: L-V
Fluid Inclusion Type: Primary
Picture number and F.I. size: 10x. 20 µm. Scale bar is 0.05 mm.

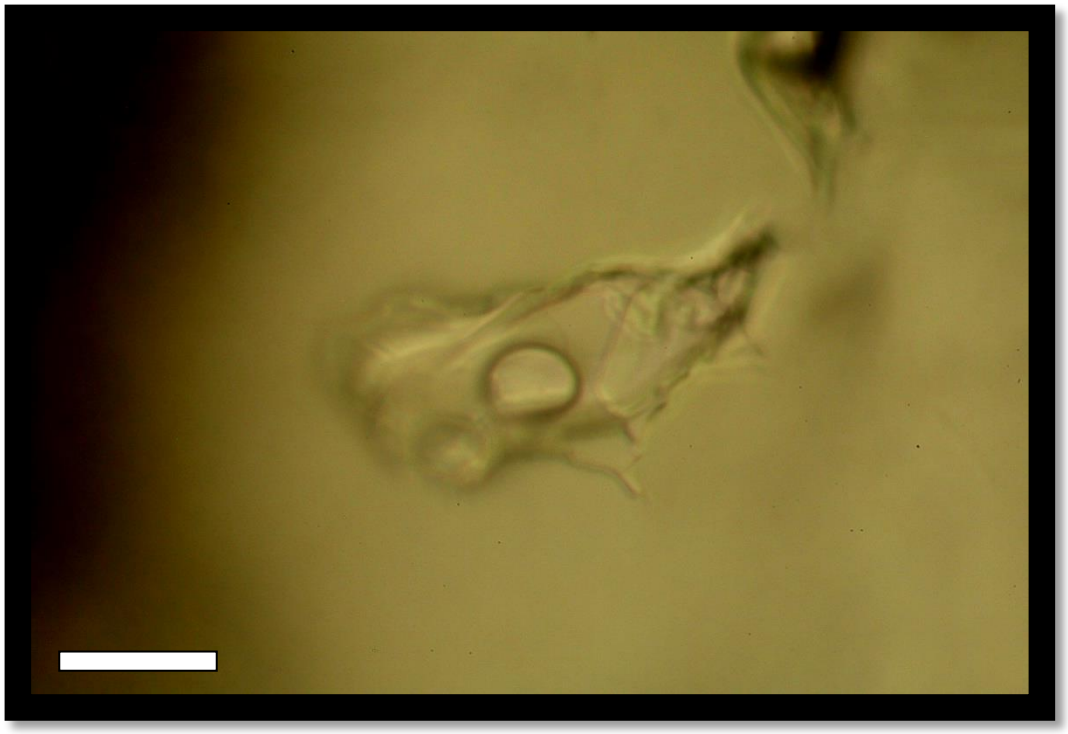

Sample: Red Cloud Bastnaesite Concentrate
Deposit: Red Cloud
Mineral: Bastnaesite
Fluid Inclusion Type: L-V
Fluid Inclusion Type: Primary or Pseudosecondary
Picture number and F.I. size: 10x. 100 µm. Scale bar is 0.05 mm.

APPENDIX 3

X-ray Diffraction Analysis

Bastnaesite 1A Red Cloud

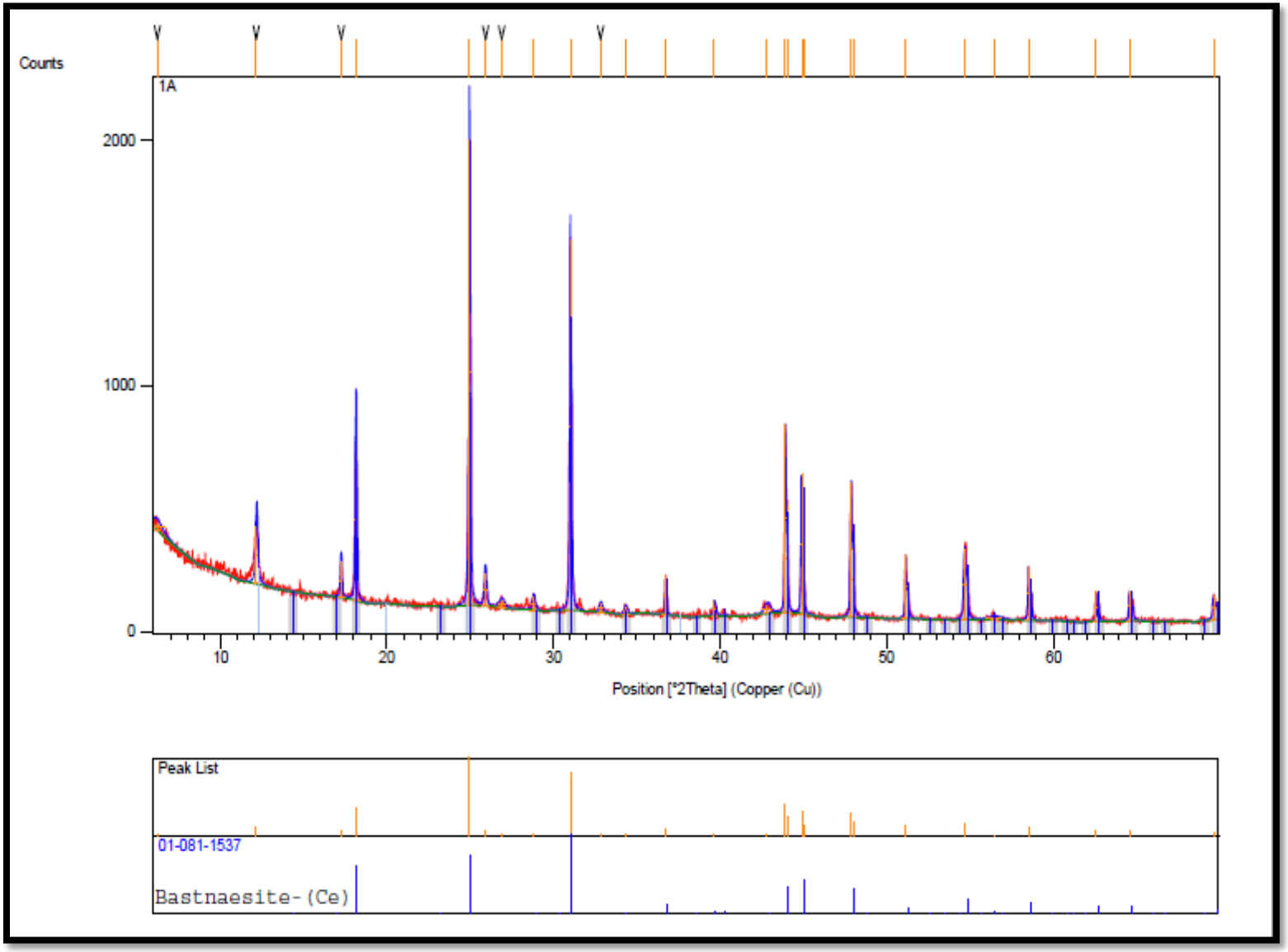

Bastnaesite 1D Red Cloud

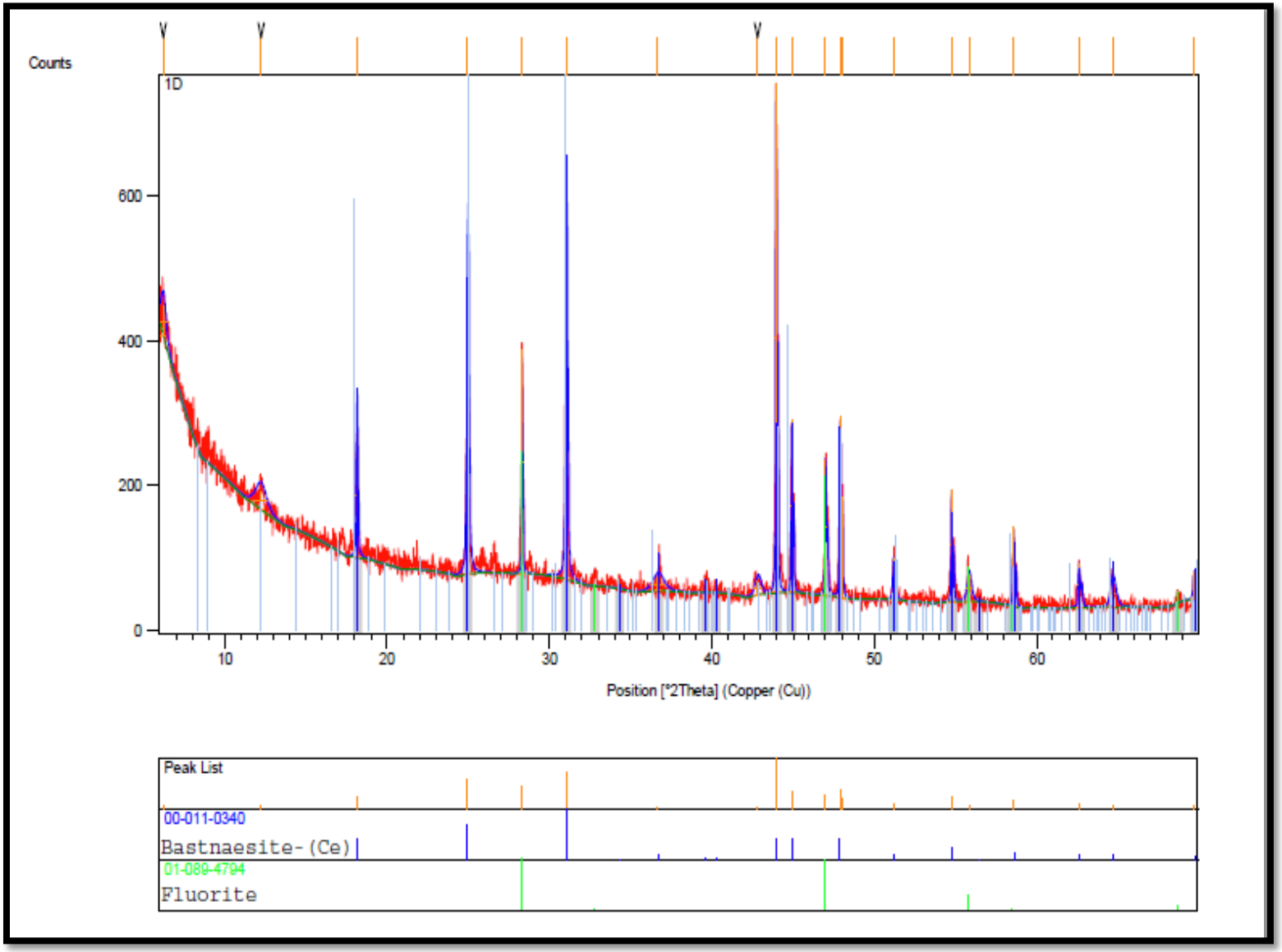

Bastnaesite 1E Red Cloud

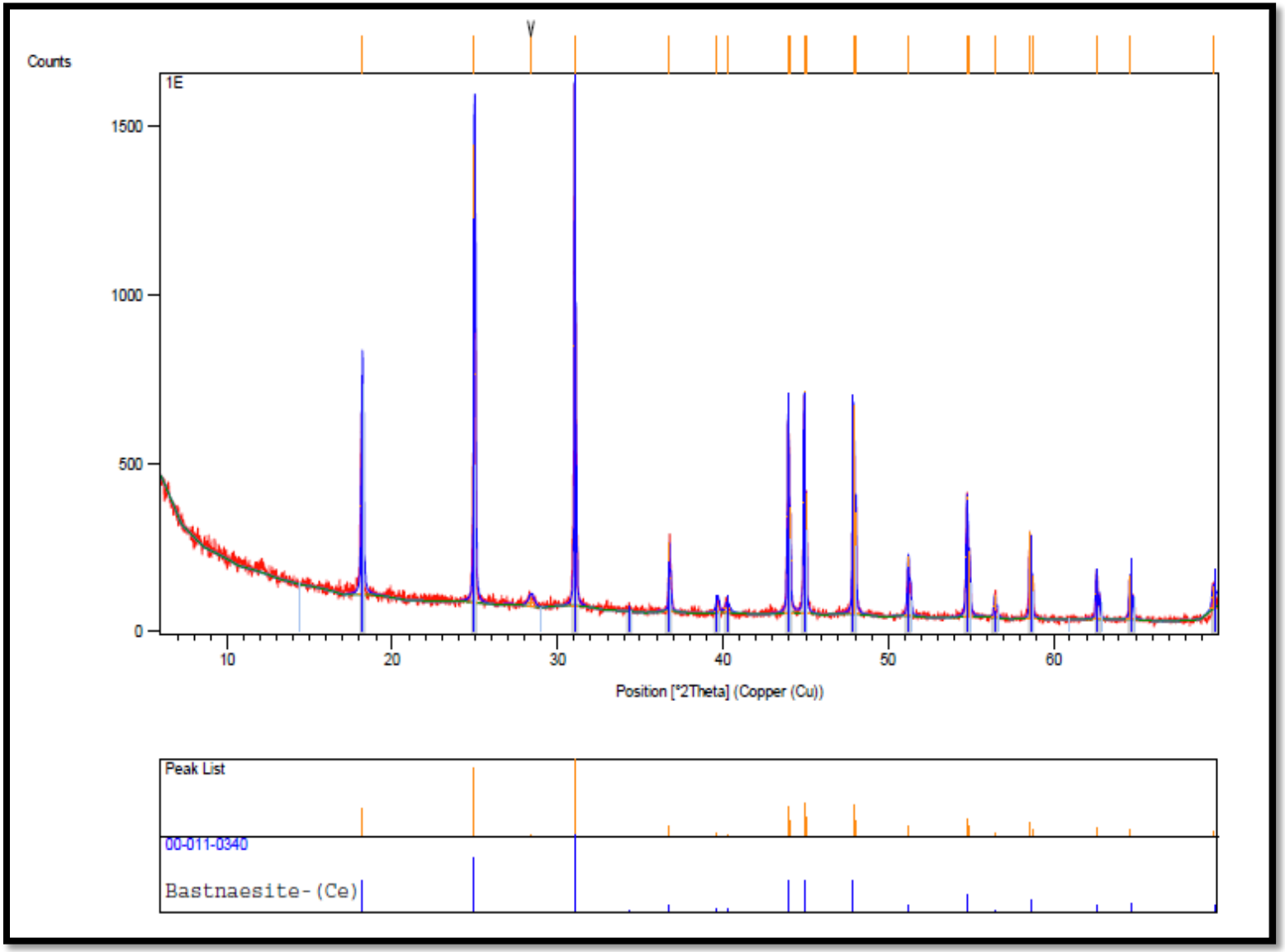

Bastnaesite Concentrate HCL Residue

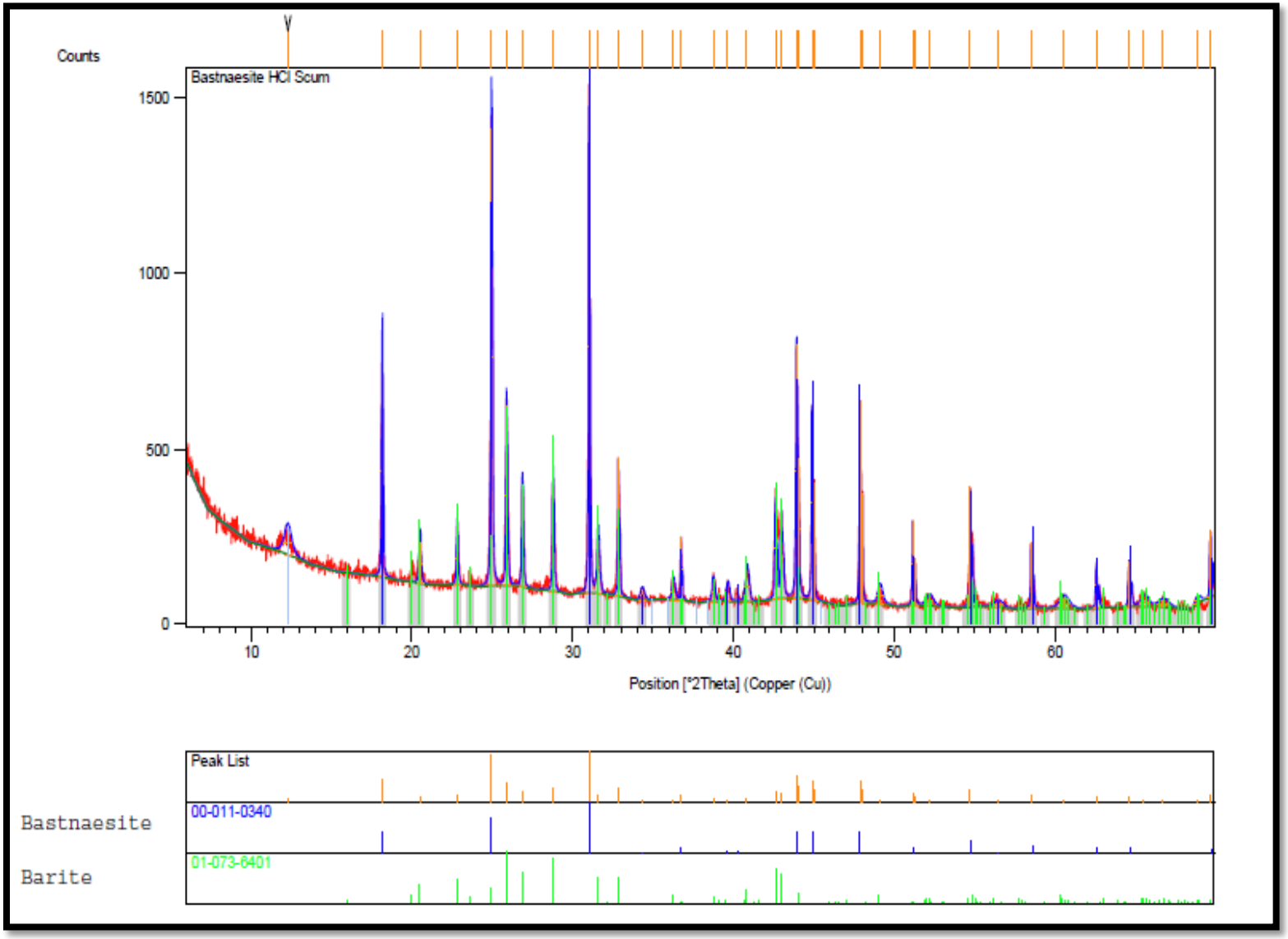

Conqueror Secondary Calcite 1

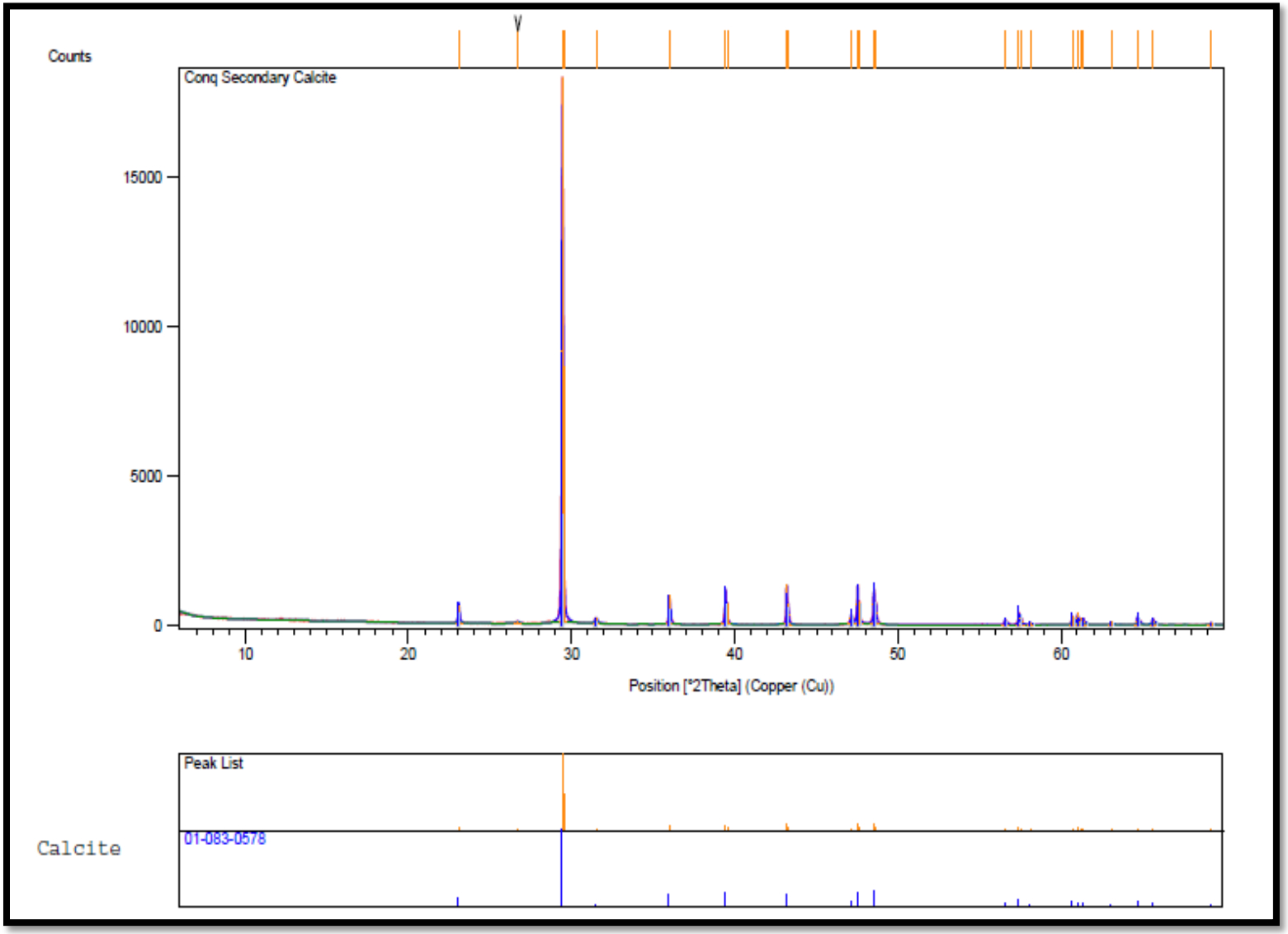

Fenite Zone, All American Iron Prospect, Whole Rock

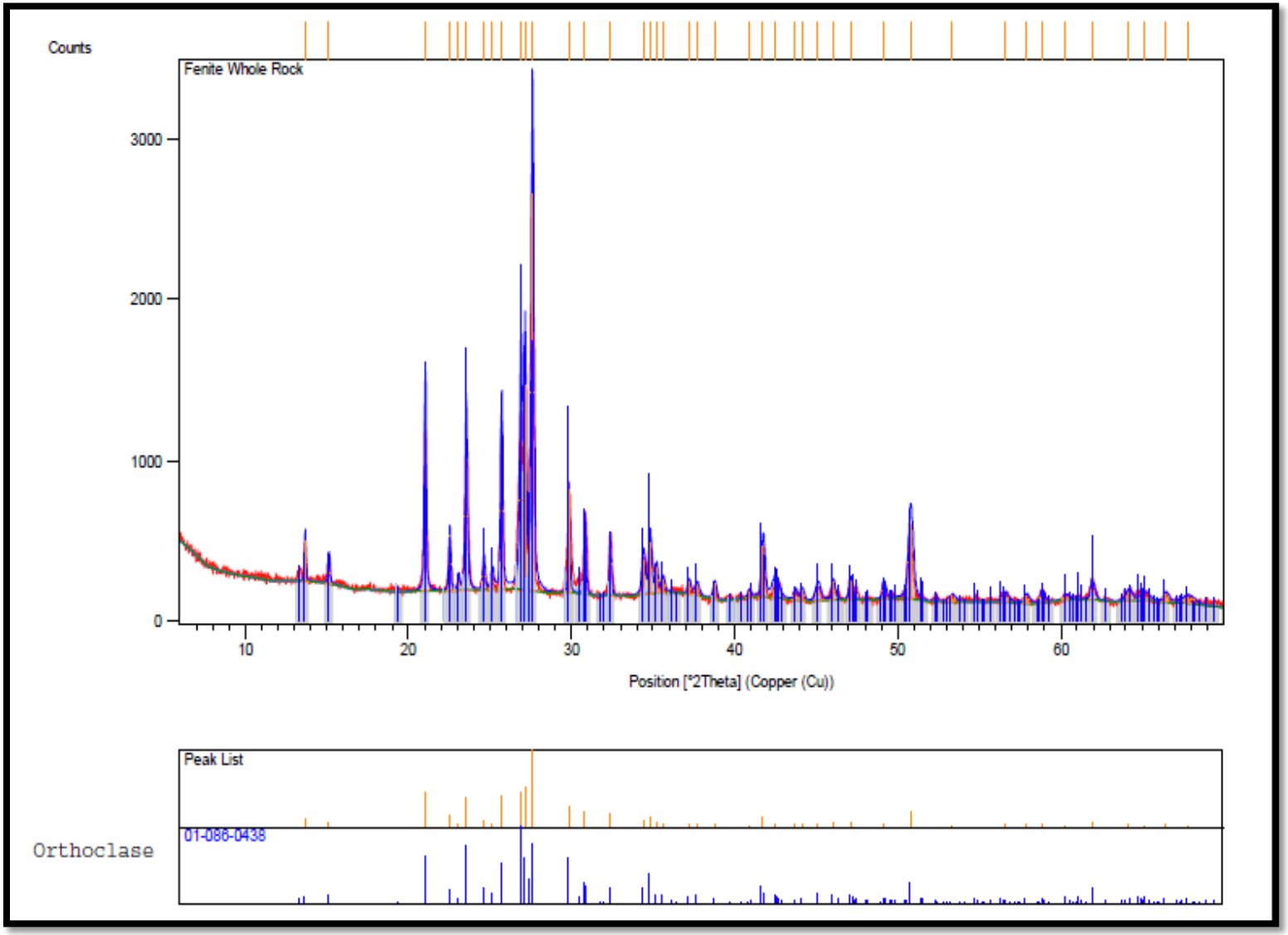

Honeywell White Phase in Fluorite Breccia

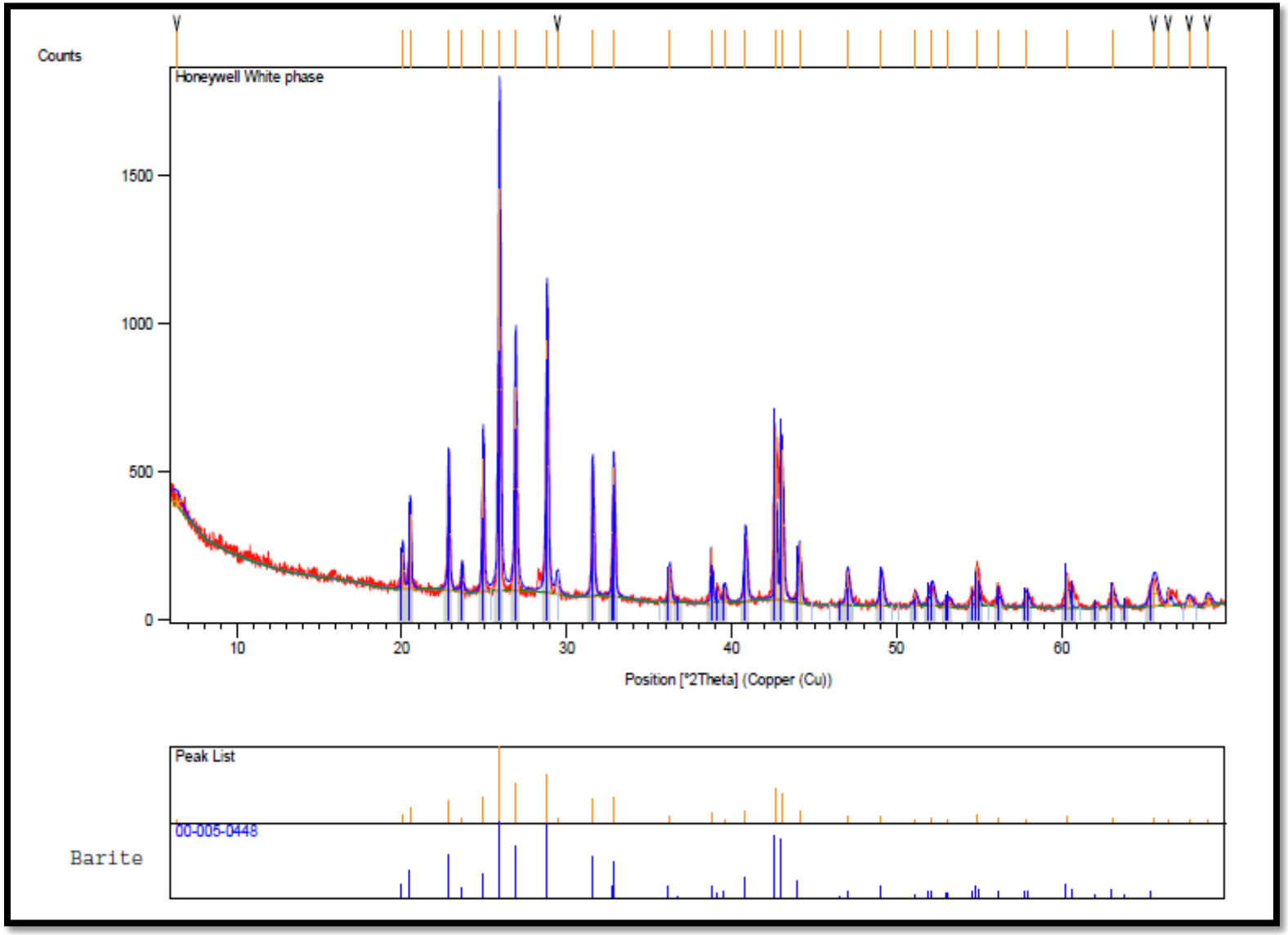

Honeywell Calcite 1

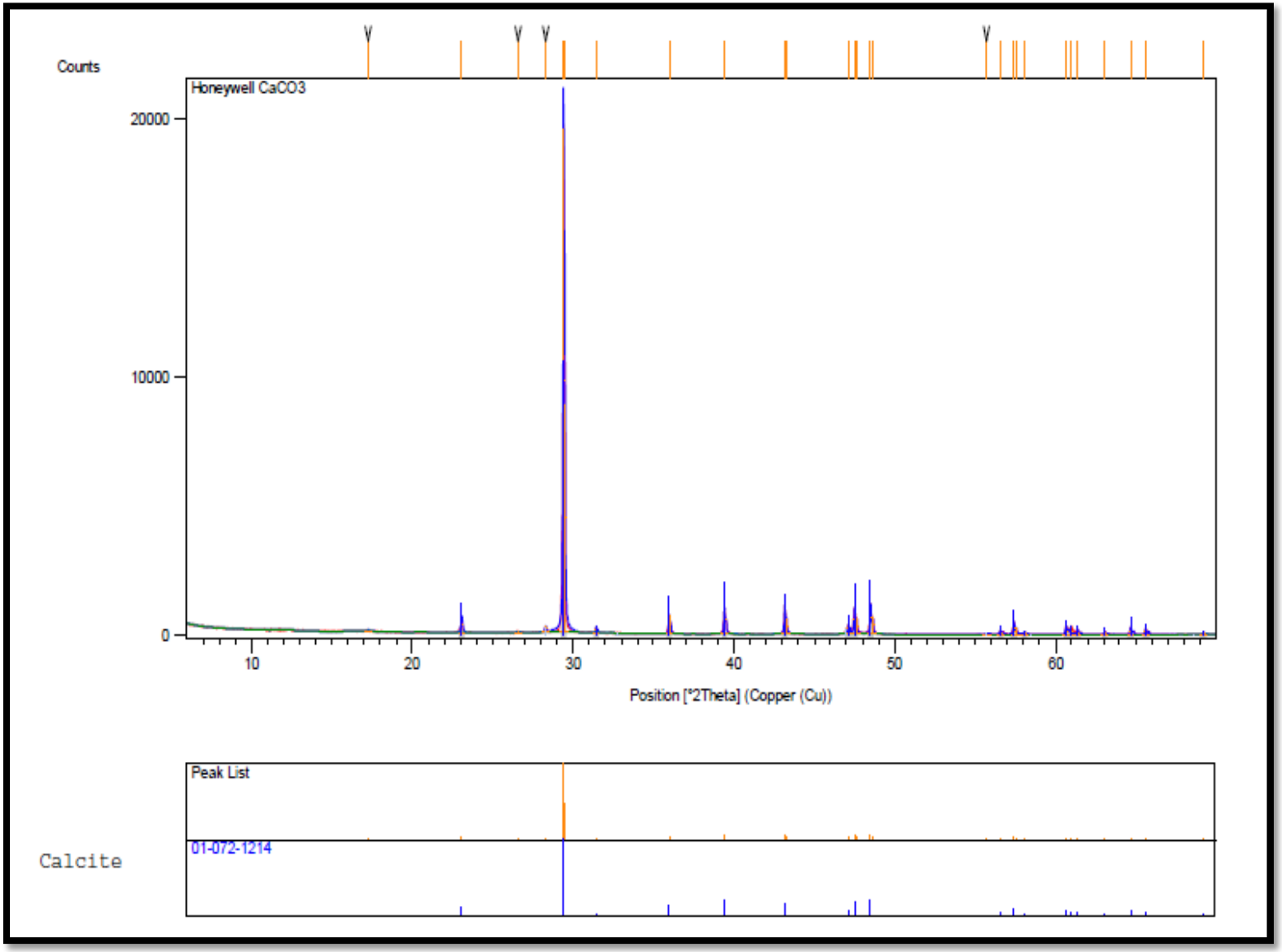

Honeywell Pyrite Replacement

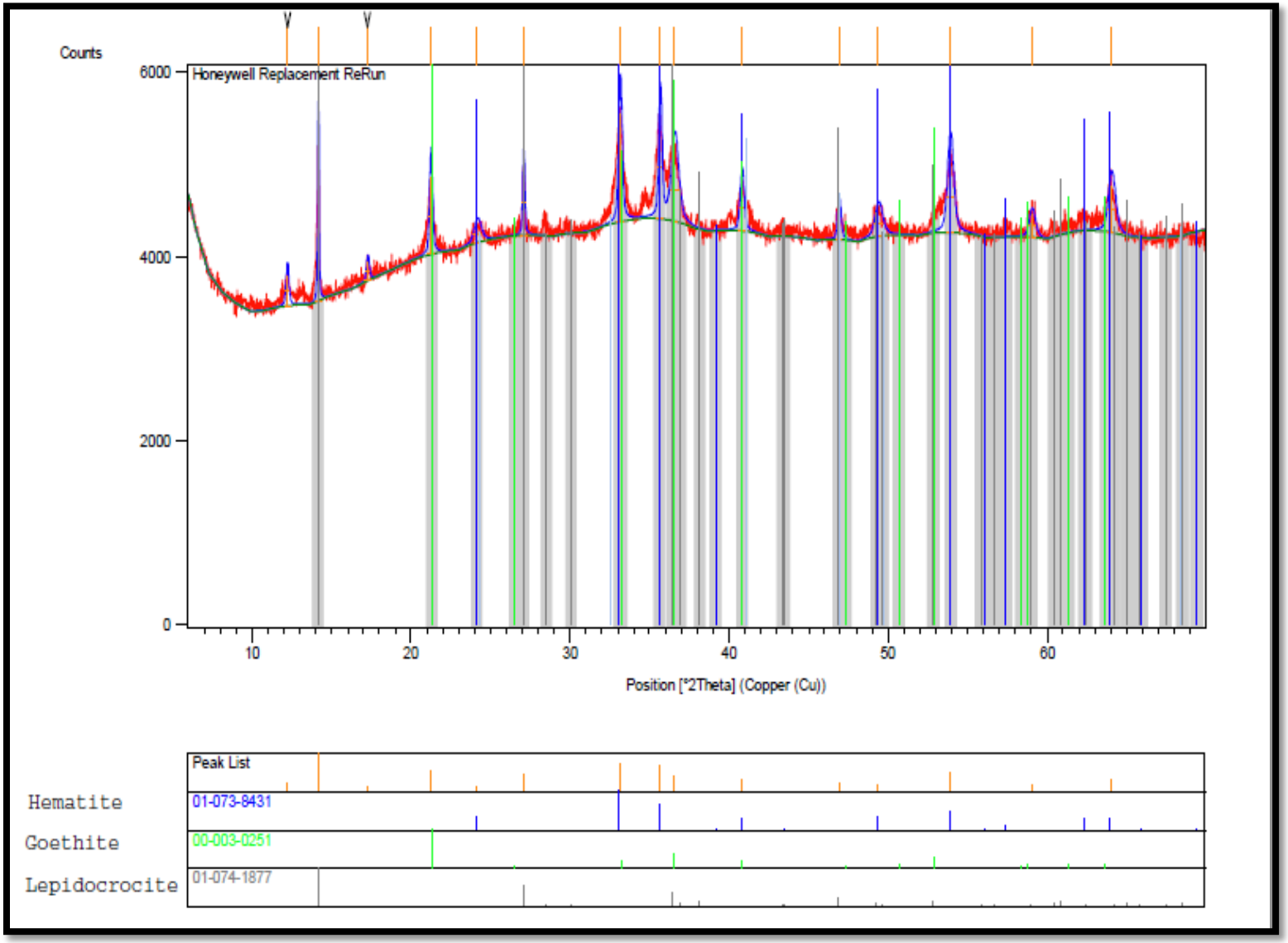

Red Cloud Sample 15 A+B

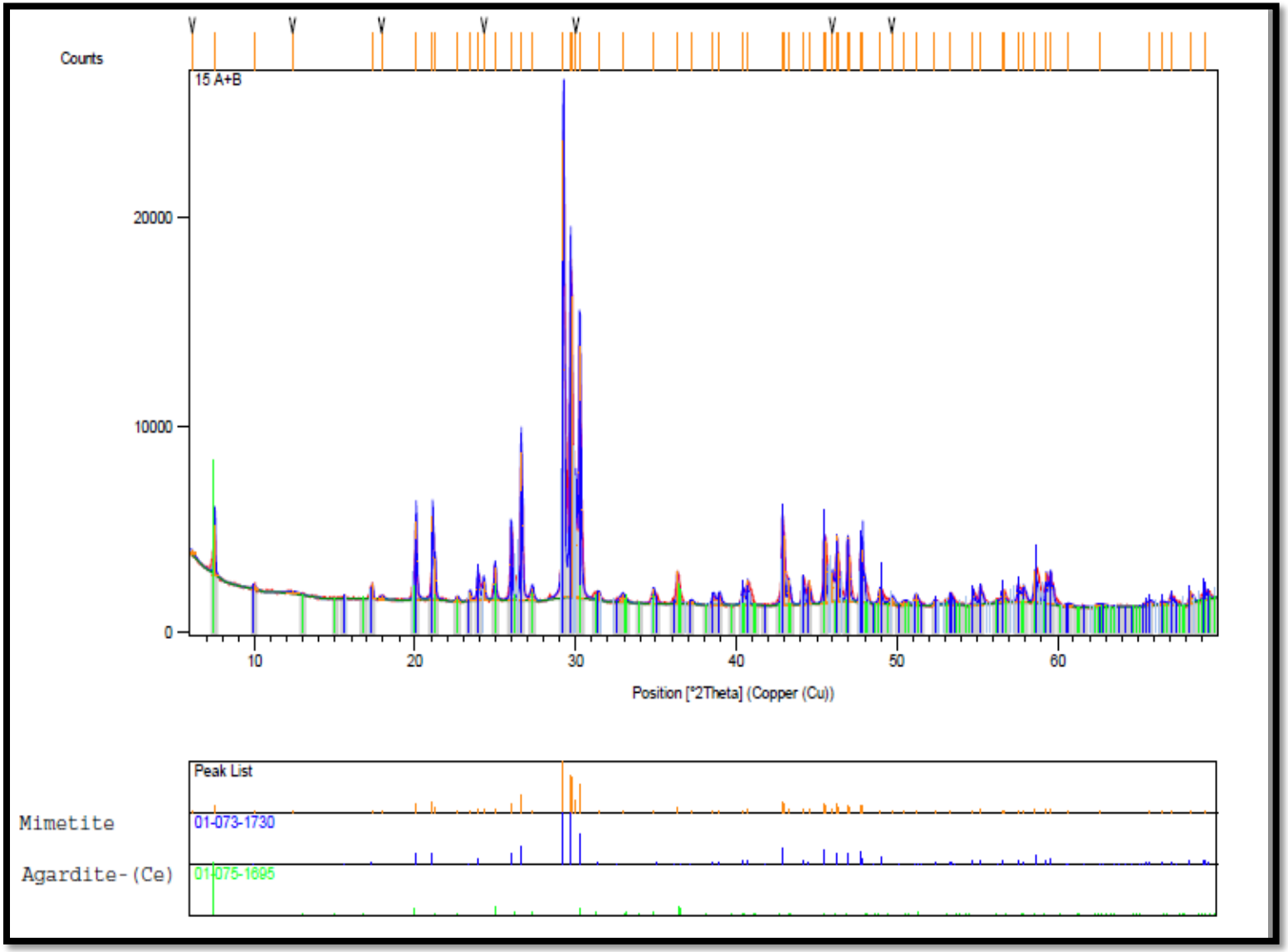

Red Cloud Pink Bastnaesite

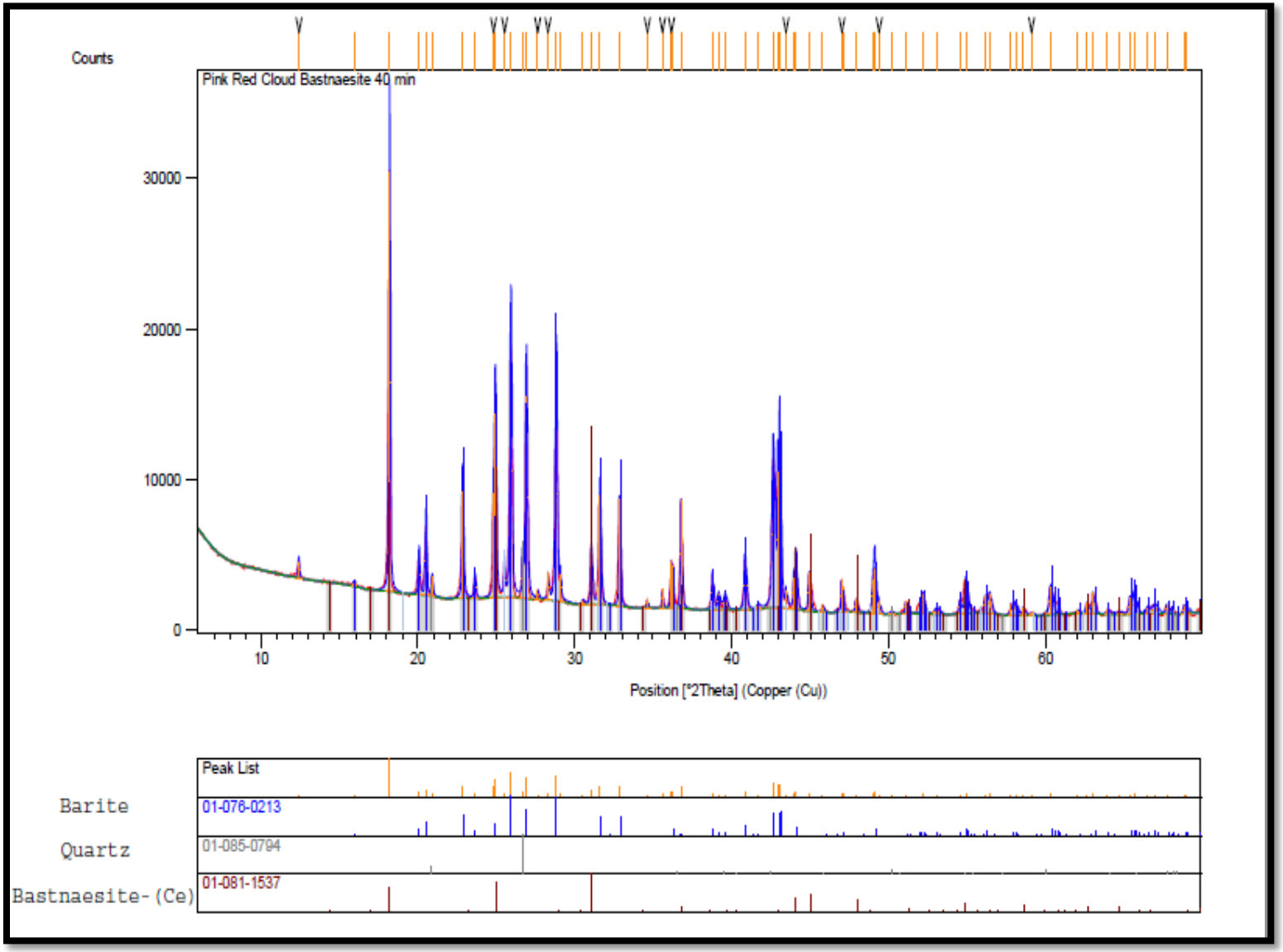

Red Cloud Sample 8A

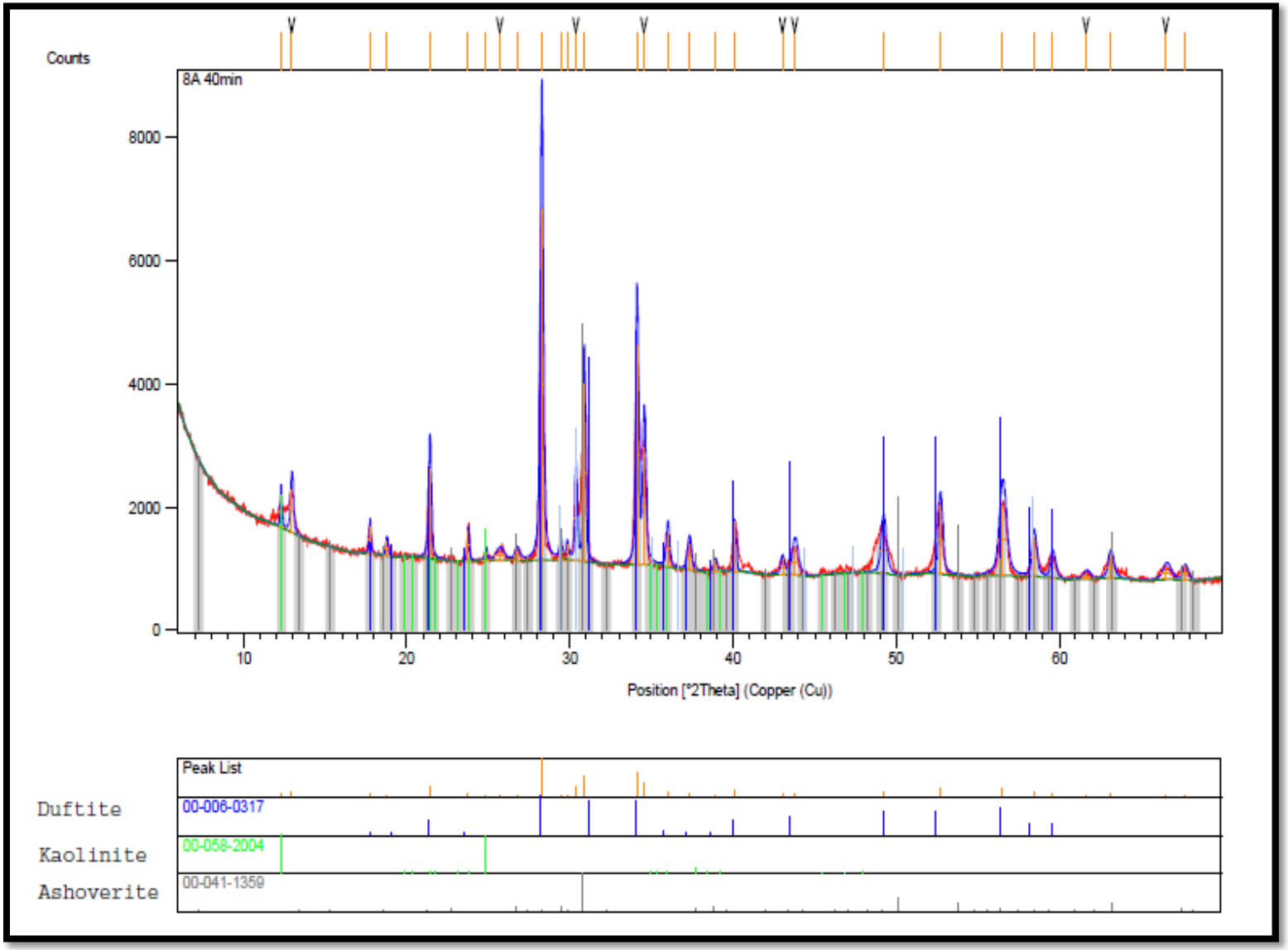

Red Cloud Unknown Weathering Products, Sample 11A-C

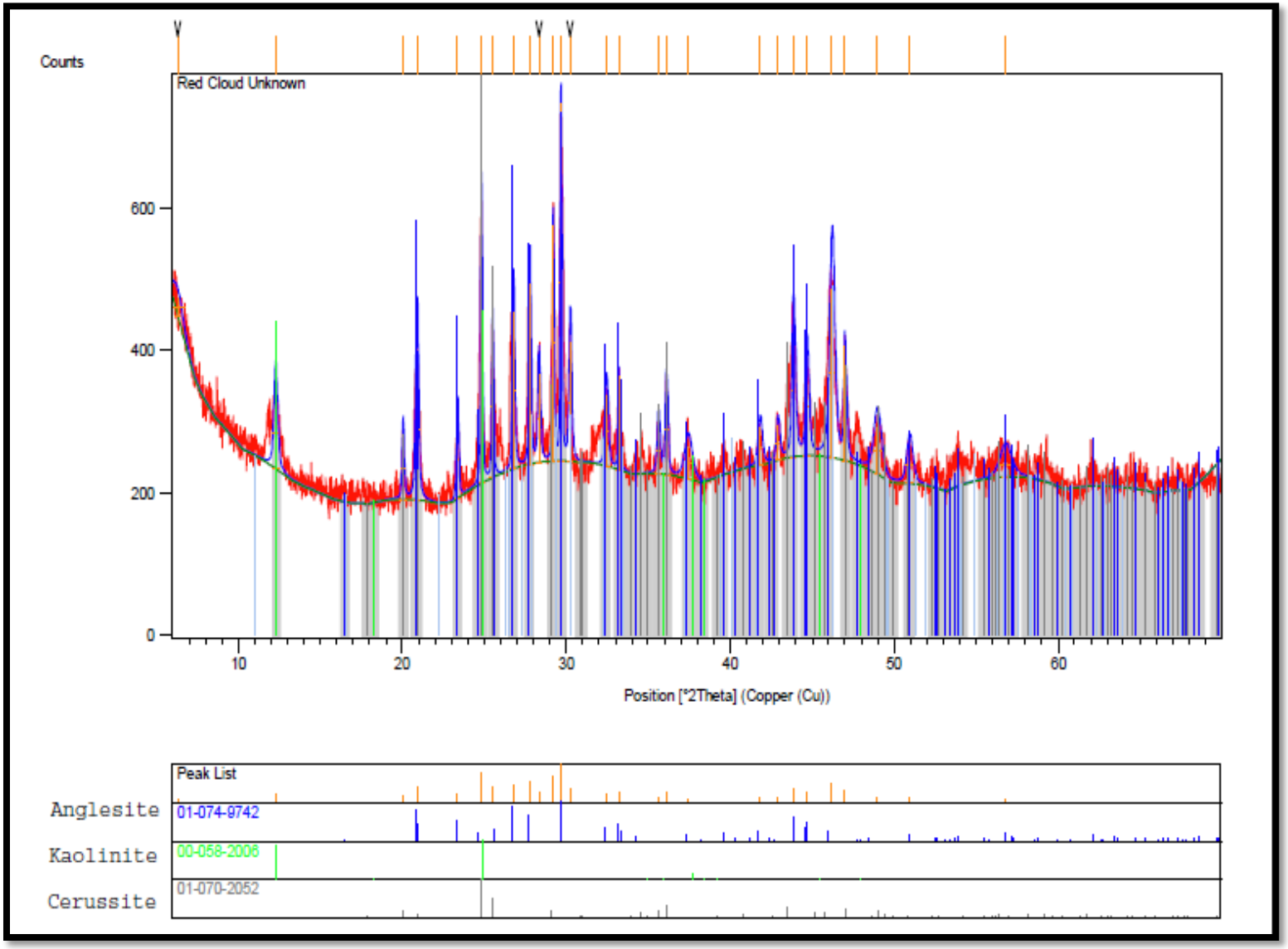

Red Cloud Sample 5A

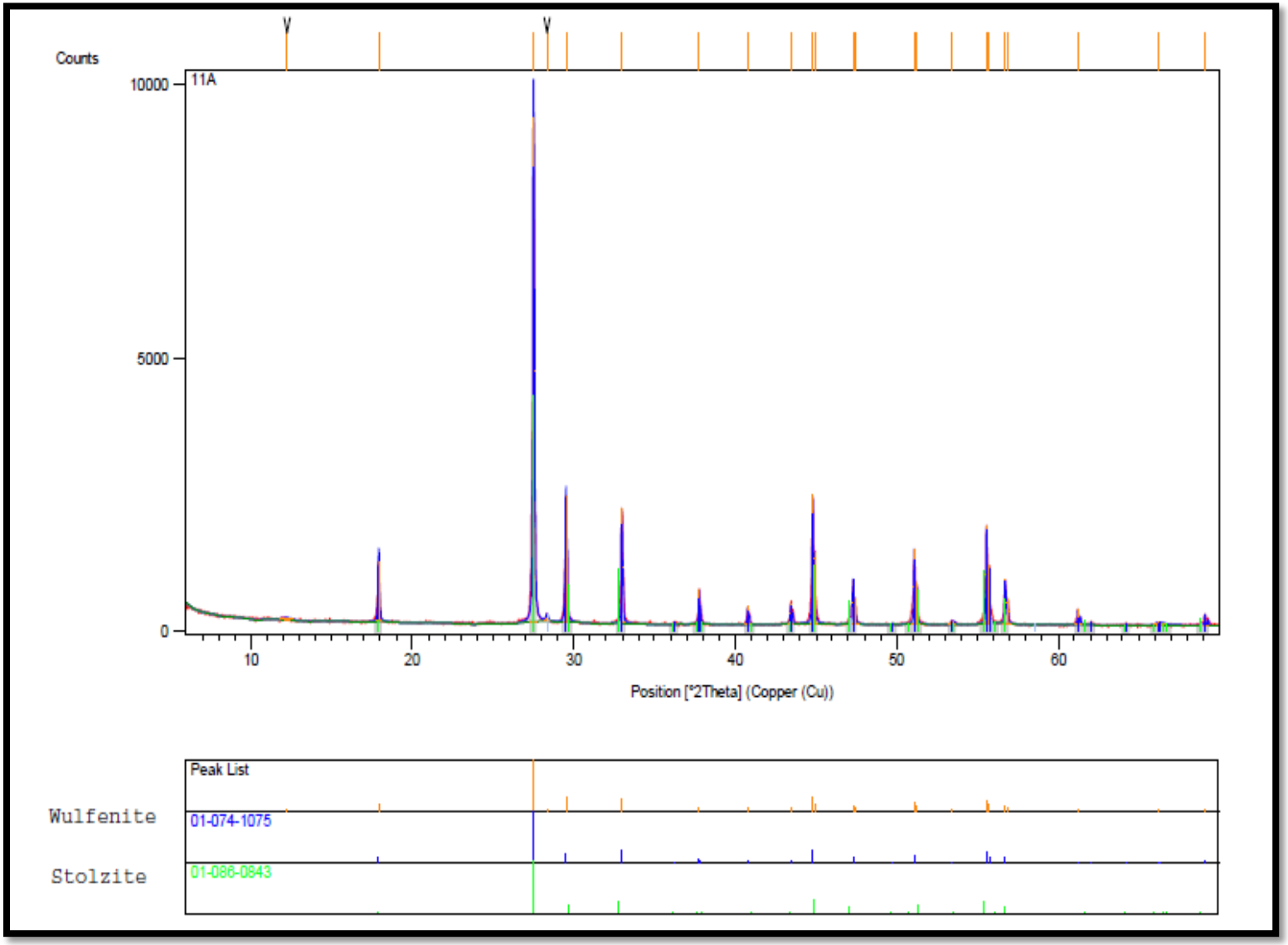

Rostite Rio Tinto

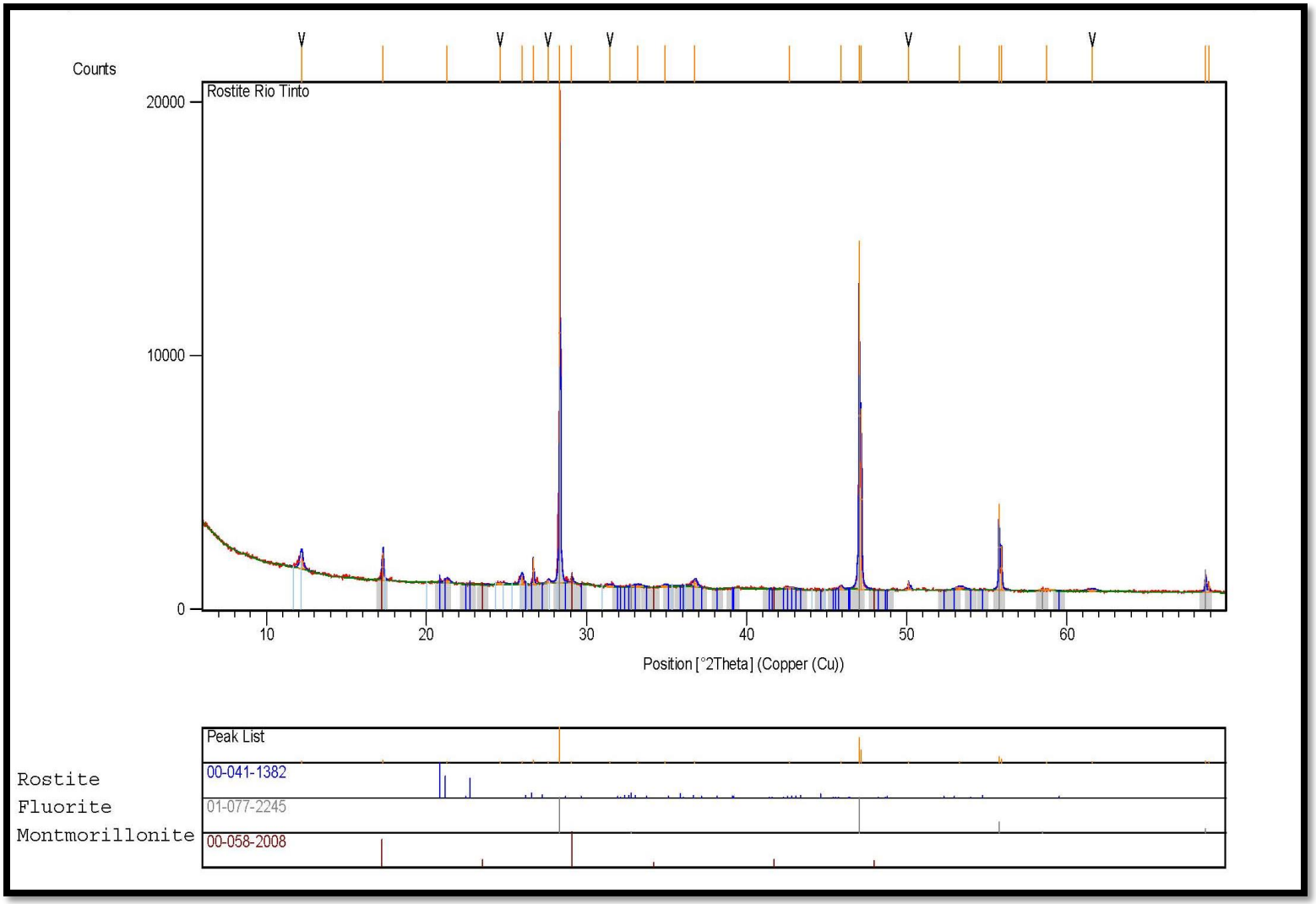

Appendix 4

Stable Isotope Results

Sample Name	Mineral	$\delta^{34}S$ vs. CDT	$\delta^{18}O_{SO4}$ vs. VSMOW	$\delta^{13}C$ vs. PDB	$\delta^{18}O$ vs. PDB
RC GL 1	Galena	1.5			
RC GL 2	Galena	1.2			
RC GL 2 DUP	Galena	-0.5			
RC GL 3	Galena	0.3			
RC GL 4	Galena	-0.8			
RC GL 5	Galena	0.4			
RC GL 6	Galena	0.7			
RC GL 7	Galena	1.1			
RC GL 8	Galena	0.0			
RC GL 13	Galena	1.6			
RC GL 13 DUP	Galena	2.1			
RC Barite 1	Galena	13.1			
RC Barite 1 DUP	Galena	13.4			
RC Barite 2	Galena	11.1			
Honeywell Barite 1	Barite	9.7			
Honeywell Barite 1 DUP	Barite	9.5			
RC GL 10A	Galena	-9.0			
RC Barite 11A	Barite	12.9			
RC Barite 11A DUP	Barite	13.5			
RC GL 10B	Galena	-7.6			
RC Barite 11B	Barite	11.1			
RC Barite 11B DUP	Barite	11.2			
RC GL 10C	Galena	-6.5			
RC GL 10C DUP	Galena	-7.9			
RC Barite 11C	Barite	11.0			
Rough Mountain Barite	Barite	9.6			
Old Hickory Galena 1	Galena	-10.4			
Old Hickory Galena 3	Galena	-17.4			
Old Hickory Brown Celestine	Celestine	1.4			
Old Hickory White Celestine	Celestine	5.2			
Rio Tinto Jarosite	Barite	-18.3			
Buckhorn Galena 1	Galena	-21.1			
Buckhorn Galena 2	Galena	-19.8			
Buckhorn Galena 3	Galena	-18.6			
Buckhorn Galena 4	Galena	-19.6			
Buckhorn Galena 5	Galena	-20.8			
Red Cloud Py eq (Gl)	Pyrite	-9.4			

Red Cloud Gl eq (Py)	Galena	-0.6			
Old Hickory Py 1 eq (Gl)	Pyrite	-11.3			
Old Hickory Py 2 eq (Gl)	Pyrite	-9.5			
Old Hickory Gl eq (Py)	Galena	-18.6			
Red Cloud Barite 1	Barite		4.0		
Red Cloud Barite 1 DUP	Barite		3.2		
Red Cloud Barite 2	Barite		5.2		
Rough Mountain Barite 1	Barite		7.8		
Rough Mountain Barite 1 DUP	Barite		6.6		
Rio Tinto Barite 2	Barite		6.1		
Honeywell Barite	Barite		5.1		
Red Cloud Barite 11A	Barite		0.5		
Red Cloud Barite 11C	Barite		4.2		
Rio Tinto Jarosite whole	Jarosite		0.1		
Rio Tinto Jarosite SO4	Barite		9.3		
Rio Tinto Jarosite SO4 DUP	Barite		8.7		
RC Pink Bast	Bastnaesite			-11.1	-14.2
Red Cloud Y Bast	Bastnaesite			-7.4	-8.5
ME 13 Y Bast DUP	Bastnaesite			-7.9	-8.5
ME 13 Y Bast	Bastnaesite			-7.6	-7.5
ME13 Y. Bast 2	Bastnaesite			-7.4	-8.1
ME13 Y. Bast 3	Bastnaesite			-8.1	-8.9
ME 13 YESO DUP	Calcite			-6.6	-7.2
ME 13 YESO	Calcite			-6.6	-7.3
ME 13 calcite vein 7b	Calcite			-6.5	-6.5
Rough mtn YESO	Calcite			0.0	-10.4
Conq Calc coating 2	Calcite			-7.2	-8.3
ME 13 calc vug 12	Calcite			-5.4	-7.6
ME 13 calc veining 1 DUP	Calcite			-6.6	-6.4
ME 13 calc veining 1	Calcite			-6.8	-7.1
Conq Calc Coating 1 DUP	Calcite			-7.3	-8.3
Conq Calc Coating 1	Calcite			-7.2	-7.9
ME 13 7a calcite vein	Calcite			-6.8	-5.3
ME 13 Calc vug dup	Calcite			-5.5	-7.1
ME 13 Calc vug	Calcite			-5.5	-6.8
Honeywell Calcite DUP	Calcite			-9.0	-8.9
Honeywell Calcite	Calcite			-9.0	-8.8
Gallnas H1 98.5 Calcite Vugs	Calcite			-3.4	-8.2
Rio Tinto Calc 2	Calcite			-7.3	-8.5

Rough Mtn Calc 2	Calcite	-5.0	-7.8
HW Calc 4	Calcite	-8.1	-8.7
Sky High Calc 2	Calcite	-5.8	-7.9
HW Calc 2	Calcite	-7.7	-8.8
Sky High Calc 1	Calcite	-6.4	-8.6

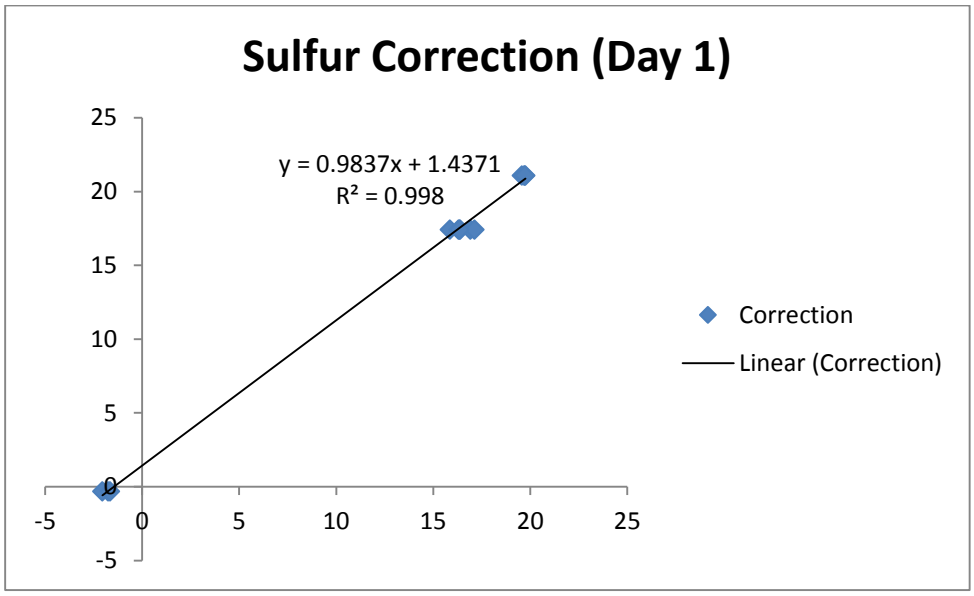

Begins at "RC GL 1"

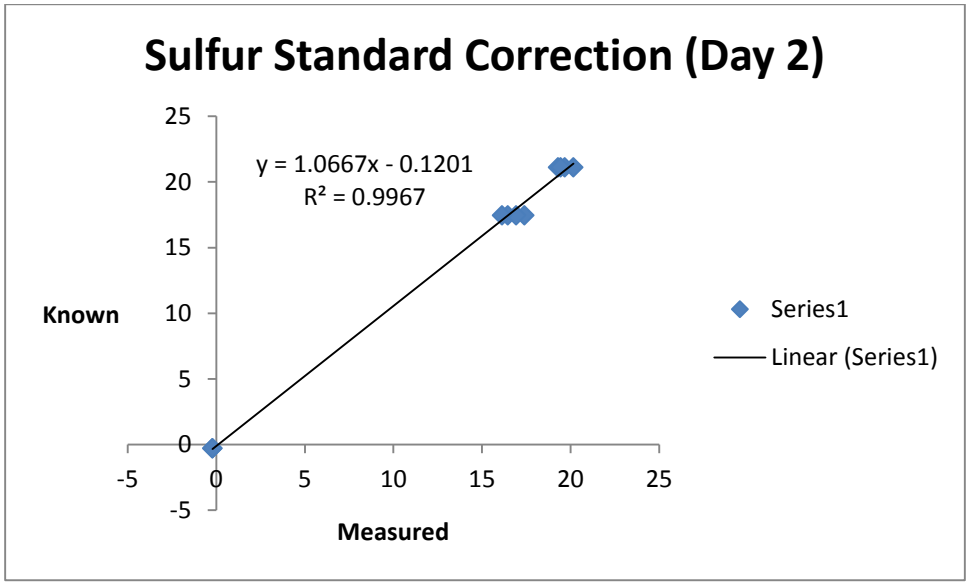

Begins at "Rough Mountain Barite"

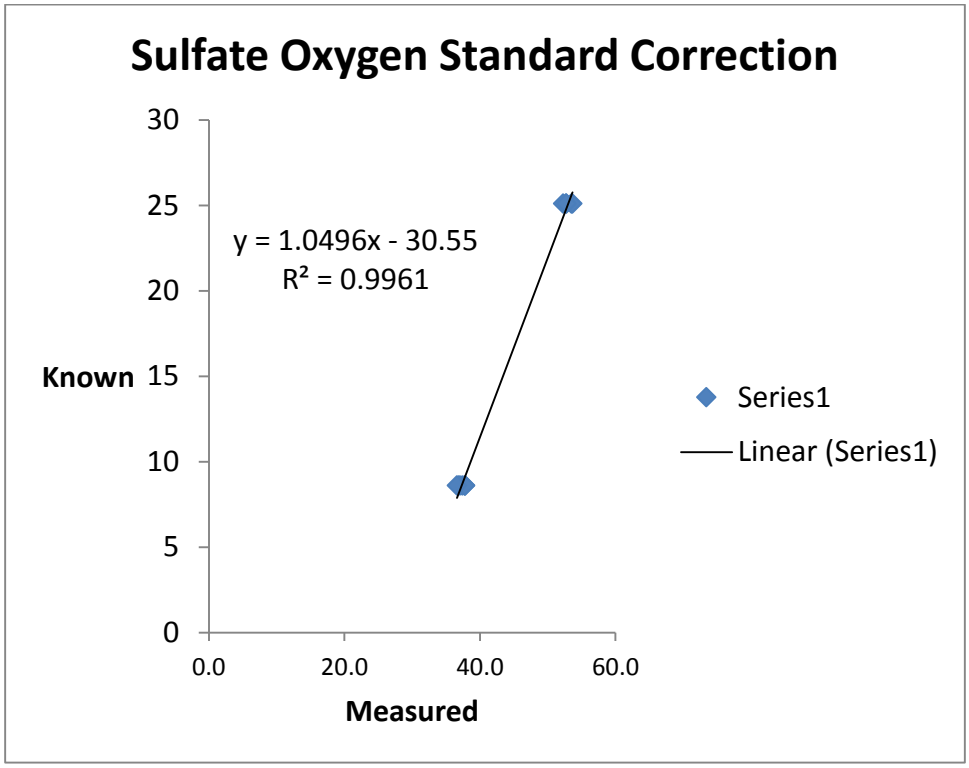
Sulfate Oxygen Standard Correction
30
25
20
15
10
5
0
Known
y = 1.0496x - 30.55
R² = 0.9961
0.0
20.0
40.0
60.0
Measured
Series1
Linear (Series1)

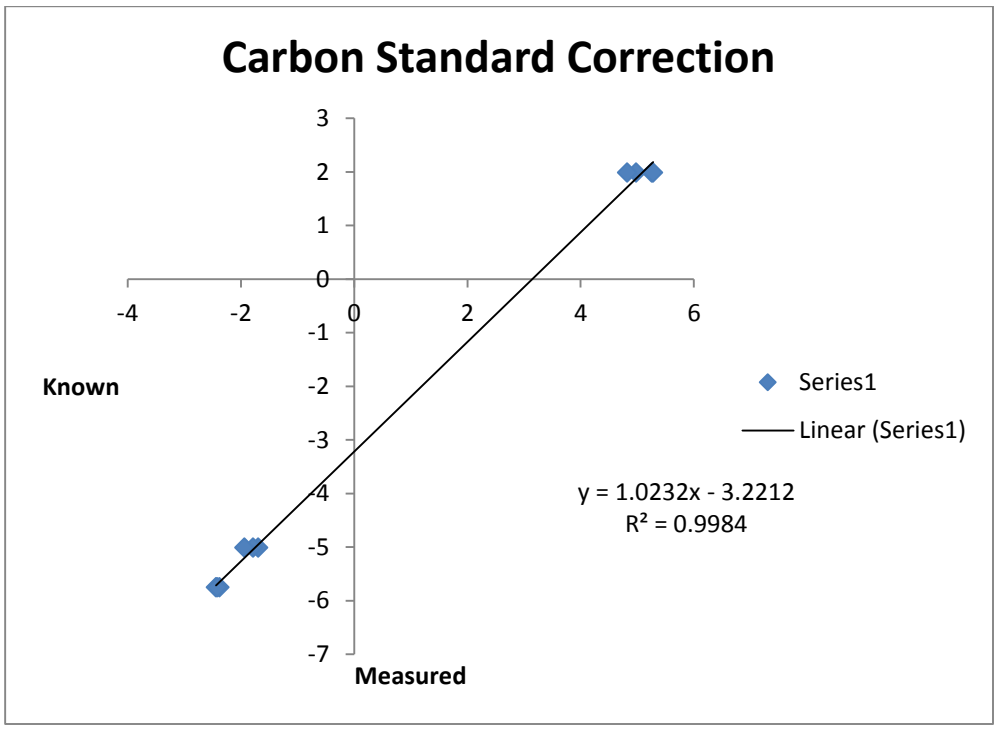
Carbon Standard Correction
3
2
1
0
-1
-2
-3
-4
-5
-6
-7
-4
-2
0
2
4
6
Known
Measured
y = 1.0232x - 3.2212
R² = 0.9984
Series1
Linear (Series1)

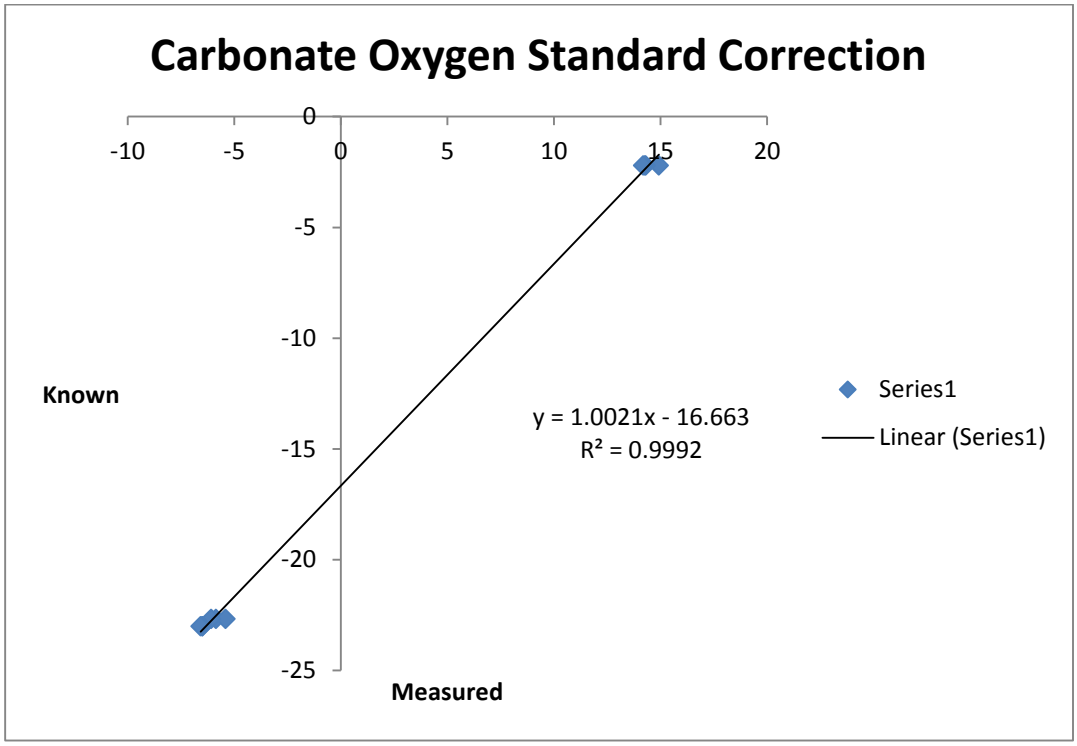
Carbonate Oxygen Standard Correction
0
-10
-5
0
5
10
15
20
-5
-10
-15
-20
-25
Known
Measured
y = 1.0021x - 16.663
R² = 0.9992
Series1
Linear (Series1)

APPENDIX 5
Electron Probe Microanalysis
Quantitative, Qualitative, and Imaging data

M and E No. 13 Bastnaesite in Fluorite Breccia

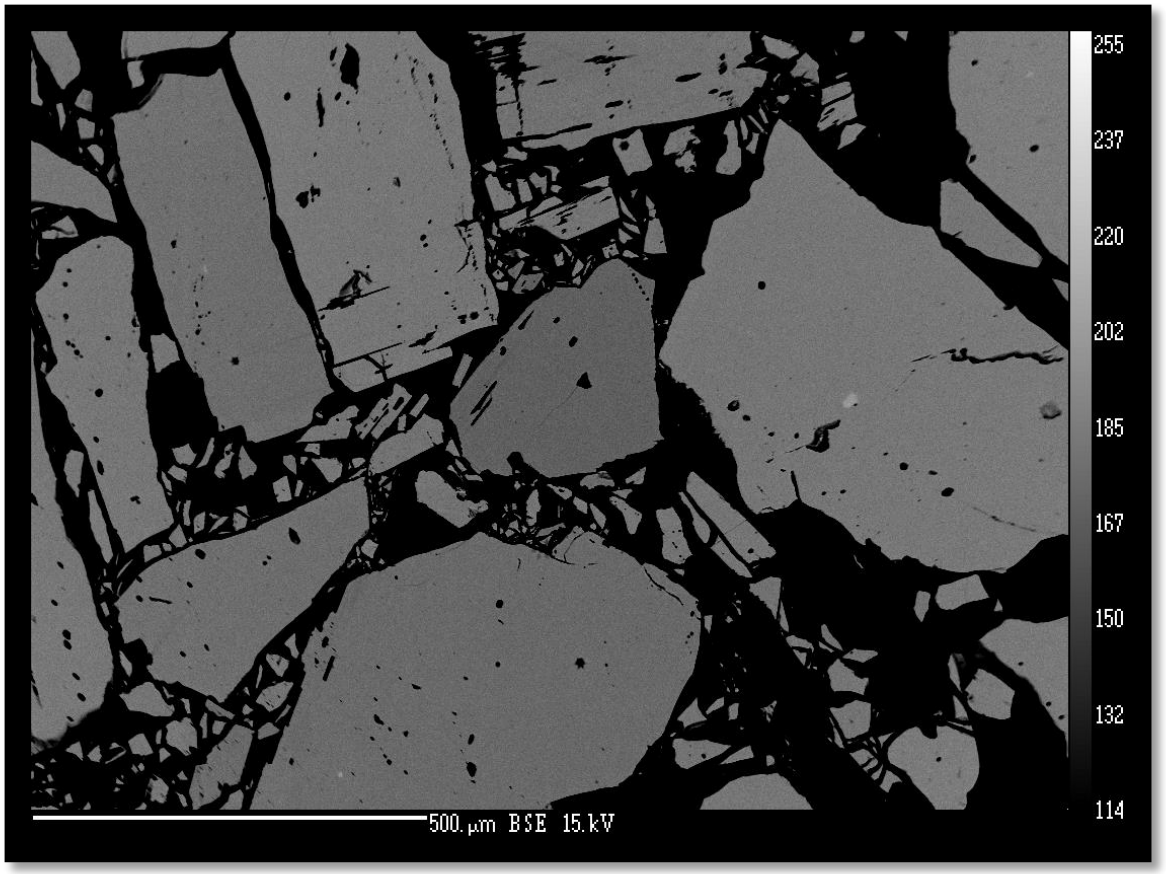

Figure 2. M and E No. 13 bastnaesite grains. Lower Z bastnaesite as a darker grain in the middle of the image. Matrix consists of quartz and fluorite.

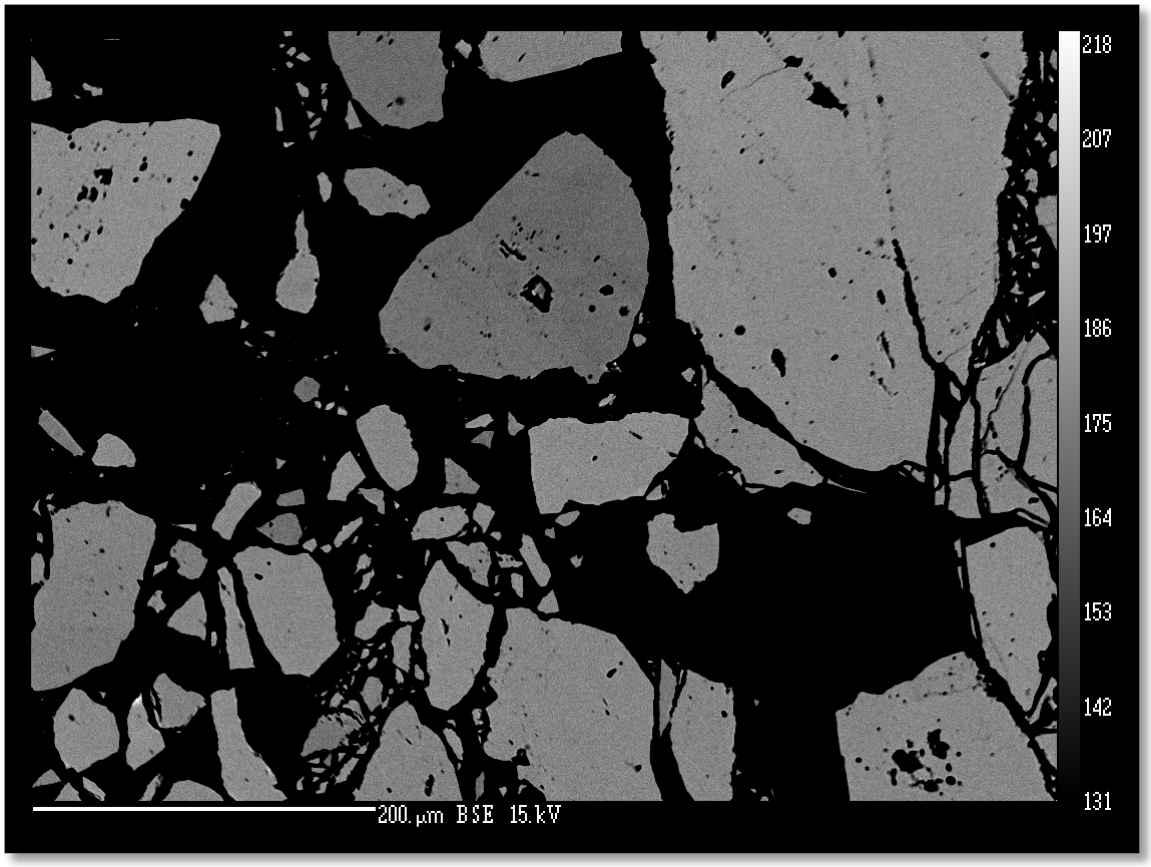

Figure 3. M and E No. 13 bastnaesite grains. Lower Z bastnaesite as a darker grain in the middle of the image**.** Matrix consists of quartz and fluorite.

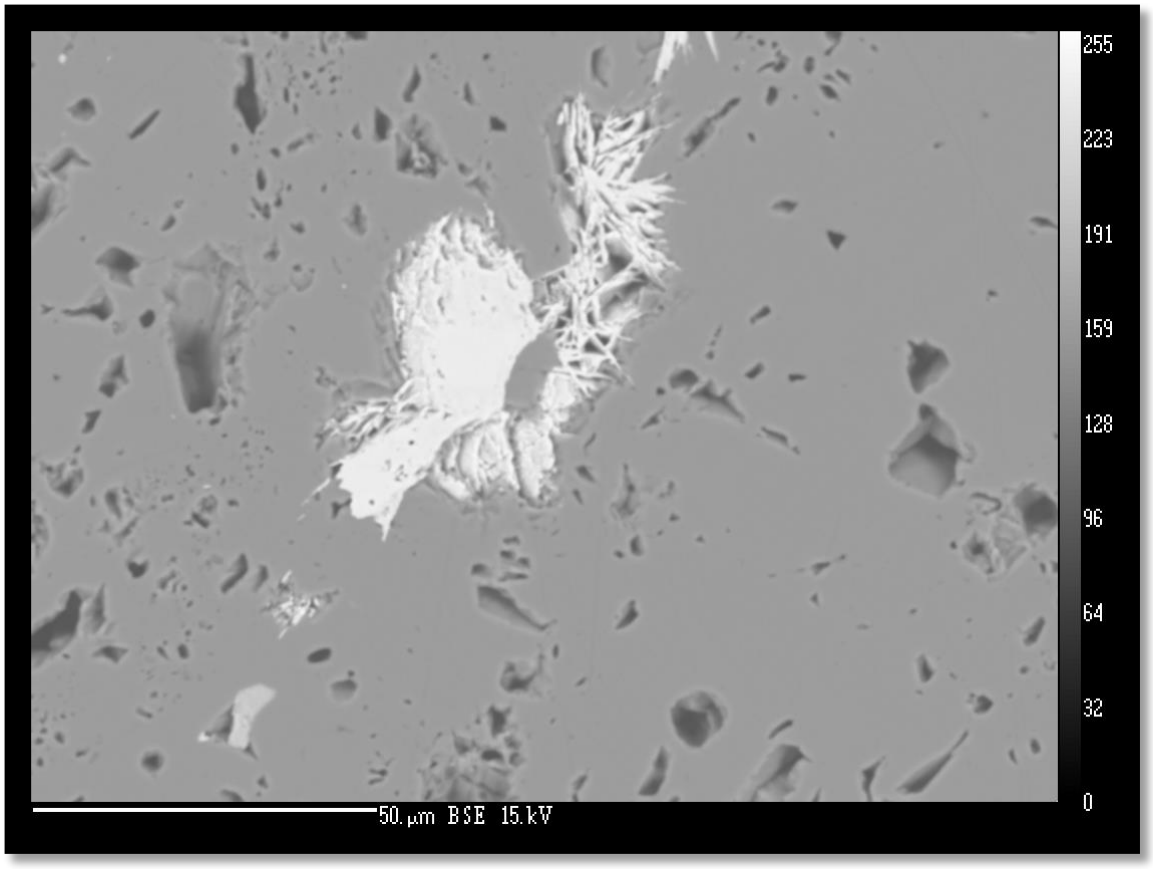

Figure 4. REE-Needle aggregate from M and E No. 13. Possible bastnaesite or parisite.

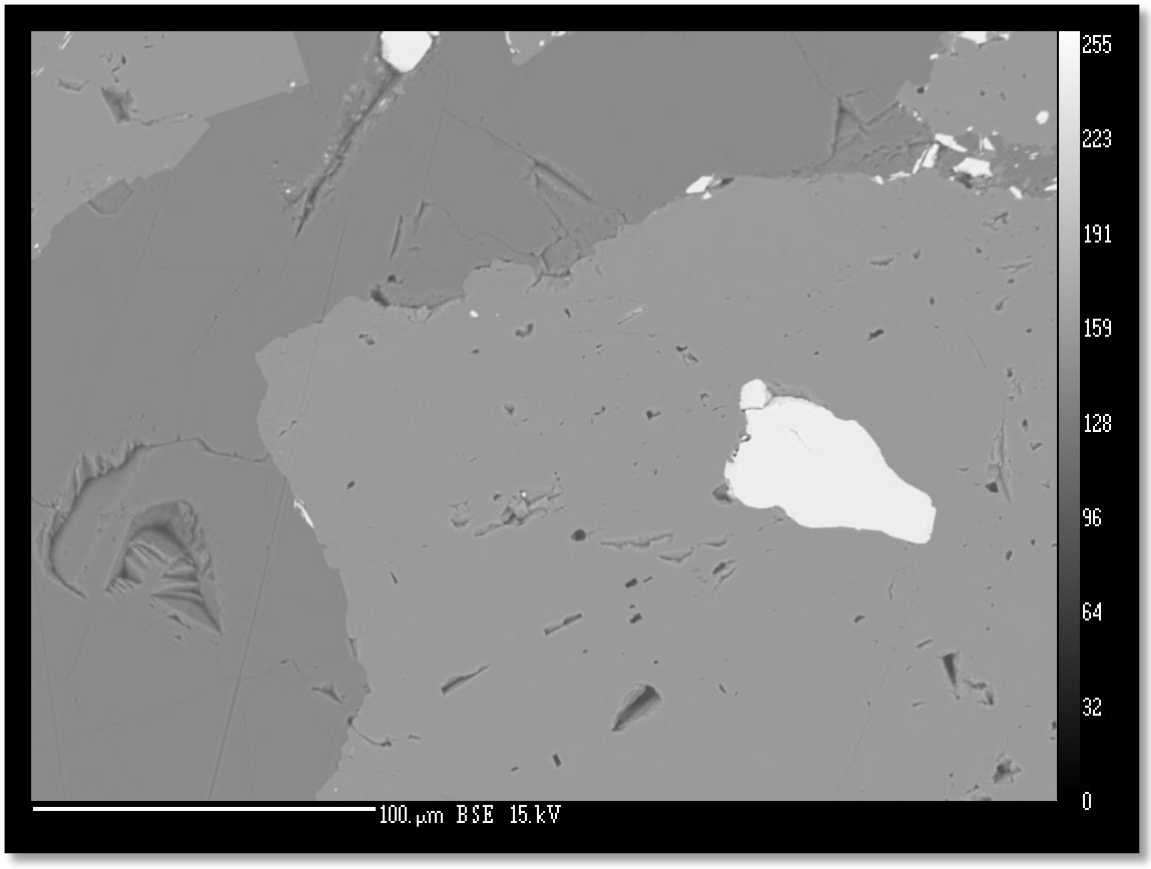

Figure 5. Bastnaesite and two chemically distinct phases of fluorite. Higher Z fluorite surrounds bastnaesite grain.

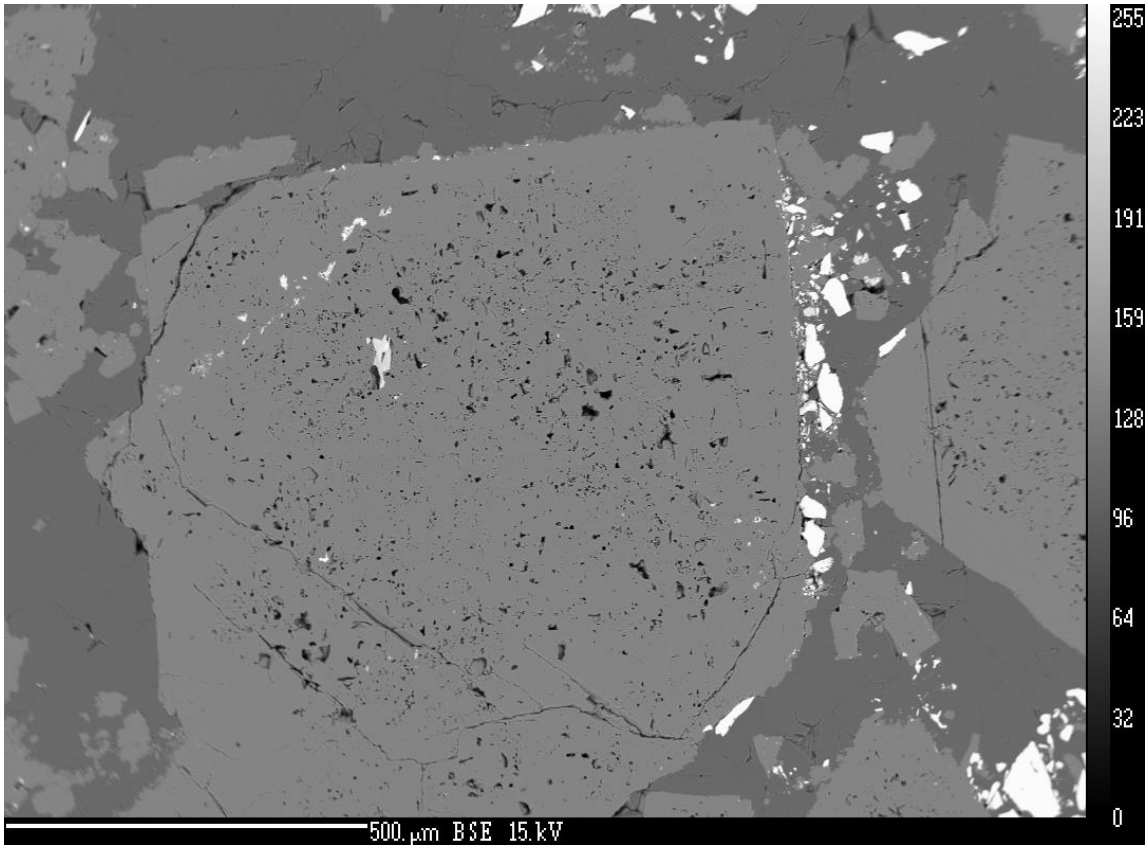

Figure 6. Bastnaesite overgrowth on fluorite grain.

Red Cloud Bastnaesite Concentrate

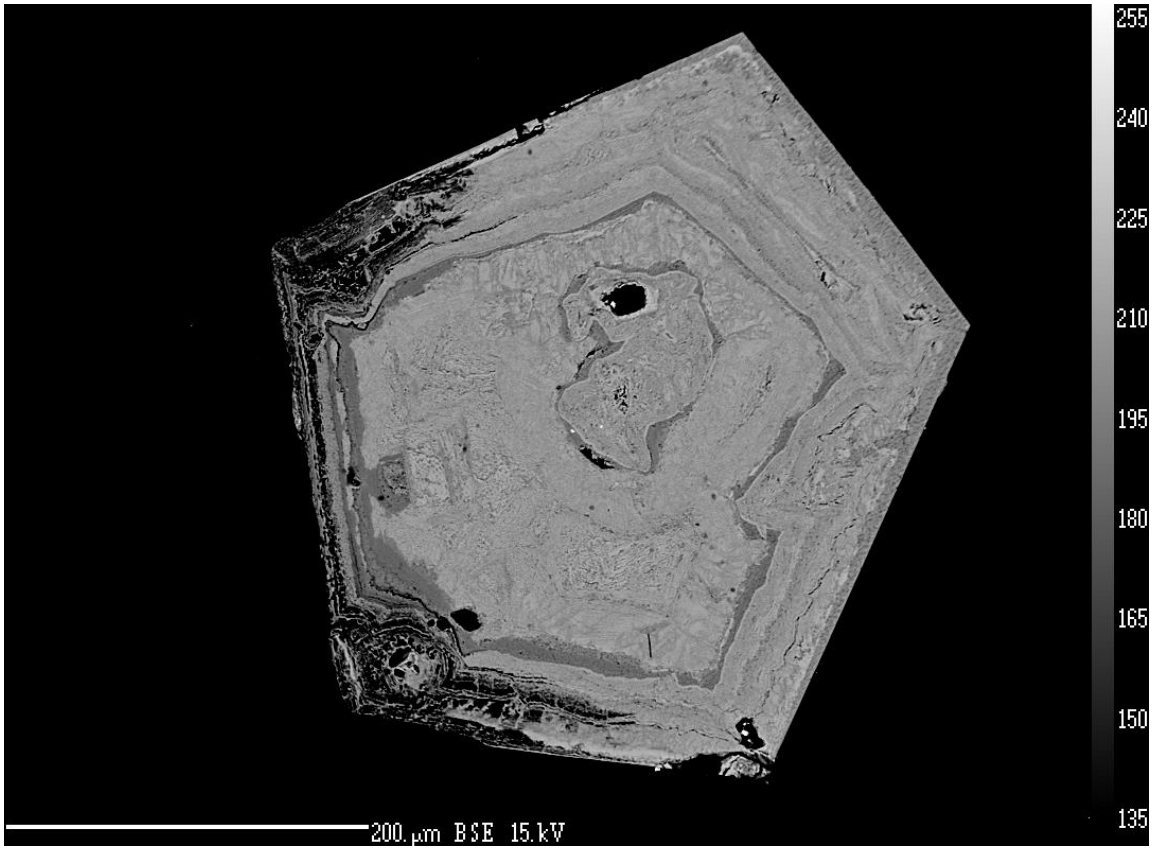

Figure 7. Goethite/hematite ps. pyrite. Distinct chemical zoning from core to rim with a very small (1 micron) relict pyrite grain.

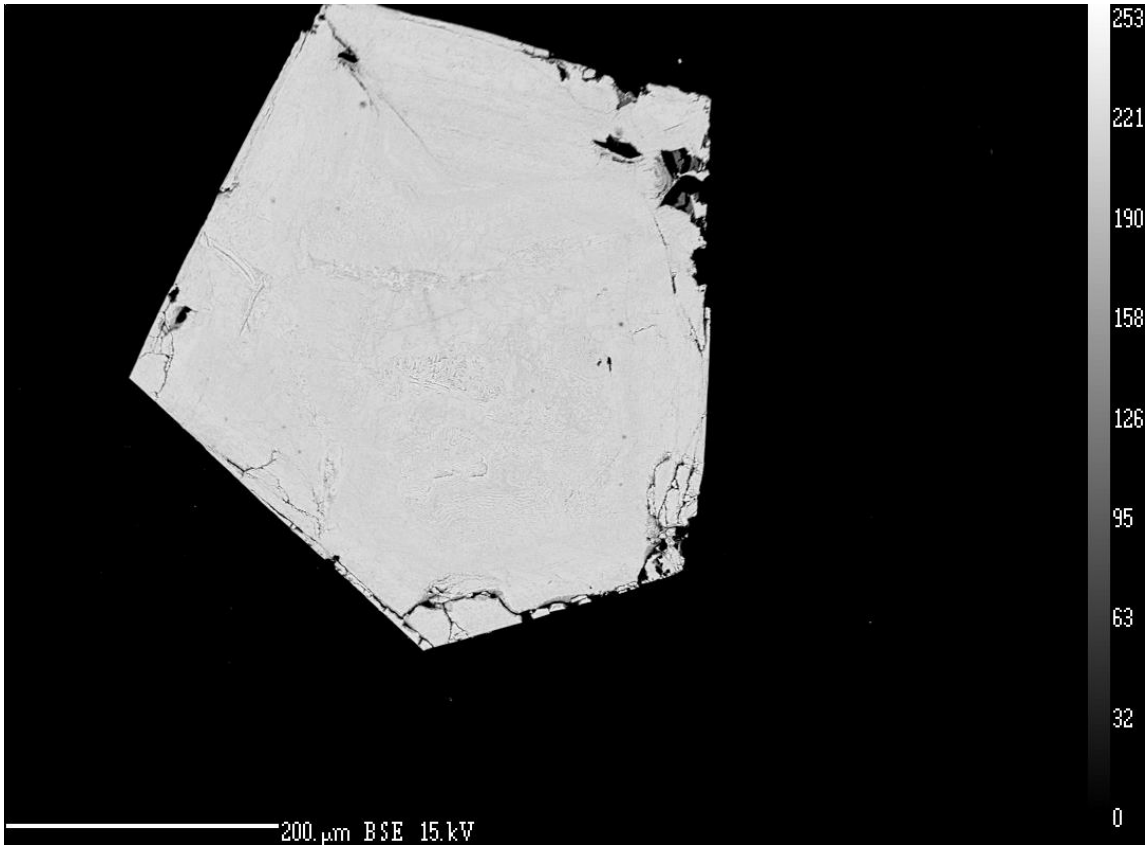

Figure 8. Goethite/hematite ps. pyrite.

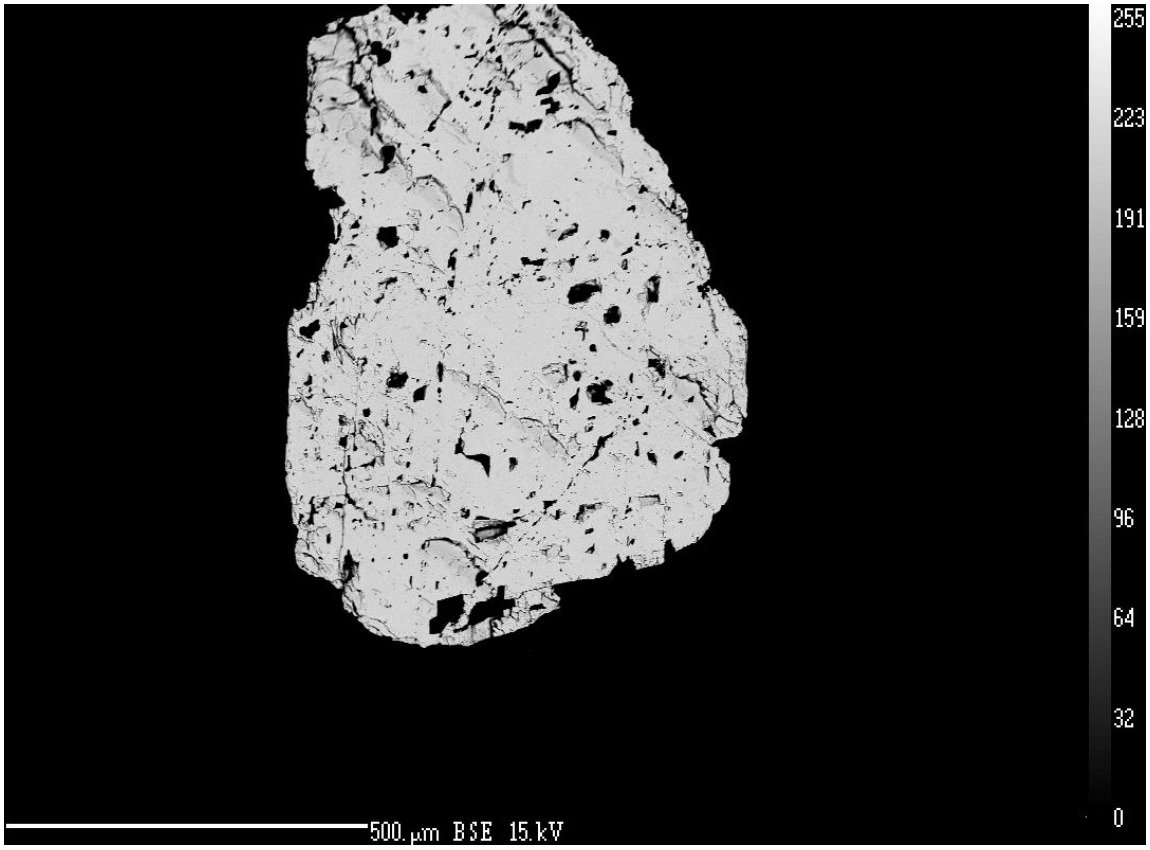

Figure 9. Bastnaesite grain from Red Cloud bastnaesite concentrate. Chemical zoning is not present.

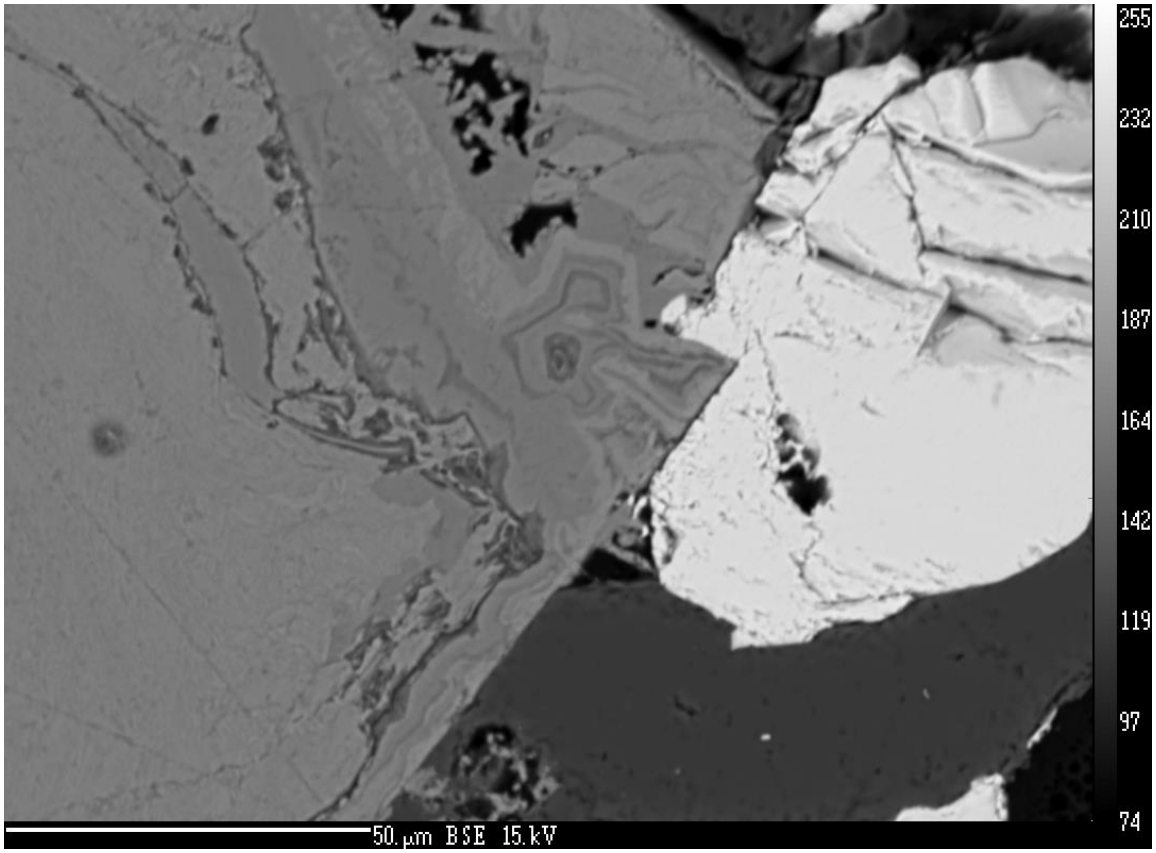

Figure 10. Bastnaesite altering growth structure of pyrite (now goethite/hematite). Quartz surrounds bastnaesite.

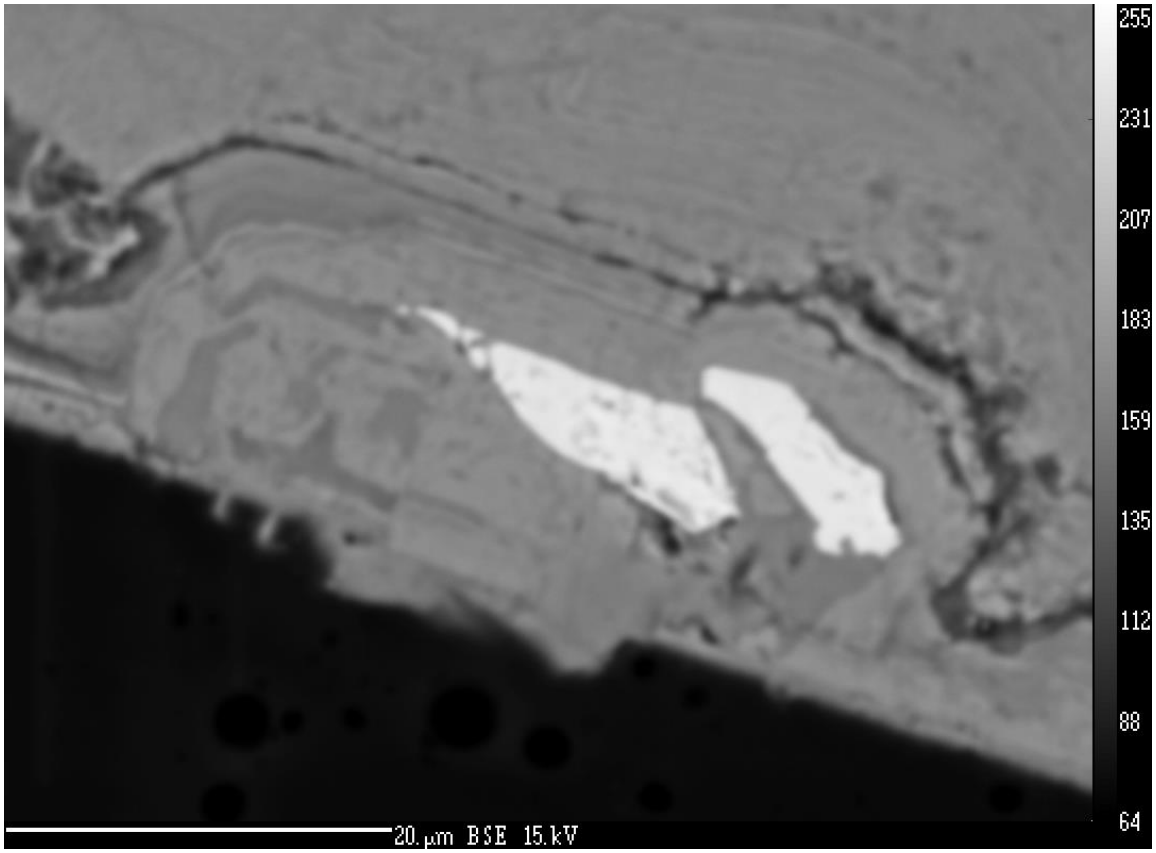

Figure 11. Bastnaesite intergrown with pyrite (now goethite/hematite).

Red Cloud Barite-Galena

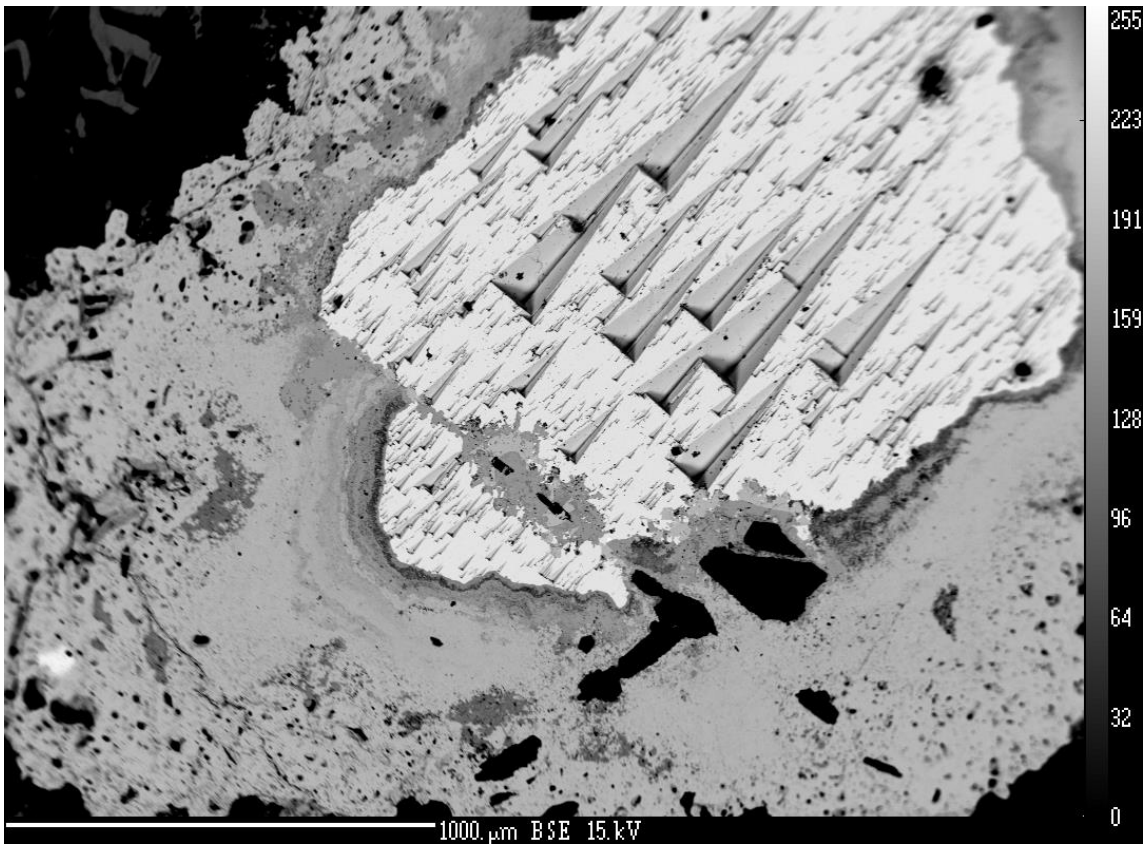

Figure 12. Galena and associated oxidation products. Grain is surrounded by quartz.

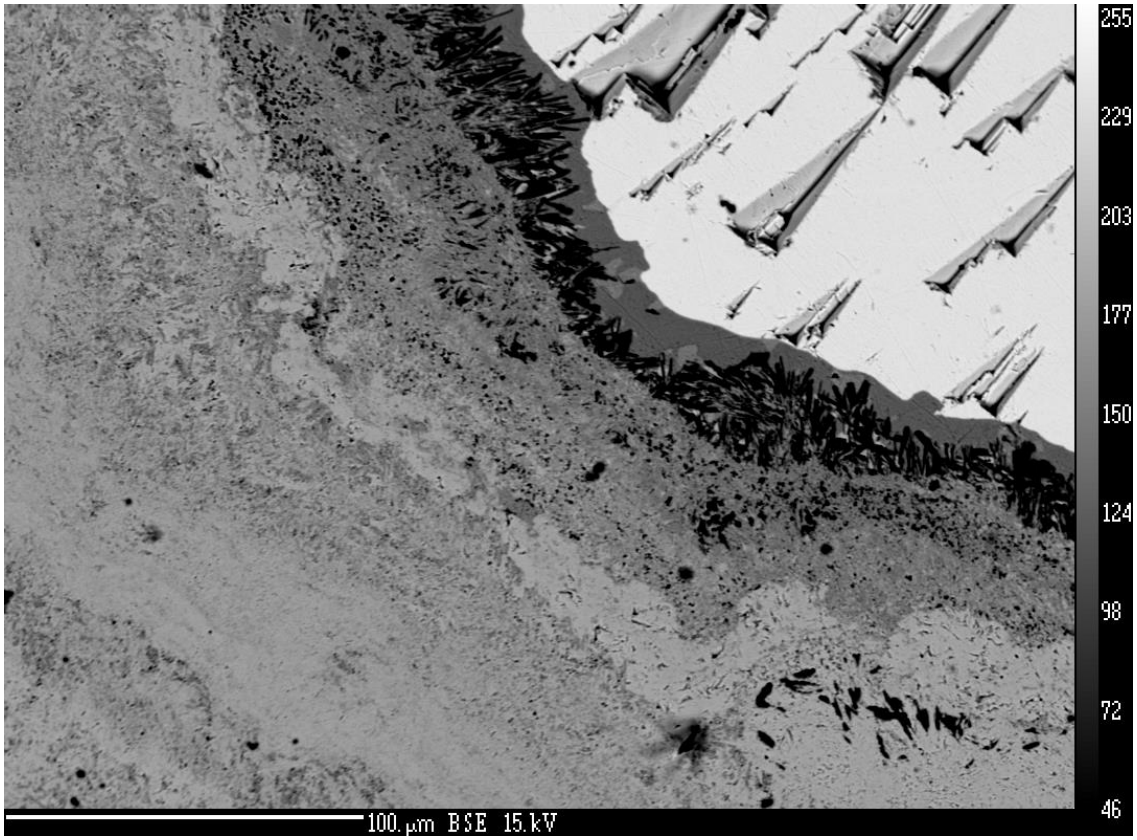

Figure 13. Gradational contact of galena, Ag-Cu sulfide, digenite/covellite and cerussite.

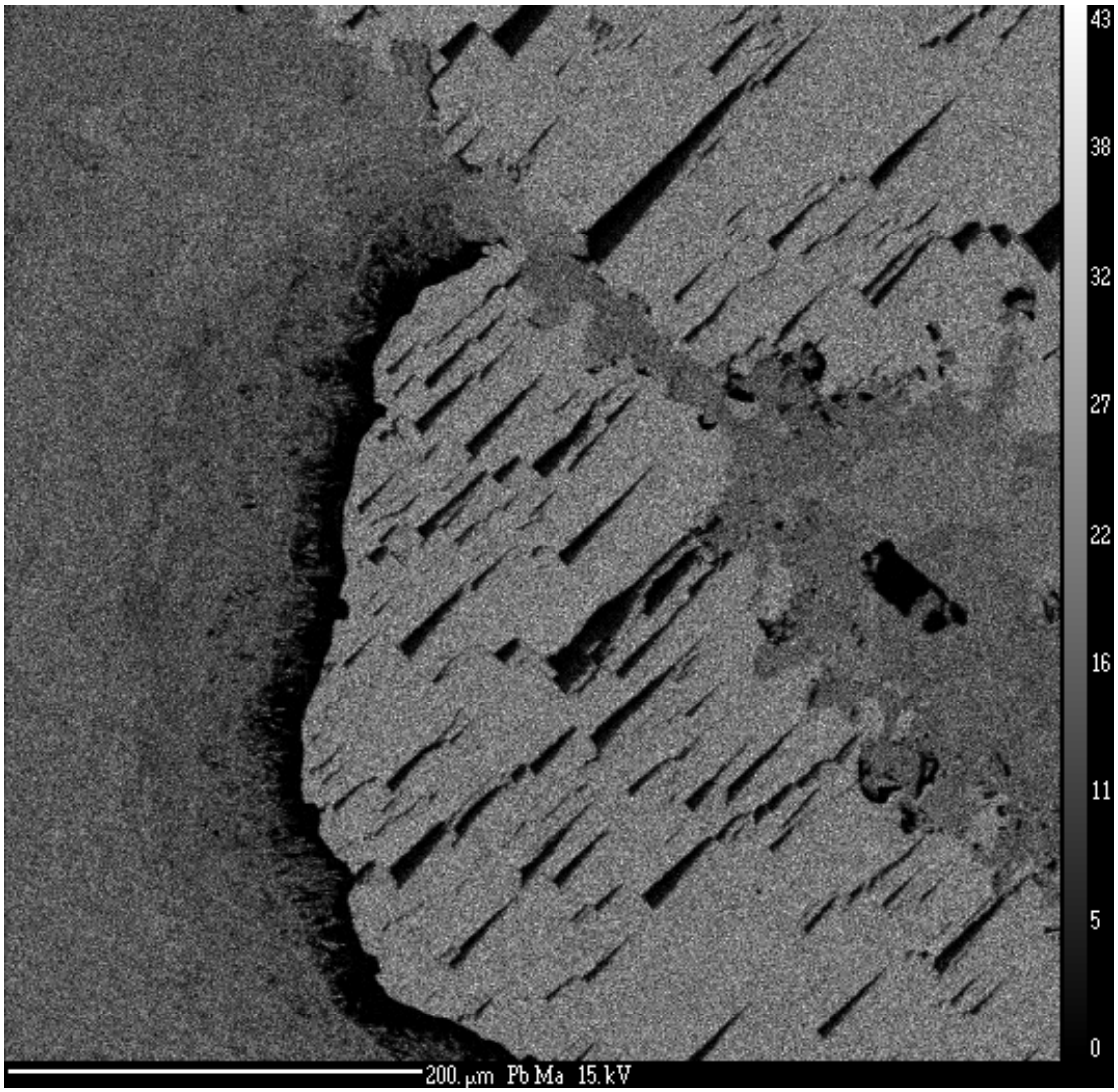

Figure 14. Lead (Pb) X-ray map of large galena grain.

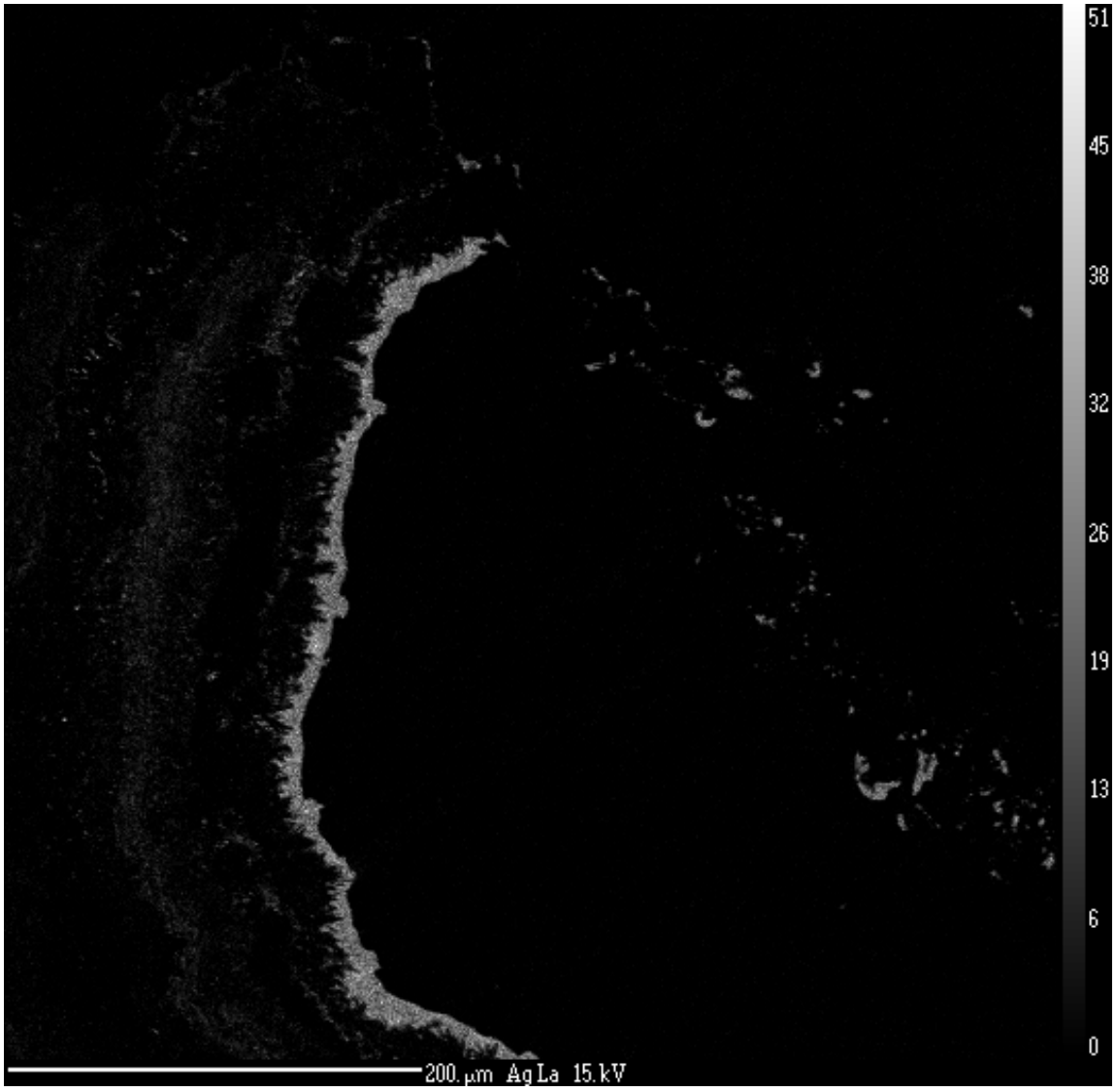

Figure 15. Silver (Ag) X-ray map around large galena grain.

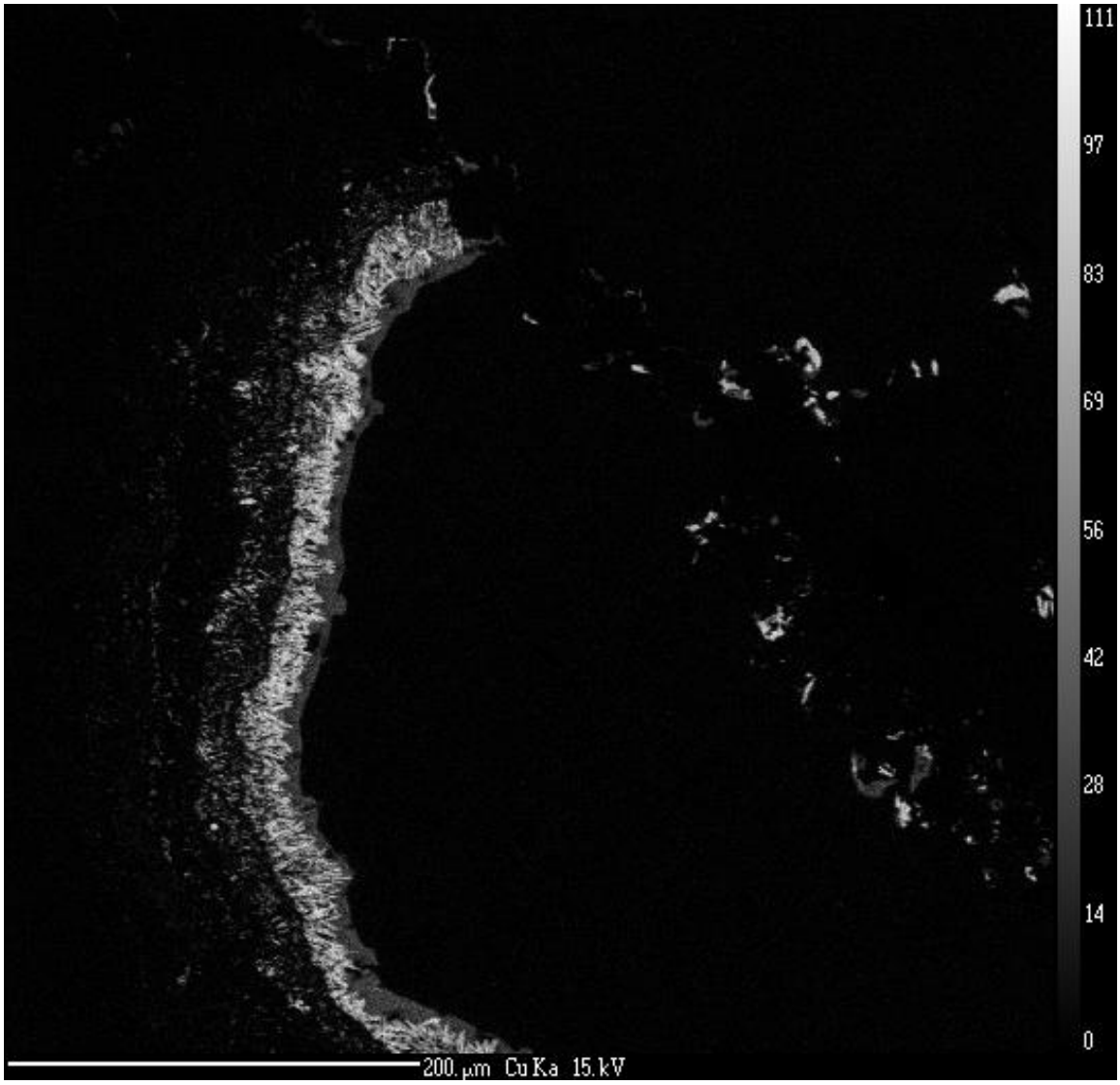

Figure 16. Copper (Cu) X-ray map around galena grain. Note copper presence in Ag rim.

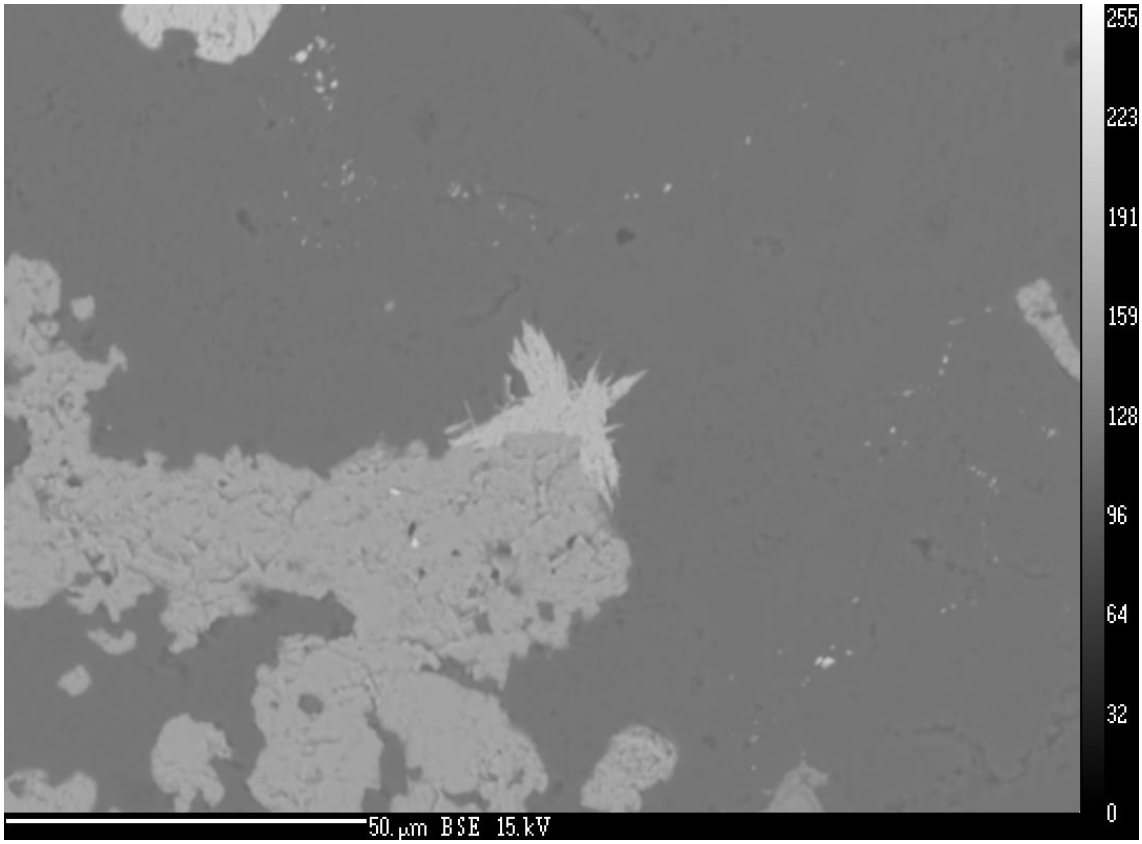

Figure 17. Fine grained REE-needle aggregate (bastnaesite/parisite?) in contact with cerussite.

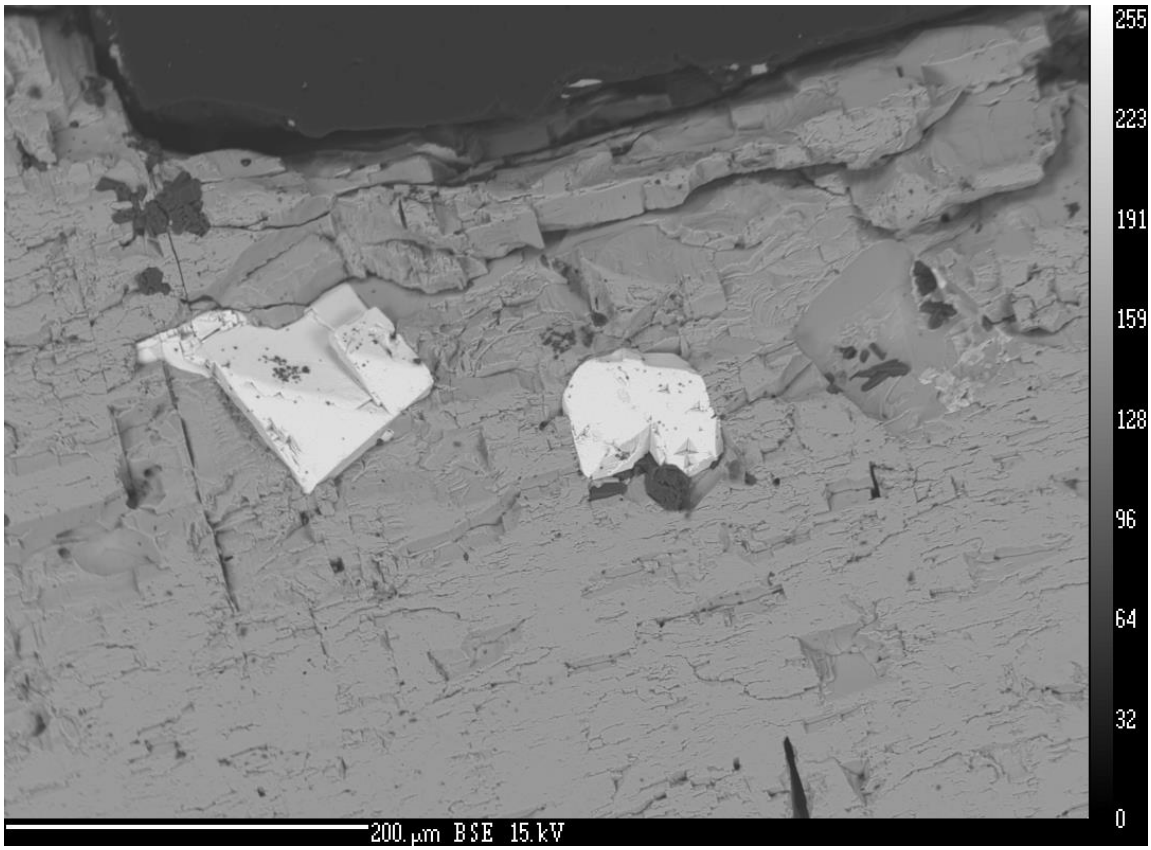

Figure 18. Galena grains within barite.

Old Hickory Fluorite-Sulfide Breccia

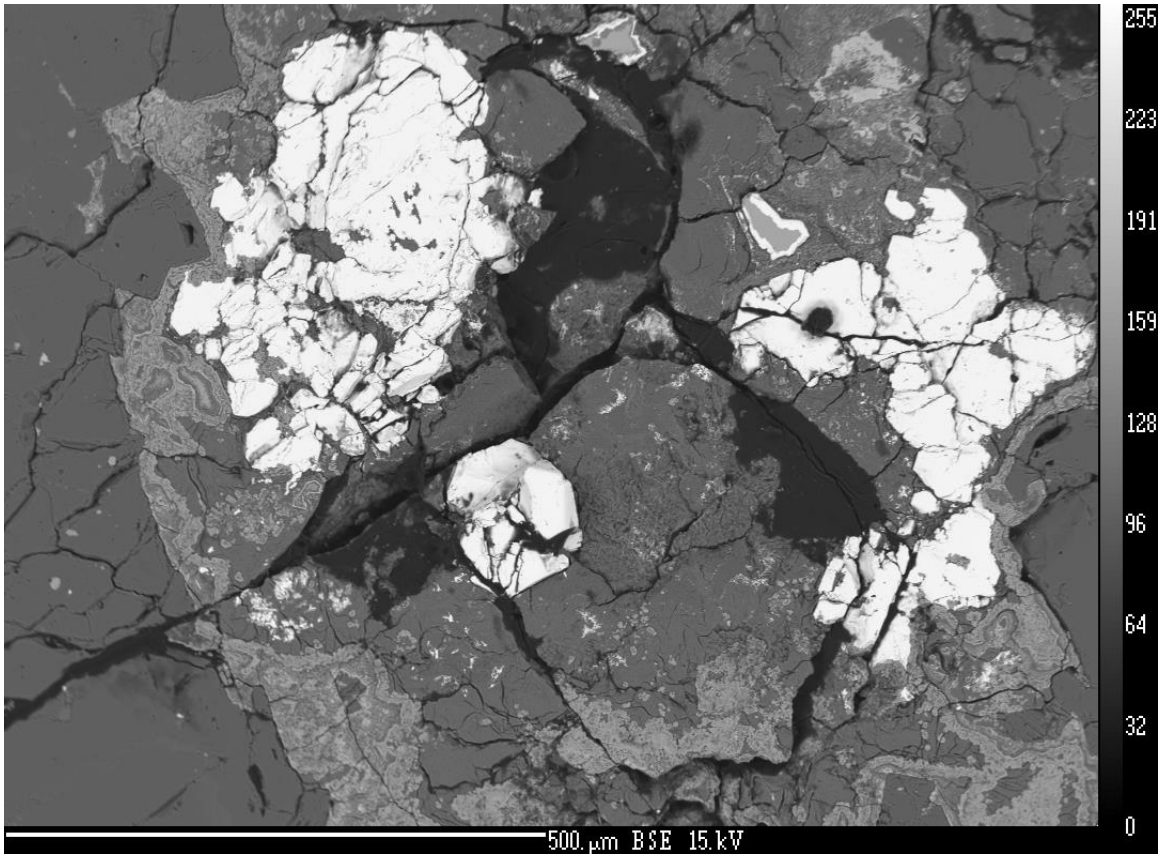

Figure 19. Mimetite and other galena oxidation products in a fluorite-quartz matrix.

DataSet/Point	**S**	**Ba**	**Pb**	**Total**	X	Y	Z	Comment		
9 / 1 .	13.4	0.145	85.188	98.733	-14483	2866	117	galena-01		
10 / 1 .	13.363	0.016	86.017	99.397	-14451	2884	117	galena-02		
11 / 1 .	13.449	0.113	85.74	99.302	-14432	2898	117	galena-03		
12 / 1 .	13.54	0	85.456	98.996	-14378	2941	116	galena-04		
69 / 1 .	12.632	0	82.813	95.445	-13787	27036	-261	RCBA-GL-021		
70 / 1 .	12.723	0	82.785	95.508	-13756	26873	-258	RCBA-GL-022		
71 / 1 .	12.653	0.081	82.676	95.41	-13990	26898	-263	RCBA-GL-023		
72 / 1 .	12.761	0.081	82.548	95.39	-14467	26654	-266	RCBA-GL-024		
73 / 1 .	12.967	0	82.808	95.775	-14423	26460	-262	RCBA-GL-025		
74 / 1 .	12.724	0.113	82.612	95.449	-13443	26809	-252	RCBA-GL-026		

75 / 1 .	12.838	0	82.396	95.235	-13780	27171	-265	RCBA-GL-027		
76 / 1 .	12.879	0	82.456	95.335	-13476	27327	-263	RCBA-GL-028		
77 / 1 .	12.809	0	83.345	96.154	-13778	27558	-272	RCBA-GL-029		
78 / 1 .	12.763	0.242	83.331	96.336	-14076	27452	-276	RCBA-GL-030		
83 / 1 .	13.415	0	86.19	99.605	-14357	2979	118	galena-05		
84 / 1 .	13.488	0.113	85.748	99.349	-14355	2958	116	galena-06		
DataSet/Point	**S**	**Ba**	**Pb**	**Sr**	**O**	**Total**	**X**	**Y**	**Z**	**Comment**
13 / 1 .	14.071	53.119	0.016	2.602	20.71	90.519	3425	-25790	14	barite-01
14 / 1 .	14.012	53.083	0.094	2.315	20.601	90.105	3432	-25815	15	barite-02
15 / 1 .	13.803	53.435	0.024	2.38	20.439	90.08	3445	-25864	14	barite-03
16 / 1 .	14.16	53.378	0.02	2.396	20.791	90.745	3442	-25892	13	barite-04
17 / 1 .	13.746	54.82	0	1.044	20.295	89.905	11893	23999	52	HWBA-01

18 / 1 .	13.723	54.963	0.061	0.958	20.28	89.984	12243	24175	50	HWBA-02
19 / 1 .	13.706	55.233	0.048	0.735	20.254	89.977	11440	23572	51	HWBA-03
20 / 1 .	13.567	54.64	0.008	1.042	20.099	89.356	12369	24071	54	HWBA-04
21 / 1 .	13.864	55.046	0.049	0.666	20.377	90.002	11601	24047	48	HWBA-05
22 / 1 .	13.814	54.223	0.049	1.301	20.347	89.734	10521	25388	46	HWBA-06
23 / 1 .	13.929	53.827	0.081	1.63	20.478	89.944	10341	25436	45	HWBA-07
24 / 1 .	13.608	55.385	0.069	0.773	20.182	90.017	10081	25283	45	HWBA-08
25 / 1 .	13.996	54.195	0	1.246	20.51	89.948	10063	24692	45	HWBA-09
26 / 1 .	14.047	55.278	0.024	0.343	20.525	90.217	9954	24843	43	HWBA-010
27 / 1 .	13.81	54.62	0.134	1.107	20.36	90.031	10835	24288	47	HWBA-011
28 / 1 .	13.983	54.43	0.146	1.273	20.542	90.375	10568	24363	50	HWBA-012
29 / 1 .	13.942	55.556	0.019	0.265	20.438	90.22	15166	28478	59	HWBA-013
30 / 1 .	13.183	55.444	0.036	0.313	19.678	88.654	15013	28408	54	HWBA-014
31 / 1 .	13.471	54.972	0	0.393	19.92	88.756	15680	27651	55	HWBA-015
32 / 1 .	13.623	55.288	0	0.53	20.133	89.573	15885	27878	62	HWBA-016
33 / 1 .	13.839	55.109	0.089	0.685	20.365	90.087	14805	28387	56	HWBA-017
34 / 1 .	13.65	54.716	0.133	0.351	20.073	88.923	14319	28463	57	HWBA-018

35 / 1 .	13.97	54.695	0.04	0.573	20.424	89.702	16497	26769	65	HWBA-019
36 / 1 .	13.797	52.99	0	2.196	20.342	89.325	16517	26899	64	HWBA-020
37 / 1 .	14.009	54.052	0.138	1.638	20.59	90.427	16504	27089	66	HWBA-021
38 / 1 .	13.964	55.01	0.105	0.581	20.461	90.121	16710	27293	69	HWBA-022
39 / 1 .	13.693	55.393	0	0.522	20.209	89.818	16092	26487	64	HWBA-023
40 / 1 .	13.87	55.749	0.02	0.475	20.427	90.541	16560	26109	67	HWBA-024
41 / 1 .	14.11	54.097	0	0.959	20.561	89.728	17283	25808	64	HWBA-025
42 / 1 .	13.706	55.214	0	0.438	20.188	89.546	16449	25943	65	HWBA-026
43 / 1 .	13.989	56.295	0	0.129	20.544	90.957	15994	25197	66	HWBA-027
44 / 1 .	14.006	54.836	0	0.23	20.402	89.473	15527	25240	60	HWBA-028
45 / 1 .	13.959	55.102	0.097	0.262	20.408	89.828	15742	25389	62	HWBA-029
46 / 1 .	13.74	56.212	0.028	0.122	20.288	90.389	16460	25921	68	HWBA-030
47 / 1 .	13.823	54.955	0.031	0.966	20.378	90.153	16691	25063	68	HWBA-031
48 / 1 .	13.986	54.082	0	1.744	20.575	90.388	17274	25791	68	HWBA-032
49 / 1 .	13.429	51.443	0.077	1.729	19.719	86.398	-16577	26644	-300	RCBA-GL-01
50 / 1 .	13.374	50.892	0.167	2.057	19.667	86.157	-16535	26505	-296	RCBA-GL-02
51 / 1 .	13.269	54.164	0.153	0.245	19.611	87.442	-16801	26728	-306	RCBA-GL-03

52 / 1 .	13.276	52.714	0.041	1.839	19.732	87.601	-18997	26982	-351	RCBA-GL-04
53 / 1 .	13.373	51.799	0	1.972	19.743	86.887	-18954	26982	-351	RCBA-GL-05
54 / 1 .	13.49	51.234	0.016	2.042	19.808	86.591	-18807	26774	-342	RCBA-GL-06
55 / 1 .	13.455	50.611	0	2.407	19.764	86.237	-18525	26618	-338	RCBA-GL-07
56 / 1 .	13.523	50.946	0.033	1.877	19.778	86.157	-19091	26644	-346	RCBA-GL-08
57 / 1 .	13.291	52.082	0	1.477	19.602	86.452	-19400	26776	-355	RCBA-GL-09
58 / 1 .	13.502	51.245	0	1.719	19.752	86.218	-19090	26379	-341	RCBA-GL-010
59 / 1 .	13.507	51.939	0	1.4	19.788	86.635	-19701	27675	-379	RCBA-GL-011
60 / 1 .	13.666	51.828	0	1.824	20.011	87.329	-19708	27748	-381	RCBA-GL-012
61 / 1 .	13.743	51.212	0.114	1.815	20.024	86.908	-19864	27839	-387	RCBA-GL-013
62 / 1 .	13.497	51.727	0.012	1.739	19.817	86.792	-19721	27452	-374	RCBA-GL-014
63 / 1 .	13.602	51.656	0.016	1.724	19.911	86.909	-19834	27594	-381	RCBA-GL-015
64 / 1 .	13.318	51.481	0	1.69	19.598	86.087	-18373	29231	-391	RCBA-GL-016
65 / 1 .	13.237	50.862	0.024	1.89	19.485	85.497	-18711	29247	-397	RCBA-GL-017
66 / 1 .	13.365	51.843	0	1.674	19.685	86.567	-18533	28872	-385	RCBA-GL-018
67 / 1 .	13.325	51.541	0	1.63	19.597	86.094	-18664	28777	-385	RCBA-GL-019
68 / 1 .	13.306	50.907	0.041	1.939	19.569	85.761	-18132	29364	-386	RCBA-GL-020

85 / 1 .	14.117	52.906	0.033	2.531	20.72	90.307	3484	-25888	11	barite-05
86 / 1 .	13.98	52.635	0.082	2.378	20.527	89.601	3445	-25910	14	barite-06

APPENDIX 6

Chemical and Sample data from Schreiner (1993)

All UTM coordinates are given in NAD27
All chemical data is given in parts per million unless otherwise stated

Sample	Description	UTM E	UTM N
2	carbonatized and fenitized intrusive breccia	430180.19	3786886
3	fenitized intrusive breccia	430196.297	3786879
4	fenitized intrusive breccia	430212.405	3786884
5	fenitized intrusive breccia	430225.06	3786891
6	carbonatized and fenitized intrusive breccia	430223.91	3786869
7	fenitized intrusive breccia	430134.17	3786857
8	carbonatized and fenitized intrusive breccia	430143.374	3786846
9	carbonatized and fenitized brecciated trachyte	430144.524	3786806
10	brecciated sandstone	430202.05	3786809
11	fractured sandstone	430199.749	3786795
12	brecciated sandstone	430219.308	3786802
13	intrusive breccia	430236.565	3786786
14	intrusive breccia	430245.769	3786776
15	intrusive breccia	430244.619	3786762
16	brecciated limestone bed	430214.706	3786787
17	brecciated limestone bed	430202.05	3786757
18	intrusive breccia	430218.157	3786749
19	intrusive breccia	430234.264	3786742
20	fragments of brecciated sandstone from stockpile	430203.2	3786775
21	fragments of fenitized andesite porphyry dike	430244.619	3786724
22	fenitized trachyte dike	430083.547	3786618
23	fenitized syenite	430020.269	3786555
24	brecciated trachyte dike in contact with brecciated limestone	430104.257	3786397
25	brecciated limestone in contact with brecciated sandstone and trachyte dike (sample 24)	430104.257	3786375
26	fenitized and fractured trachyte dike	430012.588	3786142
27	fenitized trachyte dike	430032.962	3786148
28	fenitized trachyte dike	430048.242	3786129
29	fenitized gneiss	430057.411	3786086
30	fragments of fenitized gneiss in tree roots	430018.7	3786052
31	fenitized intrusive breccia	429942.299	3786083
32	variably fenitized banded gneiss	429978.972	3786027
33	fragments of fenitized gneiss	430040.093	3786040
34	fenitized gneiss	430084.915	3786069
35	fragments of fenitized gneiss and intrusive breccia in tree	430072.691	3786026

	roots		
36	fenitized and carbonatized intrusive breccia in tree roots	430048.242	3786017
37	fragments of fenitized and carbonatized breccia in tree roots	430011.57	3786016
38	fragments of fenitized and carbonatized breccia from dump	430035	3785979
39	fragments of fenitized and carbonatized breccia from dump	430065.56	3785989
40	fragments of silicified intrusive breccia from dump	430082.878	3785999
41	fenitized gneiss	430093.065	3786010
42	fenitized sandstone	430140.943	3785972
43	carbonatized intrusive breccia	429713.094	3786041
44	fenitized intrusive breccia	429406.468	3785973
45	intrusive breccia	429390.169	3785840
46	brecciated zone in trachyte	429895.439	3785912
47	outcrop of brecciated sandstone	429944.336	3785925
48	fractured sandstone with minor breccia	430097.14	3785895
49	fragments of brecciated sandstone and trachyte from dump	430165.392	3785872
50	fragments of brecciated sandstone from dump	430154.186	3785844
51	fragments of brecciated trachyte from dump	430127.7	3785795
52	fragments of brecciated sandstone from dump	430165.392	3785811
53	fragments of brecciated sandstone from dump	430225.367	3785694
54	outcrop of trachyte	429606.131	3785618
55	fragments of fenitized intrusive breccia from dump	429739.58	3785468
56	fragments of fenitized intrusive breccia from dump	429826.168	3785379
57	fragments of intrusive breccia	429864.878	3785389
58	iron skarn in contact with trachyte	429086.537	3785545
59	fragments of iron skarn from dump	428672.571	3785106
60	fragments of intrusive breccia	429780.327	3785030
61	fragments of iron skarn from dump	429535.842	3784927
62	fragments of intrusive breccia	429457.403	3784878
63	fragments of intrusive breccia	429388.132	3784846
64	brecciated zone in sandstone	429495.094	3784784
65	fragments of intrusive breccia	429357.571	3784467
66	fragments of intrusive breccia	429175.226	3784513
67	fragments of intrusive breccia	428540.583	3784725
68	fragments of fenitized intrusive breccia	428474.368	3784563
69	outcrop altered intrusive breccia	428392.873	3784599
70	fragments of altered intrusive breccia	428297.116	3784532
71	intrusive breccia	428649.582	3784339
72	fenitized intrusive breccia	428655.694	3784313
73	fenitized intrusive breccia	428656.713	3784280
74	fragments of fenitized intrusive breccia	428657.732	3784254
75	float	428629.208	3784257
76	fenitized intrusive breccia	428597.629	3784226
77	fenitized intrusive breccia	428601.704	3784214

78	fenitized and carbonatized trachyte	428611.891	3784212
79	fenitized intrusive breccia	428622.078	3784222
80	fenitized intrusive breccia	428601.704	3784189
81	fenitized intrusive breccia	428589.48	3784202
82	fenitized intrusive breccia	428581.33	3784189
83	fractured and fenitized trachyte near edge of intrusive breccia	428497.798	3784229
84	fragments of fenitized intrusive breccia	428519.19	3784253
85	fragments fenitized trachyte in tree roots	428581.33	3784276
86	fragments of fenitized intrusive breccia	428797.292	3784268
87	fenitized intrusive breccia	428822.759	3784240
88	outcrop of fractured trachyte	428814.61	3784177
89	fractured trachyte with minor breccia	428827.853	3783580
90	fragments of brecciated trachyte from dump	428826.834	3783557
91	fragments of brecciated sandstone in float	428429.866	3783229
92	outcrop of fractured trachyte with minor breccia	429155.871	3783568
93	outcrop of brecciated zone in trachyte	429419.975	3783618
94	outcrop of brecciated zone in trachyte	429546.573	3783714
95	fragments of trachyte from dump	430121.111	3784500
96	fragments of magnetite with minor quartz from dump	430417.776	3784815
97	fenitized and carbonatized intrusive breccia	430808.567	3785416
98	fenitized and carbonatized intrusive breccia	430821.3	3785416
99	fragments of intrusive breccia in float	430983.017	3785325
100	intrusive breccia	430998.297	3785299
101	brecciated sandstone	431030.131	3785327
102	brecciated sandstone	431022.491	3785303
103	brecciated sandstone	431014.851	3785289
104	fragments of fractured sandstone from dump	431378.555	3784950
105	brecciated trachyte	431666.653	3784743
106	fractured and altered trachyte	431665.061	3784723
107	brecciated trachyte sandstone contact	431739.871	3784716
108	brecciated zone in sandstone	431967.485	3785068
109	brecciated zone in sandstone	431936.438	3785267
110	brecciated sandstone	431868.799	3785338
111	brecciated sandstone	431907	3785324
112	brecciated sandstone	431932.467	3785310
113	brecciated sandstone	431954.751	3785302
114	brecciated sandstone	431969.076	3785294
115	brecciated sandstone	432013.644	3785262
116	brecciated sandstone	432031.153	3785254
117	brecciated sandstone	432045.478	3785248
118	brecciated sandstone	432058.212	3785240
119	brecciated sandstone	432069.354	3785235
120	brecciated sandstone	432077.312	3785230

121	brecciated sandstone	432088.454	3785225
122	brecciated sandstone	432104.371	3785219
123	brecciated sandstone	432115.513	3785211
124	brecciated sandstone	432117.105	3785208
125	brecciated sandstone	432110.738	3785202
126	brecciated sandstone	432105.963	3785190
127	fractured sandstone	432094.821	3785186
128	brecciated sandstone	432125.063	3785203
129	fractured sandstone	432117.105	3785210
130	brecciated sandstone	432126.655	3785184
131	brecciated sandstone	432145.755	3785189
132	brecciated sandstone	432027.174	3785283
133	brecciated sandstone	432075.561	3785258
134	brecciated sandstone	432172.337	3785196
135	brecciated sandstone	432594.004	3785953
136	brecciated sandstone	432600.196	3785943
137	brecciated sandstone	432605.613	3785932
138	brecciated sandstone	432613.353	3785924
139	brecciated sandstone	432620.318	3785912
140	brecciated sandstone	432624.188	3785902
141	brecciated sandstone	432629.606	3785893
142	brecciated sandstone	432635.797	3785883
143	brecciated sandstone	432640.441	3785874
144	brecciated sandstone	432602.517	3785912
145	brecciated sandstone	432719.384	3785725
146	brecciated sandstone	432742.602	3785684
147	brecciated sandstone	432748.02	3785672
148	brecciated sandstone	432752.663	3785679
149	fragments of brecciated sandstone and a few fragments of limestone from dump	432762.725	3785669
150	fragments of brecciated sandstone and a few fragments of limestone from dump	432768.142	3785646
151	brecciated sandstone	432762.725	3785633
152	fractured sandstone with minor breccia	432655.222	3785547
153	brecciated sandstone	432694.454	3785257
154	brecciated limestone bed	432446.109	3785160
155	brecciated limestone bed	432475.397	3785137
156	brecciated zone in sandstone	432493.224	3785127
157	fragments of brecciated sandstone and limestone from dump	432410.998	3785084
158	brecciated sandstone contact	432424.57	3785070
159	brecciated sandstone	432429.094	3785054
160	brecciated sandstone	432446.285	3785045
161	brecciated zone in sandstone	432631.97	3785051

162	fragments of brecciated sandstone from dump	432639.528	3785021
163	fragments of brecciated sandstone from dump	432732.625	3785031
164	brecciated sandstone	432765.141	3785022
165	brecciated sandstone	432780.692	3785056
166	brecciated sandstone	432879.875	3784820
167	fluorite rich zone	432769.382	3784995
168	fluorite rich zone	432775.037	3784990
169	fluorite rich zone	432779.279	3784986
170	fluorite rich zone	432779.279	3784981
171	brecciated zone in sandstone	432745.349	3784962
172	brecciated zone in sandstone	432796.761	3784861
173	brecciated sandstone	432846.104	3784797
174	fractured sandstone	432838.146	3784828
175	brecciated sandstone	432865.205	3784815
176	brecciated sandstone	432876.852	3784832
177	brecciated sandstone	432898.63	3784818
178	brecciated sandstone	432723.543	3784831
179	brecciated sandstone	432710.809	3784793
180	brecciated sandstone	432683.751	3784796
181	brecciated sandstone	432736.277	3784777
182	fragments of brecciated limestone	432693.301	3784761
183	brecciated sandstone	432616.899	3784855
184	brecciated sandstone	432610.532	3784828
185	fractured sandstone with minor breccia	432580.29	3784828
186	brecciated sandstone	432613.716	3784785
187	brecciated sandstone	432480.013	3784872
188	brecciated sandstone	432503.888	3784840
189	fluorite, barite, quartz rich zone	432331.984	3784899
190	brecciated sandstone	432317.659	3784894
191	brecciated sandstone	432301.742	3784888
192	brecciated sandstone	432314.476	3784871
193	brecciated sandstone	432301.868	3784879
194	brecciated sandstone	432293.784	3784859
195	brecciated sandstone	432287.008	3784864
196	brecciated sandstone	432279.458	3784874
197	brecciated sandstone	432269.908	3784856
198	brecciated sandstone	432260.358	3784842
199	brecciated sandstone	432223.749	3784808
200	fragments of brecciated sandstone from dump	432236.482	3784789
201	brecciated sandstone	432201.465	3784737
202	brecciated sandstone	432182.364	3784716
203	brecciated sandstone	432158.489	3784700
204	brecciated sandstone	432125.063	3784692

205	brecciated sandstone	432029.561	3784699
206	brecciated sandstone and conglomeritic sandstone	432008.869	3784680
207	brecciated sandstone	431961.118	3784632
208	fragments of brecciated sandstone	432628.041	3784614
209	brecciated sandstone	432564.373	3784649
210	fractured and brecciated sandstone	432487.971	3784649
211	brecciated sandstone-dolomite contact	432464.096	3784608
212	brecciated sandstone-dolomite contact	432671.017	3784568
213	brecciated sandstone	432889.08	3784708
214	brecciated sandstone	432998.907	3784652
215	brecciated sandstone	433025.966	3784656
216	fractured sandstone	433024.375	3784630
217	fragments of vuggy trachyte	433030.742	3784611
218	brecciated sandstone	432912.956	3784597
219	brecciated sandstone	432900.222	3784582
220	brecciated sandstone	432897.039	3784563
221	fragments of brecciated sandstone from dump	432881.122	3784430
222	fractured and brecciated siltstone	432922.506	3784401
223	brecciated siltstone	433008.458	3784356
224	breccia zone in sandstone	432411.57	3784334
225	breccia zone in sandstone	432281.05	3784315
226	fractured and brecciated sandstone	431865.052	3784057
227	fractured and brecciated sandstone	431872.97	3784041
228	brecciated sandstone	431834.509	3784019
229	brecciated sandstone	431834.509	3784002
230	brecciated sandstone	431819.804	3783990
231	brecciated sandstone	431816.41	3784054
232	fragments of brecciated sandstone from dump	431823.255	3784057
233	brecciated sandstone	431953.285	3784009
234	brecciated sandstone	431967.991	3784013
235	brecciated sandstone	431978.172	3784016
236	brecciated sandstone	431971.385	3783997
237	fragments of brecciated sandstone from dump	431807.005	3783986
238	fragments of conglomerate from dump	432040.388	3783970
239	fenitized gneissic granite	431945.367	3783914
240	trachyte dike-gneissic granite contact	431960.073	3783898
241	calcite vein in sandstone	431445.54	3783716
242	fragments of sandstone	431591.033	3783746
243	fractured sandstone	431706.861	3783697
244	fractured sandstone	431679.652	3783709
245	brecciated sandstone	431649.419	3783702
246	fractured sandstone	431798.311	3783663
247	brecciated sandstone	432092.423	3783688

248	brecciated sandstone	432093.554	3783669
249	brecciated sandstone	432095.817	3783651
250	brecciated sandstone	432099.21	3783635
251	brecciated sandstone	432109.391	3783632
252	fenitized and fractured trachyte dike	432258.71	3783709
253	fenitized and fractured trachyte dike	432258.71	3783695
254	fragments	432284.727	3783690
255	brecciated	432313.007	3783731
256	brecciated	432315.27	3783719
257	fragments of brecciated sandstone from dump	432316.401	3783698
258	trachyte dike	432289.252	3783403
259	fractured sandstone	432379.748	3783286
260	magnetite-hematite	433473.524	3778045
293	Rio Tinto breccia	432323	3783697
294	Rio Tinto breccia	432323	3783697
295	Red Cloud fluorite breccia	431966	3784008
296	Red Cloud fluorite breccia	431966	3784008
297	Red Cloud copper	431825	3784047

Sample	Y	La	Ce	Nd	Sm	Eu	Dy	Ho	Yb	Lu	Sr	Sc	Th	U	Au ppb	Ag	Cu	Pb	Zn
2	109	1230	1570	340	41.7	9			8.8	1.1	467	4.2	22	6.5	139	0.5	301	141	398
3	44	1190	1290	215	27.3	4.2	9.1	2.3	6.4	0.85	966	4.22	38.2	9.2	222	1	223	318	1330
4	54	1830	1990	291	42.2	9.5	12.2	2.9	5.2	0.68	1174	3.45	25.8	18.9	175	3.5	3121	367	232
5	68	1430	1480	225	27.8	6.1	8.7	2.2	6.5	0.85	987	4.39	29.1	11.7	117	2.5	559	278	698
6	58	1920	2020	265	35.7	7.3	12.5	2.8	6.2	0.7	>2000	8.65	32.4	27.2	170	3.7	7220	337	411
7	113	1160	1410	330	43	8.1			8.1	1	943	2.5	67.5	14	37	<0.2	14	68	279
8	62	754	912	180	26.3	5.2			5.6	0.59	1482	2.8	38	7.9	31	<0.2	17	22	57
9	74	2100	1960	290	32.4	6.8			8.9	1	876	4.5	45	8	54	<0.2	11	47	323
10	74	2620	2350	315	35.2	7.8	11.6	3.6	5.6	0.61	>2000	1.82	5.5	4.5	30	<0.2	81	584	89
11	28	283	300	44	7.11	1.4	2	<1	2.6	0.31	378	3.21	4.8	2.4	35	0.6	62	350	100
12	<160	2570	2440	323	54	12.1	26.4	4.9	9.5	1.07	>2000	2.09	24.1	10.9	496	27.3	4250	29700	182
13	66	2840	2990	438	66.8	14.2	23.9	4.1	7.7	0.85	1175	3.75	6.4	10.5	135	<0.2	415	1869	911
14	134	2800	2970	422	63.5	12.4	21.8	5.5	13.4	1.75	>2000	7.34	9.2	10.2	28	<0.2	158	205	529
15	106	2450	2410	324	45.3	9.5	17.7	4.1	7.2	0.81	>2000	3.96	5.9	13.3	19	<0.2	263	181	297
16	92	902	871	116	18.4	3.9	8	2.6	10.9	1.68	463	2.11	5.9	4	32	0.2	19	81	103
17	61	780	796	118	18.9	4.1	5.6	1.6	4.2	0.52	1335	3.1	20.5	7.7	63	0.9	108	799	547
18	79	2650	2370	284	37.3	7.9	8	2.3	7.2	0.93	683	4.75	3.2	5.9	33	<0.2	32	321	239
19	126	3660	3580	627	77.7	16	20.9	5	14.3	1.7	973	6.66	14.4	10	80	<0.2	63	519	201
20	<200	4210	3940	565	86.3	18.8	31	6.8	13.4	1.47	>2000	3.76	19.3	42.7	610	11.2	5823	33400	933
21	33	155	200	67	12.1	3			3.1	0.41	1431	14.9	30	6.8	<5	<0.2	50	32	83
22	27	65.4	76	16	2.8	0.6			2.2	0.27	63	0.55	23	8.7	71	<0.2	10	52	43
23	30	217	280	69	10	2.5			2.5	0.33	749	1	71.3	6.4	12	<0.2	17	17	51
24	101	237	390	120	22.2	5.1			8	1	224	1	49	14	41	<0.2	18	503	123
25	418	1000	1540	470	105	27			28	3.2	380	2.8	20	20	19	<0.2	29	711	321
26	59	159	250	48	8.68	1.7	6.5	1.8	5.9	0.9	168	0.97	120	23.6	<5	<0.2	14	178	7
27	57	110	193	50	7.11	1.1	3.7	1.7	6.5	1.08	47	0.53	120	19	45	<0.2	6	26	8
28	76	96	178	56	7.64	1.4	5.8	2.2	7.5	1.13	27	0.52	130	23	19	<0.2	5	52	10
29	27	76.4	120	47	7	1.6			2.4	0.27	508	0.62	274	8.8	<5	<0.2	9	10	15
30	14	75.2	120	35	4.7	1.1			2.1	0.28	2000	0.8	34	4.5	<5	<0.2	6	17	21
31	51	149	232	82	13.5	3.1	4.2	<1	3.7	0.5	534	17	24	5	5	<0.2	26	19	62

32	15	35	49	17	3.6	1.3			1.3	0.17	350	4.6	5.1	1.2	25	<0.2	18	10	20
33	33	86.5	120	37	5.9	1.2			3.9	0.65	298	1.5	36	4.1	12	<0.2	30	102	62
34	11	29	47	14	3.2	1			1.9	0.22	896	0.38	56.6	13	<5	<0.2	8	23	20
35	27	60.7	120	43	7.5	1.9			3.1	0.47	459	3.9	33	5.2	<5	<0.2	25	71	62
36	57	283	310	64	13.4	2.7			4.2	0.5	329	4.5	23	3.1	165	<0.2	193	16	108
37	26	106	180	63	12.8	3.2			2.7	0.34	542	20.1	23	5	18	<0.2	54	18	120
38	39	310	340	86	14.6	3.3			3.5	0.39	1104	17.7	25	4.7	73	<0.2	47	28	144
39	31	139	210	81	14.9	3.7			3	0.39	1368	19	31	4.9	11	<0.2	53	20	133
40	55	281	340	110	19	4			4.2	0.49	515	18.2	23	5.5	15	<0.2	30	20	113
41	9	49	68	21	3.5	1			1.8	0.24	801	0.37	60.7	6.6	<5	<0.2	10	17	42
42	20	34	58	19	4.5	0.9			1.7	0.26	453	5.4	5.3	<1	7	<0.2	12	5	15
43	36	127	210	71	14.1	3.4			3.1	0.43	1089	10.2	27	6.2	<5	<0.2	56	12	71
44	55	200	311	94	15.5	3.5	4.8	1.6	3.9	0.55	1375	10.4	27.8	3.9	20	<0.2	34	18	69
45	53	205	327	79	16	3.8	4.1	1.2	3.7	0.55	399	10.7	32.5	5.7	12	<0.2	10	19	45
46	106	1500	1570	250	43.3	10.2	11.5	2.1	7.4	0.93	1369	6.15	27.8	14	21	<0.2	18	63	53
47	78	297	285	54	9.79	2.5	7.6	1.7	5.6	0.74	436	6.81	7.1	2.4	<5	0.4	11	51	41
48	37	91.4	98	24	4.2	0.8			2.7	0.37	640	5.7	6.3	1.7	<5	<0.2	2	21	29
49	64	522	520	86	15.2	3	10	<1	7.3	1	530	4.9	18	7	5	<0.5	22	64	156
50	87	780	793	120	20	4.9	8.5	2.9	7.3	0.93	848	6.7	10.3	9.3	<5	<0.2	27	63	87
51	162	956	1300	297	37.4	10	20.7	5	13.2	1.7	861	6.4	16	18	<5	<0.2	9	84	35
52	57	512	534	110	16.7	3.8			4.6	0.59	1797	3.7	19	6.9	<5	<0.2	9	33	88
53	117	1970	2080	295	42.1	8.1	12.7	3.1	6.3	0.7	1316	5.25	12.4	14.7	14	<0.2	20	70	20
54	42	91.1	170	45	7.4	1.7			4.6	0.62	107	0.63	63.4	10	9	<0.2	4	8	30
55	46	79.5	130	50	10.5	2.4			3.7	0.5	445	8.4	18	3.9	<5	<0.2	14	8	25
56	44	113	189	57	13.9	3.3	<4.0	<1	3.8	0.45	68	6.11	20.5	5.8	12	0.4	48	233	66
57	42	101	171	48	11.8	2.8	3.3	<1	3.1	0.44	469	8.3	22.7	3.4	7	0.2	64	52	65
58	16	436	410	53	5.8	1	2	<1	4.1	1.2	29	2.5	8	20	8	0.7	12	13	30
59	8	62.9	89	13	2.05	0.6	1.6	<1	0.9	0.13	31	0.5	13.8	18.9	<5	<0.2	88	31	41
60	32	100	182	46	10.2	2.5	5.9	1.5	2.9	0.43	646	7.41	20.9	3.2	<5	0.2	22	55	39
61	28	177	251	54	8.84	1.7	3.5	1.5	6.5	1.51	165	4.97	3.6	<1	<5	<0.2	70	340	53
62	40	193	278	66	13.6	2.9	6.5	<1	3.8	0.59	393	8.59	28	5.5	15	<0.2	28	88	45

63	48	159	245	64	13.4	3.3	7	2	3.9	0.5	559	6.57	31.3	6.2	<5	<0.2	12	26	57
64	144	813	966	161	27.8	6.5	18.3	3.6	7.8	0.95	735	1.3	56.4	4.5	30	<0.2	86	109	19
65	38	107	162	41	9.01	2.1	7.4	1.6	3.3	0.46	434	8.82	19.6	4.2	<5	0.5	11	23	32
66	37	123	180	53	10	2			3.8	0.51	295	5.7	43	9.5	<5	<0.2	7	5	33
67	38	131	198	43	8.76	1.9	6.1	<1	4	0.58	236	4.82	59.7	11.2	<5	<0.2	41	19	32
68	35	112	180	37	8.66	1.7	2.8	<1	3.6	0.52	309	5.14	54	12	<5	<0.2	23	81	78
69	41	118	183	57	8.65	1.8	4.4	<1	3.7	0.54	205	4.5	56	11.5	<5	<0.2	5	18	39
70	39	153	231	48	8.92	1.8	6.1	1.6	4.4	0.64	332	4.45	67.9	12.8	<5	<0.2	16	55	31
71	458	9000	13400	2900	200	67.8	92	17	20.9	1.8	1325	2.2	20	7.6	141	<0.2	6	72	16
72	187	1290	1960	412	54.3	10.2	18	5.5	16	2.36	352	1.9	49	9.8	27	<0.2	9	36	37
73	125	698	899	190	32	7.1			16	2.2	202	1.6	38	10	58	<0.2	25	1244	52
74	168	358	470	130	22.7	4.9			13	1.7	246	1.6	38	7.8	35	<0.2	8	180	24
75	725	18900	22100	4360	514	109	160	34	60.6	6.97	>2000	2.52	30	13	116	<0.2	108	1353	17
76	110	4500	4930	732	85.4	14.6	12.2	2.3	11.1	1.43	428	4.29	47.6	6	19	<0.2	30	402	47
77	177	4240	5010	785	103	17.6	16.7	4.6	21.4	2.6	439	3.64	36.3	6.8	24	<0.2	15	685	58
78	56	466	572	130	18.9	4.1			5.2	0.66	639	2.2	42	5.3	<5	<0.2	9	78	150
79	221	8560	9560	1440	169	28.3	33.8	7.4	26.2	3.71	496	6.3	52	9.2	29	<0.2	34	1701	82
80	696	11900	15600	2630	337	58.8	59.2	17.9	55	5.97	839	3	130	84	17	<0.2	95	64	43
81	66	880	1130	197	28.7	5.4	4.4	1.3	6.7	1.01	566	2.55	47.7	4.1	18	<0.2	178	2124	79
82	235	5860	7260	1170	156	27.7	24.8	7.2	19.3	2.64	405	4.43	42.5	7.2	24	<0.2	14	968	113
83	93	183	230	64	12.1	2.9			8	1	188	0.68	56.4	7.8	11	<0.2	12	389	43
84	160	158	220	67	14.4	3.4			12	1.5	140	2	43	7.5	<5	<0.2	4	148	24
85	54	83.2	130	42	8.4	1.9			4.3	0.63	247	0.94	50.5	3.8	<5	<0.2	2	3	11
86	548	306	380	83	19.5	4.7			40	5	90	1.5	40	13	27	<0.2	6	44	6
87	664	8860	11000	2480	330	67.7	89	19.3	43.2	5.26	437	1.93	100	17	32	<0.2	11	75	53
88	82	190	299	87	14	3.4	5.3	1.8	5.8	0.83	168	1.5	41.6	6.2	48	<0.2	9	7	58
89	<350	7690	8790	1390	231	48.4	53.6	14.7	32.2	3.76	502	4.06	122	26	71	2.9	5254	61800	554
90	<370	2290	2500	390	68.7	13.9	29.6	8.9	27.3	3.5	524	2.21	69.7	13	18	<0.2	206	3441	174
91	56	177	277	62	13.1	2.8	5.4	1.4	4.1	0.6	534	8.14	37.2	5.7	<5	<0.2	19	79	21
92	97	458	514	97	17.5	3.7	6	2.2	6.8	0.99	190	0.82	47.3	6.2	13	<0.2	10	29	23
93	80	671	796	125	21	4.4	6.2	2.6	7.7	1.19	309	2	37.3	7.6	55	<0.2	21	67	77

94	68	523	546	92	16	3.7	5.5	2.4	5.2	0.75	178	2.4	45.4	7.4	15	<0.2	17	43	115
95	52	297	422	91	16.1	2.9	5.4	2.2	4.3	0.58	802	1.44	43.1	3.7	10	<0.2	29	28	35
96	5	41.4	47	10	1.9	<0.5	<1	<1	0.6	0.1	47	0.56	2.1	8.4	6	<0.2	104	56	77
97	52	157	226	64	11.3	2.5	<2	<2	3.8	0.51	445	6.62	29	5.7	23	<0.2	19	18	74
98	52	113	175	41	9.34	2.1	4.1	<2	4	0.61	417	6.64	28.5	5.7	17	<0.2	11	13	80
99	101	190	264	62	12	2.9	4.1	<1	3.3	0.49	481	9.09	28.4	5.2	<5	<0.2	11	25	56
100	85	344	391	68	12.1	2.4	6.7	2.7	5.3	0.65	409	6.9	9.6	4.1	16	<0.2	10	22	56
101	30	96	112	24	5.14	1	2.9	1.2	2.1	0.3	85	7.27	6.5	2	11	0.2	5	6	11
102	127	6280	7280	1180	122	21.7	15.7	4.1	7.6	1.07	591	3.08	25.5	24.6	7	<0.2	15	255	52
103	112	720	755	117	18.7	3.7	8.5	3.6	8	1.06	347	7.14	8.4	4.8	<5	<0.2	75	11	67
104	47	88.8	118	36	6.52	1.4	3.1	1.5	3.2	0.47	117	6.86	8.7	2.8	15	<0.2	5	25	76
105	402	2340	3940	1060	190	45.3	42	8.3	12.9	1.73	1036	1.5	110	14	49	<0.2	135	86	51
106	122	242	380	108	16.8	3.4	8.8	2.7	8.2	1.22	366	0.93	63.6	8.1	32	<0.2	39	12	5
107	79	63.3	97	35	7.73	1.8	6.6	1.7	5.2	0.68	199	9.06	9	4.4	116	2.5	40	34	83
108	315	2370	3410	780	107	20			17	2.1	528	4.8	40	5.7	145	<0.2	14	31	203
109	95	2890	3200	650	61.7	10			7.1	0.83	384	4.8	23	4.9	43	<0.2	3	39	140
110	57	35	58	25	8.4	2.7			5	0.64	333	3.2	6.2	2.1	<5	0.5	8	18	52
111	79	997	1480	360	46.9	7.8			3.9	0.51	430	1.4	20	5.5	<5	<0.2	109	42	26
112	129	2540	3550	840	97.8	16			6.1	0.82	1056	3.8	25	12	6	<0.2	26	59	54
113	64	2330	2780	560	57.4	10			3.6	0.54	385	4.3	21	4.9	7	<0.2	16	32	109
114	75	1310	1570	320	37.9	7.1			5.3	0.63	342	4.5	13	4.3	<5	<0.2	12	21	99
115	83	8880	8340	1450	107	21			7.5	1	1836	2.4	26	5.6	12	<0.2	65	80	51
116	89	9000	9310	1500	119	17			5.2	0.93	1900	3.7	28	18	29	<0.2	87	113	117
117	66	1910	1930	330	32.9	5.5			4.6	0.49	639	3.2	11	6.9	51	<0.2	32	76	93
118	112	9000	11400	1930	155	25	25	6	11	1.3	>2000	3.4	38	19	45	<0.2	196	236	175
119	45	2660	2480	400	33.4	5			5.2	0.6	>2000	4.7	18	5.5	28	<0.2	126	53	166
120	80	5810	5320	840	63.8	12			7	1	>2000	6.5	28	4.3	49	<0.2	9	47	125
121	108	9000	9130	1360	120	23			21	1.8	>2000	4.9	39	7.1	94	<0.2	166	168	182
122	93	5970	5740	950	82.2	15			8.4	0.92	1557	3.1	21	7.4	22	<0.2	31	95	90
123	54	3790	3590	620	52.4	10			4.9	0.83	>2000	4.5	18	6.3	404	0.2	758	84	858
124	75	9000	8780	1460	112	22			13	1.4	1653	4.9	30	12	66	<0.2	39	228	268

125	105	2140	2030	370	33.9	6.3			8.3	0.94	795	4	15	5.7	78	<0.2	17	35	96
126	85	739	742	140	17.4	3.3			5.5	0.67	365	6.7	12	4.2	98	0.5	16	27	182
127	88	80	110	40	8.9	2.1			5.9	0.75	193	5.9	8.6	3.2	17	0.5	18	27	74
128	74	5670	5260	860	69.9	12			8.2	0.74	>2000	3.4	24	7.2	755	<0.2	299	66	130
129	30	142	160	48	8.3	1.9			3.7	0.51	>2000	9	10	3.1	30	0.2	11	9	241
130	96	6750	6320	1090	86.5	13			10.4	1	1758	4	30	13	75	<0.2	22	62	75
131	90	2130	2010	350	32.7	7.3			6.7	0.85	1080	6.1	14	5.8	28	<0.2	5	50	183
132	112	5680	5760	1060	92.8	17			10	1.1	1947	2.7	23	12	<5	<0.2	108	154	110
133	88	9000	14400	2160	132	18.6	17	3.9	9.4	1.29	1153	2.6	41	65	10	<0.2	19	58	2
134	84	5410	4760	780	65.7	11			7.1	1	1222	4.5	24	5.1	21	<0.2	138	74	90
135	390	4950	8000	1570	282	54.2	59.4	12.4	24.7	2.81	911	7.93	26	7.1	72	<0.2	270	127	360
136	333	1190	1980	410	79.8	16.6	34.9	6	16.1	2.17	436	8.2	13	4.9	85	<0.2	405	71	369
137	302	3330	5440	1100	200	39.8	47.6	8.2	18.1	2.27	1009	18	22.4	7.2	131	0.7	1482	166	668
138	331	1550	2450	486	92.4	19.9	40.6	8.9	17.6	2.18	631	8.35	11.7	3.1	157	1.1	435	95	579
139	349	1860	3140	780	130	27.8	46	9.4	18.6	2.22	875	9.46	14	4.2	378	<0.2	1240	157	355
140	229	526	900	260	45	10.9	28.7	6.6	12.5	1.53	687	10.8	10.8	4.2	367	1.2	824	112	247
141	171	270	470	150	28.5	7	22	4.1	10.7	1.32	460	11	10	3	329	1	423	129	192
142	356	1900	3280	704	141	29	24.8	9.6	11.8	1.37	481	21.4	12.5	18.2	96	<0.2	64	405	410
143	416	4370	7470	1580	304	60	34.1	13.5	23.5	3.04	553	22.1	27	3.6	118	<0.2	186	1711	423
144	<160	226	383	85	20	4.9	16.7	3	8.4	1.04	377	4	6.7	4.1	130	1.4	727	2151	180
145	<600	1870	3590	770	184	41.1	82.4	16.9	34.3	4.02	658	9.65	16.2	14	615	22.2	10409	24500	1578
146	<230	333	697	160	30	9.4	16.7	4	10	1.25	235	6.81	6	25	307	1.52opt	24400	228700	4342
147	<180	169	270	62	13.8	4.4	6.4	<3	5	0.7	1564	1.48	2.2	16	264	10.1opt	89200	370900	3424
148	60	847	1110	197	45.3	10.4	15.3	3.3	7.5	0.83	1126	1.6	7.9	13.9	770	14.3	10627	1578	433
149	<220	799	1720	510	98.9	22.2	32	5.6	13.9	1.74	505	2.1	7.8	16	1707	2.05opt	45300	29300	2750
150	<180	469	934	260	51	12.9	17	3	8.9	1.18	1487	2	8.7	34	531	5.75opt	88000	98500	3541
151	<270	72	153	52	18.1	6.1	35.8	6.7	24.2	3.12	1801	3.05	9	9	1137	39.7	6648	4094	670
152	110	203	385	140	27.2	6.5	14.9	3.6	9.8	1.25	1827	4.16	47.4	12.3	79	2.5	282	55	30
153	68	450	755	179	25.5	4.4	5.1	1.6	4.2	0.54	213	2.92	10	10.8	<5	<0.2	16	26	30
154	84	9000	20000	4150	200	48			31	1.6	1483	6.3	68	6.7	29	<0.2	99	406	152
155	75	283	350	89	15.6	3.5			6	0.73	358	9	6.9	4.2	45	0.3	73	236	87

156	218	784	1100	280	50.2	11			16	1.9	510	5.5	10	6.9	21	<0.2	228	52	225
157	90	6180	5840	1000	90.2	15			12	0.89	1052	5.2	21	4.6	<5	<0.2	211	85	164
158	113	9000	10500	1780	168	34			19	1.6	1036	3.8	27	2.9	42	<0.2	237	88	96
159	97	9000	10500	2050	200	39	19	1.6			1085	4.9	49	7.1	14	<0.2	393	82	194
160	129	5670	7940	1800	200	45			11	0.94	>2000	4.1	63.3	19	289	3.1	3551	575	204
161	384	5080	9860	2410	489	102	49.4	9.8	15.9	1.93	1111	5.49	123	8.9	74	<0.2	216	409	328
162	399	1290	2600	670	161	40	45	9.3	18.6	2.11	980	2.66	19	1.6	29	<0.2	575	294	234
163	212	943	1750	486	74.6	15.7	10	1.7	2.2	0.28	941	0.71	15	2.6	74	<0.2	448	1680	400
164	120	1380	2230	567	76.8	16.8	17.2	4.4	6.2	0.78	471	4.56	19	8.1	163	<0.2	127	348	74
165	<70	7380	10000	1900	254	48.1	21.9	4	9.4	1.05	1903	4.65	90.6	17	293	3.2	3813	8284	453
166	<90	5100	6570	1200	152	27.8	28	6.3	8.3	0.87	1285	7.18	52.7	14	594	13.8	8774	4288	986
167	95	6130	8020	1520	200	40.1	32	3.9	8.2	0.99	>2000	5.42	47.8	33.6	246	4.6	4240	3260	2670
168	<70	10300	13400	2570	315	58	38	7.7	10	0.94	>2000	3.84	69	65	600	<0.2	2577	5429	3337
169	<100	10800	13600	2490	291	52.5	31.8	5.9	11.2	1.17	>2000	3.91	78.2	52	526	6.9	5174	8144	9726
170	<60	10500	12800	2260	260	49.5	22.6	5.2	9.1	1.07	>2000	3.26	89	36.5	307	2.5	2800	9219	1935
171	140	312	672	208	43	10	15.6	3.1	7.1	0.89	179	4.7	13	7.9	208	0.5	219	115	161
172	<110	130	273	115	25.8	8.2	14	3.1	5.7	0.73	308	3.54	4.7	69	596	36.2	18267	17100	3853
173	82	156	306	100	21.5	5.6	11	2.4	4.4	0.51	295	3.61	6.8	10	25	2.6	365	301	154
174	119	166	304	100	23.8	6	13.4	4.1	8.7	1.08	225	9.2	12.2	6.6	11	1.3	540	296	1115
175	105	600	1170	320	53.9	13.4	17	3.5	6.7	0.71	289	7.48	16.4	26.8	99	25.8	19600	1094	2001
176	<140	3400	4450	818	119	24	27	6.3	8	1.18	794	2.64	60.6	78.9	67	13.6	18118	21400	189
177	117	549	952	320	57.6	13.9	18	4.1	8.9	1.03	1003	9.26	24.7	15	20	6	1297	446	317
178	<100	5880	9570	1940	303	59.3	19.5	2.8	4.5	0.52	>2000	2.75	77.3	37.6	150	<0.2	660	13800	726
179	190	3720	5870	1400	173	33	28.8	6.1	12.6	1.49	1331	5.2	50	15	76	0.9	1749	266	300
180	144	15700	22700	4100	539	100	24.9	2.9	5.5	0.89	915	7.51	150	19	66	<0.2	423	220	80
181	168	3460	5090	1000	150	30.8	21.7	4.8	9.6	1.1	>2000	2.55	48.8	16	25	<0.2	314	247	48
182	57	330	511	107	22.9	5.4	9.3	2.9	5.2	0.62	426	8.51	7.3	5	23	0.5	313	125	160
183	<130	6040	9450	1960	317	63.8	32.8	6.3	6.5	0.77	>2000	5.4	85.8	19.6	250	<0.2	1042	14200	792
184	<120	847	1460	420	79.6	21.7	28	7.3	9.2	1.03	1140	4.43	10	17.9	920	9.4	7297	14300	1259
185	197	344	653	200	45.6	11.8	20.1	6.5	12.3	1.47	1541	12	17.4	9.2	167	1.5	548	72	393
186	175	5020	6640	1160	149	29.8	23.3	5.9	10.3	1.23	1141	3.72	55	10.9	107	<0.2	570	510	237

187	183	3700	6200	1300	221	46.3	51.5	7.4	15.2	1.83	>2000	1.8	40	10	15	<0.2	563	1546	42
188	<200	9720	14200	2700	389	71.8	58.4	7	8.7	1.47	>2000	3.3	93.5	<20	57	<0.2	884	6457	324
189	97	9000	12000	2180	167	26			5.9	0.78	>2000	2.4	53.1	4.4	<5	<0.2	42	86	103
190	99	9000	11400	2030	162	28			6.9	0.65	>2000	2.2	46	7.2	<5	<0.2	30	93	85
191	74	2500	2100	360	27.3	5.6			4.8	0.64	634	2.8	12	3.4	13	<0.2	21	29	100
192	75	591	744	140	17.9	3.3			5.9	0.7	777	3.7	11	7	9	<0.2	52	52	235
193	130	5720	5310	860	79.9	16			9.5	1.4	1579	2.3	16	3.6	<5	<0.2	7	78	38
194	131	4630	5200	1030	104	21			94	1.1	1648	3.3	29	6.4	<5	<0.2	14	80	156
195	116	2700	3210	680	81	16			8.9	0.82	737	1.4	45	22	<5	<0.2	10	48	34
196	69	383	400	96	13.2	2.8			4.9	0.65	263	4.5	8.5	3.7	14	<0.2	42	43	86
197	128	6030	5720	1050	94.5	19			9.1	1	1437	4	25	14	23	<0.2	17	84	61
198	77	223	230	62	10.4	2.5			4.7	0.62	269	5.3	8	2	53	0.3	18	31	97
199	134	4350	4290	810	82.4	16			12	1.1	1744	2.2	12	21	6	<0.2	4	64	41
200	85	3420	3240	560	50.9	10			5.8	0.72	1130	3.4	15	6	20	<0.2	7	34	43
201	106	9000	9040	1410	102	17			11	1.7	1232	2.4	43	9.1	<5	<0.2	19	99	25
202	92	8970	8130	1320	107	20			7.4	1	>2000	2.5	28	10	8	<0.2	7	57	9
203	34	520	561	110	12.3	2.2			2.5	0.32	215	2.5	8	3.8	<5	<0.2	13	23	34
204	62	2630	2720	480	44.9	7.5			5.7	0.7	347	2.6	19	6.7	15	<0.2	13	41	39
205	221	887	1130	238	33.3	7.2	19	5.1	17.4	2.47	236	2.64	59	16.6	25	<0.2	45	41	211
206	501	19100	19300	3520	390	66.8	70	16	35.4	4.55	588	10	30	38	48	<0.2	230	331	690
207	162	250	335	85	17	4.5	14	3	8	1.05	168	4.3	6.2	3.7	28	0.6	22	30	63
208	148	3440	5260	1060	173	35.9	40	5.9	9.9	1.16	>2000	1.68	37.8	9.4	107	<0.2	196	411	40
209	209	4070	7560	2100	357	75.3	53.2	9.7	11.7	1.49	1657	13	93	10.9	102	<0.2	875	506	827
210	117	1310	2110	430	80	17.3	20.7	4	6.7	0.84	1461	3.3	22.1	9.8	31	6	376	322	113
211	154	1060	1940	510	91.6	21.1	29.3	4.7	9.1	1.09	1394	5.51	24.1	50	25	<0.2	222	190	105
212	250	3130	5630	1340	282	65	53.3	10.2	16	1.75	>2000	3.17	39.7	23	<5	<0.2	1073	731	128
213	115	92.7	186	77	18.9	5.4	12	3.1	7.5	0.95	592	8.38	14	4	23	0.7	186	93	126
214	20	54.7	77	24	6.76	2.1	6.6	<3	2.4	0.16	708	3.88	8.5	75	61	2.38opt	37000	1062	5717
215	71	14	36	20	6.8	2.5	8.3	2	3.6	0.44	115	8.16	2.9	5.4	19	36.8	10471	28	841
216	74	20	33	18	5.32	2	4.9	<1	3.1	0.41	155	6.36	3.1	3	12	9.2	4387	23	549
217	42	95.8	160	61	11.1	2.5	4.9	1.2	3.5	0.55	976	4.41	30	7	15	<0.2	110	18	61

218	203	2830	4900	1250	178	37.7	29	4.4	9.2	1.06	689	3.13	52.4	7.7	34	1.9	606	158	578
219	<150	1570	2780	760	106	28.7	19.2	3.9	7.4	0.65	1427	4.09	28.6	16	40	1.9	606	16800	241
220	<110	280	533	160	29.2	7.3	10.7	2.5	5.5	0.7	357	3	12.5	9	73	4.1	957	3561	166
221	149	7230	9970	1780	261	53	38	<3	12	0.6	>2000	5.81	52.4	9	27	5.3	175	70	228
222	155	278	780	140	23.9	5.9	11	3	12	1.83	153	1.33	77.5	18	18	<0.2	84	38	36
223	96	102	172	56	9.96	2.8	6.9	2.5	7.7	1.15	94	1.08	90.7	22	28	<0.2	12	86	42
224	263	617	1520	580	148	37.7	42.6	5.5	14.8	1.86	1073	9.34	27.7	8.6	47	0.7	533	116	694
225	179	950	1180	209	38.5	8.5	19.1	3.3	8.5	1.03	410	3.05	17.6	4.4	7	<0.2	54	41	61
226	54	81.7	126	50	7.69	1.9	6.8	1.4	4.2	0.55	127	4.75	6.9	3.8	7	0.9	270	796	588
227	<150	701	1030	205	42.6	9.1	18.8	2.4	9.9	1.13	324	5.64	13.1	22.5	27	13.1	5962	9815	2778
228	<150	354	416	119	27.7	7.3	14	4	5.2	0.87	154	4.37	8.5	70	67	3opt	13067	210600	2128
229	<120	113	199	53	15.8	3.9	10.8	2.4	6	0.75	152	3.8	7.9	13.1	14	4.5	1876	5012	4716
230	54	625	783	190	36.9	9	13	<9	5.5	0.8	317	5.87	12	195	<58	2.44opt	15173	93400	2954
231	59	44.7	78	40	7.23	1.5	5.9	1.2	4.2	0.53	172	13.4	10.3	4.5	30	2.6	728	747	397
232	<110	822	1120	204	35.9	7	9.6	3	7.8	0.92	318	8.32	14.7	17	31	9.4	3798	27600	6914
233	120	3110	3690	615	92.6	17.8	16.9	4.3	7.6	0.81	453	5.72	15.1	23.6	24	<0.2	150	115	174
234	173	9610	10200	1490	201	40	36	<4	17	1.1	942	21	31	19	<19	0.6	73	131	462
235	92	734	822	185	25.3	5.1	9.2	2.3	6.3	0.8	230	7	10	6.2	7	1.3	201	378	303
236	271	11700	12800	2040	254	43.2	35	10	25.2	2.6	709	33	50	32.7	5	<0.2	29	125	481
237	153	4760	5590	890	124	24	28	<2	11	0.9	750	2.8	16	24	<12	<0.5	135	753	65
238	79	11600	12900	1920	216	41.1	21.2	2.9	8.3	0.95	>2000	7.03	68.5	28.5	15	<0.2	1832	752	158
239	90	264	350	70	15.4	3.8	11.1	3.7	9.4	1.2	267	4.39	11.7	6.4	28	0.2	167	1057	148
240	75	374	502	107	22.7	4.3	12.2	2.9	8	1.1	341	4.59	50.2	9.7	22	<0.2	156	178	133
241	3	2.7	<5	<10	0.27	<0.1	<1	<1	<0.5	<0.1	608	0.13	<0.5	<1	<5	0.3	6	3	45
242	15	16	21	10	2.19	0.6	1	<1	0.7	0.12	131	2.63	2.6	<1	9	0.4	8	5	8
243	50	174	205	49	7.87	1.8	3.4	1	3.5	0.46	282	6.81	3.8	2.4	36	1.9	543	241	181
244	49	26	43	18	4.37	1.2	4.1	<1	3	0.42	13	4.26	7.8	2	10	0.7	173	12	44
245	45	47	78	36	63	1.6	4.1	<1	2.6	0.38	521	2.34	9.2	1.7	7	0.9	171	26	24
246	154	255	360	87	17.7	4.4	13	2.9	9.6	1.3	177	6.9	16	3	61	0.9	222	69	208
247	80	4320	5980	658	77.7	13.6	18.2	6	7.3	1.09	345	9.59	67.1	12.3	41	<0.2	311	440	182
248	95	831	1320	164	26.9	5.4	15.2	4	10.3	1.4	331	10.6	28.8	9.1	30	<0.2	148	99	231

249	142	8630	9080	1340	149	27.4	28.3	4.8	12	1.42	708	4.47	38.3	41.8	80	<0.2	678	148	624
250	81	6480	6430	880	94.9	17	11.1	2.6	9.1	1.03	1008	4.63	29.4	24.8	29	<0.2	594	171	1463
251	76	10800	12300	1900	220	39.1	24.3	4.2	9	0.96	>2000	4.61	52.9	50.7	63	<0.2	529	200	766
252	110	120	209	63	12.8	3.1	14	2.8	9.4	1.42	76	1.45	97.6	16.6	17	<0.2	75	1078	111
253	41	38.8	74	25	5.05	1.1	4.1	1.2	4.8	0.8	59	0.45	77	19	8	<0.2	158	764	116
254	<90	92.4	146	60	12.2	3.6	10.7	2.8	4.2	0.45	577	5.92	4.2	36.4	93	21	23200	12900	1782
255	43	249	370	85	20.7	5	11	1	6.3	0.9	2091	2.7	10	19	170	13	4727	30000	249
256	<140	84	175	67	15.3	4.2	12	1.9	8.4	1.02	287	2.79	9.2	13.8	149	9	1305	9077	416
257	49	467	692	140	26	6	10	<1	5.4	0.8	378	4.1	17	7	94	3.1	903	1987	194
258	47	120	224	76	12.8	3.4	4.1	<1	3.7	0.56	96	8.37	33	6.1	94	<0.2	10	6	30
259	52	41.1	74	27	6.9	1.6	5.5	1.4	3.9	0.52	116	10.5	9.4	2.6	24	<0.2	7	4	8
260	7	64.4	86	23	2.9	<1	<1	<1	0.8	<0.1	53	0.79	1.8	4	<2	<0.5	13	14	55

APPENDIX 7

Laser Ablation ICP-MS

All values are in parts per million

	La	Ce	Pr	Nd	Sm	Eu	Gd	Tb	Dy	Ho	Er	Tm	Yb	Lu
RCBST1	384300	471500	46810	113600	14960	1283	3777	266	716	61	172	0	2	0
RCBST3	340600	415000	42190	108900	17820	1778	5729	478	1639	197	544	1	73	0
RCBST4	307700	344300	32950	78510	9906	808	2528	162	451	30	97	0	0	0
RCBST5	378000	324500	27870	62450	6834	562	1733	104	266	6	45	0	0	0
RCBST6	384600	359500	31280	74470	7213	548	1721	106	249	6	46	0	0	0
RCBST7	308700	285000	25920	58000	5920	392	1403	79	225	4	45	0	0	0
RCBST8	190300	234500	25050	66550	12550	1225	3332	253	944	93	263	0	27	0
RCBST9	326400	368400	35230	84000	10200	850	2676	188	534	43	140	0	0	0
RCBST10	269100	328300	32120	77300	9966	786	2544	163	468	35	114	0	0	0
RCBST11	255000	297700	28980	69980	8311	650	2127	124	363	20	79	0	0	0
RCBST13	261100	328600	33500	84860	12840	1186	3544	245	707	59	159	0	0	0
RCBST14	288300	344100	34140	83690	10780	944	2878	194	578	47	146	0	0	0
RCBST15	243500	285100	28090	68830	8722	668	2242	131	384	20	70	0	0	0
RCBST16	462700	549000	53590	130500	16550	1393	4078	293	720	62	173	0	0	0
RCBST17	328300	348600	33970	82540	10140	838	2542	176	499	36	115	0	0	0
RCBST18	270700	307000	29030	69320	8508	667	2189	135	426	31	110	0	0	0
RCBST19	287800	354000	38600	102500	16090	1448	4153	293	876	76	196	0	2	0
RCBST20	286100	345800	35220	88910	14210	1316	4228	323	1040	104	287	0	18	0
Average	309622	349494	34141	83606	11196	963	2968	206	616	52	156	0	7	0
2 Sigma	127870	143122	14704	38434	7098	759	2222	200	697	93	238	0	36	0
% Error	41	41	43	46	63	79	75	97	113	179	153	849	535	0
M+E 13 L. Bastnaesite 2	13230	13070	1377	3810	361	68	224	22	114	14	54	0	31	0

M+E 13 L. Bastnaesite 3	10260	10730	937	2705	316	46	162	11	79	6	29	0	16	0
M+E 13 L. Bastnaesite 4	5291	6387	499	1554	144	27	82	4	51	1	19	0	10	0
Average	9594	10062	938	2690	274	47	156	13	81	7	34	0	19	0
2 Sigma	8022	6782	878	2256	229	41	142	18	64	13	36	0	22	0
% Error	84	67	94	84	84	86	91	144	78	178	105		114	